DIFFRACTION OF SH-WAVES BY SURFACE OR SUB-SURFACE

TOPOGRAPHIES WITH APPLICATION TO SOIL-STRUCTURE

INTERACTION ON SHALLOW FOUNDATIONS

by

Hao Luo

A Dissertation Presented to the
FACULTY OF THE GRADUATE SCHOOL
UNIVERSITY OF SOUTHERN CALIFORNIA
In Partial Fulfillment of the
Requirements for the Degree
DOCTOR OF PHILOSOPHY
(CIVIL ENGINEERING)

December 2008

ACKNOWLEDGMENTS

First of all, I would like to present my sincerest gratitude to my advisor Professor Vincent W. Lee. He has been directing my research on seismic wave propagation ever since he offered the course "Wave Propagation in Solids" during his sabbatical vacation in 2002 at Tianjin University in China, when I was a Master graduate student of Professor Jianwen Liang out there. Without their encouragement and guidance, my life in the United States would be much harder and this dissertation would not come into existence. I am indebted to two advisors for their generous help all through the past eight years.

I am also grateful to Professor Hung L. Wong, who has been the instructor of three courses for which I was the teaching assistant. His kindness makes us as close as friends. Professor Mihalio D. Trifunac also made many suggestions and comments on several models included in this dissertation when I took his Earthquake Engineering classes in 2006.

Also thanks to the Department of Civil Engineering for giving me an opportunity to have been a teaching assistant. This experience would be very helpful to my future career.

Finally, I would dedicate this dissertation to my parents Luo, Qianyi and Li, Yufang, and my elder brother Luo, Xiao far away in China. Their love and support insist me sustain such a long journey to the present. Without you this dissertation would not have been possible.

TABLE OF CONTENTS

LIST OF FIGURES

ABSTRACT

Seismic response of local sites is a significant problem that has been broadly researched for decades. It is an essential step in evaluating maximum intensity of earthquake effects for a specified local site that might happen in the future considering the effects of local topography or various massive artificial structures nearby, so it is crucial to seismic hazard, risk analysis, and earthquake microzonation. Seismic waves can be categorized into body waves and surface waves. Among the three types of body waves: P-, SV-, and SH-waves, the response of SH-waves, is restrained to the out-of-plane unidirection, thus is the most fundamental one and studied in this dissertation.

The objectives of this dissertation are: first, to explore diffraction of incident plane or cylindrical SH-waves by various topographies or underground irregularities; secondly, to investigate the Soil-Structure Interaction (SSI) effects. Two-dimensional plane strain models studied are as diverse as ground surface irregularities (e.g., hills, canyons, canyons), geotechnical engineering (e.g., tunnels, underground cavities, excavations, foundations), and Soil-Structure Interaction models with non-, rigid, or flexible foundations. Although the geometries adopted in those models are relatively much simpler than the ones by numerical methods, the analytical solutions gained by these simple models are indispensable in verifying solutions by various numerical methods (e.g., Finite Element Method; Boundary Element Method). All the models attempted are sitting or encased in an elastic half-space. All the materials appeared are isotropic, homogeneous, and perfectly elastic.

Wave function expansion method is used for solving all the mathematical models in an analytical scheme. The model is computed by mathematically assembling different segments together on their interfaces adjacent to each other. Finally, the problem is reduced to solving a series of infinite linear equations. The governing finite linear equation systems after truncation via this way are always ill-conditioned that require carefully coped with to ensure the accuracy of solutions.

With the analytical solution attained, the response of displacement and stress along the free ground surface are discussed. Displacement and stress residues are calculated to verify the validity of those numerical results. Great effects on dynamic stress concentration and motion nearby due to the existence of those irregularities are observed, evaluated, and analyzed.

Chapter 1

INTRODUCTION

1.1 Analytical Solutions of Wave Motion Problems in Engineering

Seismic wave diffraction and refraction due to various surface or sub-surface topographies or engineering structures have been attracting interest from earthquake engineers since 1970s. Not come singly but in pairs, Soil-Superstructure-Foundation Interaction, or often simply called Soil-Structure Interaction (SSI) problem, which has close relation with wave propagation problems, is one of the basic and front-edge subjects puzzling civil engineers. Those two problems are often regarded as the bridge connecting seismologists and civil engineers, and together compose the kernel of this dissertation.

In this dissertation, analytical solutions are discussed for diffraction of anti-plane SH-waves by some simply shaped topographies and structures underneath or above a semi-infinite unbounded solid (i.e., a solid bounded only by a plane; or referred to as half-space hereafter). Due to the existence of those surface or sub-surface irregularities, the surface ground displacement amplitude would not be a product of a factor of two any more as to the magnitude of so-called free-field motions expected at a flat site without those irregularities present. Investigation of recent major earthquakes such as 1985 Mexico City earthquake reveals that the rock motions might be amplified at the base of a building structure as high as a factor of five (Wilson, 2002). Approaches for resolving wave motion problems in engineering can be categorized into numerical and analytical methods. Though numerical methods are relatively more suitable for analyzing realistic and complex problems, analytical alternatives are indispensable to explore the dynamic mechanism and verify the accuracies of various numerical solutions. In the era of numerical computations, ample exact analytical closed-form solutions are still in need to validate and verify a variety of numerical computation methods, which are the practical ways to attempt to explain the real world – a much more complex circumstance than what the analytical approaches could be competent for. Furthermore, the rigorous step-by-step procedures to find out an exact analytical solution are the process to look deep into problems. Besides, numerical methods still have their own drawbacks such as the dilemma between discretization size and wave numbers for finite element method. That is because the larger the wave number (or frequency) of incident waves, the more oscillatory the (displacement or stress) solution is. So to represent the oscialltory characteristics by the numerical model, a certain number of mesh points per wavelength has to be applied (Lehmann, 2007). For large wave numbers, the numerical solution is disturbed due to loss of operator stability.

As a clarification, in the subsequent text, analytical or numerical solutions refer to solutions by analytical or numerical methods, respectively. But both of those methods can generate ‘numerical results’. Complicated analytical infinite series solutions have to be calculated numerically on digital computers.

It is well-known that, for a linear system, any impulsive wave can be decomposed into superposition of harmonic waves. This law also exists for the linear (elastic) response of these two waves. Therefore, studies on the response of harmonic waves bear more primitive significance, and only steady-state harmonic (sinusoidal) SH-waves are discussed in this dissertation..

1.2 Literature Review

Research on wave motion can be traced back to the Middle Ages in Europe by mathematicians. Nowadays, the wave equation is taught as a fundamental type of partial differential equations in advanced mathematics textbooks. However, investigation on wave propagation has never stopped. The exploration of wave scattered by miscellaneous objects started to become a hot research area ever since the establishment of complete Maxwell’s equations of electromagnetic waves in the latter half of the nineteenth century and progressive demand of radio communication in the early twentieth century. Electricians lead the state-of-the-art in the area of scattering and diffraction of electromagnetic waves. But electromagnetic waves, on which they focus, are transverse waves or alternatively called shear waves. And the models they studied are commonly circumstanced in a full infinite space. In addition, frequency range of electromagnetic waves (in the scale of kHz to THz even up to EHz) that attracts electricians is far beyond that of seismic waves (typically around 0.01 to 10Hz). Hence, although advances of electromagnetic wave theory shed a great deal of light upon research on seismic waves, further efforts are required due to the unique characters of seismic waves.

Seismologists are quite familiar with wave motion theory since long distance transportation of seismic energy has to be considered as a process of wave propagation. However, wave motion theory has not been appreciated by civil engineers to deal with practical engineering problems, mainly because classic Newtonian mechanics methods are accurate enough for the need of statics, analysis of harmonic vibration, and low-velocity dynamics in most routine engineering tasks. Nevertheless, World War II aroused higher demand for analyzing of high-speed vehicles like missiles. And design of surface or sub-surface blindages and structures to resist regular or nuclear explosions and their derived shock waves spurs the development of the application of elastic wave propagation theory (or called elastodynamics for short). The revival of Lamb's problems since the middle of twentieth century, which were first investigated by H. Lamb in 1904, indicates the prosperity of research for diffraction and scattering of irregularities in civil engineering (mostly concerning models of plates, rods, and slits) and earthquake engineering (mostly concerns on models embedded in a half-space especially layered media).

Due to miscellaneous numerical difficulties, most of analytical closed-form solutions hitherto in earthquake engineering are solved on the assumption that the half-space media are perfect elastic, homogeneous, and isotropic, which is adopted by this research dissertation as well. Among the available analytical solutions, circular cavities (or circular cylinder in 3-D sense) are of the simplest and most fundamental geometry. That makes them received most intensive study and based on that, people develop techniques applicable to more general shapes. Pao and Mow (1973) provided a brief solution of full circular cavity in a full-space (i.e., an unlimited medium) in their monograph regarding diffraction of various body waves including P-, SV-, and SH-waves. Lee (1977) solved the SH-waves diffraction of a full-circular cavity embedded in a half-space by means of image method. Lee and Trifunac (1979) expanded the model to a circular tunnel with one layer of lining.

Canyons and valleys probably are the first two kinds of topographies studied by earthquake engineers. Canyons refer to concave local topographies on a half-space surface while valleys are regarded as canyons filled with alluvial sediments. In 1971, Trifunac utilized Fourier-Bessel wave function expansion method to solve the scattering of plane SH waves by a semi-cylindrical alluvial valley. His follow-up paper about a semi-cylindrical canyon was published in 1973. Wong and Trifunac (1974a,c) extended the valley/canyon models to the elliptical coordinate system. Lee and Cao (1989) replaced the horizontal half-space ground surface by a circular-arc with very large radius, and obtained an approximate analytical solution of diffraction of SV-waves by circular canyons. From then on, Lee and many other researchers employed this approximation method to obtain a set of analytic solutions for P and SV-waves incidence cases. Yuan and Liao (1994, 1995) presented an improved analytical solution of the diffraction of shallow circular-arc canyon and valley for incident plane SH waves without large arc approximation.

By assuming stress/displacement auxiliary functions and making Fourier expansion on them, Yuan and Men (1992) presented a closed-form analytical solution to a semi-circular hill sitting on a half-space. The solution has been extended to arbitrary shallow hill cases in 1996 by Yuan and Liao. Lee et al (2006) adopted a convenient Cosine Half-Range Expansion to obtain an analytical solution of the same model as that of Yuan and Men (1992) with higher accuracy, especially at two rims of the hill. Detail current developments on local seismic magnitude estimation can be found in a recent intensive review by Sánchez-Sesma et al (2002).

Soil-Structure Interaction problem is one of the most classic problems connecting the two disciplines of earthquake engineering and civil engineering. The interaction effect represents the mechanism of energy transfer and dissipation among the elements of the dynamic system: subgrade soil, foundation, and superstructure or more. This interaction effect becomes more prominent while the rigidity of superstructure relatively stiffer than lower foundation and subgrade, for instance a concrete gravity dam or a reactor containment of nuclear-power plants. This effect may only be ignored when the subgrade is much harder than the flexible superstructure, for instance a high-rise or low-rise but lightweight building founded (by piles or other deep foundation) on very stiff bedrock. Traditional seismic design always assumes superstructure fixes on the ground, that is, foundation is perfect rigid and embedded into the half-space; the vibration properties of superstructure only depend on itself; and vibration of foundation is identical to the free-field response and not related to the superstructure. Generally speaking, this fixed-base assumption tends to be conservative and is adopted by most of current seismic design codes (such as ATC-3 or NEHRP-97); however, whether and how to assess the effect of SSI is a highly controversial issue in both industrial and research communities. Recent studies (Mylonakis and Gazetas, 2000; Jeremić et al, 2004) suggest that the SSI can be detrimental to the behavior of structures. And indiscriminate obedience to the dogma of beneficial effect due to SSI may lead to erroneous assessment of the safety margin of ductility and strength of buildings.

Reissner (1936, 1945) published a series of papers on vertical vibration properties of a circular rigid mass resting on an elastic semi-infinite medium. But these models are too simple to reflect the energy transmission mechanism between structures and bases. Housner (1957) brought this issue into earthquake engineers' vision by experimental observations. Parmelee (1967) first proposed a model considering the system of building and soil as a coupled system. Due to complexity of boundary conditions, only a few analytical solutions mostly based on rigid foundation assumption are currently available for engineers. Luco (1969) studied the diffraction of vertically incident plane SH waves by a shear beam erected on a rigid semi-circular foundation. Trifunac (1971) extended his solution to cases of arbitrary incident angles. In the subsequent years, closed-form analytic solutions for elliptical rigid foundation; multiple buildings and foundations for incident plane SH waves have been present (Wong and Trifunac, 1974b,1975). These solutions are all for anti-plane (SH) incident waves. Todorovska (1993a,b) discussed dynamic soil-foundation or structure interaction for in-plane incident waves, that is, P-, SV-, or surface Rayleigh waves. Hayir et al (2001) and Todorovska et al (2001) proposed a simple SSI model with a flexible foundation. Todorovska and Yousef (2006) solved scattering of similar model erected on poroelastic half-space under the impingement of in-plane body waves. A review on Soil-Structure Interaction authored by Trifunac et al (2001) provided a thorough description on the historical developments of this subject with emphasize on related experimental studies.

1.3 Organization

This dissertation is oriented towards providing a document that leads readers gradually master and conceptually understand the methodology of wave propagation theory in earthquake engineering in the sight of analytical method. It is intended to offer comprehensive guidelines for solving regular half-space models subjected to incident SH-waves, but it is not expected to become a wave propagation textbook.

In the first six chapters of this dissertation, a variety of analytical methods, ranging from Large Circular-Arc Approximation; Image Method; Auxiliary Function Method; Cosine Half-Range Transform; and an improved technique based on this transform, are employed to study the antiplane diffraction by various irregularities such as hills, canyons, valleys, and cavities, in a linearly elastic, homogeneous, and isotropic half-space. Some of them have been studied by other researchers but reexamined herein due to certain concern; some of them are new models have never been investigated or published to the knowledge of author. One of major objectives of this dissertation aims at making some comparison among those methods applied in some same simple models and providing some valuable instructions to future research on more complicated models. The remaining chapters of this dissertation treat of some Soil-Structure Interaction models. More details of individual chapters are presented as follows.

Chapter 2 briefly illustrates the physical meaning of mathematical models studied in this dissertation. Then the derivation for two-dimensional free-field response under the impingement of plane or cylindrical SH-waves is presented. Those procedures would be understood and omitted in the subsequent chapters in that they are similar but necessary for all models.

Chapter 3 develops a new approach, Cosine Half-Range Expansion, on a simple semi-cylindrical hill. This approach is more concise than the Auxiliary Function Method which aided Yuan and Men (1992) analyze the same model. Although essentially those two methods both implement Fourier transform, the new method remarkably reduces the stress and displacement residues around two rim points in contrast to the spike phenomena in the paper of Yuan and Liao (1996) that is regarded as the effect of Gibb's phenomena.

Chapter 4 concerns a shallow cylindrical canyon for the incidence of plane or cylindrical SH waves. The derivation provided by Yuan and Liao (1994), although seems theoretically perfect, confronts great numerical difficulties in solving the governing linear simultaneous equations. The numerical computation is believed to be actually based on a set of wave functions defined in another coordinate system, which means one of the boundary conditions is not necessarily satisfied for sure. According to this concern, Image Method is employed to validate the feasibility and accuracy of this alternative coordinate system. Besides, as a preparation for later chapters regarding Soil-Structure Interaction problems for cylindrical SH incidence, the scattering of shallow cylindrical canyon by incidence from a cylindrical SH-waves is analyzed.

The model studied in Chapter 5 is somewhat like a combination of the models in Chapter 3 and 6. It is a concentrically hollow semi-circular hill. Unlike the underlying subsurface cavity in Chapter 6, the semi-circular cavity here is located above the ground surface and encased in the hill.

Chapter 6 deals with an underground semi-cylindrical cavity activated by incident plane SH-waves. While it only slightly differs from a full cylindrical cavity studied by Lee earlier in 1977, this model is expected to serve as a benchmark example for mixed-boundary problems. Thus, multiple methods mentioned above are applied to this model. A detailed description of comparison among those methods is represented at the end of this chapter.

The last three chapters (Chapter 7 to 9) take Soil-Structure Interaction problems as the subject. Chapter 7 deals with a shear beam placed directly on the half-space surface without foundations. Chapter 8 addresses an extensive study on the solution of a shear beam supported on a rigid semi-cylindrical foundation by Trifunac (1972) to shallow cylindrical foundation cases. Chapter 9 adds an elastic flexible semi-cylindrical foundation beneath the model adopted in Chapter 7, and techniques from the previous two chapters are used to solve this model. Chapter 10 contains a solution of similar model as Chapter 7 but the rigid foundation in the new model is encircled by a flexible semi-cylindircal foundation.

Finally, a summary of all the preceding models is present in Chapter 11.

Each chapter of this dissertation is organized in a similar format. First a model is and illustrated; then wave functions in infinite series corresponding to various regions or origions are presented with unknown coefficient sets; then varied mathematical techniques are applied to come down to a set of infinite linear equations based on boundary conditions. At last, numerical results and case studies are provided with figures to augment the foregoing analysis and indicate the effects of diffraction and or dynamic stress concentration. Thus chapters are basically independent with each other and can be readed separately.

Chapter 2

PLANE STRAIN MODELS AND FREE FIELD RESPONSE

2.1 Plane Strain Models

Nearly all of the seismic wave propagation problems concern civil engineers are of half-space models. Despite the outer shape of earth is round, the ground surface could be simplified as a flat plane without considering the undulations on the ground because of the Sommerfeld radiation condition – the influence of local irregularities should be localized. This is a widely accepted assumption to simplify our analysis even for most numerical solutions.

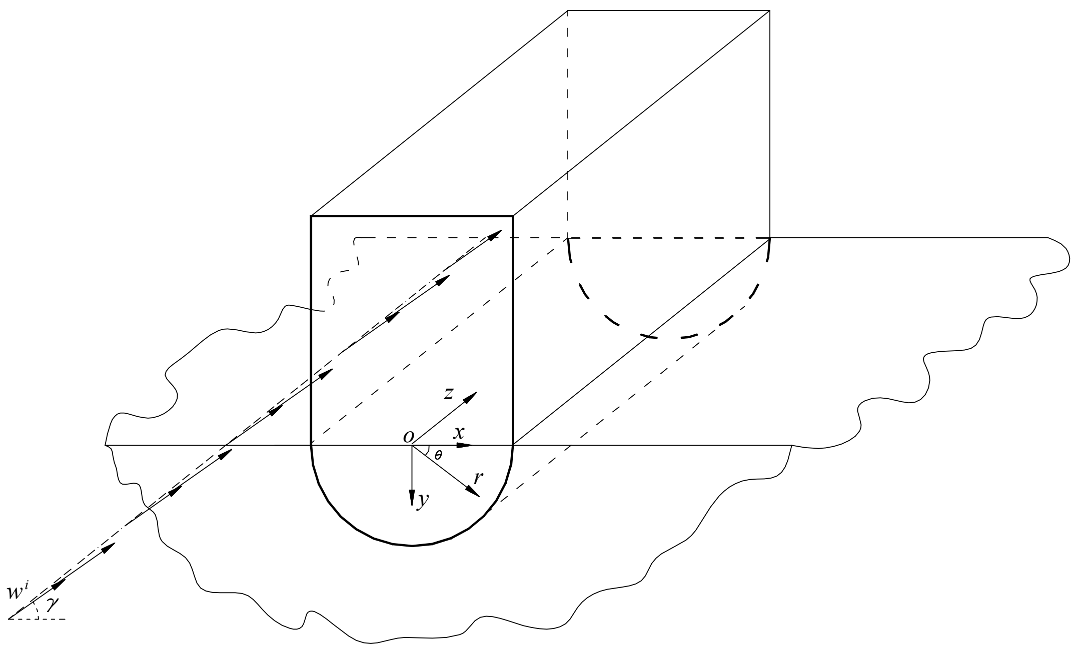

Fig. 2-1 SCHEMATIC DIAGRAM OF THREE-DIMENSIONAL PRISMATIC MODEL

In this dissertation, only two-dimensional plane strain models and SH- incident waves are discussed. In other words, from a three-dimensional point of view, the dimension in the direction normal to the paper is infinite in length. For instance, the prismatic model shown in Fig. 2-1 can be applied to retaining wall, dams, or embankments whose out-of-plane length is much greater than the other two in-plane dimensions. Based on this characteristic of geometrical configuration, the strains associated with out-of-plane length, i.e., $\varepsilon_{zz} = \varepsilon_{xz} = \varepsilon_{yz}$, are constrained by nearby material and are negligible compared to the cross-sectional strains, thus can be disregarded. On the other hand, SH-waves are kind of 'self-contained' owning a nice characteristic that it only stirs up other SH-wave(s) when it impacts a boundary separating different media. On the contrary, other two sorts of body waves, P- and SV-waves, will convert to each other when they impinge boundaries of different media. SH-waves, the abbreviation of Shear Horizontal wave, travel within the plane of paper (*x*-*y* plane), but vibrate in the *z*-direction normal to the paper plane back and forth. This dissertation adopts the geometry of irregularities in a two-dimensional sense for most cases, so it is equivalent to those models studied in other publications that, for instance, may refer to a semi-circular canyon here as a semi-cylindrical canyon in a three-dimensional sense. Therefore, this dissertation only discusses plane strain models.

2.2 Free Field Motion in the Half-Space

Two types of SH-waves are discussed in this dissertation. One is plane SH-wave as illustrated in Fig. 2-2; the other is SH point-source depicted in Fig. 2-3. Plane incident SH-waves are often used to represent far-field incident wave field aroused by seismic activities in close proximity of seismic faults or nearby major (nuclear) detonations. Cylindrical incident SH-waves are often applied to represent antiplane waves emitted from near-field linear vibration sources; or sometimes it is used to imitate a 3-dimensional point-source, which actually emits spherical waves, are more often to see in mining and underground engineering like tunneling. Here plane or cylindrical is the idealized wavefront configuration of the incident SH-waves traveling in a semi-infinite three-dimensional elastic half-space medium with propagation direction in the *x*-*y* plane and (anti-plane) particle motions in the *z*-direction.

2.2.1 Plane SH-Wave Incidence

Fig. 2-2 shows a bunch of parallel plane SH-waves $w^{(\mathrm{i})}$ is impinging upwards the ground surface L, the only external boundary of half-space. Assume the total anti-plane wave field within the half-space after scattered from L with or without various irregularities is $w = w(r,\theta)$, then it must satisfy the following differential wave equation

$$\frac{\partial^2 w}{\partial r^2}+\frac{1}{r}\frac{\partial w}{\partial r}+\frac{1}{r^2}\frac{\partial^2 w}{\partial \theta^2}+k^2 w=0 \tag{8.1}$$

Here the radial coordinate system (r,θ) originates from a center on the ground surface. For a half-space only involves SH-waves propagate inside, the following traction-free boundary conditions should be satisfied

$$\tau_{\theta z}\,|_{\theta=0,\pi}=0 \qquad (r,\theta)\in L \tag{8.2}$$

in which,

$$\tau_{\theta z}=\frac{\mu}{r}\frac{\partial w}{\partial \theta} \tag{8.3}$$

denote the total hoop stress. μ is the shear modulus of the half-space medium. In case the traction-free boundary is circular (cylindrical), the boundary condition is better to be expressed by radial stress τ_{rz} on it,

$$\tau_{rz}=\mu\frac{\partial w}{\partial r} \tag{8.4}$$

Two Cartesian coordinate systems have been set up in Fig. 2-2. The incident waves could be expressed in the coordinate $x-o-y$ as follows, in which all the harmonic time factor $\mathrm{e}^{-\mathrm{i}\omega t}$ are assumed to be understood and suppressed from every wave functions throughout this dissertation hereafter if not specified.

$$w^{(\mathrm{i})}(x,y)=\exp\left[\mathrm{i}\left(k_x x-k_y y\right)\right]=\exp\left[\mathrm{i}k\left(x\cos\gamma-y\sin\gamma\right)\right] \tag{8.5}$$

And the reflected waves could be written as

$$w^{(\mathrm{r})}(x,y)=\exp\left[\mathrm{i}\left(k_x x+k_y y\right)\right]=\exp\left[\mathrm{i}k\left(x\cos\gamma+y\sin\gamma\right)\right] \tag{8.6}$$

where $\mathrm{i}=\sqrt{-1}$ denotes the imaginary unit. $k_x=k\cos\gamma$, $k_y=k\sin\gamma$, and k are the x, y components of wave number incident SH wave, and wave number of incident wave itself, respectively.

Equations (8.5) and (8.6) comprise the free-field

$$w^{(\mathrm{ff})}=w^{(\mathrm{i})}+w^{(\mathrm{r})} \tag{8.7}$$

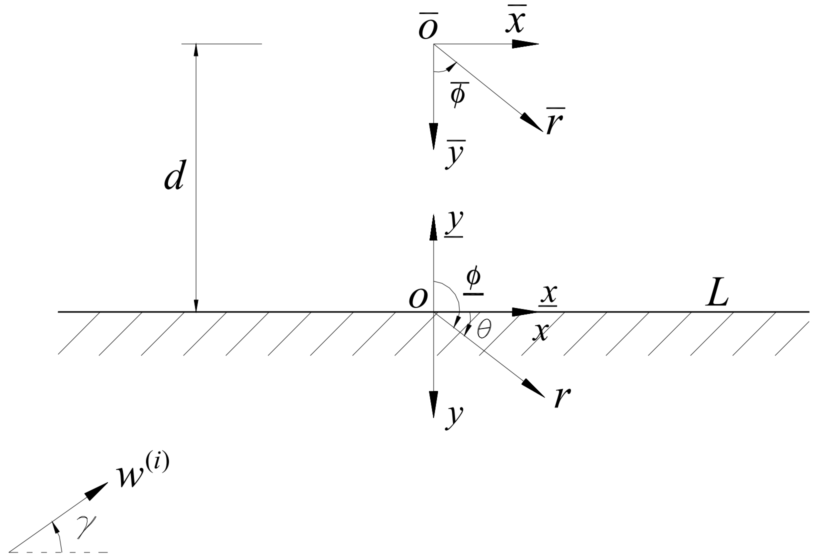

Fig. 2-2 COORDINATE SYSTEMS OF PLANE SH-WAVES FOR FREE-FIELD

Transform them into polar coordinate (r,θ) by relations $x = r\cos\theta$ and $y = r\sin\theta$ and Jacobi-Anger Expansion,

$$\mathrm{e}^{\pm \mathrm{i}z\cos\theta} = \sum_{n=-\infty}^{\infty} (\pm \mathrm{i})^n \mathrm{J}_n(z)\mathrm{e}^{\mathrm{i}n\theta} = \sum_{n=0}^{\infty} \varepsilon_n (\pm \mathrm{i})^n \mathrm{J}_n(z)\cos n\theta \tag{8.8}$$

We obtained

$$w^{(\mathrm{ff})}(r,\theta) = \sum_{n=-\infty}^{\infty} \mathrm{J}_n(kr) a_n^{(\mathrm{f},e)} \mathrm{e}^{\mathrm{i}n\theta} = \sum_{n=0}^{\infty} \mathrm{J}_n(kr) a_n^{(\mathrm{f},t)} \cos n\theta \tag{8.9}$$

where $\mathrm{J}_n(\cdot)$ is the Bessel function of the nth order and the first kind. And,

$$a_n^{(\mathrm{f},e)} = 2\mathrm{i}^n \cos n\gamma \tag{8.10}$$

$$a_n^{(\mathrm{f},t)} = 2\varepsilon_n \mathrm{i}^n \cos n\gamma \tag{8.11}$$

represent the coefficients of the exponential or trigonometric expression, respectively. Here Neumann factor $\varepsilon_0 = 1$, $\varepsilon_n = 2$ for n =1,2,3 ···. The superscripts ,*e* or ,*t* will be omitted in the subsequent chapters for brevity. Inserting equation (8.9) into (8.4) leads to the stress generated by the free-field wave

$$\tau_{rz}^{(\mathrm{ff})}(r,\theta) = \mu k \sum_{n=0}^{\infty} a_n^{(\mathrm{f},t)} \mathrm{J}_n'(kr)\cos n\theta \tag{8.12}$$

Now applying relations $\overline{x} = x$, $\overline{y} = y + d$ and identity (8.8) to transform free-field expressions to upper coordinate system $\left(\overline{r}, \overline{\phi}\right)$

$$w^{(\mathrm{ff})}\left(\overline{r}, \overline{\phi}\right) = \sum_{n=-\infty}^{\infty} \mathrm{J}_n\left(k\overline{r}\right) \overline{a}_n^{(\mathrm{f})} \mathrm{e}^{\mathrm{i}n\overline{\phi}} \tag{8.13}$$

in which,

$$\overline{a}_n^{(\mathrm{f})} = 2\cos\left(kd\sin\gamma - n\gamma\right) \tag{8.14}$$

2.2.2 Cylindrical SH-Wave Incidence

Fig. 2-3 shows that a SH-wave line source is located at O' with radial distance and incident angle with respect to horizontal axis equal R and γ, respectively. The perpendicular distance between the center $\overline{O}$ and ground surface is d.

The incident cylindrical waves with unit amplitude at center O could be expressed as follows,

$$w_{O'}^{(\mathrm{i})}(r') = \frac{\mathrm{H}_0^{(1)}\left(kr'\right)}{\left|\mathrm{H}_0^{(1)}\left(kR\right)\right|} \tag{8.15}$$

where $\mathrm{H}_n^{(1)}(\cdot)$ represents the Hankel function of the nth order and the first kind. The denominator $\left|\mathrm{H}_0^{(1)}\left(kR\right)\right|$ is a scaling factor to make the resultant displacement amplitude at center O by incident waves equal one; in other words, the resultant displacement amplitude by incident waves together with their reflection waves equal two. Here the harmonic time factor $\mathrm{e}^{-\mathrm{i}\omega t}$ is omitted just as what we did for plane SH-waves. Depending on the asymptotic properties of Hankel function, the amplitude of incident waves degenerates along with their respective radial arguments increase (Bowman et al, 1969; Pao and Mow, 1973). That conforms to the behavior of the source-emitted waves and Sommerfeld radiation condition. The reflected waves could be thought of as an image line source with respect to the flat ground surface originated at O'' shown in Fig. 2-3.

$$w_{O''}^{(\mathrm{r})}(r'') = \frac{\mathrm{H}_0^{(1)}\left(kr''\right)}{\left|\mathrm{H}_0^{(1)}\left(kR\right)\right|} \tag{8.16}$$

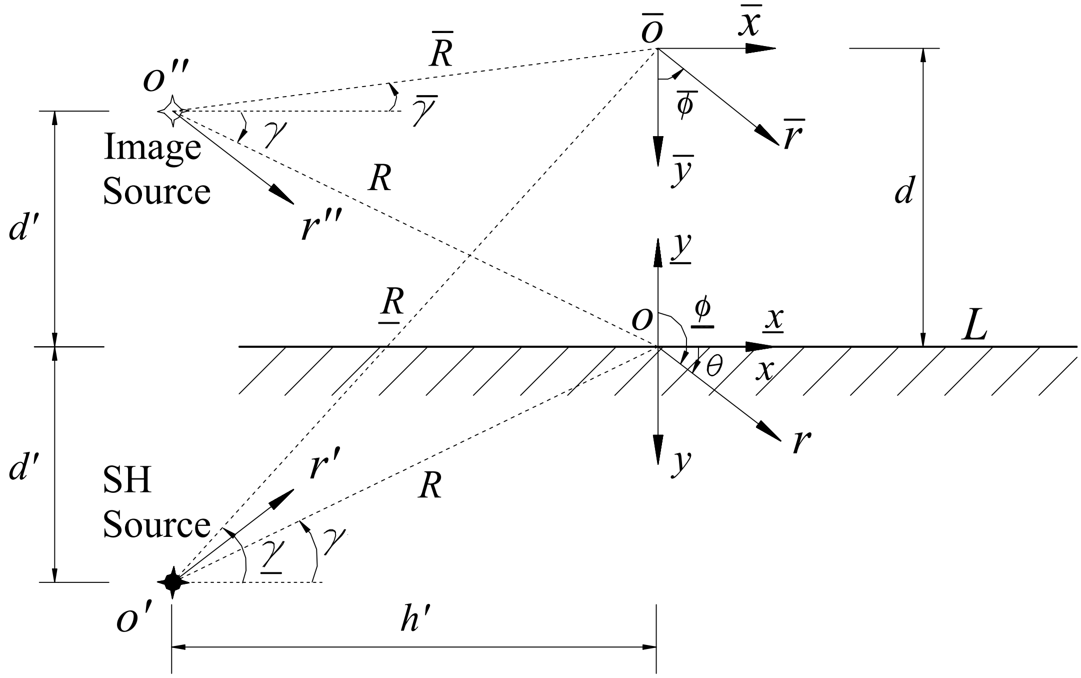

Fig. 2-3 COORDINATE SYSTEMS OF SH LINE SOURCE FOR FREE-FIELD

After Graf addition formula (introduced in section 2.3) and a set of coordinate transformations are applied, the incident and reflected wave formulae in the coordinate system (r,θ) could be obtained (MacDonald, 1902)

$$w^{(\mathrm{i})}(r,\theta)=\sum_{n=0}^{\infty}(-1)^n\frac{\mathrm{H}_n^{(1)}(kR)}{\left|\mathrm{H}_0^{(1)}(kR)\right|}\mathrm{J}_n(kr)\mathrm{e}^{\mathrm{i}n(\theta+\gamma)} \tag{8.17}$$

$$w^{(\mathrm{r})}(r,\theta)=\sum_{n=0}^{\infty}(-1)^n\frac{\mathrm{H}_n^{(1)}(kR)}{\left|\mathrm{H}_0^{(1)}(kR)\right|}\mathrm{J}_n(kr)\mathrm{e}^{\mathrm{i}n(\theta-\gamma)} \tag{8.18}$$

and the free-field in the absence of any variation of topography is the sum of these two wave fields

$$w^{(\mathrm{ff})}(r,\theta)=w^{(\mathrm{i})}+w^{(\mathrm{r})}=\sum_{n=-\infty}^{\infty}\mathrm{J}_n(kr)\,a_n^{(\mathrm{f},e)}\mathrm{e}^{\mathrm{i}n\theta}=\sum_{n=0}^{\infty}\mathrm{J}_n(kr)\,a_n^{(\mathrm{f},t)}\cos n\theta \tag{8.19}$$

where

$$a_n^{(\mathrm{f},e)}=2(-1)^n\frac{\mathrm{H}_n^{(1)}(kR)}{\left|\mathrm{H}_0^{(1)}(kR)\right|}\cos n\gamma \tag{8.20}$$

$$a_n^{(\mathrm{f},t)} = 2\varepsilon_n(-1)^n \frac{\mathrm{H}_n^{(1)}(kR)}{\left|\mathrm{H}_0^{(1)}\left(kR\right)\right|}\cos n\gamma \tag{8.21}$$

There are two ways to transform $w^{(i)}$ and $w^{(r)}$ from their respective coordinate system to polar coordinate system $\left(\overline{r},\overline{\phi}\right)$ originated at $\overline{O}$. The first approach uses Graf's formula by twice (first transforming from O' and O'' to O, then transforming to $\overline{O}$. Two Graf's formulae are of interior and exterior types in sequence.

$$w^{(\mathrm{ff})}(\overline{r},\overline{\phi}) = \sum_{n=-\infty}^{\infty} \overline{a}_n^{(\mathrm{f})}\mathrm{J}_n\left(k\overline{r}\right)\mathrm{e}^{\mathrm{i}n\overline{\phi}} \tag{8.22}$$

where

$$\overline{a}_n^{(\mathrm{f})} = \sum_{m=0}^{\infty}\varepsilon_m \mathrm{i}^m \frac{\mathrm{H}_m^{(1)}(kR)}{\left|\mathrm{H}_0^{(1)}\left(kR\right)\right|}\cos m\gamma\left[\mathrm{J}_{n+m}(kd) + \mathrm{J}_{n-m}(kd)\right] \tag{8.23}$$

In special, for $n = 0$, $\overline{a}_0^{(\mathrm{f})} = 2\sum_{m\ \mathrm{even}}^{\infty}\varepsilon_m \mathrm{i}^m \frac{\mathrm{H}_m^{(1)}(kR)}{\left|\mathrm{H}_0^{(1)}\left(kR\right)\right|}\mathrm{J}_m(kd)\cos m\gamma$.

The other approach directly transforms incident and reflected wave from their respective origin to $\overline{O}$. Both Graf's formulae are of interior type. Wave function of free field is the same as equation (8.22), but its coefficients alter to

$$\overline{a}_n^{(\mathrm{f})} = \frac{\mathrm{i}^n}{\left|\mathrm{H}_0^{(1)}\left(kR\right)\right|}\left[\mathrm{H}_n^{(1)}(k\underline{R})\mathrm{e}^{-\mathrm{i}n\underline{\gamma}} + \mathrm{H}_n^{(1)}(k\overline{R})\mathrm{e}^{-\mathrm{i}n\overline{\gamma}}\right] \tag{8.24}$$

with the following parameters

$$\overline{R} \text{ or } \underline{R} = \sqrt{\left(d \mp d'\right)^2 + h'^2}; \qquad \overline{\gamma} \text{ or } \underline{\gamma} = \arctan\left(\frac{d \mp d'}{h'}\right) \tag{8.25}$$

represent the radial distance and angles from O' or O'' to $\overline{O}$. Please refer to Fig. 2-3 for specific meanings of those parameters.

Both expressions of equations (8.23) and (8.24) have their own advantages. Equation (8.23) is much complicated than (8.24) in arithmetical sense; but has broader applicability because of the Graf's formula, especially when the location of line source is rather close to the local irregularities, i.e., R is small. Both these two expressions are adopted in the latter chapters and used alternatively without indicated.

2.3 Graf's Addition Formula

Graf's addition formula often appears in wave propagation literature when transforming wave functions among different coordinate systems. For instance, the following Graf's formula (Pao and Mow, 1973) can be used to transform wave functions from lower coordinate system $\left(\underline{r},\underline{\phi}\right)$ to the upper polar coordinate system $\left(\overline{r},\overline{\phi}\right)$ shown in Fig. 2-2

$$\mathcal{C}_n\left(k\underline{r}\right)\mathrm{e}^{\mathrm{i}n\underline{\phi}}=\sum_{m=-\infty}^{\infty}\mathrm{J}_{n+m}\left(kd\right)\mathcal{C}_m\left(k\overline{r}\right)\mathrm{e}^{\mathrm{i}m\overline{\phi}}\text{, for }\overline{r}>d \tag{8.26}$$

where $\mathcal{C}_n(\cdot)$ denotes $\mathrm{J}_n(\cdot)$ or $\mathrm{H}_n^{(1)}(\cdot)$. Note that this formula only works for $\overline{r}>d$ when $\mathrm{H}_n^{(1)}(\cdot)$ applied, please refer to Fig. 2-4(b) for details. That is why it is often referred to as exterior Graf's formula. When $C_n(\cdot)$ denotes $\mathrm{J}_n(\cdot)$, this restriction is removed. To the contrary, interior Graf's formula as follows only works for $\overline{r}<d$ when $\mathrm{H}_n^{(1)}(\cdot)$ applied (as shown in Fig. 2-4(a)), but is applicable for any $\overline{r}$ when $\mathrm{J}_n(\cdot)$ substituted.

$$C_m\left(k\underline{r}\right)\mathrm{e}^{\mathrm{i}m\underline{\phi}}=\sum_{n=-\infty}^{\infty}C_{m+n}\left(kd\right)\mathrm{J}_n\left(k\overline{r}\right)\mathrm{e}^{\mathrm{i}n\overline{\phi}}\text{, for }\overline{r}<d \tag{8.27}$$

According to Euler's formula, these two Graf's formulae can be changed to their trigonometric forms

$$C_m\left(k\underline{r}\right)\begin{Bmatrix}\cos m\underline{\phi}\\ \sin m\underline{\phi}\end{Bmatrix}=\sum_{n=-\infty}^{\infty}\mathrm{J}_{m+n}\left(kd\right)C_n\left(k\overline{r}\right)\begin{Bmatrix}\cos n\overline{\phi}\\ \sin n\overline{\phi}\end{Bmatrix}\text{, for }\overline{r}>d \tag{8.28}$$

$$C_m\left(k\underline{r}\right)\begin{Bmatrix}\cos m\underline{\phi}\\ \sin m\underline{\phi}\end{Bmatrix}=\sum_{n=-\infty}^{\infty}C_{m+n}\left(kd\right)\mathrm{J}_n\left(k\overline{r}\right)\begin{Bmatrix}\cos n\overline{\phi}\\ \sin n\overline{\phi}\end{Bmatrix}\text{, for }\overline{r}<d \tag{8.29}$$

They can be further converted to the following form with index *n* ranging from 0 to ∞

$$C_m\left(k\underline{r}\right)\begin{Bmatrix}\cos m\underline{\phi}\\ \sin m\underline{\phi}\end{Bmatrix}=\sum_{n=0}^{\infty}\frac{\varepsilon_n}{2}C_n\left(k\overline{r}\right)\begin{Bmatrix}\left[\mathrm{J}_{m+n}\left(kd\right)+\left(-1\right)^n\mathrm{J}_{m-n}\left(kd\right)\right]\cos n\overline{\phi}\\ \left[\mathrm{J}_{m+n}\left(kd\right)-\left(-1\right)^n\mathrm{J}_{m-n}\left(kd\right)\right]\sin n\overline{\phi}\end{Bmatrix}\text{, for }\overline{r}>d \tag{8.30}$$

$$C_m\left(k\underline{r}\right)\begin{Bmatrix}\cos m\underline{\phi}\\ \sin m\underline{\phi}\end{Bmatrix}=\sum_{n=0}^{\infty}\frac{\varepsilon_n}{2}\mathrm{J}_n\left(k\overline{r}\right)\begin{Bmatrix}\left[C_{m+n}\left(kd\right)+\left(-1\right)^n C_{m-n}\left(kd\right)\right]\cos n\overline{\phi}\\ \left[C_{m+n}\left(kd\right)-\left(-1\right)^n C_{m-n}\left(kd\right)\right]\sin n\overline{\phi}\end{Bmatrix},\ \text{for } \overline{r}<d \quad (8.31)$$

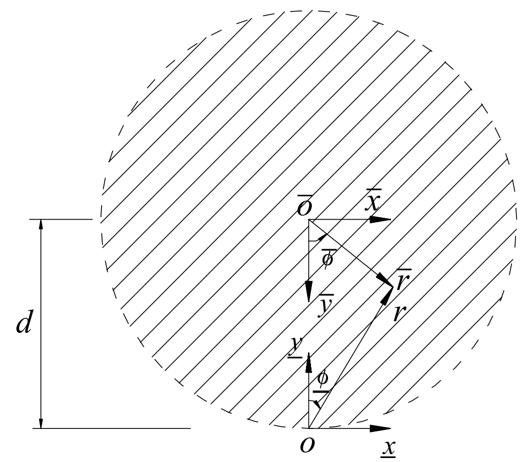

(a) Interior area

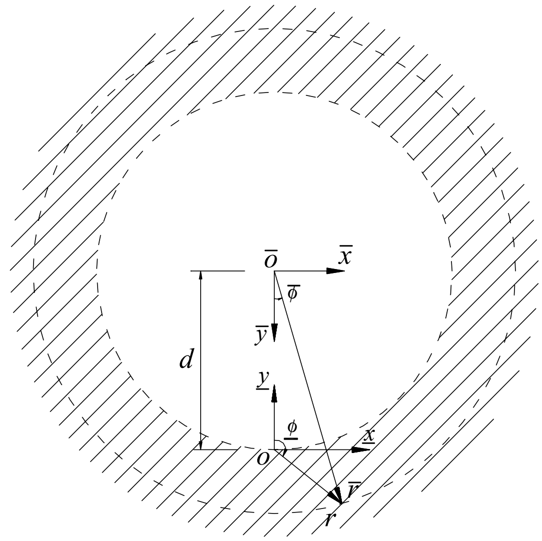

(b) Exterior area

Fig. 2-4 GRAF'S ADDITION FORMULA

Equations (8.26) through (8.31) are several kinds of forms of Graf's formula that most likely appear in related literatures. Of them undoubtedly equations (8.26) and (8.27) are the simplest pair and all other forms can be derived from them conveniently.

Chapter 3

SEMI-CYLINDRICAL HILL FOR PLANE SH-WAVES REVISITED

Hill topography, like canyons and valleys, is a sort of common local surface irregularity on the earth's surface which can cause scattering and diffraction of incoming seismic waves, resulting in significant amplifications and de-amplifications on and around the hill surface and on the nearby flat ground surfaces. The case of a semi-circular hill above a flat, elastic, homogeneous half-space surface is a kind of simple hill topography for the modeling of real surface hill topographies. Relatively speaking, hill topography presented a much higher degree of complexity than other surface or sub-surface irregularities including a canyon or alluvial valley or an underground circular cavity or tunnel in a flat half-space. It was much more difficult to formulate a simple, closed-form analytic solution.

3.1 Analytical Solutions of Hills: A Short Review

A semi-circular hill on the surface of an elastic half-space was first investigated just over 10 years ago (Yuan and Men, 1992; Yuan and Liao, 1996). Works on similar geometry, like trough or canyon, in electromagnetic waves were also completed recently (Hinders and Yaghjian, 1991; Park et al, 1992, 1993). In 2001, two companion papers regarding antiplane response of a 2-D triangular hill (or with a flexible circular foundation) by incident plane SH-waves were published by Hayir et al and Todorovska et al. Their analytical results do not agree with a previous paper (Sánchez-Sesma et al, 1982) which used a numerical boundary element method. Qiu and Liu (2005) pointed out the incorrectness in Hayir et al's paper and revisited the antiplane diffraction solution of an isosceles triangular hill using the method of complex function. To the contrary their results match with the numerical results of Sánchez-Sesma et al (1982). A solution of semi-cylindrical hill under the excitation of plane P-waves is presented by Liang et al. (2005) by means of auxiliary function method, in which the free ground surface is simulated by large arc approximation.

In Yuan et al's paper, summarized in the next section, the authors defined two auxiliary functions, one for the stress and the other for the displacement residues at the interface between the circular region of the hill with the empty space on top and the half-space medium below. Two sets of wave functions were defined, one that was finite everywhere inside the circular hill region, and the other representing outgoing waves from the circular hill to everywhere in the half-space. The coefficients of the wave series were then calculated by setting each term of both residual auxiliary functions to zero through Fourier series expansion. The solution, referred to as Auxiliary Function method in the subsequent text, can be considered as an implicit Rayleigh-Ritz method, or method of weighted residues. Yuan and Men (1992) did this for the case of incident SH waves on a semi-circular hill and Yuan and Liao (1996) generalized the solution to the case of shallow circular hill. The accuracy of the solution was evaluated by calculating the stress and displacement residual amplitudes of the auxiliary functions at the circular boundary of the hill. They found that the residual errors of computation are more significant or large on or near the rim of the hill, on both the left and right points of intersection of the circular hill with the flat half-space surface. As stated by the authors in the section "Accuracies of the solution" in the paper by Yuan and Liao (1996), they attribute "*the exhibition of the abrupt change of the stress residual near the hill*" to "*the singularity of auxiliary stress function at the two points"*, which is "*more complicated than the Gibb's phenomena*". And "*As a result, the solution presented in the paper is not accurate at the hill rim …*".

For whatever the real complicated reason was, the authors acknowledged that the use of the auxiliary residual function and the method of solution resulted in the solutions that were not accurate at the rim of the hill. In this chapter, the solution of the hill problem was re-visited. The stress and displacement boundary conditions at the interface between the circular hill and the free space on top, and the half-space medium below, were reformulated. The continuity of both the stress and displacement at every point of the interface, including the rims of the hill, was enforced and established, resulting in a closed form analytic solution that was accurate, without any overshoot of residual amplitudes at the hill rims.

3.2 A New Approach Using Cosine Half-Range Expansion

The cross section of the two-dimensional model studied in this chapter is shown in Fig. 3-1. It is identical to that considered by Yuan and Men (1992). It represents an elastic, isotropic and homogeneous half-space with a semi-cylindrical hill of radius a. The free surface of the half-space consists of a flat surface Γ and circular-arc hill boundary **L**. The rectangular coordinate (x, y) and corresponding polar coordinate (r,θ) systems are as defined in Fig. 3-1. The angle θ is measured from the horizontal *x*-axis clockwise towards the vertical *y*-axis which is pointing downwards into the half-space.

The half-space in Fig. 3-1 is divided into two regions, an interior and exterior region. The interior region **C** is the full circular region with the circular hill as the upper part and a semi-circular portion of the half-space as the lower part. This interior region has the boundary **L,** between the hill and the empty space (air) on top and **$\underline{L}$,** between the interior and exterior regions of the half-space. The exterior region, **H**, is the rest of the half-space outside the region **C**. The flat surface of the half-space beyond the hill is denoted by Γ.

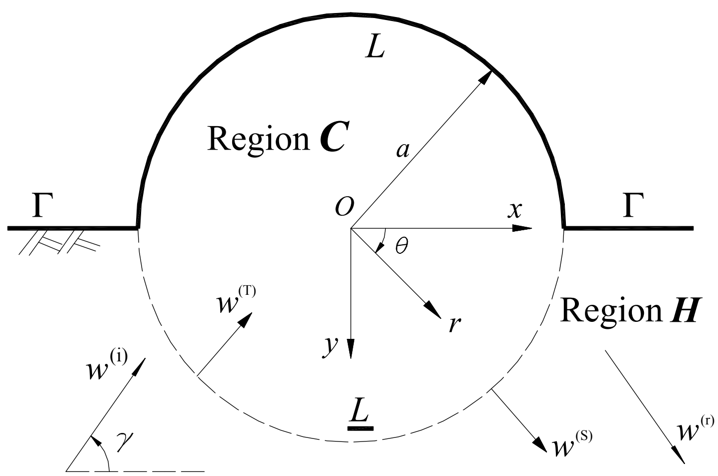

Fig. 3-1 SEMI-CYLINDRICAL HILL MODEL

The excitation of the half-space medium consists of a train of steady-state incident plane SH waves, $w^{(i)}$, with incidence angle γ and (anti-plane) particle motions in the *z*-direction. Please refer to Chapter 2 for the details of derivation of free-field motion for incident plane SH-waves, only equation (8.9) is repeated here for convenience

$$w^{(\mathrm{ff})}\left(r,\theta\right)=w^{(\mathrm{i})}+w^{(\mathrm{r})}=\sum_{n=0}^{\infty}a_{0,n}\mathrm{J}_n\left(kr\right)\cos n\theta \tag{9.1}$$

and for n=0, 1, 2, …, the coefficients of the free-field motion are

$$a_{0,n}=2\varepsilon_n\mathrm{i}^n\cos n\gamma \tag{9.2}$$

3.2.1 The Scattered and Transmitted Waves: Wave Function Series Expansion

The presence of the semi-circular Hill on top of the half-space resulted in scattered and diffracted outgoing waves in the half-space ***H*** outside the circular region of the Hill, $w^{(\mathrm{S})}$, and standing transmitted waves inside the circular region ***C*** of the hill, $w^{(t)}$. The scattered and transmitted waves, $w^{(s)}$ and $w^{(t)}$ can all be represented as wave function series, and respectively take the form:

$$\begin{gathered} w^{(\mathrm{S})}(r,\theta)=\sum_{n=0}^{\infty}A_n\mathrm{H}_n^{(1)}(kr)\cos n\theta \ \ ,\ a\le r \\ w^{(\mathrm{T})}(r,\theta)=\sum_{n=0}^{\infty}\mathrm{J}_n(kr)\left(B_n\cos n\theta+C_n\sin n\theta\right)\ ,\ r\le a \end{gathered} \tag{9.3}$$

where A_n, B_n and C_n are the unknown coefficients of the new waves to be determined. The scattered waves $w^{(\mathrm{S})}$ in the half-space region ***H*** ($r \ge a$, $0 \le \theta \le \pi$) has for $n = 0,1,2$ … $\mathrm{H}_n^{(1)}(kr)$, Hankel functions of the first kind as wave functions to correspond to outgoing waves towards infinity, satisfying Sommerfeld's radiation condition (Pao and Mow, 1973). Only the cosine functions $\cos n\theta$ for $n = 0,1,2$… are used as they form a complete orthogonal set of functions in the half-space region ***H*** ($0 \le \theta \le \pi$), which as shown below, are appropriate for the stress-free boundary condition at the half-space surface. The transmitted waves $w^{(\mathrm{T})}$ in the circular hill region *C* ($r \le a$, $-\pi \le \theta \le \pi$) has for $n = 0,1,2$ … $\mathrm{J}_n(kr)$, Bessel functions of the first kind as wave functions so that the waves are finite everywhere in the hill region *C*. Both the cosine and sine functions

$\cos n\theta$, $\sin n\theta$ for n = 0,1,2… are used as both sets together form a complete orthogonal set of functions in the full circular region ($-\pi \le \theta \le \pi$).

Each term in each of the wave functions of the total displacement field $w = w^{(\mathrm{ff})} + w^{(\mathrm{S})}$ in the half-space region ***H*** and the transmitted field $w^{(t)}$ in the circular region ***C***, all satisfies the steady-state elastic wave equation (equation (8.1)) and, with each term of $w^{(\mathrm{ff})}$ and $w^{(\mathrm{S})}$ being a cosine function, they automatically satisfy the anti-plane (SH) traction-free boundary condition at the surface of the flat half-space $\boldsymbol{\Gamma}$ (y =0 or θ= 0 and π):

$$\tau_{yz}\Big|_{y=0} = \tau_{\theta z}\Big|_{\theta=0,\pi} = \frac{\mu}{r}\frac{\partial w}{\partial \theta}\bigg|_{\theta=0,\pi} = 0 \tag{9.4}$$

The remaining boundary conditions for the waves are:

I) the traction-free condition at the surface of the circular hill, ***L*** ($r = a$, $-\pi \le \theta \le 0$) on top:

$$\tau_{rz}\Big|_{r=a} = \mu \frac{\partial w^{(\mathrm{T})}}{\partial r}\bigg|_{r=a} = 0 \tag{9.5}$$

which involves only the transmitted waves inside the circular hill.

II) the continuity of displacement and stress at ***L***, the interface between the half-space ***H*** and circular hill ***C*** ($r = a$, $0 \le \theta \le \pi$) below the hill:

$$\begin{aligned} w^{(\mathrm{ff})} + w^{(\mathrm{S})}\big|_{r=a} &= w^{(\mathrm{T})}\big|_{r=a} \\ \tau_{rz}\Big|_{r=a} = \mu \frac{\partial\left(w^{(\mathrm{ff})} + w^{(\mathrm{S})}\right)}{\partial r}\bigg|_{r=a} &= \mu \frac{\partial w^{(\mathrm{T})}}{\partial r}\bigg|_{r=a} \end{aligned} \tag{9.6}$$

These two boundary conditions are used to solve for the coefficients in the wave functions.

3.2.2 The Previous Solution Using Auxiliary Function Method

The standing transmitted waves inside the circular hill, being defined in the whole circular region C ($r \le a$, $-\pi \le \theta \le \pi$) have two different sets of boundary conditions to satisfy, namely, (Eqn(9.5)) the anti-plane zero-traction on the circular Hill, L (r = a, -π ≤ θ ≤ 0), and (Eqn(9.6)) the continuity of stress and displacement in the lower half $\underline{L}$ ($r = a$, 0 ≤ θ ≤ π). Since the two sets on the disjoint range are incompatible, Yuan and Men (1992) could not use the orthogonal properties of the trigonometric functions to satisfy the boundary conditions to solve for the unknown coefficients. Instead they define two auxiliary functions to represent the stress and displacement residuals at the circular boundary (r =a) and define the unknown coefficients so as to require the Fourier series expansion of the auxiliary functions be set to zero term by term. This numerical method falls into the category of the Method of Weighted Residues. The two auxiliary functions are the normalized stress residual, Φ(θ) and displacement residual, Ψ(θ) functions, respectively

$$\Phi(\theta) = \begin{cases} \left.\dfrac{1}{k}\dfrac{\partial w^{(\mathrm{T})}}{\partial r}\right|_{r=a} & , -\pi \le \theta \le 0\ (\pi \le \theta \le 2\pi) \\ \left.\dfrac{1}{k}\dfrac{\partial\left(w^{(\mathrm{ff})} + w^{(\mathrm{S})} - w^{(\mathrm{T})}\right)}{\partial r}\right|_{r=a} & , 0 \le \theta \le \pi \end{cases} \tag{9.7}$$
$$\Psi(\theta) = \left.\left(w^{(\mathrm{ff})} + w^{(\mathrm{S})} - w^{(\mathrm{T})}\right)\right|_{r=a} \quad , 0 \le \theta \le \pi$$

The stress residual function Φ(θ) is defined in the full range of the circular region, $-\pi \le \theta \le \pi$, at $r = a$. The displacement residual function Ψ(θ), however, is defined only in the lower half of the circular region, $0 \le \theta \le \pi$, at $r = a$.

Conceptually these auxiliary residuals functions would vanish at every angle θ at r =a, for the above boundary conditions to be satisfied. Yuan and Men (1992) next expanded these auxiliary functions in Fourier series of θ, and equate them to that calculated from the wave functions, $w^{(\mathrm{ff})}$, $w^{(\mathrm{S})}$, and $w^{(\mathrm{T})}$. Setting each term of the Fourier series to zero gives the equations for the unknown coefficients A_n, B_n and C_n, which are subsequently solved. Finding the coefficients this way by setting the terms of the residual functions to zero is also called the method of moments (Harrington, 1968; Davies, 1973; Bancroft, 1996), with the sines and cosines picked as the basis functions of the residuals. This method is very popular and is best used for topographies which are arbitrary in shape (Lee and Wu, 1994a,b; Manoogian and Lee, 1996,1999). Yuan and Liao (1996) later extended the above procedure to solve the case of a shallow hill (arc) on the surface of the half space. They plotted the residual amplitudes of the stress and displacement functions. Ideally, if the boundary conditions are exactly satisfied, these amplitudes would be numerically insignificant, or close to zero. It was found, as stated earlier, that the stress residual amplitudes on both the left and right rims ($\theta = 0,\pi$ at $r = a$) of the hill are not numerically insignificant, irrespective of how many terms used. The authors, as stated in the paper, thought that the shear stress at the rims is infinite, and that the auxiliary function $\Phi(\theta)$ is discontinuous at both rims of the hill, exhibiting a problem for the numerical solution that is more complicated than Gibb's phenomena. Here Gibb's phenomena refer to the overshoot of the auxiliary function at a point of discontinuity when it is calculated in terms of Fourier series.

3.2.3 The New Analytic Solution Using the Cosine Half-Range Expansion

We start with the same resultant wave functions, $w = w^{(\mathrm{ff})} + w^{(\mathrm{S})}$, present in the half-space and the transmitted field, $w^{(\mathrm{T})}$, in the circular hill, from Eqn. (9.1) and (9.3) with C_0=0. As stated above, the boundary conditions of equations (8) and (9) are used to determine the unknown coefficients in the wave functions. As discussed earlier, the transmitted waves in the hill $w^{(\mathrm{T})}$ are defined in the whole circular region ***C***: $r < a$, $-\pi < \theta < \pi$, while the scattered waves $w^{(\mathrm{S})}$ are defined only in the half-space region ***H***: $a < r$, $0 < \theta < \pi$. Further, the boundary conditions (Eqns (9.5) and (9.6)) at $r = a$ facing the transmitted waves $w^{(\mathrm{T})}$ are composed of two disjoint sets, one set for continuity of stress and displacement in the lower half interface $\underline{L}$, $0 < \theta < \pi$, and the other being the traction free condition in the upper half L, $-\pi < \theta < 0$. The only way the boundary conditions can be separately imposed onto the transmitted waves $w^{(\mathrm{T})}$ is to express the waves in terms of the trigonometric functions that are orthogonal in each of the half range. Note that the sine and cosine functions, being orthogonal in the full 2π-circle, are NOT orthogonal to each other on either the upper or lower π-range of the circular region. The next paragraph shows that the use of the cosine functions as an orthogonal set of functions in each of the half range, $0 < \theta < \pi$ and $-\pi < \theta < 0$, solves the problem. This method has been successful in solving other semi-circular topographies, like troughs or canyons, in electromagnetic waves diffraction problems (Hinders and Yaghjian, 1991; Park et al, 1992, 1993).

It is well known that the set of cosine functions {$\cos n\theta$, n = 0,1,2…} are orthogonal in the half range [0,π] (and similarly in [-π,0]), and any function f(θ) in the range can have a cosine series expansion:

$$
\begin{aligned}
& f(\theta) = \sum_0^\infty f_n \cos n\theta \\
& \text{with } f_n = \frac{\varepsilon_n}{\pi}\int_0^\pi f(\theta)\cos n\theta \mathrm{d}\theta
\end{aligned}
\tag{9.8}
$$

Using Eqn (11), the sine terms in Eqn (5) can be expressed in terms of the cosine functions in both ranges $[-\pi, 0]$ and $[0, \pi]$, with $\varepsilon_0 = 1$, $\varepsilon_n = 2$ for n >0, and for m = 1,2,3…

$$
\sin m\theta = \begin{cases} -\dfrac{2m}{\pi} \displaystyle\sum_{\substack{n=0 \\ n+m \text{ odd}}}^{\infty} \dfrac{\varepsilon_n}{m^2 - n^2} \cos n\theta \ , \ -\pi \le \theta \le 0 \\ +\dfrac{2m}{\pi} \displaystyle\sum_{\substack{n=0 \\ n+m \text{ odd}}}^{\infty} \dfrac{\varepsilon_n}{m^2 - n^2} \cos n\theta \ , \ 0 \le \theta \le \pi \end{cases}
\tag{9.9}
$$

Note that with the sine function being an odd function, the corresponding cosine function expansion is also defined to be equal in absolute value but of opposite sign on either side of the axis θ=0. The accuracy of this expansion is demonstrated in the section "Numerical Solutions and Verification of Accuracy" to follow.

Therefore,

$$
w^{(\mathrm{T})}(r,\theta) = \begin{cases} \displaystyle\sum_{n=0}^{\infty} \left(B_n \mathrm{J}_n(kr) - \frac{\varepsilon_n}{\pi} \sum_{\substack{m=1 \\ n+m \text{ odd}}}^{\infty} C_m \mathrm{J}_m(kr) \frac{2m}{m^2 - n^2} \right) \cos n\theta \ , \ -\pi \le \theta \le 0 \\ \displaystyle\sum_{n=0}^{\infty} \left(B_n \mathrm{J}_n(kr) + \frac{\varepsilon_n}{\pi} \sum_{\substack{m=1 \\ n+m \text{ odd}}}^{\infty} C_m \mathrm{J}_m(kr) \frac{2m}{m^2 - n^2} \right) \cos n\theta \ , \ 0 \le \theta \le \pi \end{cases}
\tag{9.10}
$$

The corresponding radial stress, $\tau_{rz}^{(\mathrm{T})}(r,\theta) = \mu \, \partial w^{(\mathrm{T})} / \partial r$, in the circular region $\boldsymbol{C}$ ($r \le a$) takes the form

$$\tau_{rz}^{(\mathrm{T})}(r,\theta)=\begin{cases}\mu k\sum_{n=0}^{\infty}\left(B_n \mathrm{J}_n'(kr)-\dfrac{\varepsilon_n}{\pi}\sum_{\substack{m=1\\ n+m\ \mathrm{odd}}}^{\infty} C_m \mathrm{J}_m'(kr)\dfrac{2m}{m^2-n^2}\right)\cos n\theta\ ,\ -\pi\le\theta\le 0\\ \mu k\sum_{n=0}^{\infty}\left(B_n \mathrm{J}_n'(kr)+\dfrac{\varepsilon_n}{\pi}\sum_{\substack{m=1\\ n+m\ \mathrm{odd}}}^{\infty} C_m \mathrm{J}_m'(kr)\dfrac{2m}{m^2-n^2}\right)\cos n\theta\ ,\ 0\le\theta\le \pi\end{cases}\tag{9.11}$$

The displacement $w=w^{(\mathrm{ff})}+w^{(\mathrm{S})}$ and radial stress $\tau_{rz}(r,\theta)=\mu\,\partial\left(w^{(\mathrm{ff})}+w^{(\mathrm{S})}\right)\big/\partial r$ in the half-space region ***H*** ($a\le r$, $0\le\theta\le\pi$) are both cosine series. For $0\le\theta\le\pi$

$$\begin{aligned} w(r,\theta)&=\sum\nolimits_{n=0}^{\infty}\left(a_{0,n}\mathrm{J}_n(kr)+A_n\mathrm{H}_n^{(1)}(kr)\right)\cos n\theta\\ \tau_{rz}(r,\theta)&=\sum\nolimits_{n=0}^{\infty}\left(a_{0,n}\mathrm{J}_n'(kr)+A_n\mathrm{H}_n^{(1)\prime}(kr)\right)\cos n\theta\end{aligned}\tag{9.12}$$

With the displacement and stress functions of both the scattered and transmitted waves all in the form of cosine series, the boundary conditions (equations (9.5) and (9.6)) are now simple and straight forward to apply. Just equate to zero each of the corresponding sums of the orthogonal cosine terms in Eqns (9.10) and (9.11):

I) **Eqn**(9.5): Traction-free boundary condition at the surface of the circular hill, ***L*** ($r = a$, $-\pi\le\theta\le 0$):

$\tau_{rz}\,|_{r=a}=\mu\,\partial w^{(\mathrm{T})}\big/\partial r\big|_{r=a}=0$ gives, from Eqn (14), for n = 0,1,2…

$$\mathrm{J}_n'(ka)B_n=\frac{\varepsilon_n}{\pi}\sum_{\substack{m=1\\ m+n\ \mathrm{odd}}}^{\infty}\left(\frac{2m}{m^2-n^2}\right)\mathrm{J}_m'(ka)C_m\tag{9.13}$$

II) **Eqn(9.6)**: Displacement and stress continuity at the interface, ***L*** ($r = a$, $0\le\theta\le\pi$), for n = 0,1,2…

$$a_{0,n}\mathrm{J}_n(ka)+\mathrm{H}_n^{(1)}(ka)A_n=\mathrm{J}_n(ka)B_n+\frac{\varepsilon_n}{\pi}\sum_{\substack{m=1\\ m+n\ \mathrm{odd}}}^{\infty}\left(\frac{2m}{m^2-n^2}\right)\mathrm{J}_m(ka)C_m\tag{9.14}$$

$$a_{0,n}\mathrm{J}_n'(ka)+\mathrm{H}_n^{(1)\prime}(ka)A_n=\mathrm{J}_n'(ka)B_n+\frac{\varepsilon_n}{\pi}\sum_{\substack{m=1\\ m+n\ \mathrm{odd}}}^{\infty}\left(\frac{2m}{m^2-n^2}\right)\mathrm{J}_m'(ka)C_m\tag{9.15}$$

Eqn(9.13), (9.14) and (9.15) provide three sets of equations for the three sets of unknowns A_n, B_n and C_n. There are many ways to solve for the unknowns, all leading to the solution of an infinite matrix equation in C_n. B_n can be computed from the C_m's from Eqn (9.13), and eliminating the C_m sums from Eqn (9.14) and (9.15) gives A_n in terms of B_n.

3.2.4 Numerical Solutions and Verification of Accuracy

A test of the accuracy of the new proposed solution in comparison with the existing solution of Yuan and Men (1992) is to evaluate the normalized stress and displacement residuals $\Phi(\theta)$ and $\Psi(\theta)$ given in Eqn (9.7) along the circular boundary, $r=a$ (Yuan and Liao, 1996). As stated above, conceptually these auxiliary residual functions would vanish at every angle θ at $r=a$, for the above boundary conditions to be satisfied. The solution would be considered good and accurate if these functions have amplitudes that are numerically insignificant.

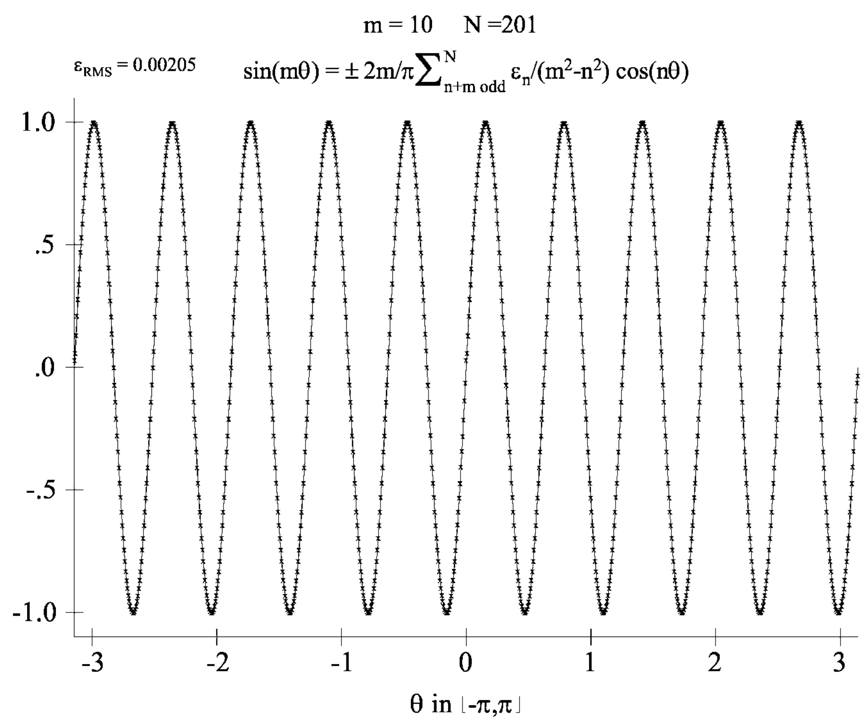

Fig. 3-2 COSINE EXPANSION OF A SINE FUNCTION

How good the present solution procedure is depends on how well are the cosine series expansions in both the upper and lower half of the circular region. In particular, it depends on how well the expansion of each sine function as a cosine series in Eqn (9.9) is. Fig. 3-2 is one such typical plot of the expansion of $\sin(m\theta)$ for m=10 in the range [-π, π]. The solid line is the actual sine function. The calculated values using the cosine series summation in Eqn (9.9) are plotted as **'*'** in the figure. They agree well, even among the end points $\theta = 0, \pm\pi$, where the rims of the hill are. The number of points used in the summation is the number of odd points up to N=201, or half of it. The RMS of the difference of the discrete set of points plotted in Figure 3.2 for comparison is $\varepsilon_{RMS} = 0.00205$. It can be smaller for larger N.

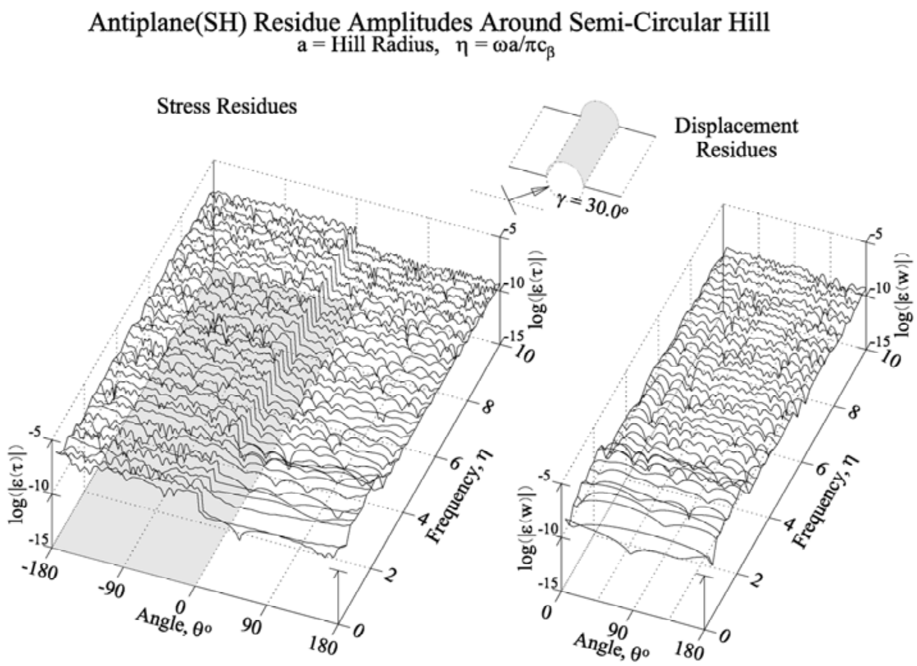

Fig. 3-3 STRESS AND DISPLACEMENT RESIDUES FOR γ = 30o INCIDENCE

Fig. 3-3 and Fig. 3-4 are the normalized stress residual $\varepsilon(\tau(\theta)) = |\Phi(\theta)|$ and displacement residual $\varepsilon(w(\theta)) = |\Psi(\theta)|$ amplitudes (Eqn(9.7)) evaluated around the circular region at various frequencies. Fig. 3-3 is for a nearly horizontal, $\gamma = 30^o$, while Fig. 3-4 is for nearly vertical incidence $\gamma = 60^o$. As in all previous works (Lee et al, 2004, Liang et al, 2004), a dimensionless frequency is used. It is also the ratio of the diameter of the hill $2a$ to the wavelength of the incident and all other waves , λ

$$\eta = \frac{\omega a}{\pi c_\beta} = \frac{ka}{\pi} = \frac{2a}{\lambda} \tag{9.16}$$

Dimensionless frequencies η in the subsequent chapters adopt similar expressions as equation (9.16) with different definition of characteristic length (the numerator $2a$ in Eqn.(9.16)).

The stress residual amplitudes are at $r = a$, for θ from -180^0 to 0^0 on top (the shaded region is on the top of the hill) and 0^o to 180^o below where it is interfaced with the half-space region $\boldsymbol{H}$. Note that in the upper half (shaded region), only the wave function of the transmitted field, $w^{(T)}$ is used, whereas in the lower half interfaced with the half-space region, all the wave functions in $w = w^{(ff)} + w^{(S)}$ and $w^{(T)}$ are involved. This may explain the apparent jump of the amplitudes (though they are insignificant in both ranges) in the common points at $\theta = 0^o$ and $\pm 180^o$.

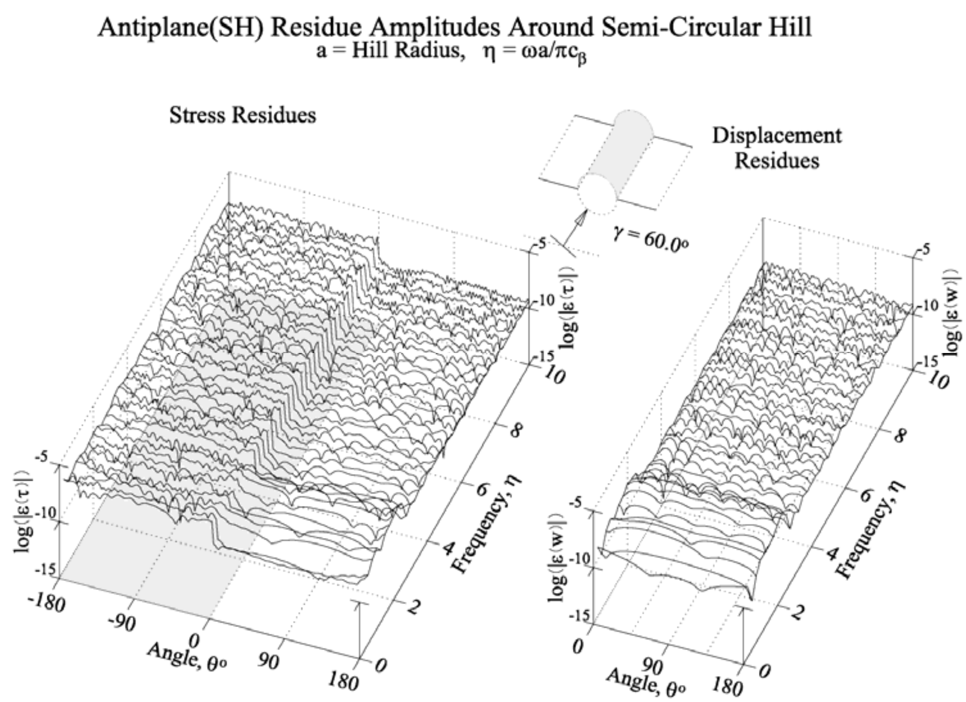

Fig. 3-4 STRESS AND DISPLACEMENT RESIDUES FOR γ = 60o INCIDENCE

The displacement residual amplitudes are only calculated from 0^o to 180^o on the lower half where the displacement residual function $\Psi(\theta)$ is defined. That is why the graph is only half the width, since it only involves the semi-circular range. It again involves all of the wave functions in $w = w^{(ff)} + w^{(S)}$ and $w^{(T)}$.

The simplicity of Eqn (9.13)-(9.15) for the coefficients A_n, B_n and C_n of the wave functions allows the computation to be carried out to higher frequencies such as η =10 and beyond. As η increases, the number of terms required also increases. The present computation uses as many as N=90 for η =10. It is seen that all the stress and displacement residuals are numerically insignificant, including those at both rims of the hill. In fact the residual amplitudes are so small they are plotted in *logarithmic scale* in the range 10^{-15} to 10^{-5}. This indicates that the stress and displacement continuity boundary conditions in Eqns (9.5) and (9.6) are well satisfied.

3.2.5 Surface Displacement Amplitudes

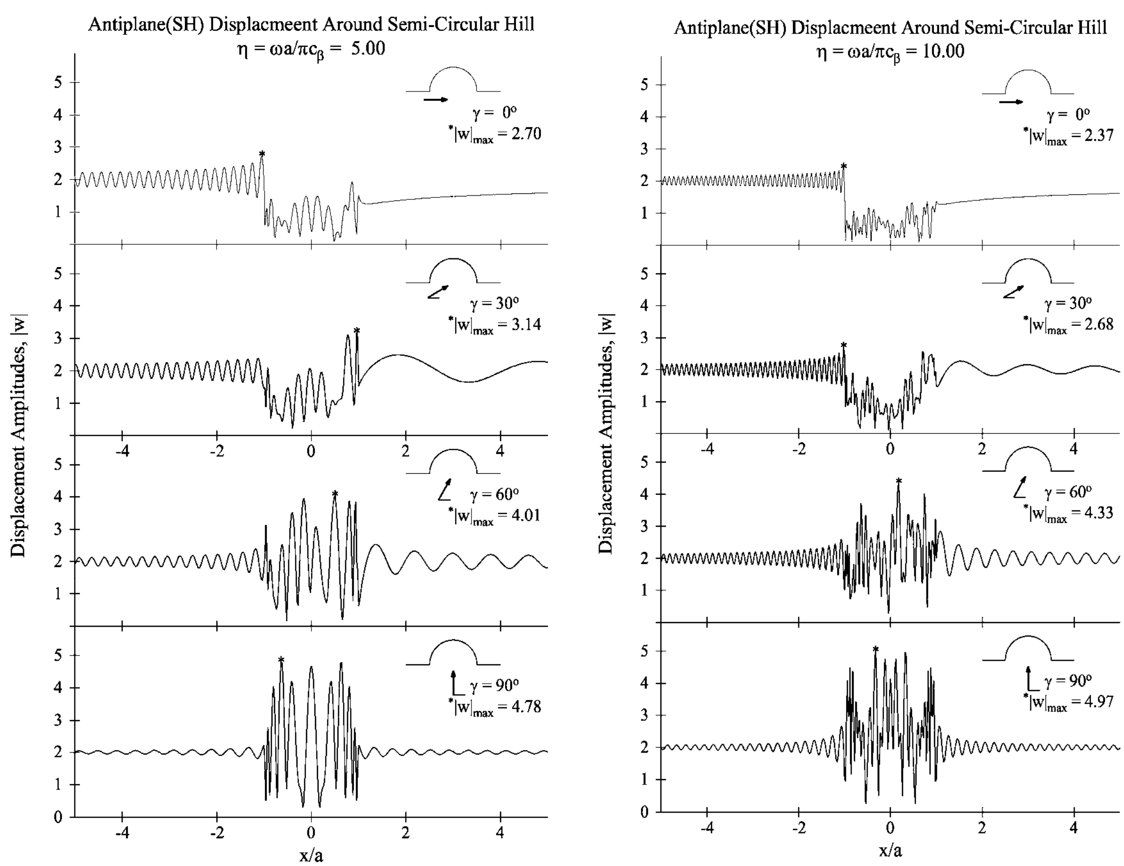

Fig. 3-5 DISPLACEMENT AMPLITUDES FOR η=5 or 10

Displacement amplitude is defined as the modulus of complex displacement w

$$|w| = \left[\mathrm{Re}^2(w) + \mathrm{Im}^2(w)\right]^{1/2} \tag{9.17}$$

The displacement amplitudes $|w|$ at the surface of the half-space on and around the hill are shown in Fig. 3-5. These are graphs of surface amplitudes along x/a from –5 to 5, at four incidence angles of $\gamma = 0$, 30, 60 and 90°. The graphs on the left are for an intermediate dimensionless frequency of $\eta = 5$, while those on the right are for $\eta = 10$, the highest η used in this study. The amplitudes in the range of x/a in [-1,1] are those on the circular surface of the hill. As in the cases of surface canyons and alluvial valleys, the displacement amplitudes to the left of the hill are more oscillatory than those to the right, resulting from diffraction by the hill as a surface topography. For nearly horizontal incidences (0° and 30°) the hill also acts as a shield for surface on the hill and to its right, shielding the waves coming from the left, resulting in a standing wave pattern. It is also noted that for nearly vertical incidences (60° and 90°), displacement is large and oscillatory on the hill surface. In fact, the maximum amplitudes of motions are all on the circular hill surface. These complicated patterns increase with increasing frequencies. The approach by Yuan and Men (1992) using the moment method of minimizing the residues for the same problem shows consistent, identical results. Their results show that the residual amplitudes are numerically insignificant (Yuan and Liao, 1996), except at the hill's rims, reaffirming the usefulness of the moment method**.**

Fig. 3-6 and Fig. 3-7 are the corresponding three-dimensional plots of the same surface displacement amplitudes versus this distance x/a on and around the hill and the dimensionless frequencies η. As was in Figure 3.3 and 3.4, the simplicity of equations (9.13)-(9.15) for the coefficients allow the computation to be carried out to as high a frequency as $\eta = 10$ and even beyond. The method of Yuan and Men (1992) only provided results for much lower η up to 3.0. Fig. 3-6 are for small (0 and 30°), while Fig. 3-7 are for larger (60 and 90°) angles of incidences. The same trend of observations for Fig. 3-5 applies here.

The method of derivation can now be applied and extended to more complex hill topography problems and for improvements of previous works on extensions of the hill problem. Liang et al (2004) extended the semi-circular hill problem to one with a full circular cavity inside. Lee et al (2004) solved the semi-circular hill problem with a semi-circular cavity inside. Both papers used the method of moment to minimize the residuals at the circular boundary introduced by Yuan and Men (1992). The present method can be used to re-visit the above problems.

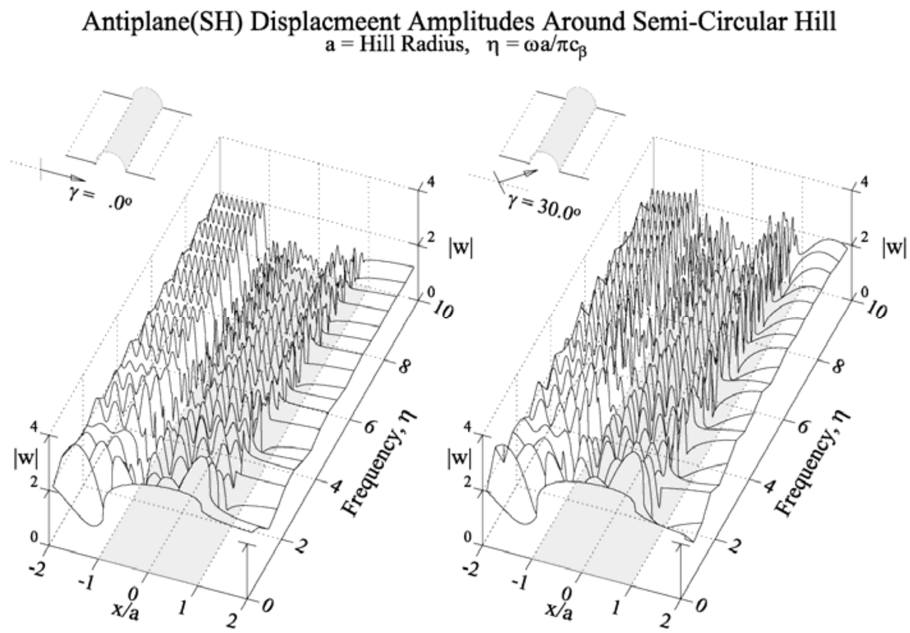

Fig. 3-6 DISPLACEMENT AMPLITUDES FOR γ = 0o AND γ = 30o

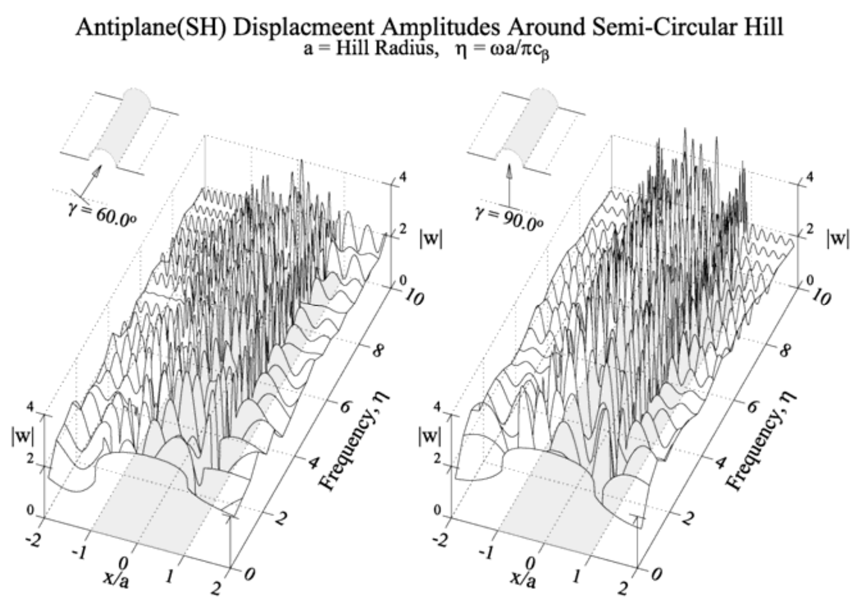

Fig. 3-7 DISPLACEMENT AMPLITUDES FOR γ = 60o AND γ =90o

3.3 Conclusions

An analytical solution for scattering of incident SH waves by a semi-cylindrical hill was derived by wave functions expansion technique.

(1) The use of Fourier cosine series improves the precision of the mixed boundary-valued problem, making the present method of derivation an improvement to that by Yuan and Men (1992), in that the stress residuals at every point of the circular boundary ($r = a$) are insignificant, including the rims of the hill.

(2) Comparison of the displacement amplitudes calculated here with those from Yuan and Men (1992) shows consistent, identical results, reaffirming the power and usefulness of the (moment) method of weighted residuals (Harrington, 1968).

(3) The present calculations extend to higher dimensionless frequencies of η=10 and beyond plays an important role in determining the displacement patterns. Higher η results in higher complexity of displacements and higher amplifications. The amplification of resulting surface displacement amplitudes at some points around the hill can be as high as two and a half times (>2!) the free-field motions at high frequencies (η=10 and beyond).

(4) The method of derivation can be applied and extended to more complex hill topography problems or for improvements of previous works on an extension of the hill problem, namely, cavity or tunnel in hill, by Lee et al (2004) and Liang et al (2004)..

Chapter 4

DIFFRACTION OF SH WAVES BY A SEMI-CIRCULAR CYLINDRICAL HILL WITH AN INSIDE SEMI-CIRCULAR CONCENTRIC TUNNEL

In Chapter 3, we discuss antiplane response of SH-waves by a semi-cylindrical hill on a half-space. In this chapter, a concentric unlined tunnel is added to the previous model. This new model is one kind of generalized Soil-Substructure-Interaction. In reality, mountain tunnel is very common. It is necessary to consider the influence from the surrounding site when tunnels or pipes are constructed through mountain in seismic area. Again, cavities are ordinary in a mountainous area, karst region especially. Most of analytical solutions hitherto focus on certain topography, as canyon, valley, hill or cavity etc, the interaction between topography and substructure, as tunnel or cavity, is studied less relatively. Diffraction from canyon above subsurface unlined tunnel (Lee et al. 1999) and multiple foundations above the subway (Lee and Chen 1998) were studied. Liang et al. (2004) studied shallow cylindrical hill and concentric (or arbitrary eccentric) unline hill.

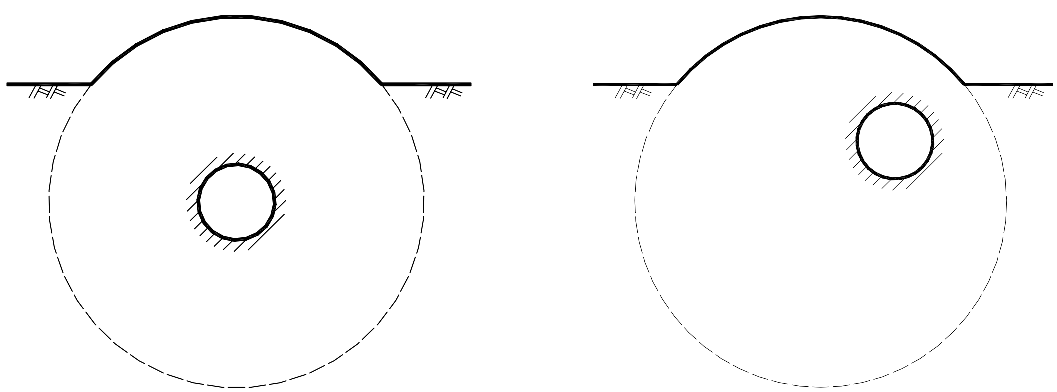

(a) Shallow Circular Hill with Concentric Tunnel (b) Shallow Circular Hill with Eccentric Tunnel

Fig. 4-1 INTERACTION OF HILL TOPOGRAPHY AND FULL-CIRCULAR UNLINED TUNNEL

In this chapter, a closed-form analytic solution of two-dimensional scattering of plane SH-waves by a semi-circular cylindrical hill with a semi-circular concentric tunnel inside on a half-space is presented using the wave functions expansion method. The solution is reduced to solving a set of infinite linear algebraic equations. Unlike the former paper (Yuan and Men 1992), Fourier expansion theorem with the form of both the complex exponential function and cosine function are used. Numerical solutions are obtained by truncation of the infinite equations and using the by singular value decomposition method. The efficiency of computer program is improved distinctly by using the algorithm of Fourier expansion theorem with the form of complex exponential function other than the sines and cosines trigonometric function. The accuracies of the numerical results are checked up by the convergence of the ground surface displacement and residual errors of boundary conditions with increasing the truncation order. The effects of the frequencies, incident angles of the incident waves and the radius of tunnel on displacement amplitude of ground surface are illustrated. It was shown that the existence of hill and tunnel has great effect on motion of ground surface nearby.

4.1 The Model

The cross section of the two-dimensional model studied in this paper is shown in Fig. 4-2. It represents an elastic, isotropic and homogeneous half-space with a semi-cylindrical hill of radius a. There is a semi-circular concentric tunnel inside the hill. The free surface of the half-space consists of a flat surface Γ and semi-circular hilly boundary L. The upper and flat ground boundary of the semi-circular tunnel are marked as L_1 and Γ_1 respectively. The radius of the tunnel is a_1. The height and half-width of the hill is h and b. It is certainly that $b = h$ for the semi-cylindrical hill.

For the convenience of solution using wave functions, the half-space can be divided into three parts as shown in Fig. 4-3. The first one is the annular region C including the hill, whose outer upper and lower boundary are L and $\underline{L}$ respectively, and the inner upper and lower boundary are L_1 and $\underline{L_1}$. The second region is the half-space canyon H, which has a common boundary $\underline{L}$ with region C and a flat ground surface boundary Γ. The last region is the semi-circular region V, the semi-circular "valley" region bounded by Γ_1 and $\underline{L_1}$. The original model is thus divided into three individual region and Fourier-Bessel wave function expansion will be used in each of these regions. The boundary conditions are: The traction-free boundary conditions on L in region C; The traction-free boundary conditions on Γ in region H; The traction-free boundary conditions on Γ_1 in region V; Displacement and Stress continuity boundary conditions on $\underline{L}$ between region C and H; Displacement and Stress continuity boundary conditions on $\underline{L_1}$ between region C and V. Note that, there are two different boundary conditions on the full circular boundary such as $L+\underline{L}$ and $L_1+\underline{L_1}$. Therefore, this model is a mixed boundary problem.

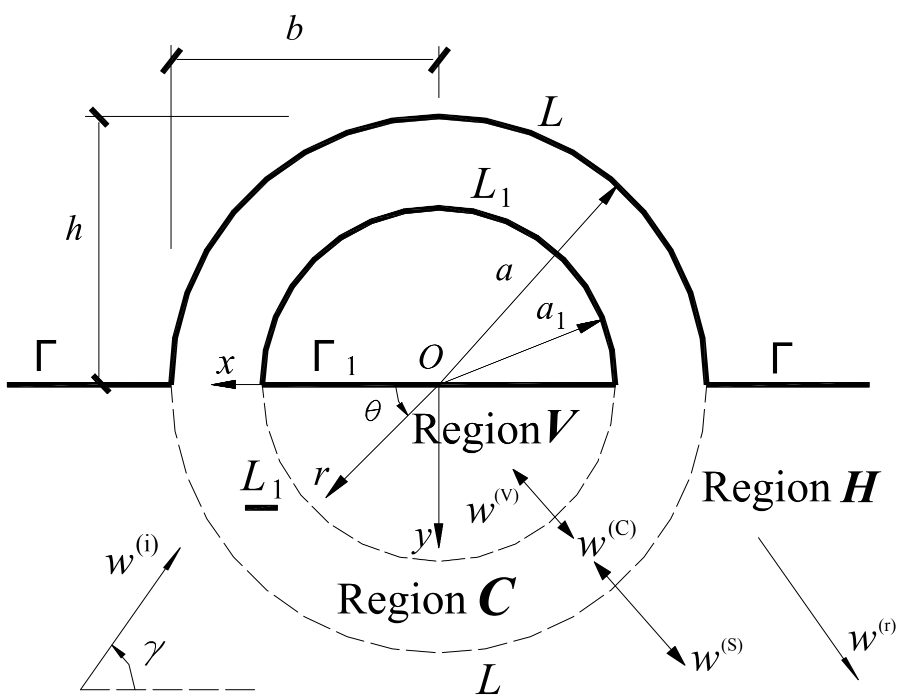

Fig. 4-2 SEMI-CYLINDRICAL HILL WITH A SEMI-CYLINDRICAL TUNNEL INSIDE

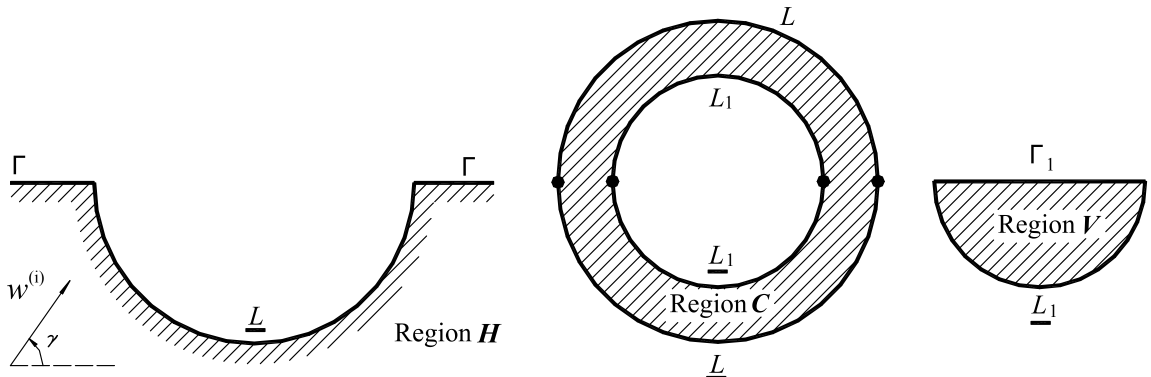

Fig. 4-3 DIVISION OF THE HALF-SPACE

4.2 The Incident and Scattered Waves: Fourier-Bessel Series Expansion

The displacement in the half-space region H can be expressed by

$$w = w^{(\mathrm{ff})} + w^{(\mathrm{S})} \tag{10.1}$$

where $w^{(\mathrm{ff})}$ represents the free field displacement in the half-space; $w^{(\mathrm{S})}$ represents the scattering displacement resulting from the interaction between the half-space and boundary $\overline{L}$.

The traction-free boundary conditions of this model are

$$\tau_{\theta z}\,|_{\theta=0,\pi} = 0 \qquad \text{at} \quad (r,\theta) \in \Gamma \tag{10.2}$$

$$\tau_{\theta z}\,|_{\theta=0,\pi} = 0 \qquad \text{at} \quad (r,\theta) \in \Gamma_1 \tag{10.3}$$

$$\tau_{rz}\,|_{r=a_1} = 0 \qquad \text{at} \quad (r,\theta) \in L \tag{10.4}$$

$$\tau_{rz}\,|_{r=a_2} = 0 \qquad \text{at} \quad (r,\theta) \in L_1 \tag{10.5}$$

where the hoop stress $\tau_{\theta z}$ and the radial stress τ_{rz} are specified by (8.3) and (8.4).

The free field displacement in the polar coordinate system (r,θ) can be written as

$$w^{(\mathrm{ff})}\left(r,\theta\right)=\sum_{n=0}^{\infty}a_{0,n}\mathrm{J}_{n}\left(kr\right)\cos n\theta \tag{10.6}$$

where

$$a_{0,n}=2\varepsilon_{n}(-\mathrm{i})^{n}\cos n\gamma \tag{10.7}$$

in which $\varepsilon_0=1$, $\varepsilon_n=2$, for n=1, 2, 3 ···. By equation (8.4)

$$\tau_{rz}^{(\mathrm{ff})}(r,\theta)=\mu k\sum_{n=0}^{\infty}a_{0,n}\mathrm{J}_{n}'(kr)\cos n\theta \tag{10.8}$$

The general solution of wave equation (8.1) satisfying the zero-stress boundary condition (10.2) is

$$w^{(\mathrm{S})}(r,\theta)=\sum_{n=0}^{\infty}A_{n}\mathrm{H}_{n}^{(1)}(kr)\cos n\theta \tag{10.9}$$

which represents the scattering wave $w^{(\mathrm{S})}$ resulting from $\underline{L}$. A_n, n = 0, 1, 2, ··· is complex coefficient to be determined and $\mathrm{H}_n^{(1)}(\cdot)$ is the Hankel function of the first kind with order n.

Inserting Eq. (10.9) into (8.3), the stress on the ground surface can be expressed as

$$\tau_{\theta z}^{(\mathrm{S})}(r,\theta)=-\frac{n\mu}{r}\sum_{n=0}^{\infty}A_{n}\mathrm{H}_{n}^{(1)}(kr)\sin n\theta \tag{10.10}$$

Apparently, θ is equal to 0 or π on the boundary Γ, resulting in the zero stress boundary condition Eq. (10.2) satisfied.

Inserting (10.9) into (8.4) gives

$$\tau_{rz}^{(\mathrm{S})}(r,\theta)=\mu k\sum_{n=0}^{\infty}A_{n}\mathrm{H}_{n}^{(1)\prime}(kr)\cos n\theta \tag{10.11}$$

The total displacement in the cylindrical region C resulting from the refracted waves as inward and outward propagating from boundaries $\underline{L}$, L and L_1, $\underline{L_1}$ separately and satisfying Eq. (8.1) can be represented as

$$w^{(\mathrm{C})}(r,\theta) = \sum_{n=-\infty}^{\infty} \left[B_n^{(1)} \mathrm{H}_n^{(1)}(kr) + B_n^{(2)} \mathrm{H}_n^{(2)}(kr) \right] \mathrm{e}^{\mathrm{i}n\theta} \tag{10.12}$$

where $B_n^{(1)}$, $B_n^{(2)}$ are respectively the constant coefficients of the outgoing ($\mathrm{H}_n^{(1)}$) and incoming ($\mathrm{H}_n^{(2)}$) Hankel wave functions, to be determined. Inserting Eq. (10.12) into Eq. (8.4) gives

$$\tau_{rz}^{(\mathrm{C})}(r,\theta) = \mu k \sum_{n=-\infty}^{\infty} \left[B_n^{(1)} \mathrm{H}_n^{(1)\prime}(kr) + B_n^{(2)} \mathrm{H}_n^{(2)\prime}(kr) \right] \mathrm{e}^{\mathrm{i}n\theta} \tag{10.13}$$

The inward wave $w^{(V)}$ in region V satisfying Eq. (8.4) and traction-free boundary condition (10.3) is given by

$$w^{(\mathrm{V})}(r,\theta) = \sum_{n=0}^{\infty} C_n \mathrm{J}_n(kr) \cos n\theta \tag{10.14}$$

where C_n are constants to be determined. Inserting Eq. (10.14) into Eq. (8.3) leads to

$$\tau_{\theta z}^{(\mathrm{V})}(r,\theta) = -\frac{n\mu}{r} \sum_{n=0}^{\infty} C_n \mathrm{J}_n(kr) \sin n\theta \tag{10.15}$$

On the flat ground surface Γ_1 of the tunnel, θ is equal to 0 or π. It is easy to realize that the zero stress boundary condition Eq. (10.3) is satisfied strictly.

Inserting Eq. (10.14) into Eq. (8.4) leads to

$$\tau_{rz}^{(\mathrm{V})}(r,\theta) = \mu k \sum_{n=0}^{\infty} C_n \mathrm{J}_n'(kr) \cos n\theta \tag{10.16}$$

4.3 Mixed Boundary Conditions

All the waves expanded as Fourier-Bessel series in each region are presented. In what follows, the boundary conditions are introduced and the equations derived for the constant coefficients.

1. The Stress Continuity Condition on $\underline{L}$ and the Traction-free Condition on L:

$$\tau_{rz}^{(\mathrm{C})}(r,\theta) = \tau_{rz}^{(\mathrm{ff})}(r,\theta) + \tau_{rz}^{(\mathrm{S})}(r,\theta) \qquad , \quad (r,\theta) \in \underline{L} \tag{10.17}$$

$$\tau_{rz}^{(\mathrm{C})}(r,\theta)=0 \qquad , \quad (r,\theta)\in L \tag{10.18}$$

Define an auxiliary function, $\Phi_1(\theta)$, at $r=a$

$$\Phi_1(\theta)=\frac{1}{\mu k}\tau_{rz}^{(\mathrm{C})}(a,\theta)=\sum_{n=-\infty}^{\infty}\left[B_n^{(1)}\mathrm{H}_n^{(1)\prime}(ka)+B_n^{(2)}\mathrm{H}_n^{(2)\prime}(ka)\right]\mathrm{e}^{\mathrm{i}n\theta}$$
$$=\begin{cases} 0 & , \quad -\pi\le\theta\le 0 \\ \dfrac{1}{\mu k}\left[\tau_{rz}^{(\mathrm{ff})}(a,\theta)+\tau_{rz}^{(\mathrm{S})}(a,\theta)\right] & , \quad 0<\theta\le\pi \end{cases}$$

$$=\begin{cases} 0 & , \quad -\pi\le\theta\le 0 \\ \displaystyle\sum_{n=0}^{\infty}\left[a_{0,n}\mathrm{J}_n'(ka)+A_n\mathrm{H}_n^{(1)\prime}(ka)\right]\cos n\theta & , \quad 0<\theta\le\pi \end{cases} \tag{10.19}$$

From Eq. (10.19), $\Phi_1(\theta)$ has an exponential Fourier series expansion on $\theta\in[-\pi,\pi]$

$$\Phi_1(\theta)=\sum_{n=-\infty}^{\infty} b_n\ \mathrm{e}^{\mathrm{i}n\theta} \tag{10.20}$$

where, $b_n=\dfrac{1}{2\pi}\displaystyle\int_{-\pi}^{\pi}\Phi_1(\theta)\mathrm{e}^{-\mathrm{i}n\theta}\mathrm{d}\theta$, for n= 0, ±1, ±2, ··· .

Compare Eq. (10.20) with Eq. (10.19), explicitly

$$b_n=B_n^{(1)}\mathrm{H}_n^{(1)\prime}(ka)+B_n^{(2)}\mathrm{H}_n^{(2)\prime}(ka) \tag{10.21}$$

and

$$b_n=\frac{1}{2\pi}\int_{-\pi}^{\pi}\Phi_1(\theta)\mathrm{e}^{-\mathrm{i}n\theta}d\theta=\frac{1}{2\pi}\int_0^{\pi}\sum_{m=0}^{\infty}\left[a_{0,m}\mathrm{J}_m(ka)+A_m\mathrm{H}_m^{(1)\prime}(ka)\right]\cos m\theta\ \mathrm{e}^{-\mathrm{i}n\theta}\mathrm{d}\theta$$
$$=\frac{1}{2}\sum_{m=0}^{\infty}\left[a_{0,m}\mathrm{J}_m'(ka)+A_m\mathrm{H}_m^{(1)\prime}(ka)\right]\eta_{m,-n} \tag{10.22}$$

in which

$$\eta_{m,\pm n}=\frac{1}{\pi}\int_0^{\pi}\cos m\theta\ \mathrm{e}^{\pm\mathrm{i}n\theta}\mathrm{d}\theta=c(m,n)\pm\mathrm{i}\cdot s(m,n) \tag{10.23}$$

(m= 0, 1, 2, ···) (n= 0, 1, 2, ···)

with

$$c(m,n)=\frac{1}{\pi}\int_0^{\pi}\cos m\theta\cos n\theta\mathrm{d}\theta=\begin{cases}1 & , \quad m=n=0\\ 1/2 & , \quad m=|n|\neq 0\\ 0 & , \quad m\neq|n|\end{cases} \tag{10.24}$$

$$s(m,n)=\frac{1}{\pi}\int_0^{\pi}\cos m\theta\sin n\theta\mathrm{d}\theta=\begin{cases}0 & , \quad m+n \quad \text{even}\\ \dfrac{2n}{\pi(n^2-m^2)} & , \quad m+n \quad \text{odd}\end{cases} \tag{10.25}$$

Therefore, compare Eq. (10.21) with Eq. (10.22), the boundary equation can be written as

$$2\left[B_n^{(1)}\mathrm{H}_n^{(1)\prime}(ka)+B_n^{(2)}\mathrm{H}_n^{(2)\prime}(ka)\right]=\sum_{m=0}^{\infty}\left[a_{0,m}\mathrm{J}_m(ka)+A_m\mathrm{H}_m^{(1)\prime}(ka)\right]\eta_{m,-n} \tag{10.26}$$

(n= 0, ±1, ±2, ···)

2. The Displacement Continuity Condition on $\underline{L}$**:**

$$w^{(\mathrm{C})}(r,\theta)=w^{(\mathrm{ff})}(r,\theta)+w^{(\mathrm{S})}(r,\theta) \qquad , \quad (r,\theta)\in\underline{L} \tag{10.27}$$

Define an auxiliary function $\Psi_1(\theta)$, for $\theta\in[0,\pi]$:

$$\Psi_1(\theta)=w^{(\mathrm{C})}(a,\theta)=\sum_{n=-\infty}^{\infty}\left[B_n^{(1)}\mathrm{H}_n^{(1)}(ka)+B_n^{(2)}\mathrm{H}_n^{(2)}(ka)\right]\mathrm{e}^{in\theta}$$

$$=\left[w^{(\mathrm{ff})}(a,\theta)+w^{(\mathrm{S})}(a,\theta)\right]=\sum_{m=0}^{\infty}\left[a_{0,m}\mathrm{J}_m(ka)+A_m\mathrm{H}_m^{(1)}(ka)\right]\cos m\theta \tag{10.28}$$

It is easy to see that $\Psi_1(\theta)$ is (a cosine even) function about θ in the interval $[0,\pi]$. Making $\Psi_1(\theta)$ cosine series Fourier expansion on $\theta\in[0,\pi]$:

$$\Psi_1(\theta)=\sum_{m=0}^{\infty}a_m\cos m\theta \tag{10.29}$$

with,

$$a_m=(\varepsilon_m/\pi)\int_0^{\pi}\Psi_1(\theta)\cos m\theta\mathrm{d}\theta,\quad \varepsilon_0=1,\ \varepsilon_m=2,\ m=1,2,3...$$

Compare Eq. (10.29) with Eq. (10.28)

$$a_m = a_{0,m}\mathrm{J}_m(ka) + A_m \mathrm{H}_m^{(1)}(ka) \tag{10.30}$$

and

$$a_m = \varepsilon_m \sum_{n=-\infty}^{\infty} \left[B_n^{(1)} \mathrm{H}_n^{(1)}(ka) + B_n^{(2)} \mathrm{H}_n^{(2)}(ka) \right] \eta_{m,n} \tag{10.31}$$

with $\eta_{m,n}$ defined earlier in Eq. (10.23).

Hence, Compare Eq. (10.30) with Eq. (10.31)

$$\varepsilon_m \sum_{n=-\infty}^{\infty} \left[B_n^{(1)} \mathrm{H}_n^{(1)}(ka) + B_n^{(2)} \mathrm{H}_n^{(2)}(ka) \right] \eta_{m,n} = a_{0,m}\mathrm{J}_m(ka) + A_m \mathrm{H}_m^{(1)}(ka) \tag{10.32}$$

(m=0, 1, 2, ⋯)

3. The Stress Continuity Condition on $\underline{L_1}$ and Traction-free Condition on L_1 :

$$\tau_{rz}^{(\mathrm{C})}(r,\theta) = \tau_{rz}^{(\mathrm{V})}(r,\theta) \qquad , \quad (r,\theta) \in \underline{L_1} \tag{10.33}$$

$$\tau_{rz}^{(\mathrm{C})}(r,\theta) = 0 \qquad , \quad (r,\theta) \in L_1 \tag{10.34}$$

Define an auxiliary function $\Phi_2(\theta)$, at $r = a_1$

$$\Phi_2(\theta) = \tau_{rz}^{(\mathrm{C})}(a_1,\theta) = \sum_{n=-\infty}^{\infty} \left[B_n^{(1)} \mathrm{H}_n^{(1)\prime}(ka_1) + B_n^{(2)} \mathrm{H}_n^{(2)\prime}(ka_1) \right] \mathrm{e}^{in\theta}$$

$$= \begin{cases} 0 & , \quad -\pi \le \theta \le 0 \\ \tau_{rz}^{(V)}(a_1,\theta) & , \quad 0 < \theta \le \pi \end{cases} = \begin{cases} 0 & , \quad -\pi \le \theta \le 0 \\ \displaystyle\sum_{n=0}^{\infty} C_n \mathrm{J}_n'(ka_1)\cos n\theta & , \quad 0 < \theta \le \pi \end{cases} \tag{10.35}$$

Similarly, Making Eq. (10.35), $\Phi_2(\theta)$, an exponential Fourier series expansion on $\theta \in [-\pi, \pi]$

$$\Phi_2(\theta) = \sum_{n=-\infty}^{\infty} b_n' \, \mathrm{e}^{in\theta} \tag{10.36}$$

where, $b_n' = \dfrac{1}{2\pi}\int_{-\pi}^{\pi} \Phi_2(\theta)\mathrm{e}^{-in\theta}\mathrm{d}\theta$, for n= 0, ±1, ±2, ⋯ .

Compare Eq. (10.36) with Eq. (10.35)

$$b_n' = B_n^{(1)}\mathrm{H}_n^{(1)\prime}(ka_1) + B_n^{(2)}\mathrm{H}_n^{(2)\prime}(ka_1) \tag{10.37}$$

and

$$b_n' = \frac{1}{2\pi}\int_{-\pi}^{\pi}\Phi_2(\theta)\mathrm{e}^{-\mathrm{i}n\theta}\mathrm{d}\theta = \frac{1}{2\pi}\int_0^{\pi}\sum_{m=0}^{\infty}C_m\mathrm{J}_m'(ka_1)\cos m\theta\ \mathrm{e}^{-\mathrm{i}n\theta}\mathrm{d}\theta = \frac{1}{2}\sum_{m=0}^{\infty}C_m\mathrm{J}_m'(ka_1)\eta_{m,-n} \tag{10.38}$$

in which, $\eta_{m,-n}$ is just like Eq. (10.23). Hence, compare Eq. (10.37) with Eq. (10.38)

$$2\left[B_n^{(1)}\mathrm{H}_n^{(1)\prime}(ka_1) + B_n^{(2)}\mathrm{H}_n^{(2)\prime}(ka_1)\right] = \sum_{m=0}^{\infty}C_m\mathrm{J}_m'(ka_1)\eta_{m,-n} \tag{10.39}$$

(n= 0, ±1, ±2, ···)

4. The Displacement Continuity Condition on $\underline{L_1}$ **:**

$$w^{(\mathrm{C})}(r,\theta) = w^{(\mathrm{V})}(r,\theta) \quad , \quad (r,\theta)\in \underline{L_1} \tag{10.40}$$

Define an auxiliary function $\Psi_2(\theta)$. When $\theta\in[0,\pi]$,

$$\Psi_2(\theta) = w^{(\mathrm{C})}(a_1,\theta) = \sum_{n=-\infty}^{\infty}\left[B_n^{(1)}\mathrm{H}_n^{(1)}(ka_1) + B_n^{(2)}\mathrm{H}_n^{(2)}(ka_1)\right]\mathrm{e}^{\mathrm{i}n\theta}$$

$$= w^{(\mathrm{V})}(a_1,\theta) = \sum_{m=0}^{\infty}C_m\mathrm{J}_m(ka_1)\cos m\theta \tag{10.41}$$

It i-s easy to see that $\Psi_2(\theta)$ is an even function about θ in the interval $\theta\in[-\pi,\pi]$. Making $\Psi_2(\theta)$ cosine series Fourier expansion on $\theta\in[0,\pi]$:

$$\Psi_2(\theta) = \sum_{m=0}^{\infty}a_m'\cos m\theta \tag{10.42}$$

where, as in Eq. (10.29), $a_m' = (\varepsilon_m/\pi)\int_0^{\pi}\Psi_2(\theta)\cos\theta\mathrm{d}\theta$; $m = 0,1,2...$

Compare Eq. (10.41) with Eq. (10.42)

$$a'_m = C_m \mathrm{J}_m(ka_1) \tag{10.43}$$

and

$$a'_m = \varepsilon_m \sum_{n=-\infty}^{\infty} \left[B_n^{(1)} \mathrm{H}_n^{(1)}(ka_1) + B_n^{(2)} \mathrm{H}_n^{(2)}(ka_1) \right] \eta_{m,n} \tag{10.44}$$

in which, $\eta_{m,n}$ is defined in Eq. (10.23). Combing Eq. (10.43) and Eq. (10.44)

$$\varepsilon_m \sum_{n=-\infty}^{\infty} \left[B_n^{(1)} \mathrm{H}_n^{(1)}(ka_1) + B_n^{(2)} \mathrm{H}_n^{(2)}(ka_1) \right] \eta_{m,n} = C_m \mathrm{J}_m(ka_1) \tag{10.45}$$

(m=0, 1, 2, ···)

The system of equations resulting from boundary conditions deduced above is Eq.(10.26), (10.32), (10.39) and (10.45). Using Eq. (10.32), the set of coefficients $\{A_m\}$ can be expressed in terms of the sets $\{B_n^{(1)}\}$ and $\{B_n^{(2)}\}$. Then, $\{A_m\}$ can be eliminated if the expression be substituted into Eq. (10.26). After a series of simplification, the equation (10.26) can be written as a function only of the unknown sets of coefficients $\{B_n^{(1)}\}$ and $\{B_n^{(2)}\}$, resulting in the following infinite system of equations:

$$\sum_{l=-\infty}^{\infty} \left[M_{nl}^{(1)}(ka) B_l^{(1)} + M_{nl}^{(2)}(ka) B_l^{(2)} \right] = m_n \tag{10.46}$$

(n= 0, ±1, ±2, ···)

in which

$$M_{nl}^{(j)}(ka) = E_{nl}^{(3)}(ka) \mathrm{H}_l^{(j)}(ka) - \mathrm{H}_n^{(j)\prime}(ka) \delta_{nl} \tag{10.47}$$

$$m_n = \frac{1}{2} \sum_{m=0}^{\infty} a_{0,m} \left[\frac{\mathrm{H}_m^{(1)\prime}(ka)}{\mathrm{H}_m^{(1)}(ka)} \mathrm{J}_m(ka) - \mathrm{J}'_m(ka) \right] \eta_{m,-n} \tag{10.48}$$

and $\delta_{nl} = 0$ if $n \neq l$ and $\delta_{nn} = 1$.

$$E_{nl}^{(j)}(ka) = \sum_{m=0}^{\infty} \frac{\varepsilon_m}{2} \frac{C_m^{(j)'}(ka)}{C_m^{(j)}(ka)} \eta_{m,-n} \eta_{m,l} \tag{10.49}$$

with, for j=1, 2, 3, 4

$$C_m^{(1)}(ka) = \mathrm{J}_m(ka),\ C_m^{(2)}(ka) = \mathrm{Y}_m(ka),\ C_m^{(3)}(ka) = \mathrm{H}_m^{(1)}(ka) \text{ and } C_m^{(4)}(ka) = \mathrm{H}_m^{(2)}(ka)$$

Similarly, for Eq. (10.38) and (10.44), we extract the set of coefficients $\{C_m\}$ from Eq. (10.44) and substitute it into Eq. (10.38). With $\{C_m\}$ eliminated,

$$\sum_{l=-\infty}^{\infty} \left[N_{nl}^{(1)}(ka_1) B_l^{(1)} + N_{nl}^{(2)}(ka_1) B_l^{(2)} \right] = 0 \tag{10.50}$$

(n= 0, ±1, ±2, ···)

where,

$$N_{nl}^{(j)}(ka_1) = E_{nl}^{(1)}(ka_1) \mathrm{H}_l^{(j)}(ka_1) - \mathrm{H}_n^{(j)\prime}(ka_1) \delta_{nl} \tag{10.51}$$

The system of equations (10.46) and (10.50) can be solved by truncating the infinite matrix into a sufficiently large finite matrix. The number of terms considered must be large enough to satisfy the required accuracy. Because of the ill-condition of the matrix, in this paper, the equations are solved using the subroutines of LAPACK (Anderson et al. 1999) and using SVD (Singular Value Decomposition) (Golub and Loan 1996) method.

If replace the term $B_n^{(1)} \mathrm{H}_n^{(1)\prime}(ka) + B_n^{(2)} \mathrm{H}_n^{(2)\prime}(ka)$ by $B_n \mathrm{J}_n'(ka)$ in Eq. (10.26) and $B_n^{(1)} \mathrm{H}_n^{(1)}(ka) + B_n^{(2)} \mathrm{H}_n^{(2)}(ka)$ by $B_n \mathrm{J}_n(ka)$ in Eq. (10.32), and get rid of Eq. (10.39) and (10.45), the Eq. (10.26) and (10.32) are reduced to the infinite set of linear algebraic equations for the analytical solution for the hill of a semi-circular cross-section (as the model of Yuan and Men 1992). The numerical results indicate that these two solutions are equivalent.

4.4 Surface Displacements and Stress Amplitudes

The dimensionless parameters to be used in subsequent figures are defined as follows: stress residual error on the free surface L of the hill

$$\left|\varepsilon(\tau)\right| = |\,\tau_{rz}^{(\mathrm{C})}(r,\theta)\,| / \mu k \qquad (r,\theta) \in L \tag{10.52}$$

and displacement and stress residual errors on the interface $\underline{L}$ and $\underline{L_1}$

$$\left|\varepsilon(w)\right| = |\,w^{(\mathrm{C})}(r,\theta) - w^{(\mathrm{ff})}(r,\theta) - w^{(\mathrm{S})}(r,\theta)\,| \qquad (r,\theta) \in \underline{L} \tag{10.53}$$

$$\left|\varepsilon(\tau)\right| = |\,\tau_{rz}^{(\mathrm{C})}(r,\theta) - \tau_{rz}^{(\mathrm{ff})}(r,\theta) - \tau_{rz}^{(\mathrm{S})}(r,\theta)\,| / \mu k \qquad (r,\theta) \in \underline{L} \tag{10.54}$$

$$\left|\varepsilon(w)\right| = |\,w^{(\mathrm{C})}(r,\theta) - w^{(\mathrm{V})}(r,\theta)\,| \qquad (r,\theta) \in \underline{L_1} \tag{10.55}$$

$$\left|\varepsilon(\tau)\right| = |\,\tau_{rz}^{(\mathrm{C})}(r,\theta) - \tau_{rz}^{(\mathrm{V})}(r,\theta)\,| / \mu k \qquad (r,\theta) \in \underline{L_1} \tag{10.56}$$

and the stress residual error on the wall of the tunnel L_1

$$\left|\varepsilon(\tau)\right| = |\,\tau_{rz}^{(\mathrm{C})}(r,\theta)\,| / \mu k \qquad (r,\theta) \in L_1 \tag{10.57}$$

Since the stress residual errors on the free flat ground surface Γ and tunnel surface Γ_1 equal zero strictly by setting the wave functions, they are not discussed here.

Furthermore, the dimensionless frequency η is defined as ratio of the width of hill $2a$ and wavelength of incident wave λ

$$\eta = \frac{2a}{\lambda} = \frac{ka}{\pi} = \frac{\omega a}{\pi c_\beta} \tag{10.58}$$

Thus, the problem can be characterized in terms of the dimensionless frequency η, the radius of the tunnel to that of the hill a_1 / a, and the incident angle γ.

The resulting motion will be characterized by $|\,w\,|$, the dimensionless displacement amplitudes of total motion w, and relative phases on the free surface, where for $(r,\theta) \in \Gamma + L$

$$|w| = \left\{ [\mathrm{Re}(w)]^2 + [\mathrm{Im}(w)]^2 \right\}^{1/2} \Big/ w_0 \text{;} \quad \mathrm{Phase}(w) = \tan^{-1}(\mathrm{Im}(w)/\mathrm{Re}(w)) \qquad (10.59)$$

in which $\mathrm{Re}(.)$ and $\mathrm{Im}(.)$ represent the real and imaginary parts of the complex argument respectively.

4.4.1 Analysis of Accuracy

In order to check up the approach trend of the numerical results to the genuine solution of the problem, Fig. 4-4~Fig. 4-7 demonstrate the behavior of $\varepsilon(w)$ and $\varepsilon(\tau)$ on various boundaries for *a*=10.0, a_1=5.0, γ=90^0, different truncation order *n* and dimensionless frequency η (η=0.5 and 5.0). In all figures, the longitudinal axis is characterized by logarithmic coordinates.

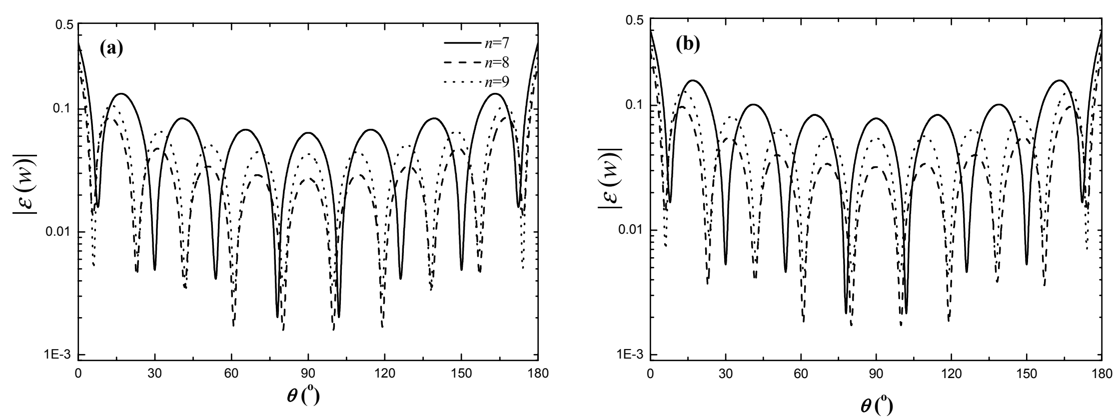

(a) The residual displacement on $\underline{L_1}$, (b) The residual displacement on $\underline{L}$

Fig. 4-4 THE RESIDUAL DISPLACEMENT FOR $\eta = 0.5$, a_1/a=5/10, γ=90^o

As seen from Fig. 4-4~Fig. 4-5, the errors on various boundaries don't converge synchronously. That's because there are two sets of Fourier transform on two different circular boundaries, namely $L+\underline{L}$ and $L_1+\underline{L_1}$, and the convergent speed of them doesn't consistent. Besides, when the frequencies of incident SH waves are small, the truncation orders are small too. For example, in the Fig. 4-4, Fig. 4-5 and Fig. 4-6, Fig. 4-7, the truncation orders are 10 and 29, respectively. Thus, both of these two Fourier expansions may not converge together at the same truncation order. Fig. 4-6 ~ Fig. 4-7 show that the displacement and stress errors approach zero with increasing the truncation order when frequency of incident wave is large enough. In fact, there is similar phenomenon that appears when the radius ratio a_1/a is too small or large. Therefore, in this analysis, only moderate cases are discussed for the purpose of ensuring the accuracy of numerical results.

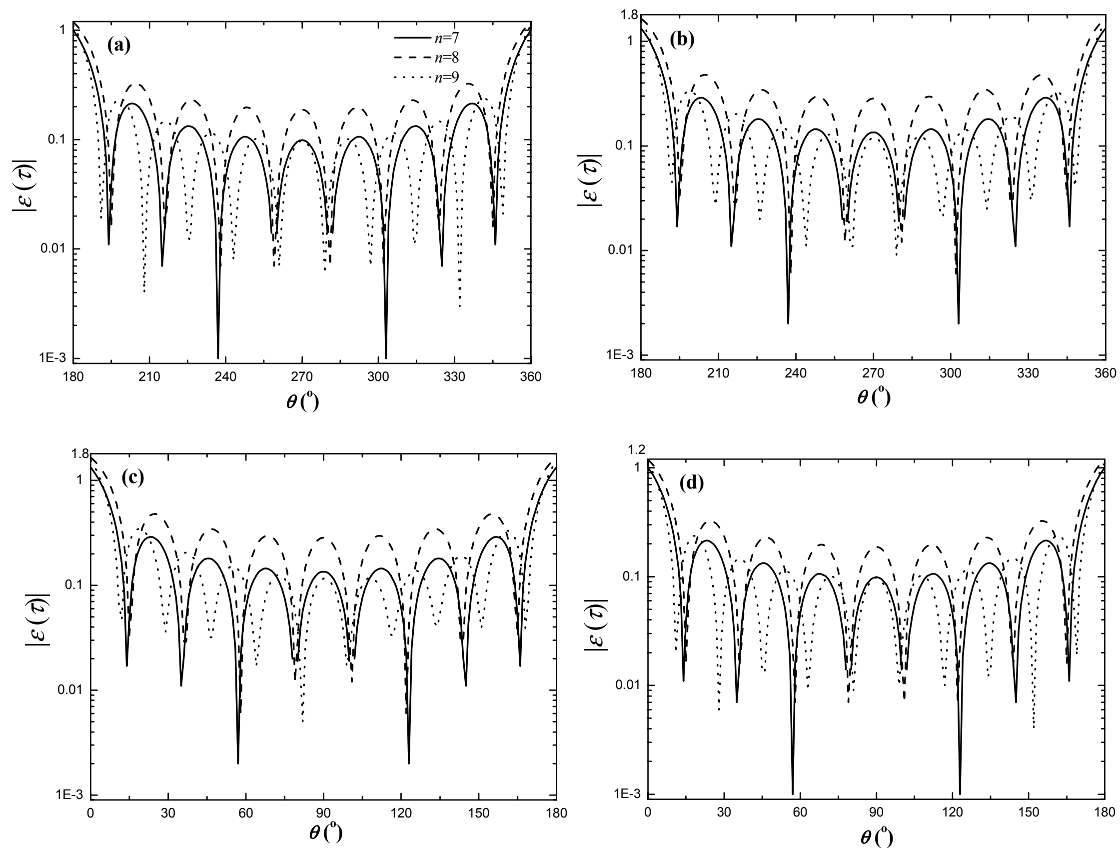

(a) The residual stress on L, (b) The residual stress on L_1, (c) The residual stress on $\underline{L_1}$, (d) The residual stress on $\underline{L}$

Fig. 4-5 THE RESIDUAL STRESS FOR $\eta = 0.5$, a_1/a=5/10, γ=90°

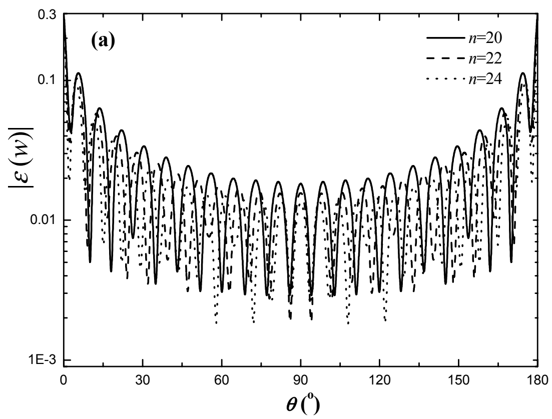

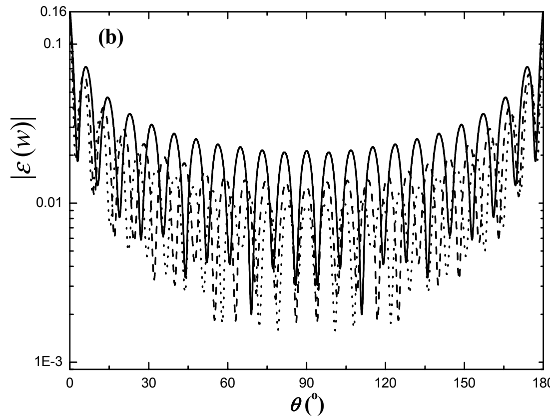

(a) The residual displacement on $\underline{L_1}$, (b) The residual displacement on $\underline{L}$

Fig. 4-6 THE RESIDUAL DISPLACEMENT FOR $\eta = 5.0$, a_1 / a=5/10, γ=90°

It can be seen from the above figures that the residual stresses at every hill outer rims and tunnel inner rims remain a relatively high value even the truncation order *n* increase. The reason is that the hill outer rims and tunnel inner rims are singular points for stress (Yuan and Liao 1996); and the stress auxiliary function $\Phi_1(\theta)$ and $\Phi_2(\theta)$ is discontinuous at the rims, namely at the points of $\theta = 0, \pi$ the stress functions defined for 360 degree have 'jumps', from nonzero to zero on the hill surface, so the Gibb's phenomena, namely overshooting at points of discontinuity, appear while Fourier series expansion is made to $\Phi_1(\theta)$ and $\Phi_2(\theta)$. Therefore, the stresses as well as displacements at the four rims are not accurate in this paper. However, the Figures 3~6 indicate that on average, all residuals converge to zero on the entire boundary of auxiliary functions. This means that with Fourier series expansion, the effect of hill and tunnel rims on the accuracy of the solution is limited only in the very small region near the hill and tunnel rims.

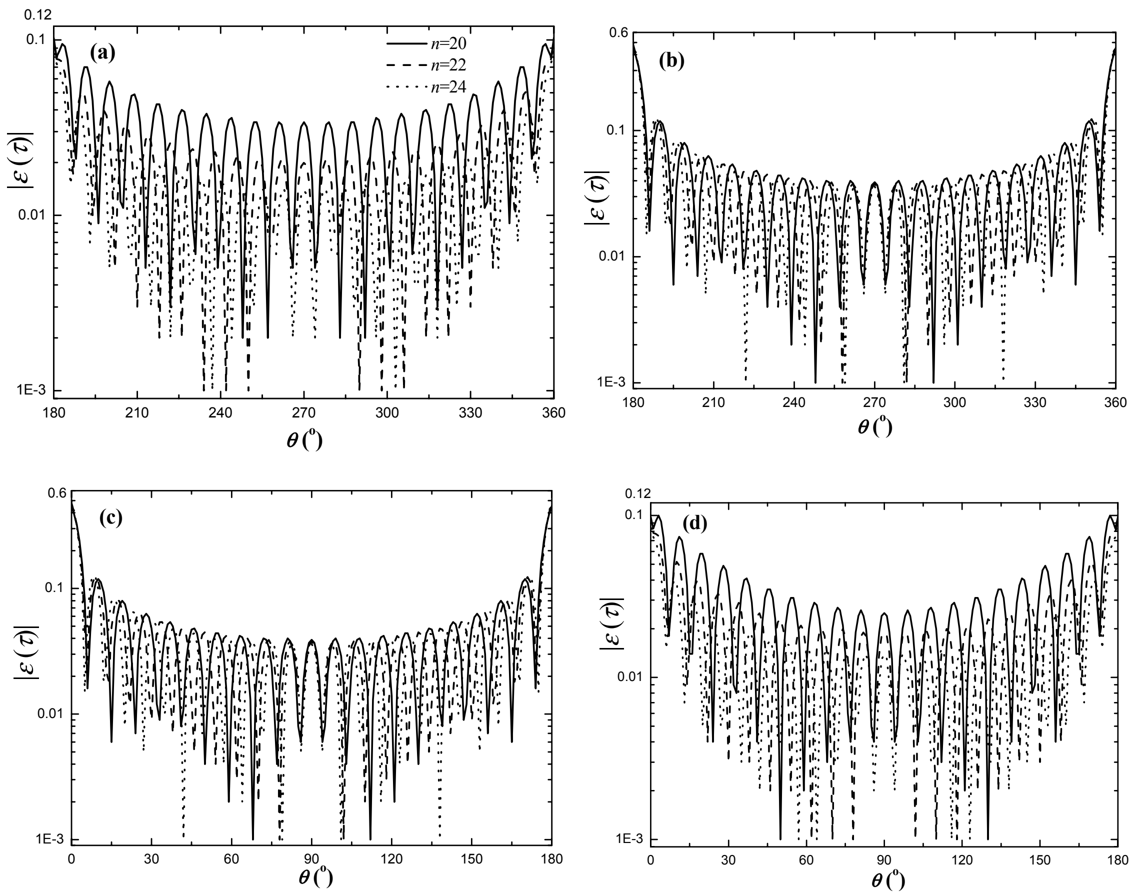

(a) The residual stress on L, (b) The residual stress on L_1, (c) The residual stress on $\underline{L_1}$, (d) The residual stress on $\underline{L}$

Fig. 4-7 THE RESIDUAL STRESS ON VARIOUS BOUNDARIES FOR $\eta = 5.0$, a_1/a=5/10, γ=90^o

4.4.2 Some Three-Dimensional Figures

Fig. 4-8~Fig. 4-15 show the surface displacement amplitudes, plotted versus the dimensionless distance x/a and the dimensionless frequency, η, for angles of incidence γ =90^o (vertical) and 0^o (horizontal) and corresponding to the radius ratio of tunnel and hill as a_1/a=5/10 and 3/10. In these figures, the displacement amplitudes on the surface of the hill are plotted along the axis x/a in the interval $-1 \le x/a \le 1$. The point $x/a = -1$ corresponds to the left rim of the hill, $x/a = 0$ to the top and

$x/a=1$ to the right rim. The incident SH waves are assumed to arrive from the left ($x/a<0$) in all cases except of case for that of vertical incidence (γ=90°). It can be seen from the four figures, the complexity of the surface displacements increases with increasing frequency η. For horizontal incidence (γ=0°), the complexity of the surface displacement amplitudes increases on the side of the half space facing the incoming waves ($x/a<-1$), and becomes relatively smoother on the other side ($x/a>1$). The zone behind the surface (canyon, valley or hill) and subsurface (cavity or inclusion) topographies is often referred to as the shadow zone.

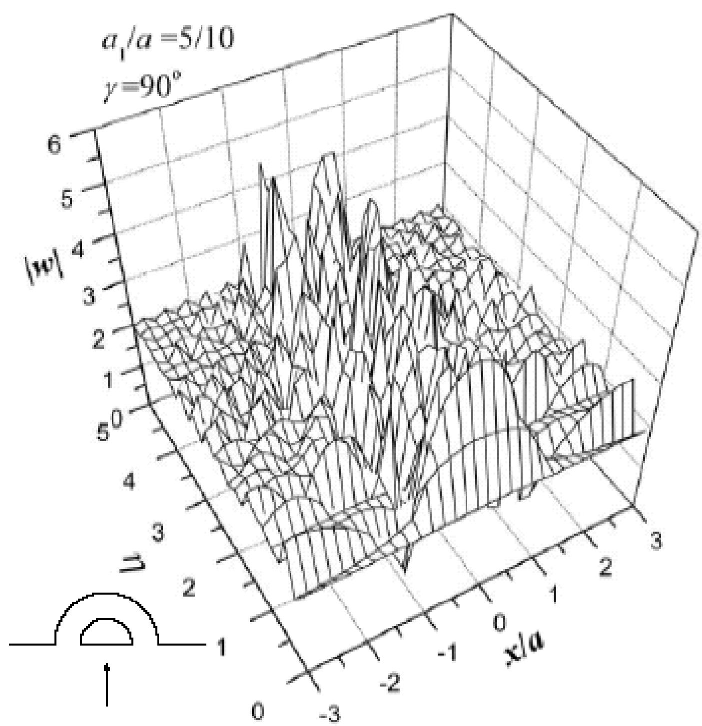

Fig. 4-8 DISPLACEMENT AMPLITUDES VERSUS DIMENSIONLESS FREQUENCY:
$a_1/a=5/10$, γ**=90°**

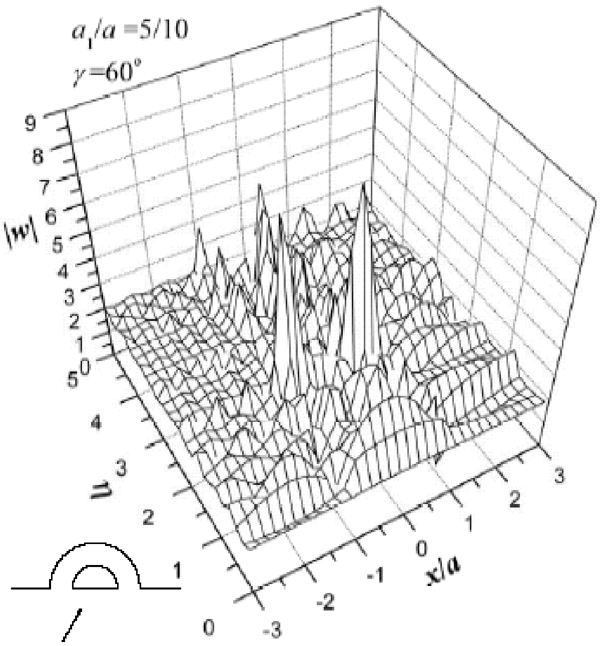

Fig. 4-9 DISPLACEMENT AMPLITUDES VERSUS DIMENSIONLESS FREQUENCY:

$a_1 / a = 5/10$, γ**=60º**

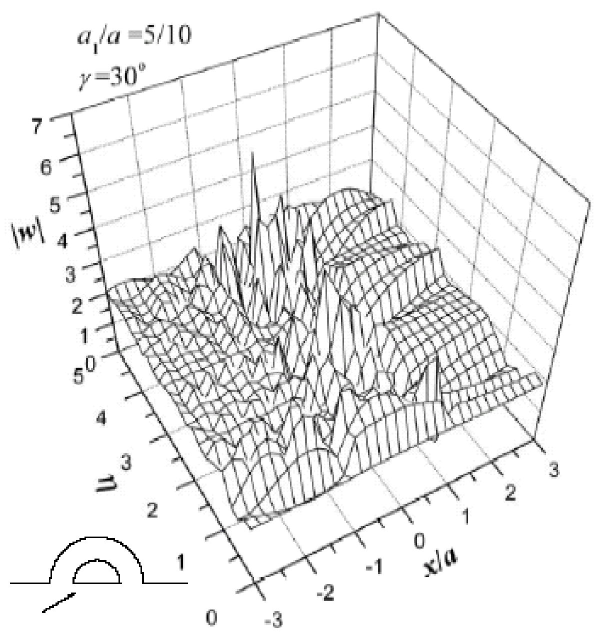

Fig. 4-10 DISPLACEMENT AMPLITUDES VERSUS DIMENSIONLESS FREQUENCY:

$a_1 / a = 5/10$, γ**=30º**

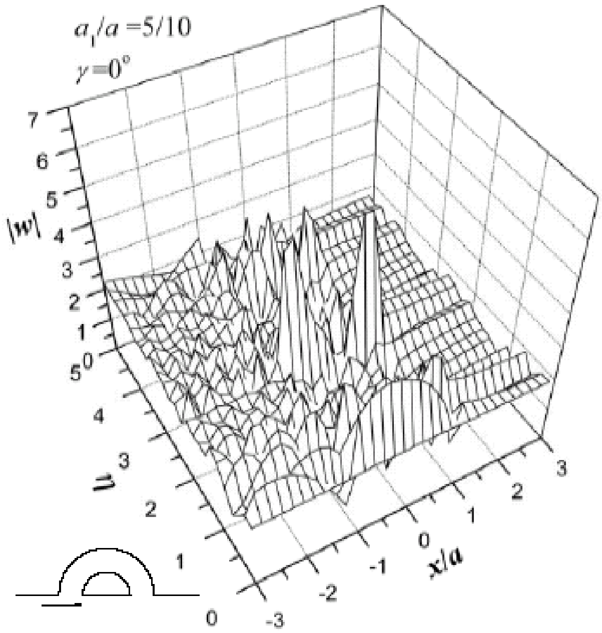

Fig. 4-11 DISPLACEMENT AMPLITUDES VERSUS DIMENSIONLESS FREQUENCY:

$a_1/a = 5/10$, γ=0°

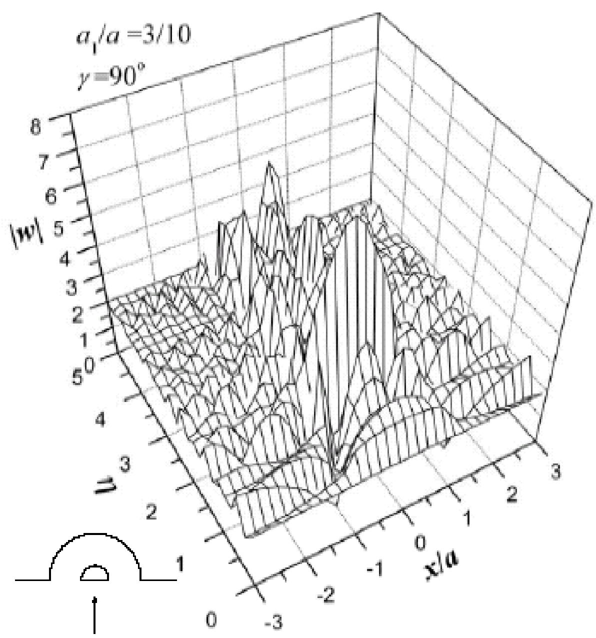

Fig. 4-12 DISPLACEMENT AMPLITUDES VERSUS DIMENSIONLESS FREQUENCY:

$a_1/a = 3/10$, γ=90°

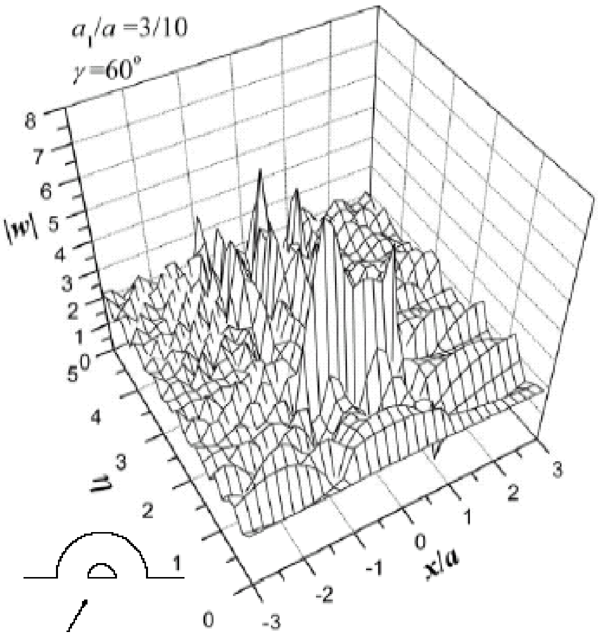

Fig. 4-13 DISPLACEMENT AMPLITUDES VERSUS DIMENSIONLESS FREQUENCY:

$a_1 / a = 3/10$, γ=60°

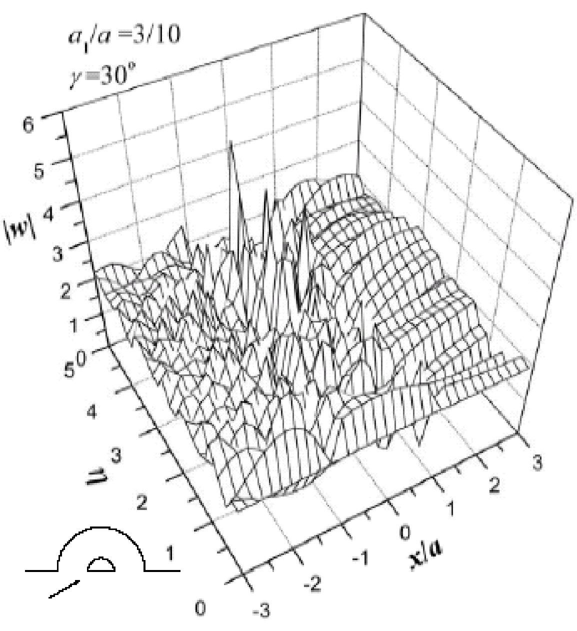

Fig. 4-14 DISPLACEMENT AMPLITUDES VERSUS DIMENSIONLESS FREQUENCY:

$a_1 / a = 3/10$, γ=30°

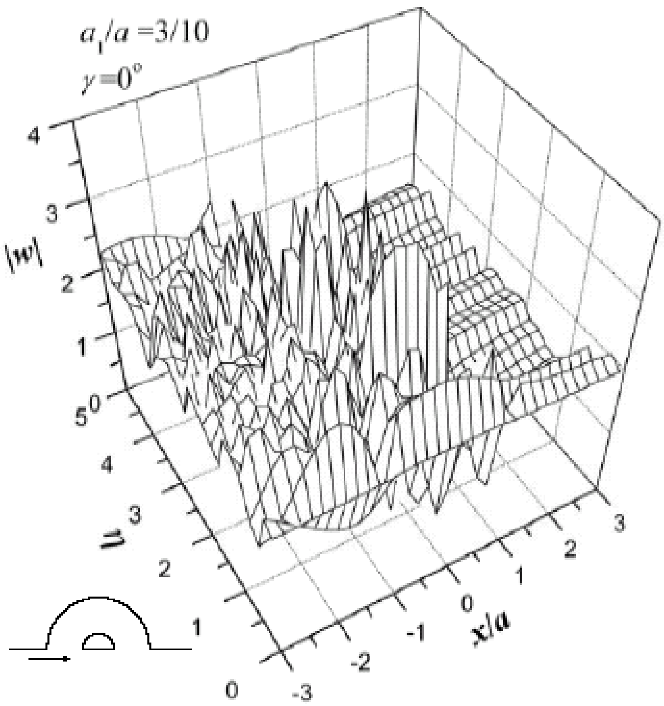

Fig. 4-15 DISPLACEMENT AMPLITUDES VERSUS DIMENSIONLESS FREQUENCY:

$a_1 / a = 3/10$, γ=0°

The maximum amplitudes as high as 8.5 around when $\eta \approx 2.2$ are observed near the left rim of hill in Fig. 4-9. Liang et al. (2004), in studying diffraction of SH waves by hill with concentric circular tunnel, made similar observation. However, in the study of diffraction of SH waves by none-tunnel hill (Yuan and Liao 1996), the displacement amplitudes only reach 3.9. These phenomena just as echo may be explained by the fact that, some diffracted waves are more easily reflected time after time between the hill surface and the top surface of the tunnel, resulting in a standing wave pattern there. This mechanism of wave motion acts similarly in the study of diffraction of SH waves by canyon above subsurface tunnel (Lee et al. 1999). At low frequencies (e.g. less than 0.05), the graph shows that every point on the half-space surface and the hill has displacement amplitudes closing to 2.0, but as frequencies slightly increases (e.g. larger than 0.1), the displacement amplitudes in the hills can greatly increase as a result of diffraction.

4.4.3 Some Two-Dimensional Results of the Ground Surface Displacements

Fig. 4-16~Fig. 4-19 show the effects of the incident angle and dimension of tunnel on the ground surface displacements. The calculated parameters are: the ratio of tunnel and hill are a_1/a =3/10 and 5/10, dimensionless frequency η=3.0 and 5.0, and at four different incident angles 90°, 60°, 30° and 0°.

Viewing from Figures below, we can find that the incident angles of SH-waves and the dimension of tunnel can both affect the pattern of the surface displacements. If the tunnel doesn't exist, a shadow zone can be observed behind the canyon by horizontal incident SH-wave (Yuan and Liao 1996). The same phenomena can be observed in the subsequent figures. The displacement amplitudes behind the hill for horizontal incident SH waves are always lower than those of the free field and those in front of the hill. The same observations have also previously been made for the case of SH waves incident on canyon (Cao and Lee 1989) and underground cavity (Lee 1977). In the figure 16 and 18, vertical incidence cases, ground motion is concentrated in the hill region (i.e., $x/a \in [-1,1]$). It may be explained by the frequencies of incident SH-wave are close to certain natural vibration frequencies of the hill-tunnel system and resonances occur in these two cases.

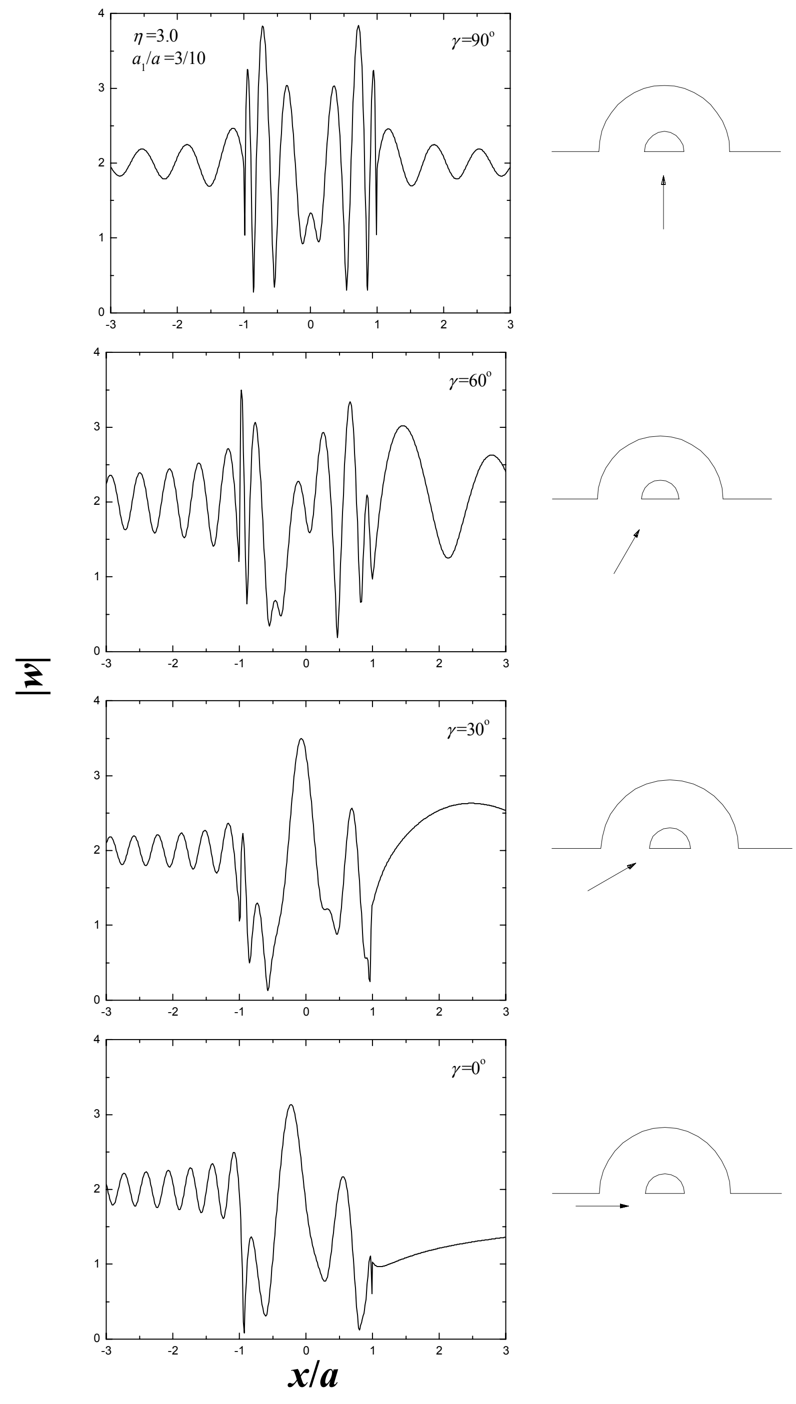

Fig. 4-16 SURFACE DISPLACEMENT AMPLITUDES AT FOUR ANGLES OF INCIDENCE,

$\eta = 3.0, \ a_1 / a = 3/10$

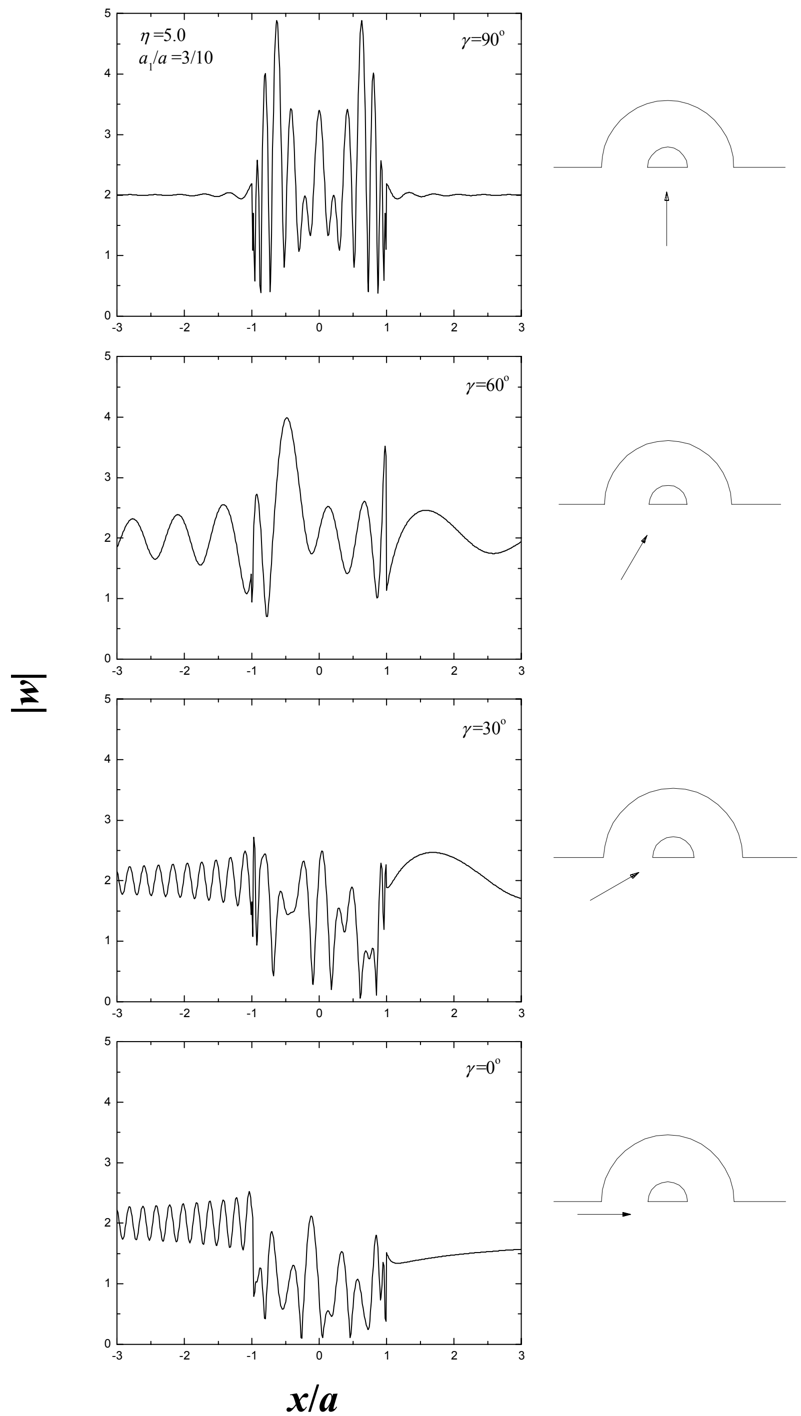

Fig. 4-17 SURFACE DISPLACEMENT AMPLITUDES AT FOUR ANGLES OF INCIDENCE,

$\eta = 5.0$, $a_1 / a = 3/10$

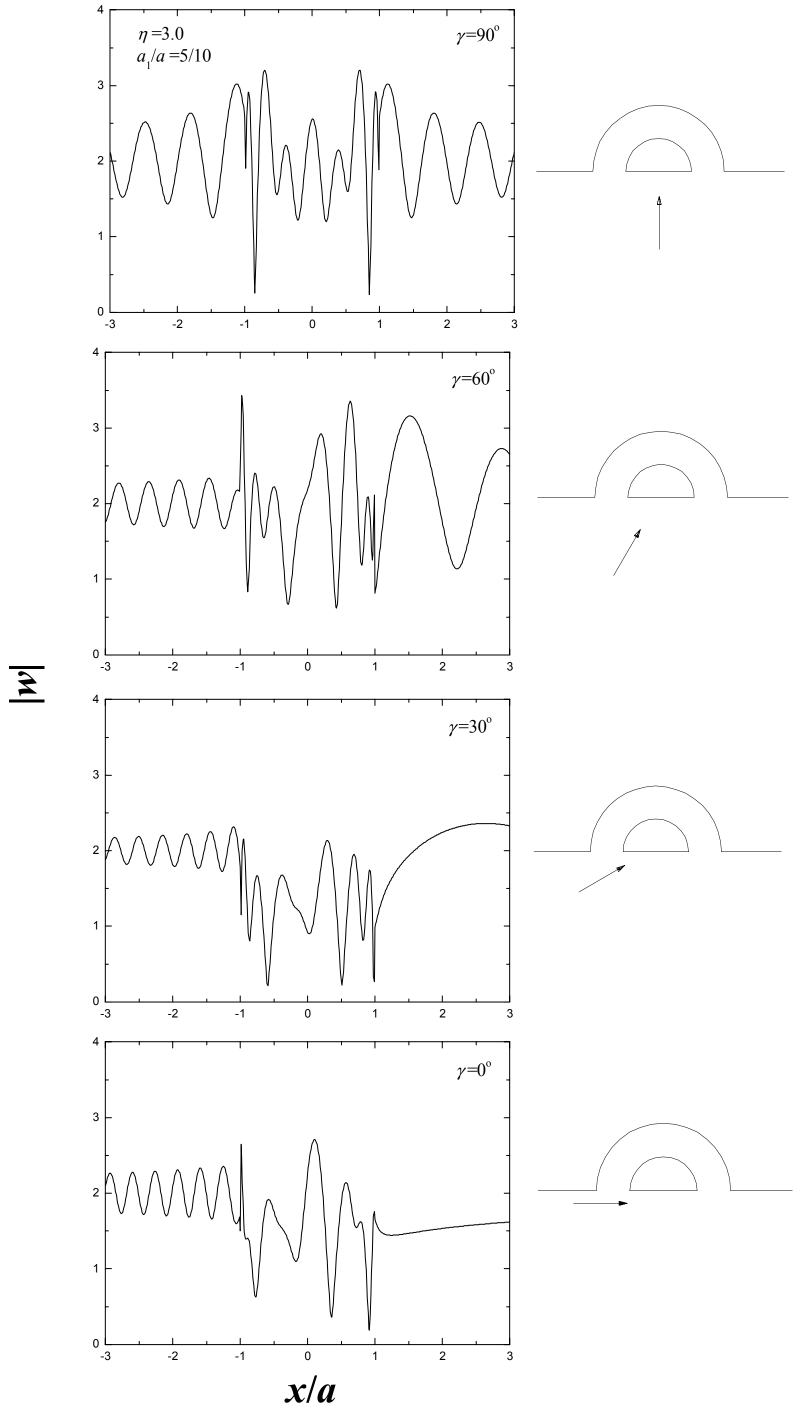

Fig. 4-18 SURFACE DISPLACEMENT AMPLITUDES AT FOUR ANGLES OF INCIDENCE,

$$\eta = 3.0,\ a_1 / a = 5/10$$

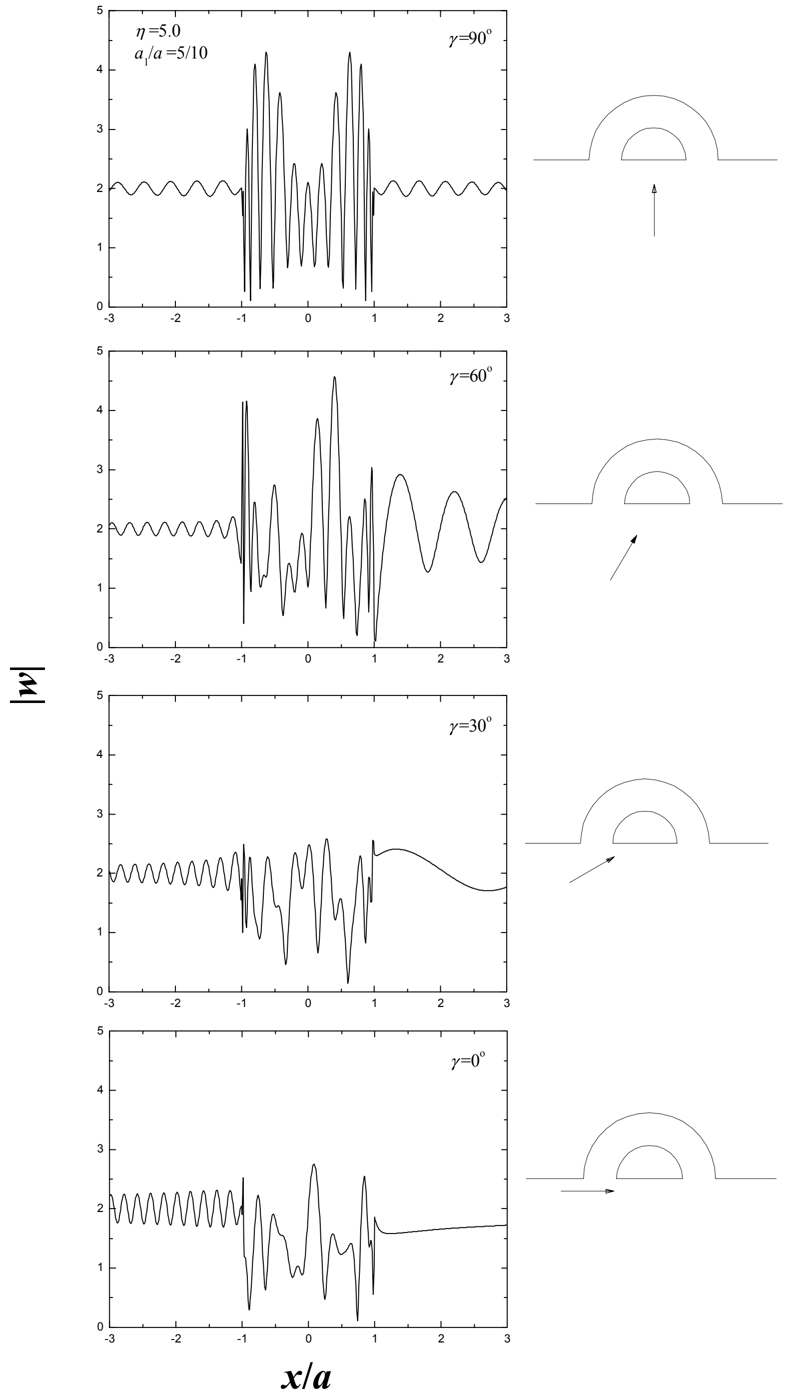

Fig. 4-19 SURFACE DISPLACEMENT AMPLITUDES AT FOUR ANGLES OF INCIDENCE,

$$\eta = 5.0,\ \ a_1 / a = 5/10$$

4.5 Conclusions

An analytical solution for scattering of incident SH waves by a semi-cylindrical hill with a concentric semi-cylindrical tunnel was derived by wave functions expansion and auxiliary functions technique. Complex exponential and cosine forms of Fourier expansion theorem are used. This method may be applied for further studies involving mixed boundary problem.

(1) The amplification of surface displacement amplitudes at some points around the hill can be as high as two times the free-field motions.

(2) The utilization of complex exponential and cosine forms of Fourier expansion theorem can improve the efficiency and precision of mixed boundary problems, however, the range of resoluble cases is still limited by the Gibb's phenomena, the complexity of model and precision of variables of computer language.

(3) The incident angles of SH-waves and the dimension of tunnel can both affect the pattern of the surface displacements. As the none-tunnel hill cases, a shadow zone is observed behind the canyon.

(4) The dimensionless frequency η play an important role in determining the displacement patterns. Larger values of η will result in higher complexity of displacements and in higher amplifications.

Chapter 5

SHALLOW CYLINDRICAL CANYON OR VALLEY FOR INCIDENT PLANE OR CYLINDRICAL SH-WAVES

In practice, by the effect of gravity and erosion, nearly all the canyons (if modeled by a segment of circular-arc) are likely to be in the shape of a minor arc other than a major one. Hence only shallow cylindrical canyons or valleys are discussed in this chapter. If needed, deep canyons or valleys can be analyzed through almost the same steps as those represented later with slight changes.

Canyon and valley are the first ones to be studied by earthquake engineers to investigate the effect of topographies to seismic wave propagation. Trifunac published two cornerstone papers on antiplane response of semi-cylindrical alluvial valley (1971) and semi-cylindrical canyon (1973) by incident SH-waves. Yuan and Liao expand those two models into shallow cylindrical section cases in 1995 and 1994, respectively.

At the beginning of this chapter, the derivation of semi- or shallow cylindrical canyon for incident SH-waves, which notwithstanding is essentially the same as the previous solution by Trifunac (1973) or Yuan and Liao (1994), is presented briefly to provide a complete vision on this subject. Next the incident waves are changed to cylindrical SH-waves emitted from a neighboring point source. Then a new approach which applies precisely on the boundary segment is elaborated. This intricate approach validates the effectiveness of extending the traction-free boundary condition from a circular segment to the whole circle, the implied correct method adopted by almost all the preceding researchers. The results of both methods agree with another straightforward method, the Image Method, which will be used again in the next chapter for a sub-surface cavity model. Finally, the diffraction of cylindrical SH-waves by semi- or shallow cylindrical valley is examined in the last section.

5.1 Shallow Cylindrical Canyon

5.1.1 Plane or Cylindrical SH-Wave Incidence by a Previous Approach

The cross section of the two-dimensional model studied in this section is shown in Fig. 5-1. It represents an elastic, isotropic and homogeneous half-space with a shallow cylindrical canyon of radius a. The free surface of the half-space consists of a flat surface L and circular-arc sag boundary $\underline{L}$. The shape of the canyon can be characterized by the height-to-width ratio, h/b, where h and b represent the depth and half-width of the canyon respectively. Three rectangular coordinate systems (x, y), $(\underline{x}, \underline{y})$, and $(\overline{x}, \overline{y})$ and three corresponding polar systems (r, θ), $(\underline{r}, \underline{\phi})$, and $(\overline{r}, \overline{\phi})$ are defined in Fig. 5-1. Fig. 5-2 shows the sketch of incident cylindrical wave cases. Please refer to Section 2.2.2 for the notation meanings to avoid redundancy.

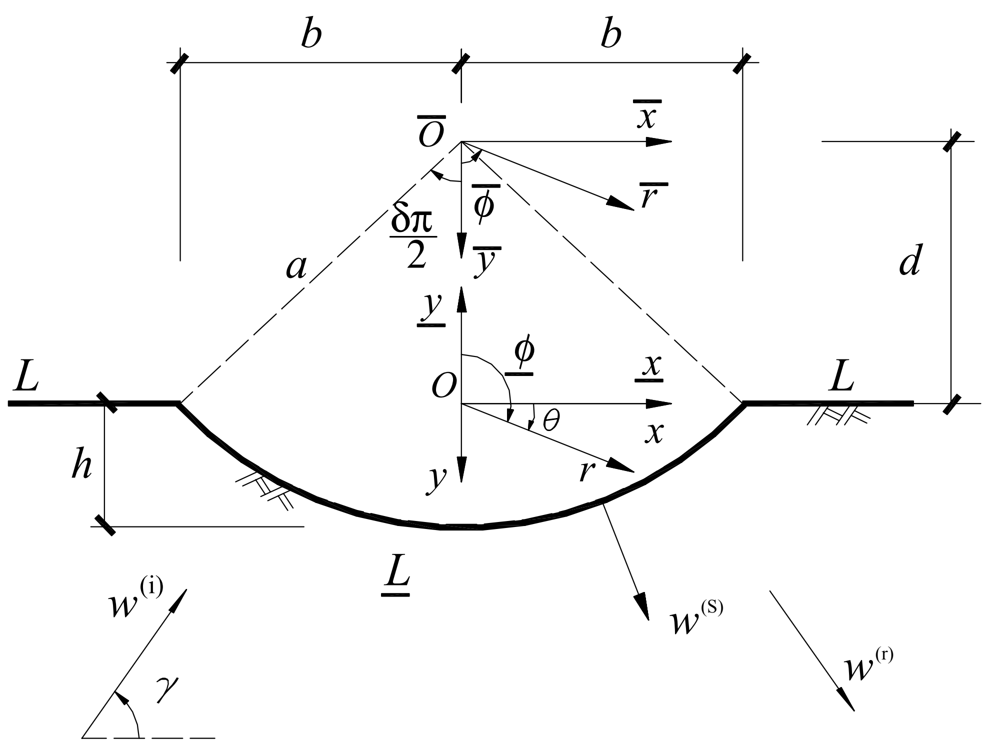

Fig. 5-1 SHALLOW CYLINDRICAL CANYON (INCIDENT PLANE SH-WAVES)

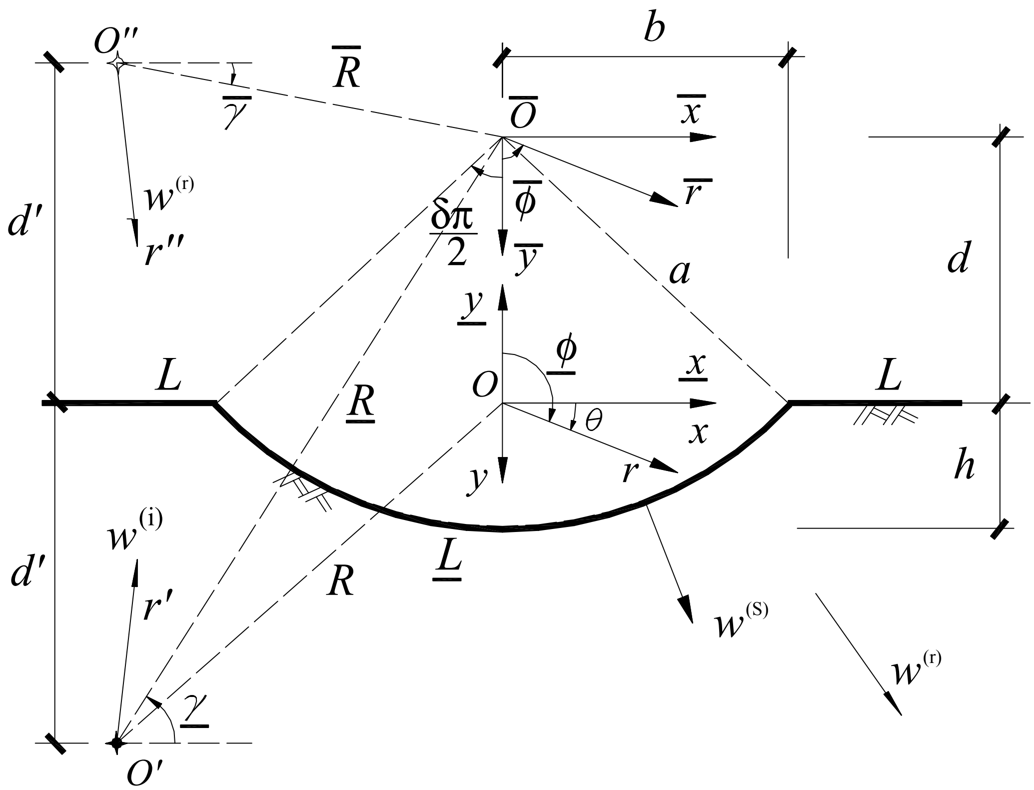

Fig. 5-2 SHALLOW CYLINDRICAL CANYON (INCIDENT CYLINDRICAL SH-WAVES)

The total displacement field w consists of free field displacement $w^{(ff)}$ and scattered displacement $w^{(S)}$ resulting from the interaction between the half-space and shallow cylindrical boundary $\underline{L}$.

The traction-free boundary conditions are

$$\tau_{\theta z}\,|_{\theta=0,\pi}=0 \qquad \text{at} \quad (r,\theta)\in L \tag{11.1}$$

$$\tau_{\overline{r}z}\,|_{\overline{r}=a}=0 \qquad \text{at} \quad (\overline{r},\overline{\phi})\in \underline{L} \tag{11.2}$$

where the hoop stress $\tau_{\theta z}$ and the radial stress τ_{rz} are specified by equations (8.3) and (8.4), respectively.

The free-field wave motion expressions listed below are just copied from Section 2.2 in Chapter 2. The free field displacements in the lower polar coordinate system (r,θ) are

$$w^{(\mathrm{ff})}\left(r,\theta\right)=\sum_{n=0}^{\infty}a_n^{(\mathrm{f})}\mathrm{J}_n\left(kr\right)\cos n\theta \tag{11.3}$$

where

$$a_n^{(\mathrm{f})}=\begin{cases}2\varepsilon_n \mathrm{i}^n\cos n\gamma & \text{, for plane waves}\\ 2\varepsilon_n(-1)^n\dfrac{\mathrm{H}_n^{(1)}(kR)}{\left|\mathrm{H}_0^{(1)}\left(kR\right)\right|}\cos n\gamma & \text{, for cylindrical waves}\end{cases} \tag{11.4}$$

The free field displacements in the upper polar coordinate system $(\bar{r},\bar{\phi})$ are

$$w^{(\mathrm{ff})}(\bar{r},\bar{\phi})=\sum_{m=-\infty}^{\infty}\bar{a}_m^{(\mathrm{f})}\mathrm{J}_m\left(k\bar{r}\right)\mathrm{e}^{\mathrm{i}m\bar{\phi}} \tag{11.5}$$

in which,

$$\bar{a}_m^{(\mathrm{f})}=\begin{cases}2\cos\left(kd\sin\gamma-m\gamma\right) & \text{, for plane waves}\\ \dfrac{\mathrm{i}^m}{\left|\mathrm{H}_0^{(1)}\left(kR\right)\right|}\left[\mathrm{H}_m^{(1)}(k\underline{R})\mathrm{e}^{-\mathrm{i}m\underline{\gamma}}+\mathrm{H}_m^{(1)}(k\bar{R})\mathrm{e}^{-\mathrm{i}m\bar{\gamma}}\right] & \text{, for cylindrical waves}\end{cases} \tag{11.6}$$

with the following parameters for cylindrical waves

$$\bar{R}\ \text{or}\ \underline{R}=\sqrt{\left(d\mp d'\right)^2+h'^2};\qquad \bar{\gamma}\ \text{or}\ \underline{\gamma}=\arctan\left(\frac{d\mp d'}{h'}\right) \tag{11.7}$$

The wave field in the half-space scattered in the presence of the shallow canyon is

$$w^{(\mathrm{S})}(r,\theta)=\sum_{n=0}^{\infty}A_n\mathrm{H}_n^{(1)}\left(kr\right)\cos n\theta \tag{11.8}$$

where, the A_n are a set of complex unknowns to be determined by boundary conditions.

$$\tau_{\theta z}^{(\mathrm{S})}(r,\theta)=\frac{\mu}{r}\frac{\partial w^{(\mathrm{S})}(r,\theta)}{\partial\theta}=-\frac{\mu}{r}\sum_{n=0}^{\infty}n\mathrm{J}_n(kr)A_n\sin n\theta \tag{11.9}$$

Since $\theta = 0, \pi$ on the flat boundary L, traction-free boundary condition Eqn. (11.1) is satisfied automatically. Rewrite (11.8) into its exponential form in terms of $\left(\underline{r}, \underline{\phi}\right)$ by relation $\underline{r} = r$, $\underline{\phi} = \pi/2 + \theta$

$$w^{(\mathrm{S})}(\underline{r}, \underline{\phi}) = \sum_{n=-\infty}^{\infty} \underline{A}_n \mathrm{H}_n^{(1)}\left(k\underline{r}\right) \mathrm{e}^{\mathrm{i}n\underline{\phi}} \tag{11.10}$$

where, $\underline{A}_n = \dfrac{(-\mathrm{i})^{|n|}}{\varepsilon_{|n|}} A_{|n|}$ for $n = 0, \pm 1, \pm 2, \cdots$.

After applying Graf's formula (8.26), scattered wave $w^{(\mathrm{S})}$ in the lower coordinate $\left(\underline{r}, \underline{\phi}\right)$ could be transformed to the upper coordinate $\left(\overline{r}, \overline{\phi}\right)$

$$w^{(\mathrm{S})}(\overline{r}, \overline{\phi}) = \sum_{m=-\infty}^{\infty} \overline{A}_m \mathrm{H}_m^{(1)}\left(k\overline{r}\right) \mathrm{e}^{\mathrm{i}m\overline{\phi}} \tag{11.11}$$

in which,

$$\overline{A}_m = \sum_{n=-\infty}^{\infty} \underline{A}_n \mathrm{J}_{n+m}(kd) = \sum_{n=0}^{\infty} \frac{A_n}{2} (-\mathrm{i})^n \left[\mathrm{J}_{m+n}(kd) + \mathrm{J}_{m-n}(kd)\right] \tag{11.12}$$

Then the radial stress on boundary $\underline{L}$ can be calculated in the polar coordinate system $\left(\overline{r}, \overline{\phi}\right)$ through Eqn(8.4) and boundary condition (11.2) can be written as

$$\tau_{\overline{r}z}\left(\overline{r}, \overline{\phi}\right) = \mu \frac{\partial\left(w^{(\mathrm{ff})} + w^{(\mathrm{S})}\right)}{\partial \overline{r}} = \mu k \sum_{m=-\infty}^{\infty} \left(\overline{a}_m^{(\mathrm{f})} \mathrm{J}_m'\left(k\overline{r}\right) + \overline{A}_m \mathrm{H}_m^{(1)\prime}\left(k\overline{r}\right)\right) \mathrm{e}^{\mathrm{i}m\overline{\phi}} = 0 \tag{11.13}$$

Whereas equation (11.13) only works for the range of $-\dfrac{\delta\pi}{2} \le \overline{\phi} \le \dfrac{\delta\pi}{2}$, all the previous researchers (Trifunac 1973; Yuan and Liao 1994; and much more) assume it exists all along the whole perimeter of the circle $-\pi \le \overline{\phi} \le \pi$, i.e., $\overline{\phi}$ can be any value. Under this assumption, the terms within the brackets in equation (11.13) must equal zero, and that leads to the following explicit expression of the only set of unknowns $\overline{A}_m$

$$\overline{A}_m = -\frac{\mathrm{J}'_m(ka)}{\mathrm{H}^{(1)\prime}_m(ka)}\,\overline{a}^{(\mathrm{f})}_m \quad \text{for } m = 0, \pm 1, \pm 2, \cdots \tag{11.14}$$

By now this model looks like has been solved perfectly and displacements or stresses within the whole half-space are determinable by wave functions (11.11) and (11.5) or their derivatives in the coordinate system $\left(\overline{r}, \overline{\phi}\right)$. However, those two wave functions are actually transformed from equations (11.10) and (11.3) in the coordinate system $\left(\underline{r}, \underline{\phi}\right)$ by Graf's formula. They satisfy traction-free boundary condition (11.1) automatically but (11.11) and (11.5) do not necessarily. According to this concern, Yuan and Liao (1994) returned the coordinate system of equation (11.14)back to $\left(\underline{r}, \underline{\phi}\right)$ and get the following infinite linear equations in terms of A_n after substituting Eqn.(11.12)

$$\sum_{n=0}^{\infty} \frac{A_n}{2}(-\mathrm{i})^n \left[\mathrm{J}_{m+n}(kd) + \mathrm{J}_{m-n}(kd)\right] = -\frac{\mathrm{J}'_m(ka)}{\mathrm{H}^{(1)\prime}_m(ka)}\,\overline{a}^{(\mathrm{f})}_m \quad \text{for } m = 0, \pm 1, \pm 2, \cdots \tag{11.15}$$

They can be computed simultaneously after truncating to finite orders. This approach sounds like perfect but actually has severe difficulties on convergence due to some unclear numerical reason. Therefore the only feasible way is to apply equation (11.14) by assuming that horizontal zero-stress boundary condition (11.1) are still satisfied strictly after coordinate transformation.

In case of the canyon studied is semi-cylindrical, equation (11.15) reduces to

$$A_n = -\frac{\mathrm{J}'_n(ka)}{\mathrm{H}^{(1)\prime}_n(ka)}\,a^{(\mathrm{f})}_n \quad \text{for } n = 0, 1, 2, \cdots \tag{11.16}$$

In summary, rigorously speaking, this classic approach used by many researchers in the past is based on the feasibility of two assumptions: One is the error induced by extending the applicability of traction-free boundary condition from a circular segment to the whole circle; the other is whether we can set up and solve the governing equations the in the upper coordinate system $\left(\overline{r},\overline{\phi}\right)$ other than the lower one (r,θ). In the next several sections of this chapter these two assumptions are respectively referred to as Assumption I or Assumption II for short. The succeeding two sections 5.1.2 and 5.1.3 are present on the purpose of verifying these two assumptions.

5.1.2 A New Approach Precisely Applying the Fractional Boundary Condition

The approach elaborated in this section is only new on how to applying the boundary conditions precisely on the specific segment of the boundary circular-arc of concern. Therefore this relatively more complicated approach aims at verifying the validation of Assumption I mentioned at the end of previous section. All derivations and equations prior to the application of boundary conditions are exactly the same as equations (11.1) through (11.12) in the previous section. The upcoming derivations are worked out as a continuation of them.

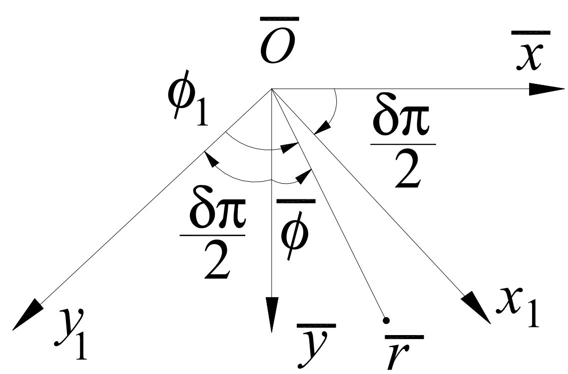

Fig. 5-3 ROTATION OF THE UPPER POLAR COORDINATE SYSTEM

Rotate clockwise by $\delta\pi/2$ to polar coordinate system $\left(r_1,\phi_1\right)$, then the free-field and scattered wave field expressions could be rewritten as follows by $r_1=\overline{r}$ and $\phi_1=\delta\pi/2+\overline{\phi}$,

$$w^{(\mathrm{ff})}(r_1,\phi_1)=\sum_{m=-\infty}^{\infty}\overline{a}_m^{(\mathrm{f})}\mathrm{e}^{-\mathrm{i}m\frac{\delta\pi}{2}}\mathrm{J}_m\left(kr_1\right)\mathrm{e}^{\mathrm{i}m\phi_1} \tag{11.17}$$

$$w^{(\mathrm{S})}(r_1,\phi_1)=\sum_{m=-\infty}^{\infty}\overline{A}_m \mathrm{e}^{-\mathrm{i}m\frac{\delta\pi}{2}}\mathrm{H}_m^{(1)}\left(kr_1\right)\mathrm{e}^{\mathrm{i}m\phi_1} \tag{11.18}$$

The sole boundary condition not satisfied in this model is the traction-free condition on $\underline{L}$ ($\overline{r}=a,\ -\delta\pi/2\le\overline{\phi}\le\delta\pi/2$), the bottom of canyon. It can be written as

$$\tau_{\overline{r}z}^{(\mathrm{ff})}(a,\overline{\phi})+\tau_{\overline{r}z}^{(\mathrm{S})}(a,\overline{\phi})=0\quad \square -\delta\pi/2\le\overline{\phi}\le\delta\pi/2 \tag{11.19}$$

Next, boundary condition equation will be precisely built up on the limited range of circular-arc in the polar coordinate $\left(r_1,\phi_1\right)$ based on orthogonal set $\left\{\cos\left(n\phi_1/\delta\right)\right\}$ on the interval $0\le\phi_1\le\delta\pi$, which could be validated by the following equality

$$\int_0^{\delta\pi}\cos\frac{n}{\delta}\phi_1\cos\frac{m}{\delta}\phi_1\mathrm{d}\phi_1=0\quad \text{when}\ \ m\neq n \tag{11.20}$$

Suppose we want to represent a given function $F\left(\phi_1\right)$ in terms of orthogonal functions $\left\{\cos\left(n\phi_1/\delta\right)\right\}$ in the form of following series expansion (Hamming, 1971)

$$F\left(\phi_1\right)=\sum_{n=0}^{\infty}f_n\cos\frac{n}{\delta}\phi_1 \tag{11.21}$$

where

$$f_n=\frac{\int_0^{\delta\pi}F\left(\phi_1\right)\cos\frac{m}{\delta}\phi_1\mathrm{d}\phi_1}{\int_0^{\delta\pi}\cos^2\frac{m}{\delta}\phi_1\mathrm{d}\phi_1}=\frac{2}{\delta\pi}\int_0^{\delta\pi}F\left(\phi_1\right)\cos\frac{m}{\delta}\phi_1\mathrm{d}\phi_1 \tag{11.22}$$

Thus, for the traction-free boundary condition represented in $\left(r_1,\phi_1\right)$,

$$\tau_{r_1z}^{(\mathrm{ff})}(a,\phi_1)+\tau_{r_1z}^{(\mathrm{S})}(a,\phi_1)=0\ \square\ 0\le\phi_1\le\delta\pi \tag{11.23}$$

Stress functions $\tau_{r_1z}^{(\mathrm{ff})}(a,\phi_1)$ and $\tau_{r_1z}^{(\mathrm{S})}(a,\phi_1)$ can be expanded to the following infinite series,

$$\begin{cases} \tau_{r_1 z}^{(\mathrm{ff})}\left(a,\phi_1\right)=\sum_{n=0}^{\infty}\tau_n^{\mathrm{ff}}\cos\frac{n}{\delta}\phi_1 \\ \tau_{r_1 z}^{(\mathrm{S})}\left(a,\phi_1\right)=\sum_{n=0}^{\infty}\tau_n^{\mathrm{S}}\cos\frac{n}{\delta}\phi_1 \end{cases} \tag{11.24}$$

where

$$\begin{Bmatrix} \tau_n^{\mathrm{ff}} \\ \tau_n^{\mathrm{S}} \end{Bmatrix}=\frac{2\mu k}{\delta\pi}\sum_{m=-\infty}^{\infty}\mathrm{e}^{-\mathrm{i}m\frac{\delta\pi}{2}}\left(\int_0^{\delta\pi}\mathrm{e}^{\mathrm{i}m\phi_1}\cos\frac{n}{\delta}\phi_1\mathrm{d}\phi_1\right)\begin{Bmatrix} \overline{a}_m^{(\mathrm{f})}\mathrm{J}_m'(ka) \\ \overline{A}_m\mathrm{H}_m^{(1)\prime}(ka) \end{Bmatrix} \tag{11.25}$$

$(n = 0, 1, 2, \cdots)$

Substitution of Eqn.(11.24) into (11.23) leads to the following set of infinite linear equations by setting series terms $\tau_n^{\mathrm{ff}}+\tau_n^{\mathrm{S}}$ equal zero,

$$\sum_{m=-\infty}^{\infty}S_{nm}\overline{A}_m=p_n \tag{11.26}$$

where,

$$S_{nm}=\mathrm{H}_m^{(1)\prime}\left(ka\right)\mathrm{e}^{-\mathrm{i}m\frac{\delta\pi}{2}}\alpha_{nm} \tag{11.27}$$

$$p_n=-\sum_{m=-\infty}^{\infty}\overline{a}_m^{(\mathrm{f})}\mathrm{J}_m'(ka)\mathrm{e}^{-\mathrm{i}m\frac{\delta\pi}{2}}\alpha_{nm} \tag{11.28}$$

$$\alpha_{nm}=\int_0^{\delta\pi}\mathrm{e}^{\mathrm{i}m\phi_1}\cos\frac{n}{\delta}\phi_1\mathrm{d}\phi_1=c(n,m)+\mathrm{i}\cdot s(n,m) \tag{11.29}$$

with

$$\begin{aligned} c(n,m)&=\int_0^{\delta\pi}\cos m\phi_1\cos\frac{n}{\delta}\phi_1\mathrm{d}\phi_1 \\ &=\begin{cases} \delta\pi & ,\quad m=n=0 \\ \frac{1}{2}\left[\frac{1}{2m}\sin\left(2m\delta\pi\right)+\delta\pi\right] & ,\quad |m|=\frac{n}{\delta}\neq 0 \\ \frac{\delta}{2}\left[\frac{\sin\left(m\delta+n\right)\pi}{m\delta+n}+\frac{\sin\left(m\delta-n\right)\pi}{m\delta-n}\right] & ,\quad |m|\neq\frac{n}{\delta} \end{cases} \end{aligned} \tag{11.30}$$

$$s(n,m)=\int_0^{\delta\pi}\sin m\phi_1\cos\frac{n}{\delta}\phi_1\mathrm{d}\phi_1$$

$$=\begin{cases}0 & , \quad m=n=0 \\ \dfrac{1}{4m}\left[1-\cos\left(2m\delta\pi\right)\right] & , \quad |m|=\dfrac{n}{\delta}\neq 0 \\ \dfrac{\delta}{2}\left[\dfrac{1-\cos\left(m\delta+n\right)\pi}{m\delta+n}+\dfrac{1-\cos\left(m\delta-n\right)\pi}{m\delta-n}\right] & , \quad |m|\neq\dfrac{n}{\delta}\end{cases} \tag{11.31}$$

$(m = 0, \pm1, \pm2, \cdots)$ $(n= 0, 1, 2, \cdots)$

Thus coefficients $\overline{A}_m$ are solvable and their numerical results will be discussed and compared in section 5.1.4 below. Note that this new approach is still on the basis of Approximation II with Approximation I removed.

5.1.3 Reexamined Once Again by the Image Method

Image Method (or Method of Images) is a common method often used in electromagnetic wave theory to satisfy the boundary condition that the tangential component of electrical or magnetic field to the surface of a conduct is zero. Based on the similar concept, it is also widely used in seismic wave propagation research to satisfy the traction-free boundary condition on a flat ground surface especially for subsurface models like tunnels (Lee and Trifunac, 1979) or inclusions (Yuan, 1996). Actually, it is also applicable conditionally for some surface models like canyons.

The sketches of cross section of the two-dimensional models studied in this section are depicted in Fig. 5-4 and Fig. 5-5, similar to Fig. 5-1 and Fig. 5-2 except a condition that the ratio of height and width h/b must be larger than $1/\sqrt{3}$, that is, $d<h$ or $\delta\leq 2/3$, the origin of image SH-waves source $\underline{O}$ is located above the canyon surface. With this condition, the singular point $\underline{O}$ would not interfere with the wave field in the half-space and make the image method applicable to these somewhat deep canyons.

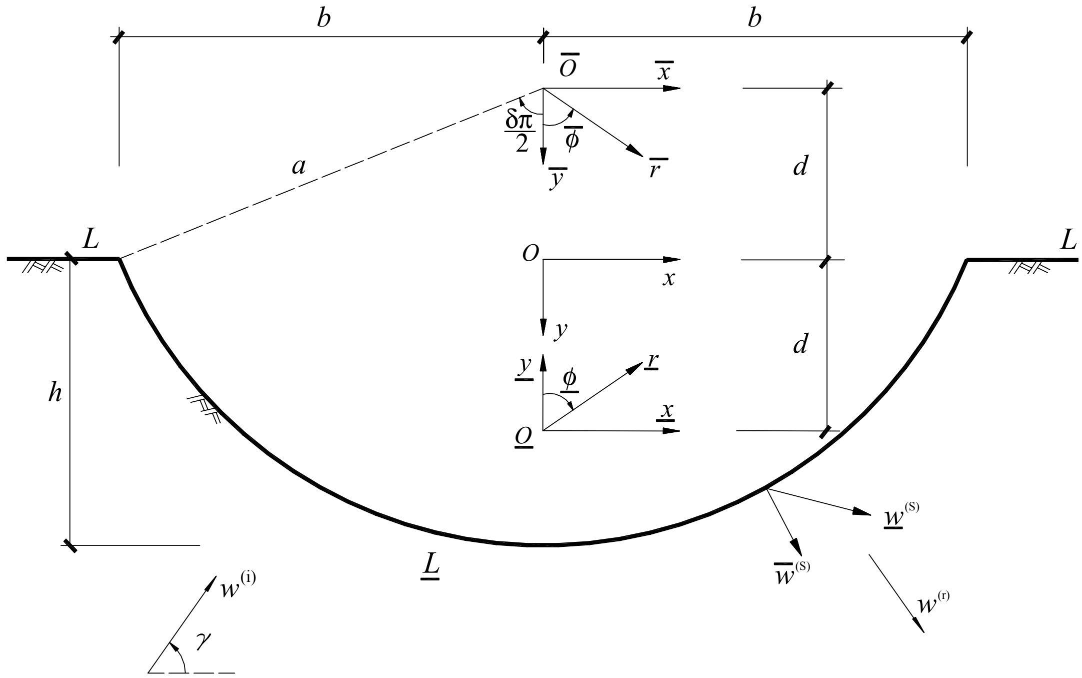

Fig. 5-4 SHALLOW CYLINDRICAL CANYON BY IMAGE METHOD (INCIDENT PLANE SH-WAVES)

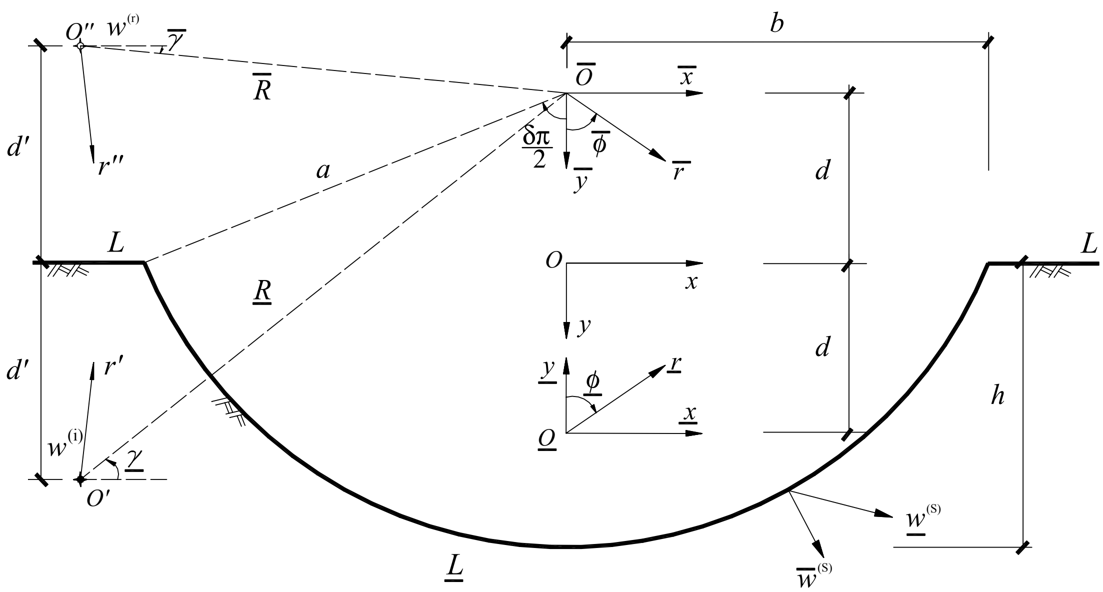

Fig. 5-5 SHALLOW CYLINDRICAL CANYON BY IMAGE METHOD (INCIDENT CYLINDRICAL SH-WAVES)

The expressions of free-field have nothing to change as previous section so they are omitted in this section. The scattered wave field in the half-space by the shallow canyon is restated here same as equation (11.11)

$$\overline{w}^{(\mathrm{S})}(\overline{r},\overline{\phi}) = \sum_{n=-\infty}^{\infty} A_n \mathrm{H}_n^{(1)}\left(k\overline{r}\right)\mathrm{e}^{\mathrm{i}n\overline{\phi}} \tag{11.32}$$

where, the A_n are a set of complex unknowns to be determined by boundary conditions. As the essence of image method, another mirror image of the scattered wave with the same form and coefficients is assumed to locate at $\underline{O}$ in respect to the ground surface.

$$\underline{w}^{(\mathrm{S})}(\underline{r},\underline{\phi}) = \sum_{m=-\infty}^{\infty} A_m \mathrm{H}_m^{(1)}\left(k\underline{r}\right)\mathrm{e}^{\mathrm{i}m\underline{\phi}} \tag{11.33}$$

Thus traction-free boundary condition on the ground surface would be satisfied automatically since those two similar scattered waves counteract with each other on their symmetric surface.

When the ratio of height and width h/b is larger than $1/\sqrt{3}$, that is, $d < h$, the origin of image SH wave source $\underline{O}$ is located above the canyon surface. So we applies the following exterior Graf's formula (equation (8.26)) to transform the image scattered wave to the upper polar coordinate system,

$$C_m\left(k\underline{r}\right)\mathrm{e}^{\mathrm{i}m\underline{\phi}} = \sum_{n=-\infty}^{\infty} \mathrm{J}_{m+n}\left(2kd\right)C_n\left(k\overline{r}\right)\mathrm{e}^{\mathrm{i}n\overline{\phi}}\text{, for } \overline{r} > 2d \tag{11.34}$$

where $C_n(\cdot)$ denotes $\mathrm{J}_n(\cdot)$ or $\mathrm{H}_n^{(1)}(\cdot)$. On the other hand, if h/b is less than $1/\sqrt{3}$, that is, $d > h$, the origin of image SH wave source $\underline{O}$ is located below the canyon surface. So the following interior Graf's formula (equation (8.27)) should be applied instead

$$C_m\left(k\underline{r}\right)\mathrm{e}^{\mathrm{i}m\underline{\phi}} = \sum_{n=-\infty}^{\infty} C_{m+n}\left(2kd\right)\mathrm{J}_n\left(k\overline{r}\right)\mathrm{e}^{\mathrm{i}n\overline{\phi}}\text{, for } \overline{r} < 2d \tag{11.35}$$

By those two Graf's formulae $\underline{w}^{(\mathrm{S})}$ should be rewritten respectively as

$$\underline{w}^{(\mathrm{S})}(\overline{r},\overline{\phi})=\begin{cases}\sum_{n=-\infty}^{\infty} A_n^* \mathrm{H}_n^{(1)}\left(k\overline{r}\right)\mathrm{e}^{in\overline{\phi}}, \text{ for } r>2\mathrm{d} \\ \sum_{n=-\infty}^{\infty} A_n^* \mathrm{J}_n\left(k\overline{r}\right)\mathrm{e}^{in\overline{\phi}}, \text{ for } r>2\mathrm{d}\end{cases} \tag{11.36}$$

in which,

$$A_n^*=\begin{cases}\sum_{m=-\infty}^{\infty} A_m \mathrm{J}_{n+m}(2kd), \text{ for } r>2\mathrm{d} \\ \sum_{m=-\infty}^{\infty} A_m \mathrm{H}_{n+m}^{(1)}(2kd), \text{ for } r>2\mathrm{d}\end{cases} \tag{11.37}$$

The sole boundary condition remains in this problem is the traction-free condition on $\underline{L}$ ($\overline{r}=a,\ -\delta\pi/2\le\overline{\phi}\le\delta\pi/2$), the bottom of canyon. In all previous similar papers, especially those discussing the same model as this one, the following equation are applied

$$\tau_{\overline{r}z}^{(\mathrm{ff})}(a,\overline{\phi})+\overline{\tau}_{\overline{r}z}^{(\mathrm{S})}(a,\overline{\phi})+\underline{\tau}_{\overline{r}z}^{(\mathrm{S})}(a,\overline{\phi})=0 \quad,\quad -\delta\pi/2\le\overline{\phi}\le\delta\pi/2 \tag{11.38}$$

As a simplification, expanding the effective range of $\overline{\phi}$ to the whole circular range so that equation (11.19) is equivalent to the following set of equations

$$\begin{cases}\overline{a}_n^{(\mathrm{f})}\mathrm{J}_n'\left(ka\right)+A_n\mathrm{H}_n^{(1)\prime}\left(ka\right)+\mathrm{H}_n^{(1)\prime}\left(ka\right)\sum_{m=-\infty}^{\infty}A_m\mathrm{J}_{m+n}\left(2kd\right)=0, \text{ for } h/b>1/\sqrt{3} \\ \overline{a}_n^{(\mathrm{f})}\mathrm{J}_n'\left(ka\right)+A_n\mathrm{H}_n^{(1)\prime}\left(ka\right)+\mathrm{J}_n'\left(ka\right)\sum_{m=-\infty}^{\infty}A_m\mathrm{H}_{m+n}^{(1)}\left(2kd\right)=0, \text{ for } h/b<1/\sqrt{3}\end{cases} \tag{11.39}$$

and it could be written in the following form of infinite linear equations

$$\begin{cases}\sum_{m=-\infty}^{\infty}\left[\mathrm{J}_{m+n}\left(2kd\right)+\delta_{nm}\right]A_m=-\overline{a}_n^{(f)}\dfrac{\mathrm{J}_n'\left(ka\right)}{\mathrm{H}_n^{(1)\prime}\left(ka\right)}, \text{ for } h/b>1/\sqrt{3} \\ \sum_{m=-\infty}^{\infty}\left[\mathrm{H}_{m+n}^{(1)}\left(2kd\right)+\dfrac{\mathrm{H}_n^{(1)\prime}\left(ka\right)}{\mathrm{J}_n'\left(ka\right)}\delta_{nm}\right]A_m=-\overline{a}_n^{(f)}, \text{ for } h/b<1/\sqrt{3}\end{cases} \tag{11.40}$$

$(n = 0, \pm1, \pm2, \cdots)$

in which $\delta_{nm} = 1$ when $n = m$; otherwise $\delta_{nm} = 0$

Governing equations (11.40) can then be truncated and solved for coefficients A_m ($m = 0, \pm 1, \pm 2, \cdots$). Substitution of A_m into equations (11.32) and (11.33) brings on the solution of scattered wave field.

5.1.4 Validation and Comparison of Numerical Results

5.1.4.1 Comparison of Plane Waves Results

After trials of calculation, we found that the mirror method presented in section 5.1.3 is in perfect agreement with old method presented in section 5.1.1 in terms of ground surface isplacement amplitude results. Comparisons of these two methods are omitted for brevity. Hence in this section, only numerical results by methods from section 5.1.1 and 5.1.2 are compared. In the following two figures, curves labeled by 'Old Method' is the one used in section 5.1.1; the other set of curves 'New Method' is referred to the method adopted in section 5.1.2.

Observation of these figures indicates that for small frequency, two methods match well as shown in Fig. 5-6. For high incident wave frequency as shown in Fig. 5-8, however, apparent discrepancies by the two methods can be observed.

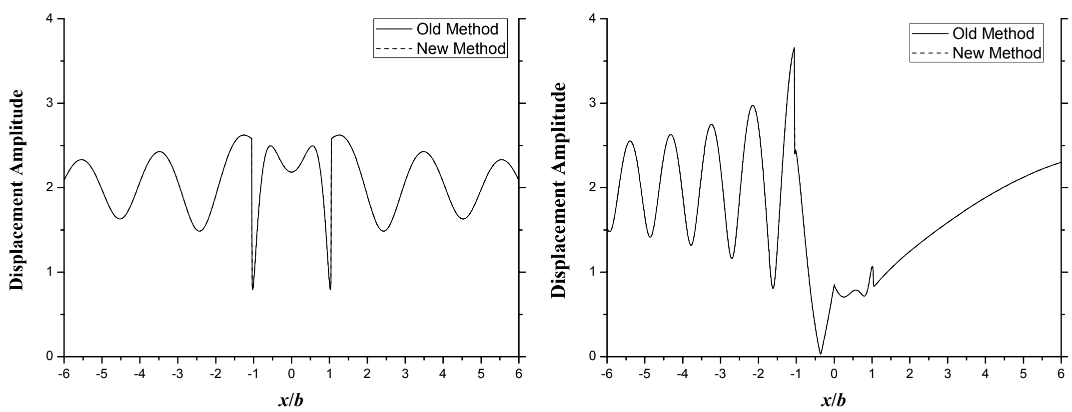

Fig. 5-6 SURFACE DISPLACEMENT AMPLITUDE OF SHALLOW CYLINDRICAL CANYON FOR $\eta = 1$, $h/b = 0.75$, $\gamma = 90^{\circ}$ AND 30°

On the other hand, wave motions become more drasticly when frequencies of incident waves go higher. This is a common phenomenon for time-domain local site wave propagation analysis. For grazing incidence cases, the steady-state displacement is amplified prominently at the left rim of the canyon. To the contrary, wave motions on the other (shade) side are deamplified. This is called "Screening Effect" or "Shielding Effect" in wave motion theory.

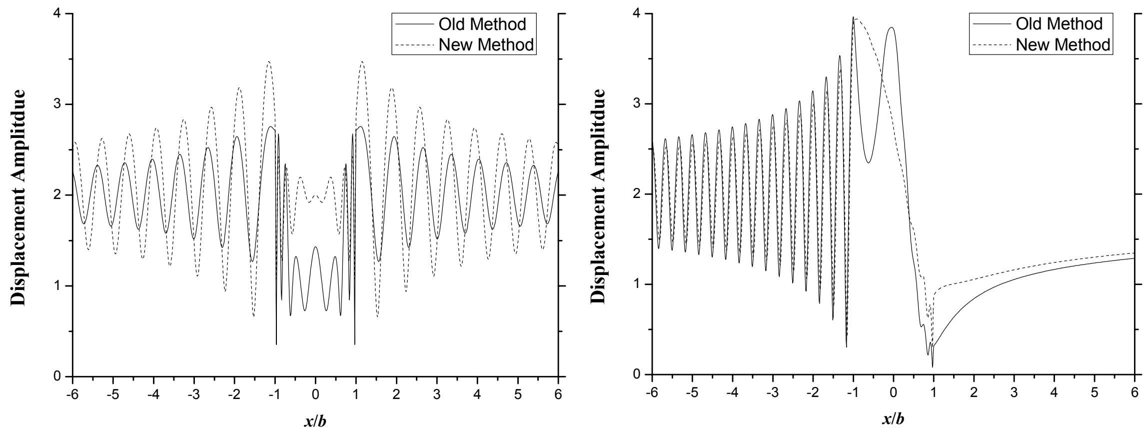

Fig. 5-7 SURFACE DISPLACEMENT AMPLITUDE OF SHALLOW CYLINDRICAL CANYON FOR $\eta = 3$, $h/b = 0.9$, $\gamma = 90^{\circ}$ **AND** 0°

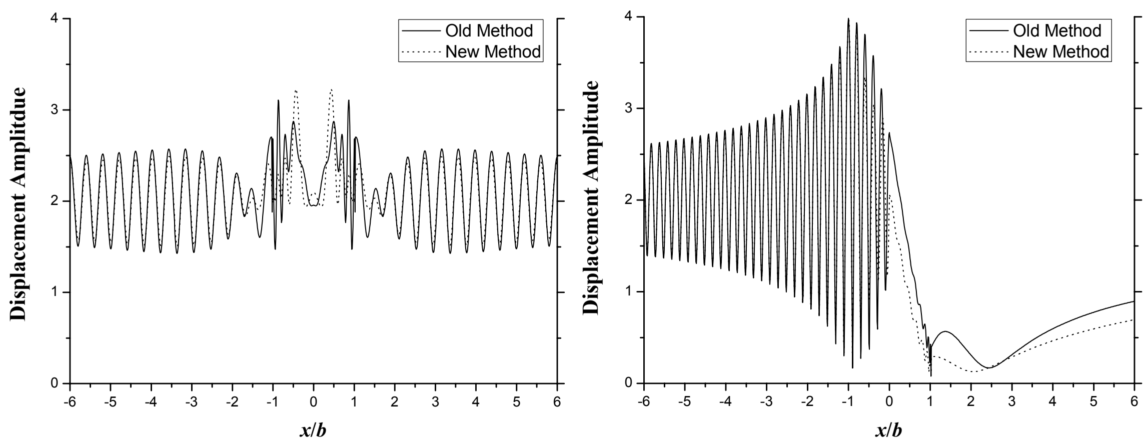

Fig. 5-8 SURFACE DISPLACEMENT AMPLITUDE OF SHALLOW CYLINDRICAL CANYON FOR $\eta = 5$, $h/b = 0.8$, $\gamma = 90^{\circ}$ **AND** 0°

5.1.4.2 Case Study of Cylindrical SH-Waves Results

This section studies ground surface displacement of a shallow canyon excited by incide nt cylindrical SH-waves. The (de)-amplification effects are influenced by depth-width ratio of canyon, incident angle and

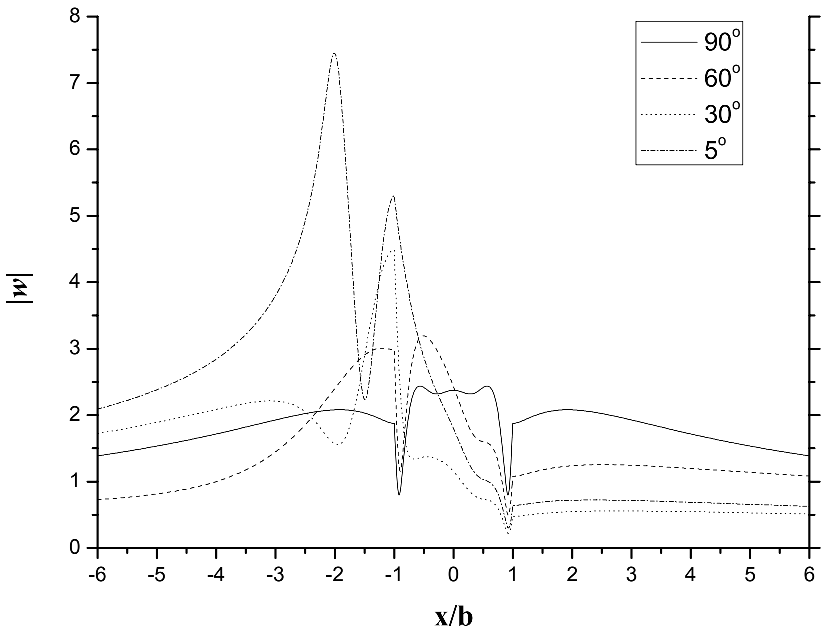

Fig. 5-9 SURFACE DISPLACEMENT AMPLITUDE OF SHALLOW CYLINDRICAL CANYON SUBJECTED TO INCIDENT CYLINDRICAL SH-WAVES FOR $\eta = 1$, $h/b = 1$, $R/a = 2$, $\gamma = 90^{\circ}, 60^{\circ}, 30^{\circ}$, **AND** 5°

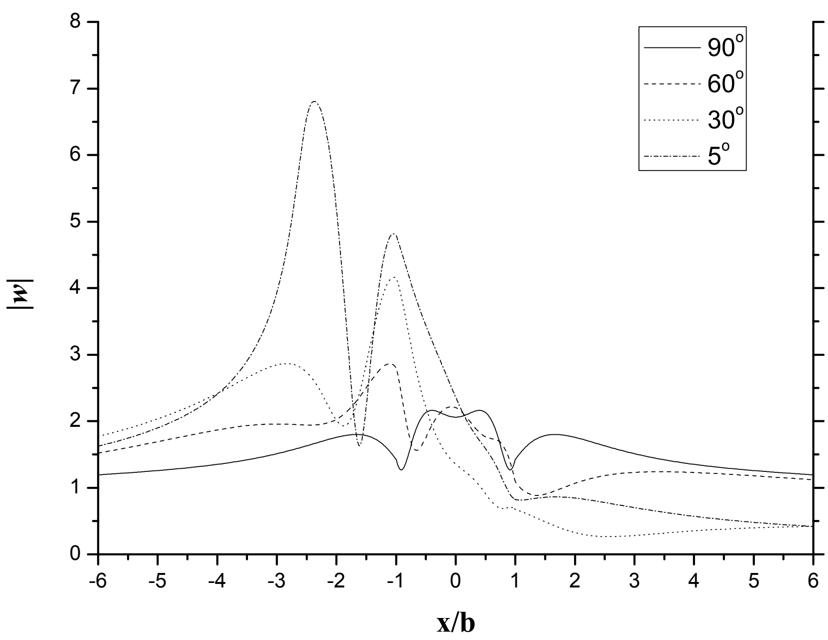

Fig. 5-10 SURFACE DISPLACEMENT AMPLITUDE OF SHALLOW CYLINDRICAL CANYON SUBJECTED TO INCIDENT CYLINDRICAL SH-WAVES FOR $\eta = 1$, $h/b = 0.5$, $R/a = 2$, $\gamma = 90^{\circ}, 60^{\circ}, 30^{\circ}$, **AND** 5°

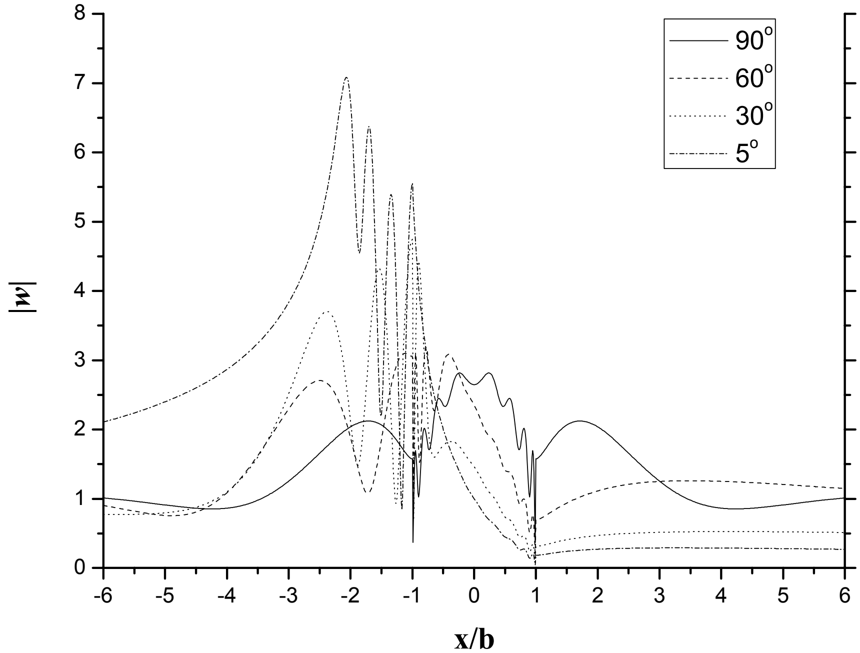

Fig. 5-11 SURFACE DISPLACEMENT AMPLITUDE OF SHALLOW CYLINDRICAL CANYON SUBJECTED TO INCIDENT CYLINDRICAL SH-WAVES FOR $\eta = 3$, $h/b = 1$, $R/a = 2$, $\gamma = 90^{\circ}, 60^{\circ}, 30^{\circ}$, **AND** 5°

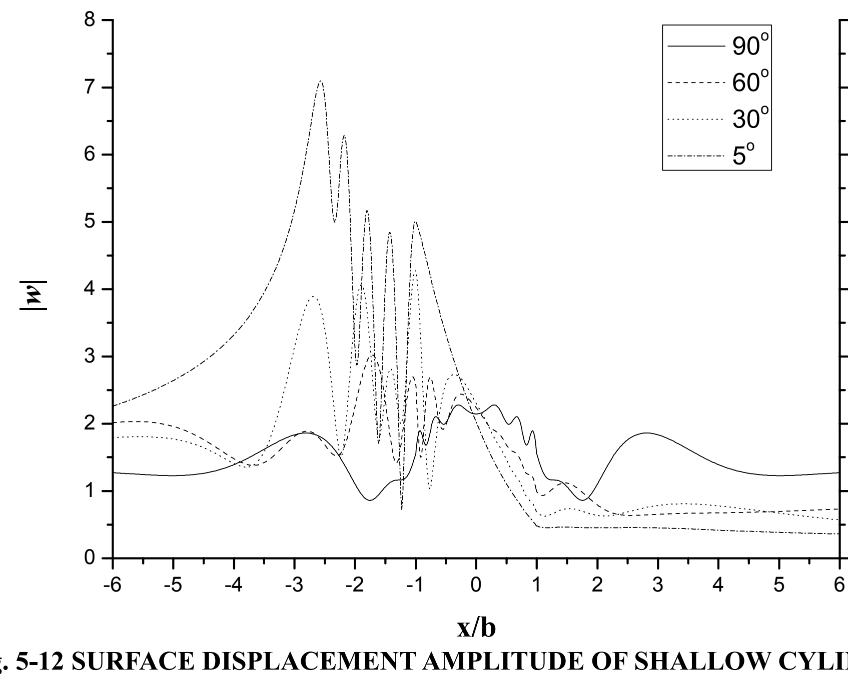

Fig. 5-12 SURFACE DISPLACEMENT AMPLITUDE OF SHALLOW CYLINDRICAL CANYON SUBJECTED TO INCIDENT CYLINDRICAL SH-WAVES FOR $\eta = 3$, $h/b = 0.5$, $R/a = 2$, $\gamma = 90^{\circ}, 60^{\circ}, 30^{\circ}$, **AND** 5°

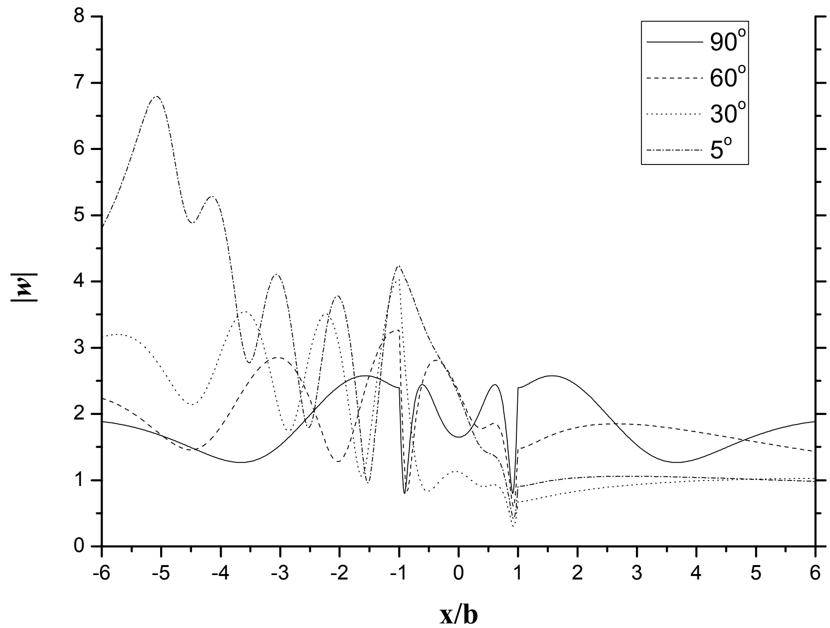

Fig. 5-13 SURFACE DISPLACEMENT AMPLITUDE OF SHALLOW CYLINDRICAL CANYON SUBJECTED TO INCIDENT CYLINDRICAL SH-WAVES FOR $\eta=1$, $h/b=1$, $R/a=5$, $\gamma=90^{\circ},60^{\circ},30^{\circ}$, **AND** 5°

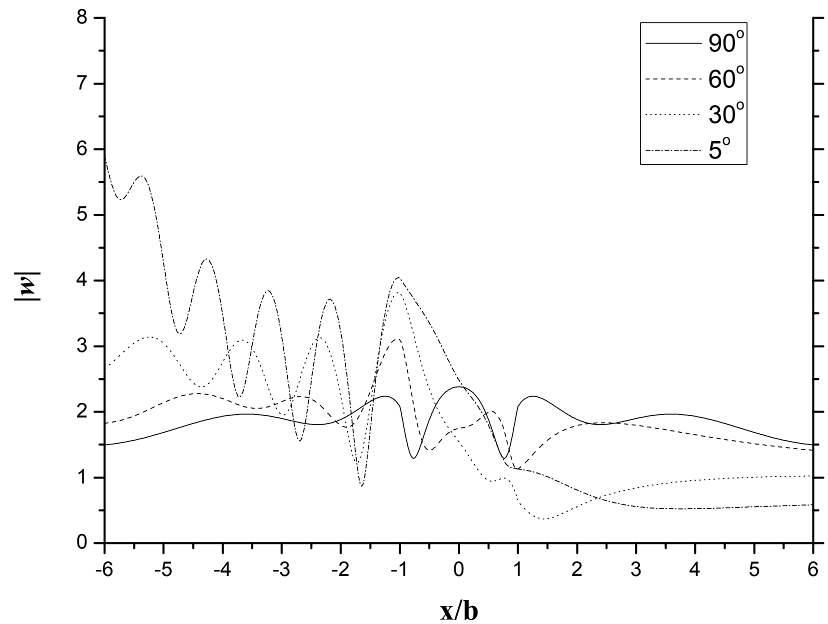

Fig. 5-14 SURFACE DISPLACEMENT AMPLITUDE OF SHALLOW CYLINDRICAL CANYON SUBJECTED TO INCIDENT CYLINDRICAL SH-WAVES FOR $\eta=1$, $h/b=0.5$, $R/a=5$, $\gamma=90^{\circ},60^{\circ},30^{\circ}$, **AND** 5°

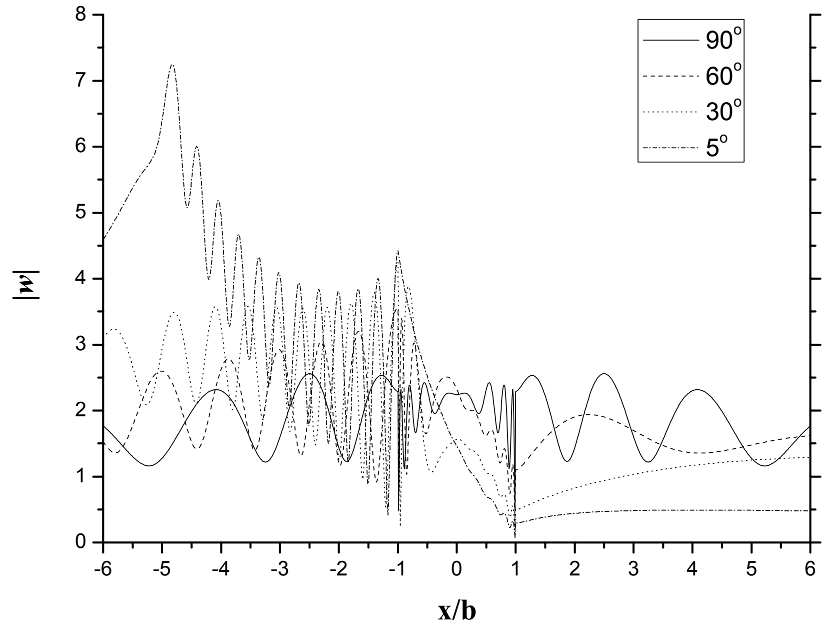

Fig. 5-15 SURFACE DISPLACEMENT AMPLITUDE OF SHALLOW CYLINDRICAL CANYON SUBJECTED TO INCIDENT CYLINDRICAL SH-WAVES FOR $\eta=3$, $h/b=1$, $R/a=5$, $\gamma=90^{\circ},60^{\circ},30^{\circ}$, **AND** 5°

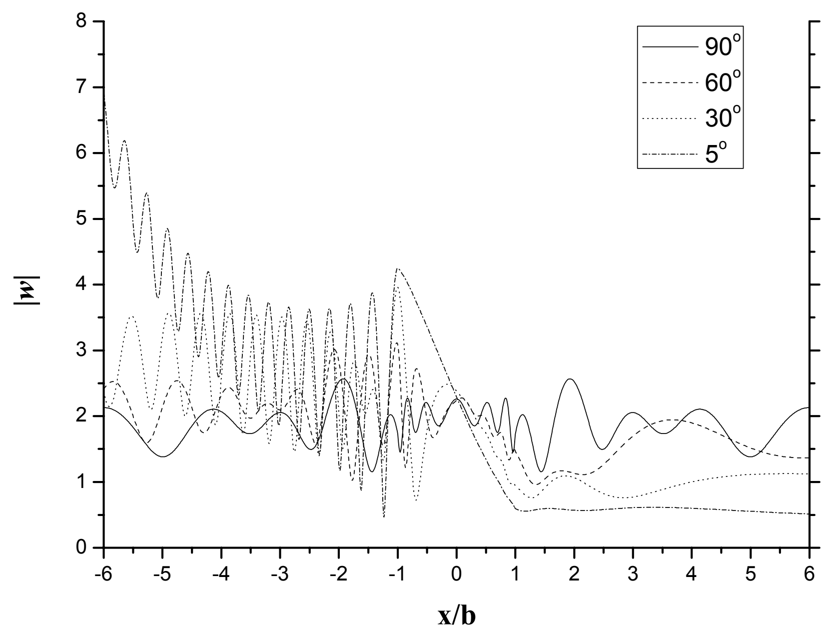

Fig. 5-16 SURFACE DISPLACEMENT AMPLITUDE OF SHALLOW CYLINDRICAL CANYON SUBJECTED TO INCIDENT CYLINDRICAL SH-WAVES FOR $\eta=3$, $h/b=0.5$, $R/a=5$, $\gamma=90^{\circ},60^{\circ},30^{\circ}$, **AND** 5°

frequency of incident waves, and location of source of cylindrical waves. Each plot of Fig. 5-9 and Fig. 5-16 examines displacement curves for four different angles of incidence (90^o, 60^o, 30^o, 5^o).

The reason why 5^o is selected to examine grazing incidence other than using 0^o is to avoid the singularity produced by placing point source right on the edge of half-space. As the figures shown, the general trend of displacement amplitudes excited by cylindrical waves is similar to the case of incident plane waves. The peak of curves is approximately located around the projected point of wave source point on the ground. The maximum value of displacement peak is beyond 7. Considering the amplitudes discussed here are normalized and dimensionless, engineers may not ignore such an amplification effect that is as large as 3.5 times of free-field response.

5.2 Shallow Cylindrical Valley for Incident Cylindrical SH-Waves

Analytical solutions of diffraction of semi- or shallow cylindrical valley for incident plane SH-waves have been well studied earlier by Trifunac (1971) and Yuan and Liao (1995). The model of this section is exactly as what Yuan and Liao considered with the exception of the type of incident waves. The incident plane SH-waves are replaced by an antiplane point source which can be put anywhere in the proximity of the valley including the interior of the alluvial valley. The cross section of the two-dimensional model studied in this section as shown in Fig. 5-17 is basically similar to the canyon model except some sediment medium fill the canyon and make the ground surface flat. The media contained in the valley and outside in the half-space are characterized by their shear modulus and wave numbers μ_1, k_1 and μ, k, respectively.

Fig. 5-18 illustrates a depict for a special case; when $h = b = a$ or $\delta = 1$, the model reduces to a semi-cylindrical valley, which is the same as the one studied much earlier by Trifunac (1971). However, that paper is for incident plane SH-waves but this section deals with incident cylindrical SH-waves which are resulted from an adjacent SH point-source.

The derivation of free field is omitted but the expressions of wave functions in various coordinate systems are listed below.

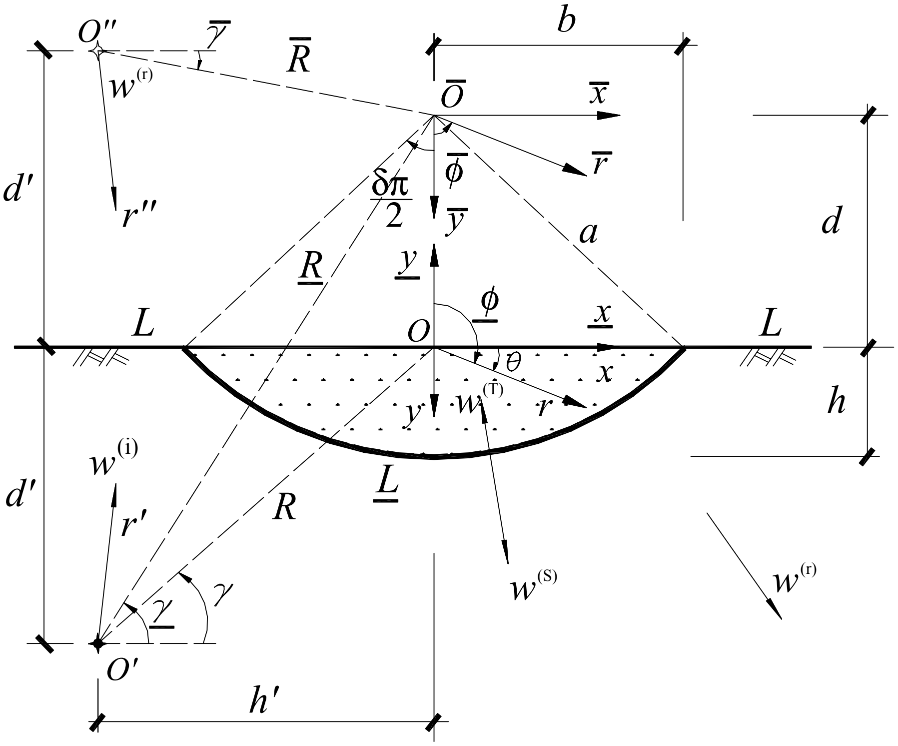

Fig. 5-17 SHALLOW CYLINDRICAL VALLEY FOR INCIDENT CYLINDRICAL SH-WAVES

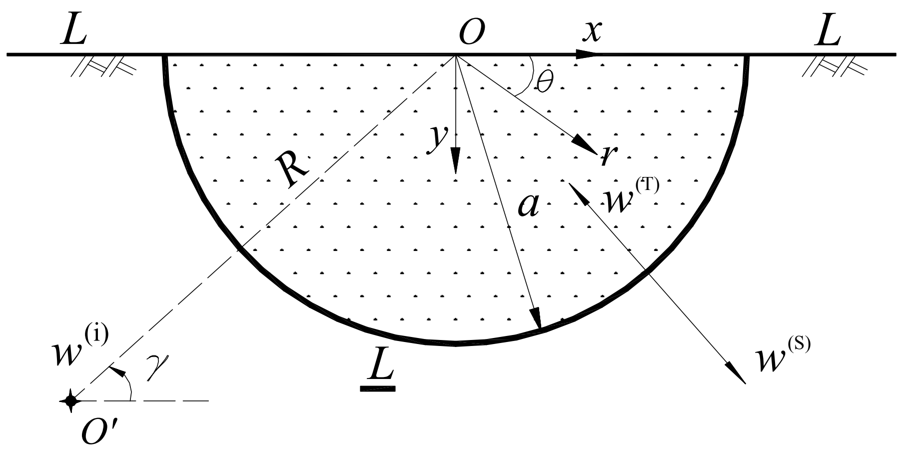

Fig. 5-18 A SPECIAL CASE - SEMI-CYLINDRICAL VALLEY

$$w^{(\mathrm{ff})}\left(r,\theta\right)=w^{(\mathrm{i})}+w^{(\mathrm{r})}=\begin{cases}\sum_{n=0}^{\infty}\mathrm{J}_n\left(kr\right)a_n^{(\mathrm{f})}\cos n\theta \quad , R>R^* \\ \sum_{n=0}^{\infty}\mathrm{H}_n^{(1)}\left(k_1 r\right)a_n^{(\mathrm{f})}\cos n\theta \ , R<R^*\end{cases} \tag{11.41}$$

$$w^{(\mathrm{ff})}(\overline{r},\overline{\phi})=\begin{cases}\sum_{n=-\infty}^{\infty}\overline{a}_n^{(\mathrm{f})}\mathrm{J}_n\left(k\overline{r}\right)\mathrm{e}^{\mathrm{i}n\overline{\phi}} \quad , R>R^* \\ \sum_{n=-\infty}^{\infty}\overline{a}_n^{(\mathrm{f})}\mathrm{H}_n^{(1)}\left(k_1\overline{r}\right)\mathrm{e}^{\mathrm{i}n\overline{\phi}} \ , R<R^*\end{cases} \tag{11.42}$$

where

$$a_n^{(\mathrm{f})}=\begin{cases}2\varepsilon_n(-1)^n\dfrac{\mathrm{H}_n^{(1)}(kR)}{\left|\mathrm{H}_0^{(1)}\left(kR\right)\right|}\cos n\gamma \ , R>R^* \\ 2\varepsilon_n(-1)^n\dfrac{\mathrm{J}_n(k_1R)}{\left|\mathrm{H}_0^{(1)}\left(k_1R\right)\right|}\cos n\gamma \ , R<R^*\end{cases} \tag{11.43}$$

$$\overline{a}_n^{(\mathrm{f})}=\begin{cases}\dfrac{\mathrm{i}^n}{\left|\mathrm{H}_0^{(1)}\left(kR\right)\right|}\left[\mathrm{H}_n^{(1)}(k\underline{R})\mathrm{e}^{-\mathrm{i}n\underline{\gamma}}+\mathrm{H}_n^{(1)}(k\overline{R})\mathrm{e}^{-\mathrm{i}n\overline{\gamma}}\right] \ , R>R^* \\ \dfrac{\mathrm{i}^n}{\left|\mathrm{H}_0^{(1)}\left(k_1R\right)\right|}\left[\mathrm{J}_n(k_1\underline{R})\mathrm{e}^{-\mathrm{i}n\underline{\gamma}}+\mathrm{J}_n(k_1\overline{R})\mathrm{e}^{-\mathrm{i}n\overline{\gamma}}\right] \ , R<R^*\end{cases} \tag{11.44}$$

or presented by a series formula

$$\overline{a}_n^{(\mathrm{f})}=\begin{cases}\sum_{m=0}^{\infty}\varepsilon_m\mathrm{i}^m\dfrac{\mathrm{H}_m^{(1)}(kR)}{\left|\mathrm{H}_0^{(1)}\left(kR\right)\right|}\cos m\gamma\left[\mathrm{J}_{n+m}(kd)+\mathrm{J}_{n-m}(kd)\right] \quad , R>R^* \\ \sum_{m=0}^{\infty}\varepsilon_m\mathrm{i}^m\dfrac{\mathrm{J}_m(k_1R)}{\left|\mathrm{H}_0^{(1)}\left(k_1R\right)\right|}\cos m\gamma\left[\mathrm{J}_{n+m}(k_1d)+\mathrm{J}_{n-m}(k_1d)\right] \ , R<R^*\end{cases} \tag{11.45}$$

$$\overline{R}\ \text{or}\ \underline{R}=\sqrt{\left(d\mp d'\right)^2+h'^2}; \qquad \overline{\gamma}\ \text{or}\ \underline{\gamma}=\arctan\left(\frac{d\mp d'}{h'}\right) \tag{11.46}$$

in those equations R^* stands for the length of radius vector within the valley in the direction of center O and wave source origin O', and is regarded as the criterion of whether the point source is inside/outside of the valley. (Note for semi-cylindrical valley, $R^* = a$)

$$R^* = a \frac{\cos\left(\arcsin\left(d \cos\gamma / a\right) + \gamma\right)}{\cos\gamma} \tag{11.47}$$

The scattered wave field in the half-space and transmitted waves within the valley can be written respectively as

$$w^{(\mathrm{S})}(r,\theta) = \sum_{n=0}^{\infty} A_n \mathrm{H}_n^{(1)}\left(kr\right)\cos n\theta \tag{11.48}$$

$$w^{(\mathrm{T})}(r,\theta) = \sum_{n=0}^{\infty} B_n \mathrm{J}_n\left(k_1 r\right)\cos n\theta \tag{11.49}$$

After applying the following Graf's formula

$$C_n\left(k\underline{r}\right)\mathrm{e}^{\mathrm{i}n\underline{\phi}} = \sum_{m=-\infty}^{\infty} \mathrm{J}_{n+m}\left(kd\right) C_m\left(k\overline{r}\right)\mathrm{e}^{\mathrm{i}m\overline{\phi}} \text{ , for } \overline{r} > d \tag{11.50}$$

where $C_n(\cdot)$ denotes $\mathrm{J}_n(\cdot)$ or $\mathrm{H}_n^{(1)}(\cdot)$. Equations (11.48) and (11.49) can be rewritten to

$$w^{(\mathrm{S})}(\overline{r},\overline{\phi}) = \sum_{m=-\infty}^{\infty} \overline{A}_m \mathrm{H}_m^{(1)}\left(k\overline{r}\right)\mathrm{e}^{\mathrm{i}m\overline{\phi}} \tag{11.51}$$

$$w^{(\mathrm{T})}(\overline{r},\overline{\phi}) = \sum_{m=-\infty}^{\infty} \overline{B}_m \mathrm{J}_m\left(k_1\overline{r}\right)\mathrm{e}^{\mathrm{i}m\overline{\phi}} \tag{11.52}$$

in which,

$$\overline{A}_m = \sum_{n=0}^{\infty} \frac{A_n}{2}(-\mathrm{i})^n\left[\mathrm{J}_{m+n}(kd) + \mathrm{J}_{m-n}(kd)\right] \tag{11.53}$$

$$\overline{B}_m = \sum_{n=0}^{\infty} \frac{B_n}{2}(-\mathrm{i})^n\left[\mathrm{J}_{m+n}(kd) + \mathrm{J}_{m-n}(kd)\right] \tag{11.54}$$

The boundary conditions could be categorized into the following two cases,

1) When $R > R^*$, the point source locates outside of the valley,

$$\begin{cases} w^{(\mathrm{ff})}\left(\bar{r},\bar{\phi}\right)+w^{(\mathrm{S})}\left(\bar{r},\bar{\phi}\right)=w^{(\mathrm{T})}\left(\bar{r},\bar{\phi}\right) \\ \mu\dfrac{\partial}{\partial\bar{r}}\left(w^{(\mathrm{ff})}\left(\bar{r},\bar{\phi}\right)+w^{(\mathrm{S})}\left(\bar{r},\bar{\phi}\right)\right)=\mu_1\dfrac{\partial}{\partial\bar{r}}w^{(\mathrm{T})}\left(\bar{r},\bar{\phi}\right) \end{cases}, \quad \text{for } \bar{r}=a \text{ and } \phi\in[0,2\pi]$$

Substitution of aforementioned wave functions leads to

$$\begin{cases} \bar{a}_m^{(\mathrm{f})}\mathrm{J}_m\left(ka\right)+\bar{A}_m\mathrm{H}_m^{(1)}\left(ka\right)=\bar{B}_m\mathrm{J}_m\left(k_1a\right) \\ \mu k\left[\bar{a}_m^{(\mathrm{f})}\mathrm{J}'_m\left(ka\right)+\bar{A}_m\mathrm{H}_m^{(1)\prime}\left(ka\right)\right]=\mu_1k_1\bar{B}_m\mathrm{J}'_m\left(k_1a\right) \end{cases}$$

After solving this binary linear system of equations, the two sets of unknowns are

$$\begin{Bmatrix}\bar{A}_m\\ \bar{B}_m\end{Bmatrix}=\begin{Bmatrix} \dfrac{\dfrac{\mu_1k_1}{\mu k}\mathrm{J}'_m\left(k_1a\right)\mathrm{J}_m\left(ka\right)-\mathrm{J}_m\left(k_1a\right)\mathrm{J}'_m\left(ka\right)}{\mathrm{H}_m^{(1)\prime}\left(ka\right)\mathrm{J}_m\left(k_1a\right)-\dfrac{\mu_1k_1}{\mu k}\mathrm{H}_m^{(1)}\left(ka\right)\mathrm{J}'_m\left(k_1a\right)}\bar{a}_m^{(\mathrm{f})} \\ \dfrac{\mathrm{H}_m^{(1)\prime}\left(ka\right)\mathrm{J}_m\left(ka\right)-\mathrm{H}_m^{(1)}\left(ka\right)\mathrm{J}'_m\left(ka\right)}{\mathrm{H}_m^{(1)\prime}\left(ka\right)\mathrm{J}_m\left(k_1a\right)-\dfrac{\mu_1k_1}{\mu k}\mathrm{H}_m^{(1)}\left(ka\right)\mathrm{J}'_m\left(k_1a\right)}\bar{a}_m^{(\mathrm{f})} \end{Bmatrix} \tag{11.55}$$

(m = 0, ±1, ±2, ···)

2) When $R < R^*$, the point source locates inside the valley,

$$\begin{cases} w^{(\mathrm{S})}\left(\bar{r},\bar{\phi}\right)=w^{(\mathrm{ff})}\left(\bar{r},\bar{\phi}\right)+w^{(\mathrm{T})}\left(\bar{r},\bar{\phi}\right) \\ \mu\dfrac{\partial}{\partial\bar{r}}w^{(\mathrm{S})}\left(\bar{r},\bar{\phi}\right)=\mu_1\dfrac{\partial}{\partial\bar{r}}\left(w^{(\mathrm{ff})}\left(\bar{r},\bar{\phi}\right)+w^{(\mathrm{T})}\left(\bar{r},\bar{\phi}\right)\right) \end{cases}, \quad \text{for } \bar{r}=a \text{ and } \phi\in[0,2\pi]$$

Similarly insert those wave functions into it. Note that different free-field motion expression is used here.

$$\begin{cases} \bar{A}_m\mathrm{H}_m^{(1)}\left(ka\right)=\bar{a}_m^{(\mathrm{f})}\mathrm{H}_m^{(1)}\left(k_1a\right)+\bar{B}_m\mathrm{J}_m\left(k_1a\right) \\ \mu k\bar{A}_m\mathrm{H}_m^{(1)\prime}\left(ka\right)=\mu_1k_1\left[\bar{a}_m^{(\mathrm{f})}\mathrm{H}_m^{(1)\prime}\left(k_1a\right)+\bar{B}_m\mathrm{J}'_m\left(k_1a\right)\right] \end{cases}$$

Thus we have the following coefficients for the inside cases.

$$
\begin{Bmatrix} \overline{A}_m \\ \overline{B}_m \end{Bmatrix} = \left\{ \begin{array}{c} \dfrac{\mathrm{J}_m(k_1a)\mathrm{H}_m^{(1)\prime}(k_1a) - \mathrm{J}'_m(k_1a)\mathrm{H}_m^{(1)}(k_1a)}{\dfrac{\mu k}{\mu_1 k_1}\mathrm{H}_m^{(1)\prime}(ka)\mathrm{J}_m(k_1a) - \mathrm{H}_m^{(1)}(ka)\mathrm{J}'_m(k_1a)} \overline{a}_m^{(\mathrm{f})} \\ \dfrac{\mathrm{H}_m^{(1)}(ka)\mathrm{H}_m^{(1)\prime}(k_1a) - \dfrac{\mu k}{\mu_1 k_1}\mathrm{H}_m^{(1)\prime}(ka)\mathrm{H}_m^{(1)}(k_1a)}{\dfrac{\mu k}{\mu_1 k_1}\mathrm{H}_m^{(1)\prime}(ka)\mathrm{J}_m(k_1a) - \mathrm{H}_m^{(1)}(ka)\mathrm{J}'_m(k_1a)} \overline{a}_m^{(\mathrm{f})} \end{array} \right\} \tag{11.56}
$$

$(m = 0, \pm 1, \pm 2, \cdots)$

For the semi-cylindrical valley, just simply replace the free-field coefficient $\overline{a}_m^{(\mathrm{f})}$ in equations (11.55) and (11.56) by $a_m^{(\mathrm{f})}$.

The model illustrated in Fig. 5-19 below represents an antiplane point source locating exactly at the center of a semi-cylindrical valley. As of this extremely simplified case, the solution is reduced to a set of straightforward algebraic expressions.

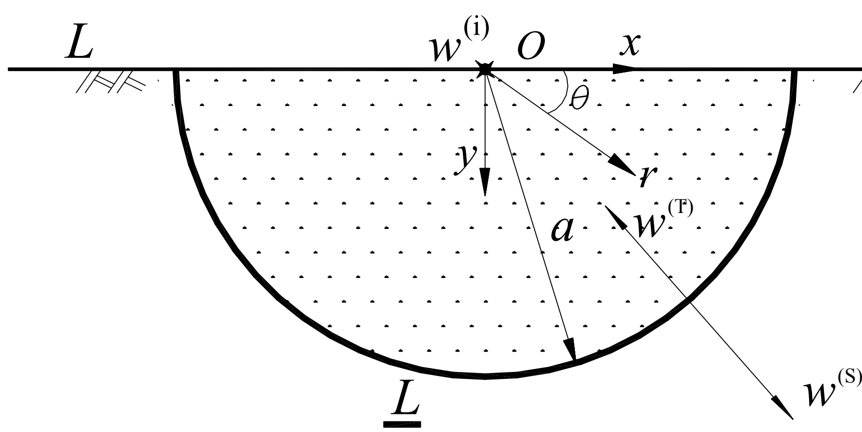

Fig. 5-19 A SPECIAL CASE OF SEMI-CYLINDRICAL VALLEY: WAVE SOURCE LOCATES AT VALLEY CENTER

The wave functions of incident, scattered and transmitted waves could be written as,

$$
w^{(\mathrm{i})}(r) = \frac{2\mathrm{H}_0^{(1)}(k_1 r)}{\left|\mathrm{H}_0^{(1)}(k_1 a)\right|} \tag{11.57}
$$

$$w^{(\mathrm{S})}(r) = A_0 \mathrm{H}_0^{(1)}(kr) \tag{11.58}$$

$$w^{(\mathrm{T})}(r) = B_0 \mathrm{H}_0^{(2)}(k_1 r) \tag{11.59}$$

Note that here equation (11.57) has amplitude of 2 to represent the combination motion induced by incident and its image point source, hence get compatible with the general solution presented earlier. Then the displacement and stress continuity boundary conditions on interface $\underline{L}$ can be written as

$$\begin{cases} \dfrac{2\mathrm{H}_0^{(1)}(k_1 a)}{\left|\mathrm{H}_0^{(1)}(k_1 a)\right|} + B_0 \mathrm{H}_0^{(2)}(k_1 a) = A_0 \mathrm{H}_0^{(1)}(ka) \\ \mu_1 k_1 \left[\dfrac{2\mathrm{H}_0^{(1)\prime}(k_1 a)}{\left|\mathrm{H}_0^{(1)}(k_1 a)\right|} + B_0 \mathrm{H}_0^{(2)\prime}(k_1 a) \right] = \mu k A_0 \mathrm{H}_0^{(1)\prime}(ka) \end{cases} \tag{11.60}$$

By this equation the two coefficients could be solved

$$\begin{Bmatrix} A_0 \\ B_0 \end{Bmatrix} = \begin{Bmatrix} \dfrac{\mathrm{H}_0^{(1)\prime}(k_1 a)\mathrm{H}_0^{(2)}(k_1 a) - \mathrm{H}_0^{(2)\prime}(k_1 a)\mathrm{H}_0^{(1)}(k_1 a)}{\dfrac{\mu k}{\mu_1 k_1}\mathrm{H}_0^{(1)\prime}(ka)\mathrm{H}_0^{(2)}(k_1 a) - \mathrm{H}_0^{(1)}(ka)\mathrm{H}_0^{(2)\prime}(k_1 a)} \dfrac{2}{\left|\mathrm{H}_0^{(1)}(k_1 a)\right|} \\ \dfrac{\mathrm{H}_0^{(1)\prime}(ka)\mathrm{H}_0^{(1)}(k_1 a) - \dfrac{\mu k}{\mu_1 k_1}\mathrm{H}_0^{(1)\prime}(ka)\mathrm{H}_0^{(1)}(k_1 a)}{\dfrac{\mu k}{\mu_1 k_1}\mathrm{H}_0^{(1)\prime}(ka)\mathrm{H}_0^{(2)}(k_1 a) - \mathrm{H}_0^{(1)}(ka)\mathrm{H}_0^{(2)\prime}(k_1 a)} \dfrac{2}{\left|\mathrm{H}_0^{(1)}(k_1 a)\right|} \end{Bmatrix} \tag{11.61}$$

5.2.1 Numerical Results of Shallow Cylindrical Valley Subjected to Cylindrical SH-Waves

Fig. 5-20 is the sole figure in this section that incorporates displacement amplitudes for four incident angles. Its patterns are very similar to the canyon model. The screening effect also exists for valleys.

Fig. 5-21 through Fig. 5-26 are plotted in order to exhibit the influence of depth-width ratio (h/b) of the valley configurations. Roughly speaking, h/b does not have considerable effects on the amplitude of ground motion. For low frequency cases of incident waves, low h/b cases might have larger ground displacement response, as shown in Fig. 5-21.

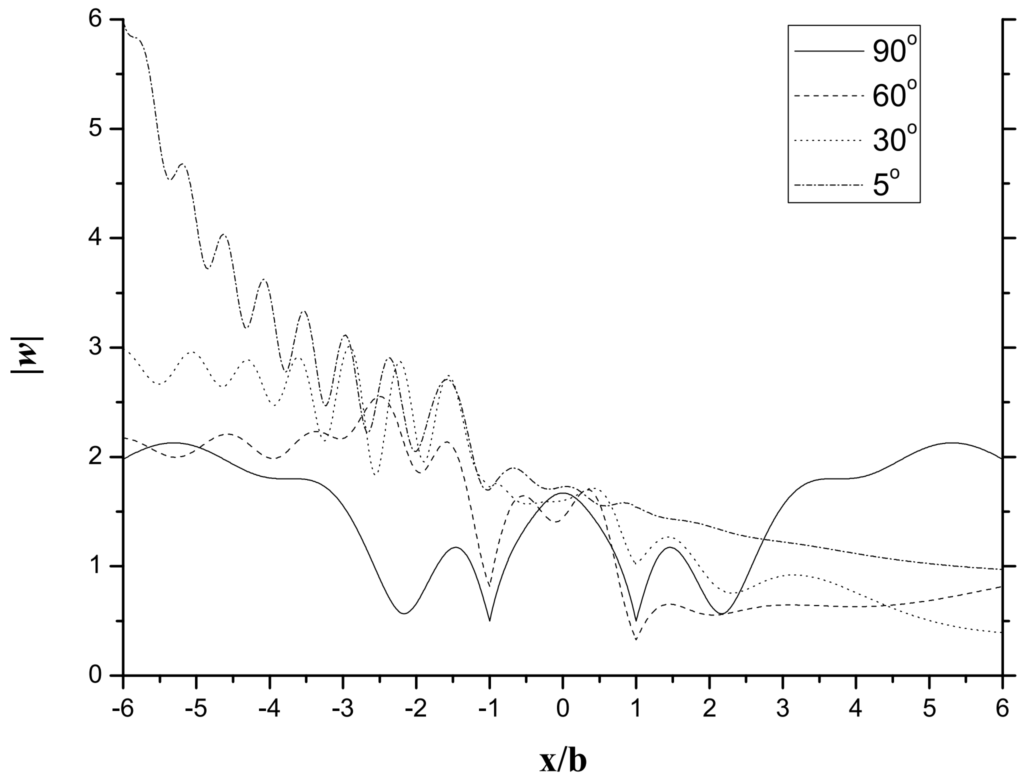

Fig. 5-20 SURFACE DISPLACEMENT AMPLITUDE OF SHALLOW CYLINDRICAL VALLEY SUBJECTED TO INCIDENT CYLINDRICAL SH-WAVES FOR $\eta = 2$, $h/b = 0.25$, $R/a = 3$, $\mu_1/\mu = 2$, $k_1/k = 0.9$, $\gamma = 90^{\circ}, 60^{\circ}, 30^{\circ}$, **AND** 5°

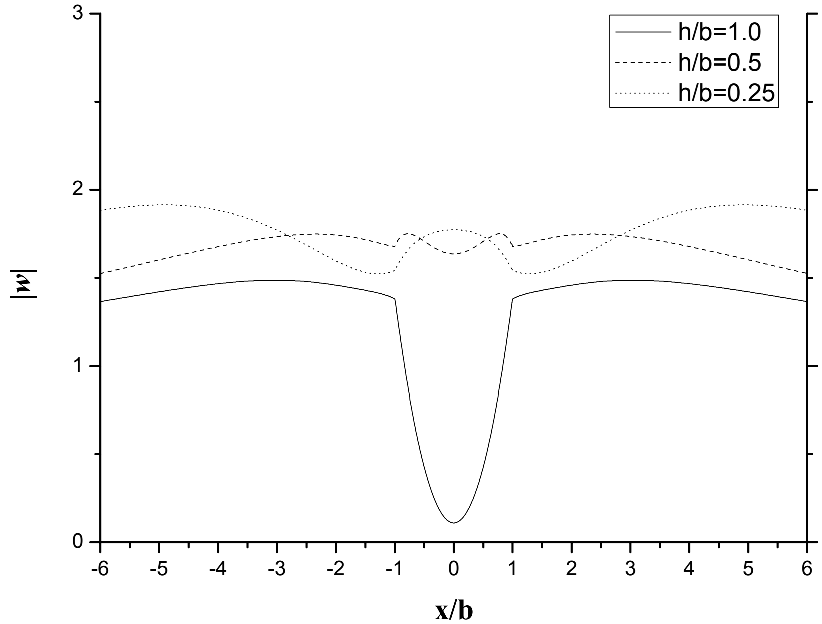

Fig. 5-21 SURFACE DISPLACEMENT AMPLITUDE OF SHALLOW CYLINDRICAL VALLEY SUBJECTED TO INCIDENT CYLINDRICAL SH-WAVES FOR $\eta = 0.5$， $\gamma = 90^{\circ}$， $R/a = 3$， $\mu_1/\mu = 2$， $k_1/k = 0.9$， $h/b = 1.0, 0.5$ **AND** 0.25

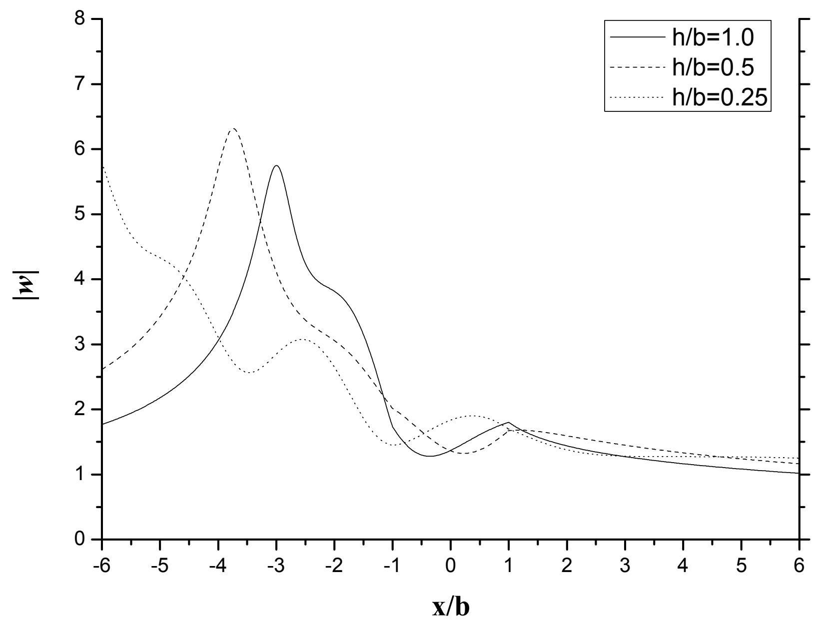

Fig. 5-22 SURFACE DISPLACEMENT AMPLITUDE OF SHALLOW CYLINDRICAL VALLEY SUBJECTED TO INCIDENT CYLINDRICAL SH-WAVES FOR $\eta = 0.5$， $\gamma = 5^{\circ}$， $R/a = 3$， $\mu_1/\mu = 2$， $k_1/k = 0.9$， $h/b = 1.0, 0.5$ **AND** 0.25

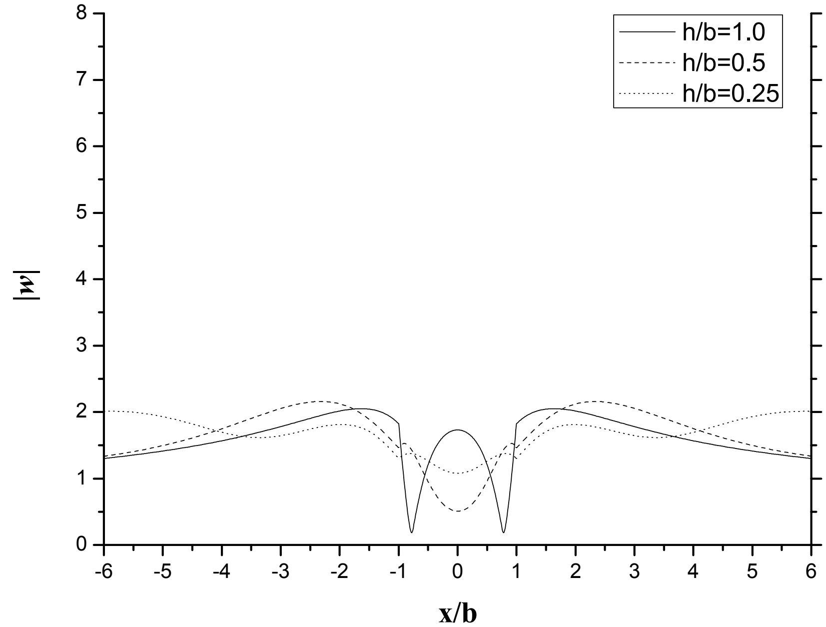

Fig. 5-23 SURFACE DISPLACEMENT AMPLITUDE OF SHALLOW CYLINDRICAL VALLEY SUBJECTED TO INCIDENT CYLINDRICAL SH-WAVES FOR $\eta = 1$, $\gamma = 90^{\circ}$, $R/a = 3$, $\mu_1/\mu = 2$, $k_1/k = 0.9$, $h/b = 1.0, 0.5$ **AND** 0.25

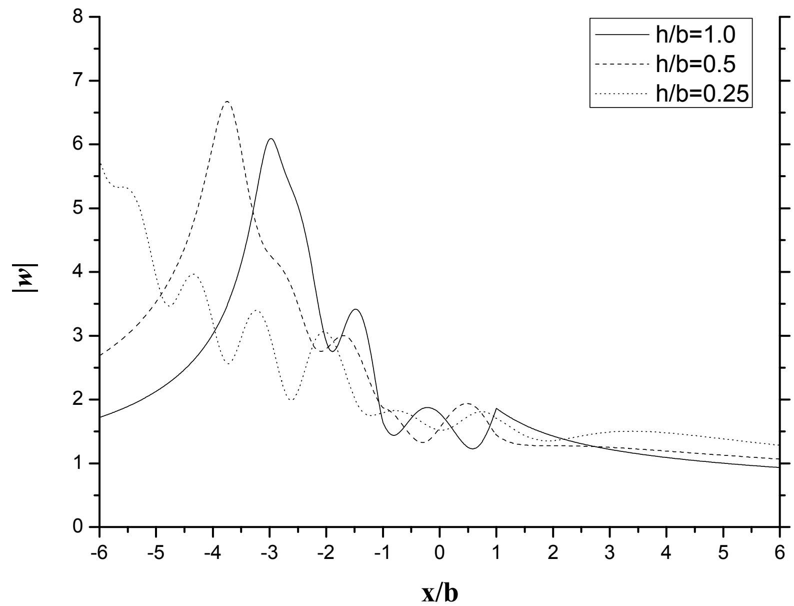

Fig. 5-24 SURFACE DISPLACEMENT AMPLITUDE OF SHALLOW CYLINDRICAL VALLEY SUBJECTED TO INCIDENT CYLINDRICAL SH-WAVES FOR $\eta = 1$, $\gamma = 5^{\circ}$, $R/a = 3$, $\mu_1/\mu = 2$, $k_1/k = 0.9$, $h/b = 1.0, 0.5$ **AND** 0.25

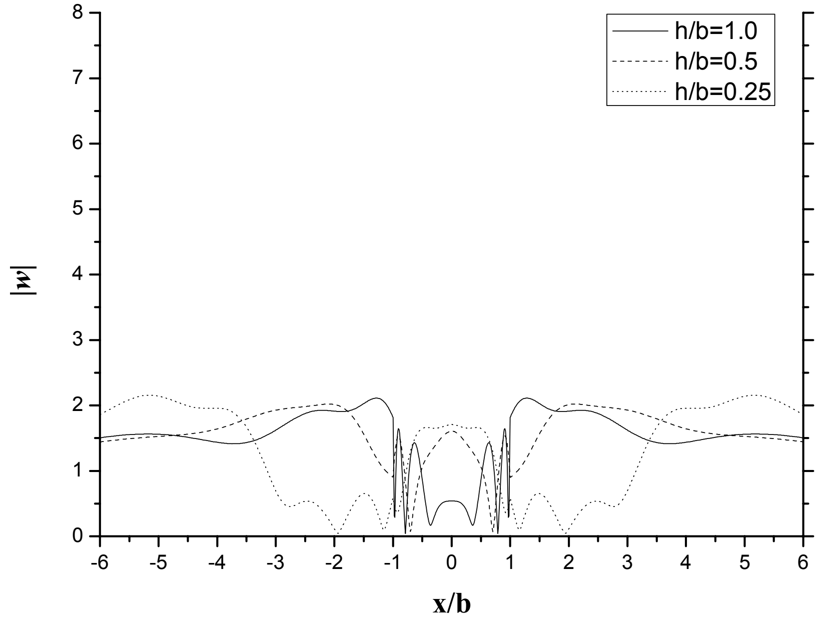

Fig. 5-25 SURFACE DISPLACEMENT AMPLITUDE OF SHALLOW CYLINDRICAL VALLEY SUBJECTED TO INCIDENT CYLINDRICAL SH-WAVES FOR $\eta = 3$, $\gamma = 90^{\mathrm{o}}$, $R/a = 3$, $\mu_1/\mu = 2$, $k_1/k = 0.9$, $h/b = 1.0, 0.5$ **AND** 0.25

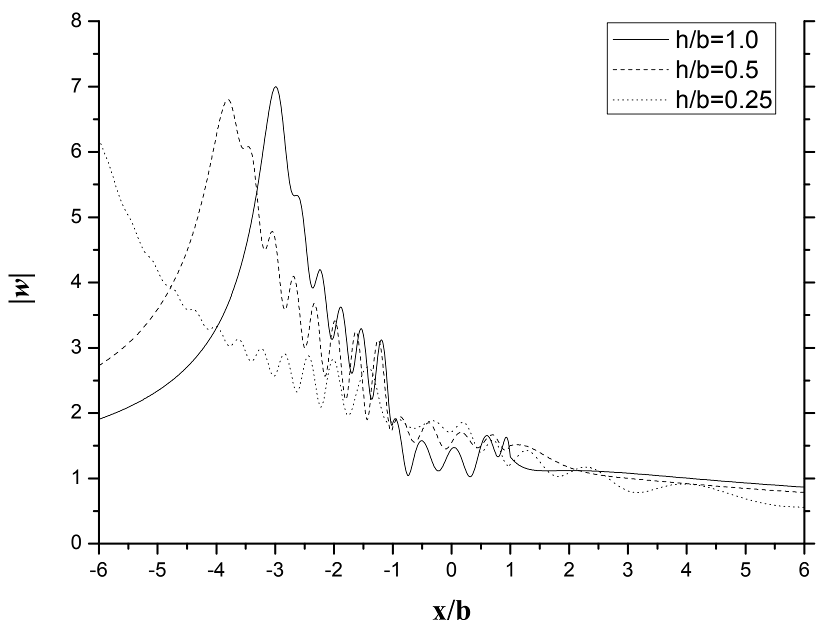

Fig. 5-26 SURFACE DISPLACEMENT AMPLITUDE OF SHALLOW CYLINDRICAL VALLEY SUBJECTED TO INCIDENT CYLINDRICAL SH-WAVES FOR $\eta = 3$, $\gamma = 5^{\mathrm{o}}$, $R/a = 3$, $\mu_1/\mu = 2$, $k_1/k = 0.9$, $h/b = 1.0, 0.5$ **AND** 0.25

Chapter 6

SEMI-CYLINDRICAL CAVITY FOR PLANE SH-WAVES IN A HALF-SPACE

Within the available analytic solutions, circular cavity models are of the simplest and most fundamental ones. Most of early solutions are concerning full circle models, such as a full-circular (or 3-D cylindrical) cavity (Lee, 1977), tunnel with one layer of lining (Lee and Trifunac, 1979), or elastic inclusion (Yuan, 1996) embedded underground in a half-space, all solved by use of the image method. For those full-circular models, boundary conditions are convenient to be applied in that radial and angular components of wave functions are completely decoupled. Those models are often used to analyze underground tunnels. In reality, the shapes of tunnel cross section (or called profile) are most likely circular or mouth profiles (Kolymbas 2005). Other conceivable profiles even include rectangular ones but fairly rare. The geometrical shape of mouth profile is composed of circular sections but is very similar to a semi-circle except that the former's invert is curved. Yuan and Men (1992) presented a closed-form analytical solution to a semi-circular hill sitting on a half-space and this solution was extended to arbitrary shallow hill by Yuan and Liao (1996). These are the first two closed-form analytical solutions on Mixed-Boundary Problems. Mixed boundary condition indicates that for different parts of the boundary, various boundary condition equations are applied. In other words, radial and angular components are coupled together. Shown in Fig. 3-1, the upper portion of hill circle corresponds to traction-free boundary condition; the lower portion corresponds to displacement and stress continuity boundary conditions.

In the first section of this chapter, auxiliary function method, which was first introduced by Yuan and Mean (1992), is briefly represented to solve the scattering and diffraction of plane SH-waves by a semi-cylindrical cavity in a half-space. In the other section the Cosine Half-Range Expansion method is generalized to a lemma specifically applicable to the same model. With this lemma, the governing equations are established on the basis of residues of various boundary conditions. The concept of this model becomes much more legible and straightforward in comparison to the auxiliary function method. The objective of this chapter aims at making some comparison between these two methods (and even more methods in the future) applied in the same simple model, taking it as a benchmark example, and hopefully providing some instructions to future research on some more complicated mixed-boundary models.

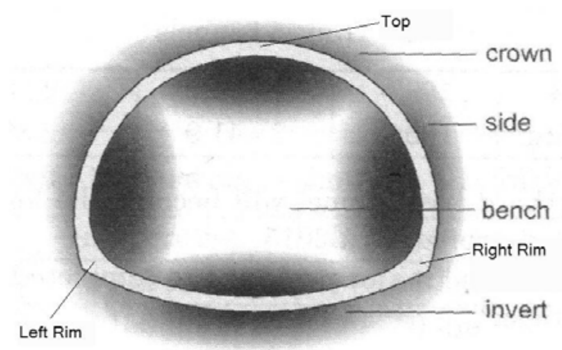

Fig. 6-1 PARTS OF MOUTH PROFILE OF A TUNNEL (ADAPTED FROM KOLYMBAS 2005)

6.1 Solution by Auxiliary Function Method

The model studied all through this chapter is an underground semi-circular cavity or cavern, or thought of as an unlined tunnel, in a homogeneous, perfectly elastic, and isotropic half-space, as illustrated in Fig. 6-2. A bound of parallel harmonic incident SH-waves hit the models from the deep earth by angel γ with respect to the horizontal. The radius and depth of the center of cavity to the ground surface are denoted by a and d, respectively.

In order to apply the boundary conditions effectively, the model is divided into two regions as shown in Fig. 6-3, D and Λ. Λ denotes the semi-circular region surrounded by boundaries L and $\underline{L}$, and D is the rest of the model, the same as the full-circular cavity model solved much earlier (Lee, 1977).

The traction-free boundary conditions are summarized below

$$\tau_{\phi_0 z}\,|_{\phi_0=\pm\pi/2}=0 \qquad (r_0,\phi_0)\in \Gamma \tag{12.1}$$

$$\tau_{\theta z}\,|_{\theta=0,\pi}=0 \qquad (r,\theta)\in L \tag{12.2}$$

$$\tau_{rz}\,|_{r=a}=0 \qquad (r,\theta)\in \overline{L} \tag{12.3}$$

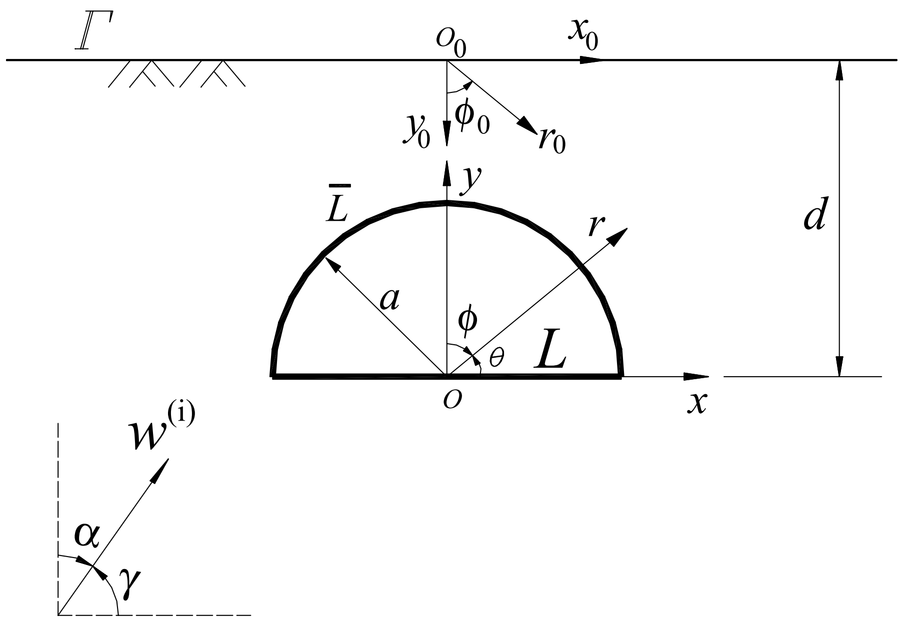

Fig. 6-2 SEMI-CYLINDRICAL CAVITY IN A HALF-SPACE

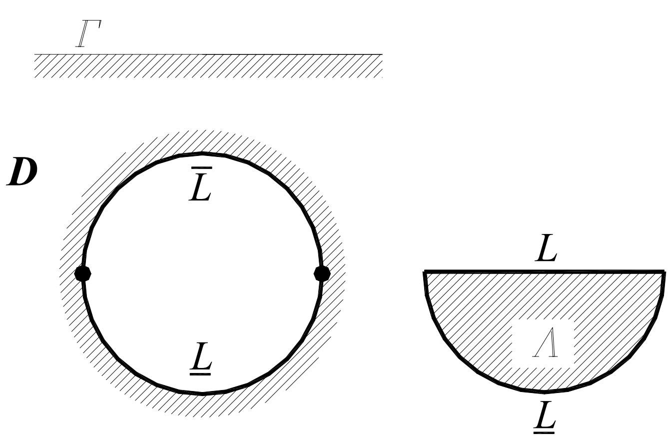

Fig. 6-3 REGION SPLITTING OF SEMI-CYLINDIRCAL CAVITY

The free-field waves are defined in terms of the (r,ϕ) polar coordinate system

$$w^{(\mathrm{ff})}\left(r,\phi\right)=w^{(\mathrm{i})}+w^{(\mathrm{r})}=\sum_{n=0}^{\infty}\mathrm{J}_n\left(kr\right)\left(a_{0,n}\cos n\phi+b_{0,n}\sin n\phi\right) \tag{12.4}$$

in which,

$$\begin{cases} a_{0,n}=\begin{cases}-2\varepsilon_n\mathrm{i}^{n+1}\sin\left(n\pi/2\right)\sin n\alpha\sin\left(kd\sin\alpha\right) & \text{, when } n \text{ odd}\\ 2\varepsilon_n\mathrm{i}^{n}\cos\left(n\pi/2\right)\cos n\alpha\cos\left(kd\sin\alpha\right) & \text{, when } n \text{ even}\end{cases}\\ b_{0,n}=\begin{cases}2\varepsilon_n\mathrm{i}^{n}\sin\left(n\pi/2\right)\cos n\alpha\cos\left(kd\sin\alpha\right) & \text{, when } n \text{ odd}\\ 2\varepsilon_n\mathrm{i}^{n+1}\cos\left(n\pi/2\right)\sin n\alpha\sin\left(kd\sin\alpha\right) & \text{, when } n \text{ even}\end{cases}\end{cases} \tag{12.5}$$

and the scattered waves were assumed as

$$w^{(\mathrm{S})}(r,\phi)=\sum_{n=0}^{\infty}\mathrm{H}_n^{(1)}\left(kr\right)\left(A_n\cos n\phi+B_n\sin n\phi\right) \tag{12.6}$$

The transmitted wave in the lower semi-cylindrical region Λ beneath the cavity is assumed as follows (Yuan and Liao, 1996)

$$w^{(\mathrm{T})}(r,\phi)=\sum_{n=0}^{\infty}\mathrm{J}_n(kr)\left(C_n\delta_n^{(1)}\cos n\phi+D_n\delta_n^{(2)}\sin n\phi\right) \tag{12.7}$$

in which C_n and D_n are complex unknowns to be determined. And,

$$\begin{cases}\delta_n^{(1)}=1+(-1)^n=\begin{cases}0 & \text{when } n \text{ odd}\\ 2 & \text{when } n \text{ even}\end{cases}\\ \delta_n^{(2)}=1-(-1)^n=\begin{cases}2 & \text{when } n \text{ odd}\\ 0 & \text{when } n \text{ even}\end{cases}\end{cases} \tag{12.8}$$

$$\tau_{\phi z}^{(\mathrm{T})}(r,\phi)=\frac{\mu}{r}\frac{\partial w^{(\mathrm{T})}}{\partial\phi}=-\frac{\mu}{r}\sum_{n=0}^{\infty}n\mathrm{J}_n\left(kr\right)\left(C_n\delta_n^{(1)}\sin n\phi-D_n\delta_n^{(2)}\cos n\phi\right) \tag{12.9}$$

With these two factor functions (12.8), the traction-free boundary condition (12.9) on the flat boundary L ($\phi=\pm\pi/2$) is satisfied automatically. But they also make the odd and even terms of C_n and D_n

meaningless, which results in the governing equations (12.18) and (12.23) over-determined and have to be solved by Least-Square Method.

The remaining boundary conditions are represented by the following stress and displacement auxiliary functions

$$\Phi(\phi)=\begin{cases}\tau_{rz}^{(\mathrm{ff})}(a,\phi)+\tau_{rz}^{(\mathrm{S})}(a,\phi)+\tau_{1rz}^{(\mathrm{S})}(a,\phi)\ , & -\dfrac{\pi}{2}+2k\pi\le\phi\le\dfrac{\pi}{2}+2k\pi\\ \tau_{rz}^{(\mathrm{ff})}(a,\phi)+\tau_{rz}^{(\mathrm{S})}(a,\phi)+\tau_{1rz}^{(\mathrm{S})}(a,\phi)-\tau_{rz}^{(\mathrm{t})}(a,\phi)\ , & \text{otherwise}\end{cases}\tag{12.10}$$

$$\Psi(\phi)=\begin{cases}0 & ,\ -\dfrac{\pi}{2}+2k\pi\le\phi\le\dfrac{\pi}{2}+2k\pi\\ w^{(\mathrm{ff})}(a,\phi)+w^{(\mathrm{S})}(a,\phi)+w_1^{(\mathrm{S})}(a,\phi)-w^{(\mathrm{t})}(a,\phi)\ , & \text{otherwise}\end{cases}\tag{12.11}$$

$$\left(k=0,\pm1,\pm2,\pm3,\cdots\right)$$

Thus, for $-\pi\le\phi\le\pi$, equations $\Phi(\phi)=0$ and $\Psi(\phi)=0$ are equivalent to the zero-stress associated with stress continuity conditions along the whole circular boundary $\overline{L}+\underline{L}$, and the displacement continuity condition at the lower semi-circular boundary $\underline{L}$, respectively. Therefore, by making Fourier expansion on those two auxiliary functions and set all coefficients equal to zero, all three boundary condition equations (12.1) through (12.3) could be satisfied. By that we obtained the following four sets of infinite linear equations in terms of four sets of unknowns A_n, C_n and B_n, D_n.

$$\mathrm{J}_l'(ka)a_{0,l}+\mathrm{H}_l^{(1)\prime}(ka)A_l+\mathrm{J}_l'(ka)A_l^*=\sum_{n=0}^{\infty}\mathrm{J}_l'(ka)\delta_n^{(1)}\lambda_{ln}C_n\tag{12.12}$$

$$\sum_{n=0}^{\infty}\left[\mathrm{J}_n(ka)a_{0,n}+\mathrm{H}_n^{(1)}(ka)A_n+\mathrm{J}_n(ka)A_n^*\right]\lambda_{\mathrm{ln}}=\sum_{n=0}^{\infty}\mathrm{J}_n(ka)\delta_n^{(1)}\lambda_{ln}C_n\tag{12.13}$$

$$\mathrm{J}_l'(ka)b_{0,l}+\mathrm{H}_l^{(1)\prime}(ka)\cdot B_l+\mathrm{J}_l'(ka)B_l^*=\sum_{n=0}^{\infty}\mathrm{J}_n'(ka)\delta_n^{(2)}\mu_{ln}D_n\tag{12.14}$$

$$\sum_{n=0}^{\infty}\left[\mathrm{J}_n(ka)b_{0,n}+\mathrm{H}_n^{(1)}(ka)B_n+\mathrm{J}_n(ka)B_n^*\right]\mu_{ln}=\sum_{n=0}^{\infty}\mathrm{J}_n(ka)\delta_n^{(2)}\mu_{ln}D_n\tag{12.15}$$

where, $l = 0,1,2,3,\ldots$, and

$$\lambda_{ln} = \begin{cases} 1/2 & \text{, when } n = l \\ -\dfrac{\varepsilon_l}{2\pi}\dfrac{\sin(\frac{n+l}{2}\pi)}{n+l} - \dfrac{\varepsilon_l}{2\pi}\dfrac{\sin(\frac{n-l}{2}\pi)}{n-l} & \text{, when } n \neq l \end{cases} \tag{12.16}$$

$$\mu_{ln} = \begin{cases} 0 & , n = l = 0 \\ \dfrac{1}{\pi}\dfrac{\sin(\frac{n+l}{2}\pi)}{n+l} - \dfrac{1}{\pi}\dfrac{\sin(\frac{n-l}{2}\pi)}{n-l}, & n \neq l \\ \dfrac{1}{2} & , n = l \neq 0 \end{cases} \tag{12.17}$$

After elimnation, A_n and C_n need to be solved simultaneously; so does B_n and D_n. Each one of those two sets of equations is an over-determined equation due to those functions $\delta_n^{(1)}$ and $\delta_n^{(2)}$ as mentioned earlier.

$$\begin{cases} \sum_{n=0}^{\infty} RTA_{ln} A_n + \sum_{n=0}^{\infty} RC_{ln} C_n = \mathrm{J}_l'(ka) A_{0,l} \\ \sum_{n=0}^{\infty} JHA_{ln} A_n + \sum_{n=0}^{\infty} JC_{ln} C_n = \sum_{n=0}^{\infty} \mathrm{J}_n(ka) \lambda_{ln} A_{0,n} \end{cases} \quad (l=0,1,2,\ldots) \tag{12.18}$$

where,

$$RC_{ln} = \mathrm{J}_n(ka)\delta_n^{(1)}\lambda_{ln} \tag{12.19}$$

$$RTA_{ln} = -\delta_{ln}\mathrm{H}_l^{(1)\prime}(ka) - P_{ln}^{+}\mathrm{J}_l'(ka) \tag{12.20}$$

$$JC_{ln} = \mathrm{J}_n(ka)\delta_n^{(1)}\lambda_{ln} \tag{12.21}$$

$$JHA_{ln} = -\lambda_{ln}\mathrm{H}_n^{(1)}(ka) - \sum_{m=0}^{\infty} \mathrm{J}_m(ka) P_{mn}^{+} \lambda_{lm} \tag{12.22}$$

$$\begin{cases} \sum_{n=0}^{\infty} RTB_{ln} B_n + \sum_{n=0}^{\infty} RD_{ln} D_n = \mathrm{J}_l'(ka) B_{0,l} \\ \sum_{n=0}^{\infty} JHB_{ln} B_n + \sum_{n=0}^{\infty} JD_{ln} D_n = \sum_{n=0}^{\infty} \mathrm{J}_n(ka) \mu_{ln} B_{0,n} \end{cases} \quad (l\text{=}0,1,2,\ldots) \tag{12.23}$$

where,

$$RD_{ln} = \mathrm{J}_n(ka) \delta_n^{(2)} \mu_{ln} \tag{12.24}$$

$$RTB_{ln} = -\delta_{ln} \mathrm{H}_l^{(1)\prime}(ka) - P_{ln}^{-} \mathrm{J}_l(ka) \tag{12.25}$$

$$JD_{ln} = \mathrm{J}_n(ka) \delta_n^{(2)} \mu_{ln} \tag{12.26}$$

$$JHB_{ln} = -\mu_{ln} \mathrm{H}_n^{(1)}(ka) - \sum_{m=0}^{\infty} \mathrm{J}_m(ka) P_{mn}^{-} \mu_{lm} \tag{12.27}$$

After A_n, B_n, C_n, and D_n determined from equations (12.18) and (12.23), substitution of them into wave functions (12.6) and (12.7) leads to the solution of total wave field.

6.2 Solution by Improved Cosine Half-Range Expansion

6.2.1 Wave Functions

The equation of free-field waves is defined in the (r,θ) coordinate system other than (r,ϕ) in the preceding section shown in Fig. 6-2

$$w^{(\mathrm{ff})}(r,\theta) = \sum_{n=0}^{\infty} \mathrm{J}_n(kr)\left(a_{0,n} \cos n\theta + b_{0,n} \sin n\theta\right) \tag{12.28}$$

where for n =1,2,3…

$$\begin{cases} a_{0,n} = 2\varepsilon_n \mathrm{i}^n \cos n\gamma \cos\left(kd \sin\gamma\right) \\ b_{0,n} = -2\varepsilon_n \mathrm{i}^{n+1} \sin n\gamma \sin\left(kd \sin\gamma\right) \end{cases} \tag{12.29}$$

Substituting Eqn. (12.28) into (8.4), we obtain

$$\tau_{rz}^{(\mathrm{ff})}(r,\theta) = \mu k \sum_{n=0}^{\infty} \mathrm{J}_n'(kr)\left(a_{0,n} \cos n\theta + b_{0,n} \sin n\theta\right) \tag{12.30}$$

The total transmitted field within the semi-circular region Λ could be represented as a set of convergent standing waves only with cosine terms in (r,θ)

$$w^{(\mathrm{T})}(r,\theta)=\sum_{n=0}^{\infty}\mathrm{J}_n\left(kr\right)C_n\cos n\theta \tag{12.31}$$

where C_n are a set of complex unknowns to be determined by boundary conditions. Substituting (12.31) into (8.3)

$$\tau_{\theta z}^{(\mathrm{T})}(r,\theta)=\frac{\mu}{r}\frac{\partial w^{(\mathrm{T})}(r,\theta)}{\partial\theta}=-\frac{\mu}{r}\sum_{n=0}^{\infty}n\mathrm{J}_n(kr)C_n\sin n\theta \tag{12.32}$$

Since $\theta=0,\pi$ on the flat boundary L, traction-free boundary condition Eqn.(12.2) is satisfied automatically.

Substituting Eqn. (12.31) to (8.4), we obtain

$$\tau_{rz}^{(\mathrm{T})}(r,\theta)=\mu\frac{\partial w^{(\mathrm{T})}(r,\theta)}{\partial r}=\mu k\sum_{n=0}^{\infty}\mathrm{J}_n'(kr)C_n\cos n\theta \tag{12.33}$$

Applying the image method by assuming an imaginary full cylindrical cavity placed as its opposite mirror above the ground surface, an additional set of outgoing waves was scattered from the center O_1 shown in Fig. 6-4. Thus the traction-free boundary condition for the scattered waves are satisfied automatically, and the scattering displacement field is composed of $w^{(\mathrm{S})}$ and $w_1^{(\mathrm{S})}$ whose expressions in their respective polar coordinates could be written as

$$w^{(\mathrm{S})}(r,\phi)=\sum_{n=0}^{\infty}\mathrm{H}_n^{(1)}\left(kr\right)\left(A_n\cos n\phi+B_n\sin n\phi\right) \tag{12.34}$$

$$w_1^{(\mathrm{S})}(r_1,\phi_1)=\sum_{m=0}^{\infty}\mathrm{H}_m^{(1)}\left(kr_1\right)\left(A_m\cos m\phi_1+B_m\sin m\phi_1\right) \tag{12.35}$$

where A_m and B_m are complex constants to be determined. Substituting Eqn.(12.34) to (8.4),

$$\tau_{rz}^{(S)}(r,\phi)=\mu k\sum_{n=0}^{\infty}\mathrm{H}_n^{(1)\prime}\left(kr\right)\left(A_n\cos n\phi+B_n\sin n\phi\right) \tag{12.36}$$

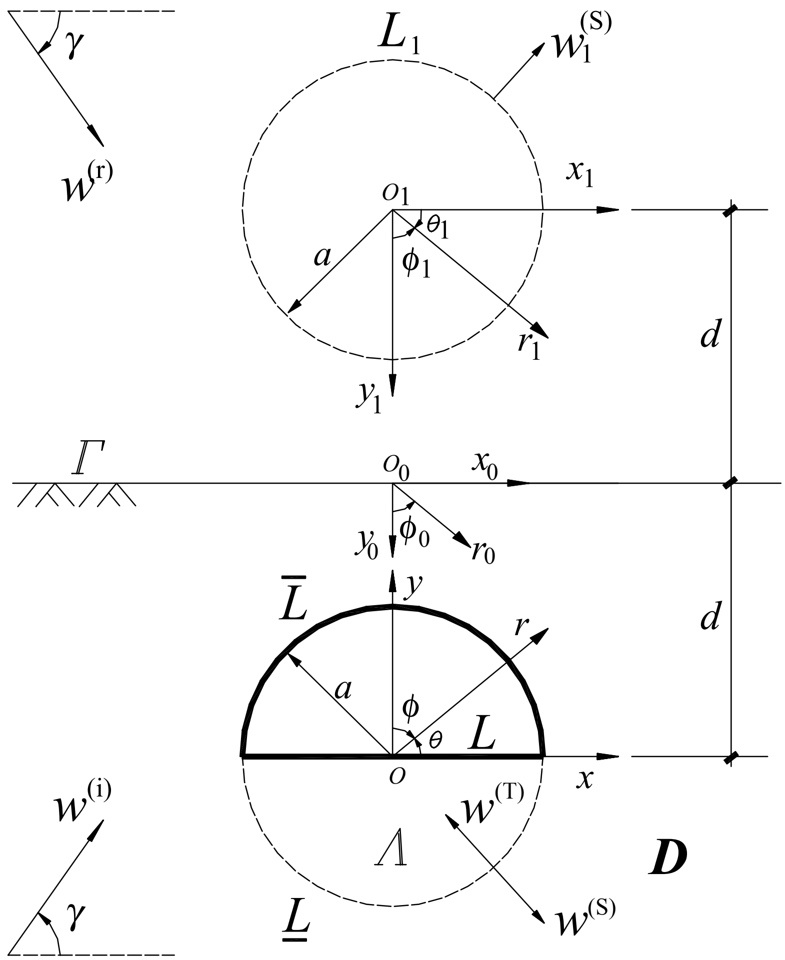

Fig. 6-4 WAVE FIELDS ANALYSIS BY IMAGE METHOD

For the purpose of transforming scattering field $w_1^{(s)}$ from coordinate (r_1,ϕ_1) to (r,ϕ), the following Graf's formula identical to equation (8.31) has been adopted

$$\mathrm{H}_m^{(1)}(kr_1)\begin{Bmatrix}\cos m\phi_1\\ \sin m\phi_1\end{Bmatrix}=\sum_{n=0}^{\infty}\mathrm{J}_n(kr)\frac{\varepsilon_n}{2}\begin{Bmatrix}\left[\mathrm{H}_{m+n}^{(1)}(2kd)+(-1)^n\mathrm{H}_{m-n}^{(1)}(2kd)\right]\cos n\phi\\ \left[\mathrm{H}_{m+n}^{(1)}(2kd)-(-1)^n\mathrm{H}_{m-n}^{(1)}(2kd)\right]\sin n\phi\end{Bmatrix} \tag{12.37}$$

Substituting Eqn(12.37) into (12.35), expression of $w_1^{(S)}$ in the polar coordinate (r,ϕ) could be got,

$$w_1^{(\mathrm{S})}(r,\phi)=\sum_{n=0}^{\infty}\mathrm{J}_n\left(kr\right)\left(A_n^*\cos n\phi+B_n^*\sin n\phi\right) \tag{12.38}$$

in which,

$$\begin{cases} A_n^* = \sum_{m=0}^{\infty} P_{nm}^{+} A_m \\ B_n^* = \sum_{m=1}^{\infty} P_{nm}^{-} B_m \end{cases} \tag{12.39}$$

with

$$P_{nm}^{\pm}=\frac{\varepsilon_n}{2}\left[\mathrm{H}_{m+n}^{(1)}(2kd)\pm(-1)^n\,\mathrm{H}_{m-n}^{(1)}(2kd)\right] \tag{12.40}$$

Substituting Eqn.(12.38) into (8.4), we obtain

$$\tau_{1rz}^{(\mathrm{S})}(r,\phi)=\mu k\sum_{n=0}^{\infty}\mathrm{J}_n'\left(kr\right)\left(A_n^*\cos n\phi+B_n^*\sin n\phi\right) \tag{12.41}$$

To apply boundary conditions in the same polar coordinate system (r,θ), equations (12.34) and (12.38) need to be transformed to (r,θ) by correlation $\theta=\pi/2-\phi$,

$$w^{(\mathrm{S})}(r,\theta)=\sum_{n=0}^{\infty}\mathrm{H}_n^{(1)}\left(kr\right)\left(E_n\cos n\theta+F_n\sin n\theta\right) \tag{12.42}$$

$$w_1^{(\mathrm{S})}(r,\theta)=\sum_{n=0}^{\infty}\mathrm{J}_n\left(kr\right)\left(E_n^*\cos n\theta+F_n^*\sin n\theta\right) \tag{12.43}$$

where

$$E_n=A_n\cos\left(n\pi/2\right)+B_n\sin\left(n\pi/2\right)=\begin{cases} \left(-1\right)^m A_{2m}=\hat{A}_{2m} & n=2m \\ \left(-1\right)^m B_{2m+1}=\hat{B}_{2m+1} & n=2m+1 \end{cases} \tag{12.44}$$

$$F_n=A_n\sin\left(n\pi/2\right)-B_n\cos\left(n\pi/2\right)=\begin{cases} -\left(-1\right)^m B_{2m}=\hat{B}_{2m} & n=2m \\ \left(-1\right)^m A_{2m+1}=\hat{A}_{2m+1} & n=2m+1 \end{cases} \tag{12.45}$$

$$E_n^* = A_n^* \cos(n\pi/2) + B_n^* \sin(n\pi/2) = \begin{cases} (-1)^m A_{2m}^* = \hat{A}_{2m}^* & n = 2m \\ (-1)^m B_{2m+1}^* = \hat{B}_{2m+1}^* & n = 2m+1 \end{cases} \tag{12.46}$$

$$F_n^* = A_n^* \sin(n\pi/2) - B_n^* \cos(n\pi/2) = \begin{cases} -(-1)^m B_{2m}^* = \hat{B}_{2m}^* & n = 2m \\ (-1)^m A_{2m+1}^* = \hat{A}_{2m+1}^* & n = 2m+1 \end{cases} \tag{12.47}$$

Or rather the new 'cap' variables could be summarized in another form as,

$$\hat{A}_n = \begin{cases} (-1)^{\frac{n}{2}} A_n & , n \text{ even} \\ (-1)^{\frac{n-1}{2}} A_n & , n \text{ odd} \end{cases}, \text{ and } \hat{A}_n^* = \begin{cases} (-1)^{\frac{n}{2}} A_n^* & , n \text{ even} \\ (-1)^{\frac{n-1}{2}} A_n^* & , n \text{ odd} \end{cases} \tag{12.48}$$

$$\hat{B}_n = \begin{cases} -(-1)^{\frac{n}{2}} B_n & , n \text{ even} \\ (-1)^{\frac{n-1}{2}} B_n & , n \text{ odd} \end{cases}, \text{ and } \hat{B}_n^* = \begin{cases} -(-1)^{\frac{n}{2}} B_n^* & , n \text{ even} \\ (-1)^{\frac{n-1}{2}} B_n^* & , n \text{ odd} \end{cases} \tag{12.49}$$

E_n and F_n could also be expressed by them directly,

$$E_n = \begin{cases} \hat{A}_n = (-1)^{\frac{n}{2}} A_n & n \text{ even} \\ \hat{B}_n = (-1)^{\frac{n-1}{2}} B_n & n \text{ odd} \end{cases}, \text{ and } F_n = \begin{cases} \hat{B}_n = -(-1)^{\frac{n}{2}} B_n & n \text{ even} \\ \hat{A}_n = (-1)^{\frac{n-1}{2}} A_n & n \text{ odd} \end{cases} \tag{12.50}$$

$$E_n^* = \begin{cases} \hat{A}_n^* = (-1)^{\frac{n}{2}} A_n^* & n \text{ even} \\ \hat{B}_n^* = (-1)^{\frac{n-1}{2}} B_n^* & n \text{ odd} \end{cases}, \text{ and } F_n^* = \begin{cases} \hat{B}_n^* = -(-1)^{\frac{n}{2}} B_n^* & n \text{ even} \\ \hat{A}_n^* = (-1)^{\frac{n-1}{2}} A_n^* & n \text{ odd} \end{cases} \tag{12.51}$$

Those equations listed here looks somewhat redundant, but would be convenient for further reference.

6.2.2 Boundary Conditions

6.2.2.1 The boundary condition equations

Aside from the automatically-satisfied traction-free boundary conditions (12.1) through (12.2), the rest of boundary conditions could be summarized as follows,

Displacement and stress continuity conditions on the lower semi-circular interface $\underline{L}$,

$$w^{(\mathrm{ff})}(a,\theta)+w^{(\mathrm{S})}(a,\theta)+w_1^{(\mathrm{S})}(a,\theta)=w^{(\mathrm{T})}(a,\theta) \qquad -\pi\le\theta\le 0 \tag{12.52}$$

$$\tau_{rz}^{(\mathrm{ff})}(a,\theta)+\tau_{rz}^{(\mathrm{S})}(a,\theta)+\tau_{1rz}^{(\mathrm{S})}(a,\theta)=\tau_{rz}^{(\mathrm{T})}(a,\theta) \qquad -\pi\le\theta\le 0 \tag{12.53}$$

and the traction-free condition on the upper semi-circular boundary $\overline{L}$, which were represented in Eqn. (12.3) above

$$\tau_{rz}^{(\mathrm{ff})}(a,\theta)+\tau_{rz}^{(\mathrm{S})}(a,\theta)+\tau_{1rz}^{(\mathrm{S})}(a,\theta)=0 \qquad 0\le\theta\le\pi \tag{12.54}$$

Substitution of the displacement and stress equations in (r,θ) into Eqns. (12.52) and (12.53), together with replacing θ by $-\theta$, lead to the following two equations exist for $0\le\theta\le\pi$,

$$\sum_{n=0}^{\infty}\begin{matrix}\left[\left(a_{0,n}+E_n^*-C_n\right)\mathrm{J}_n\left(ka\right)+E_n\mathrm{H}_n^{(1)}\left(ka\right)\right]\cos n\theta \\ -\left[\left(b_{0,n}+F_n^*\right)\mathrm{J}_n\left(ka\right)+F_n\mathrm{H}_n^{(1)}\left(ka\right)\right]\sin n\theta\end{matrix}=0 \tag{12.55}$$

$$\sum_{n=0}^{\infty}\begin{matrix}\left[\left(a_{0,n}+E_n^*-C_n\right)\mathrm{J}_n'\left(ka\right)+E_n\mathrm{H}_n^{(1)\prime}\left(ka\right)\right]\cos n\theta \\ -\left[\left(b_{0,n}+F_n^*\right)\mathrm{J}_n'\left(ka\right)+F_n\mathrm{H}_n^{(1)\prime}\left(ka\right)\right]\sin n\theta\end{matrix}=0 \tag{12.56}$$

Similarly, for $0\le\theta\le\pi$, Eqn.(12.54) could be expanded to

$$\sum_{n=0}^{\infty} \begin{matrix} \left[\left(a_{0,n}+E_n^*\right)\mathrm{J}'_n(ka)+E_n\mathrm{H}_n^{(1)\prime}(ka)\right]\cos n\theta \\ +\left[\left(b_{0,n}+F_n^*\right)\mathrm{J}'_n(ka)+F_n\mathrm{H}_n^{(1)\prime}(ka)\right]\sin n\theta \end{matrix} = 0 \qquad (12.57)$$

Define three functions to simplify the expressions,

$$\begin{aligned} c_n(ka) &= C_n\mathrm{J}_n(ka) \\ e_n(ka) &= \left(a_{0,n}+E_n^*\right)\mathrm{J}_n(ka)+E_n\mathrm{H}_n^{(1)}(ka) \\ f_n(ka) &= \left(b_{0,n}+F_n^*\right)\mathrm{J}_n(ka)+F_n\mathrm{H}_n^{(1)}(ka) \end{aligned} \qquad (12.58)$$

and $c'_n(ka),\ e'_n(ka),\ f'_n(ka)$ can be simply defined as the derivatives of corresponding Bessel and Hankel functions in each function. The boundary conditions then all take a similar form, respectively at $r = a$ for $0 \le \theta \le \pi$:

$$\sum\left(e_n(ka)-c_n(ka)\right)\cos n\theta = \sum f_n(ka)\sin n\theta \qquad (12.55)^*$$

$$\sum\left(e'_n(ka)-c'_n(ka)\right)\cos n\theta = \sum f'_n(ka)\sin n\theta \qquad (12.56)^*$$

$$\sum e'_n(ka)\cos n\theta = -\sum f'_n(ka)\sin n\theta \qquad (12.57)^*$$

Substitution of Eqn. (12.57)* into (12.56)* leads to

$$2\sum e'_n(ka)\cos n\theta = \sum c'_n(ka)\cos n\theta \qquad (12.59)$$

, so for n=0, 1, 2…

$$c'_n(ka) = 2e'_n(ka) \qquad (12.60)$$

Or expand as,

$$C_n\mathrm{J}'_n(ka) = 2\left[\left(a_{0,n}+E_n^*\right)\mathrm{J}'_n(ka)+E_n\mathrm{H}_n^{(1)\prime}(ka)\right]$$, or rewrite as,

$$C_n = 2\left[a_{0,n} + E_n^* + \frac{\mathrm{H}_n^{(1)\prime}(ka)}{\mathrm{J}_n'(ka)} E_n \right] \tag{12.61}$$

which is C_n explicitly in terms of the set $\{E_n\}$. Further,

$$c_n(ka) = C_n \mathrm{J}_n(ka) = 2\left[\left(a_{0,n} + E_n^*\right) \mathrm{J}_n(ka) + \frac{\mathrm{H}_n^{(1)\prime}(ka)\mathrm{J}_n(ka)}{\mathrm{J}_n'(ka)} E_n \right] \tag{12.62}$$

This will enable C_n to be first eliminated from the equations to be solved.

6.2.2.2 The sines and cosines as orthogonal functions in $[0, \pi]$

Notice that Eqns (12.55)* through (12.57)* are all of the same form, for $0 \le \theta \le \pi$,

$$\sum_{n=0}^{\infty} p_n \cos n\theta = \sum_{m=1}^{\infty} q_m \sin m\theta \tag{12.63}$$

For $n = 0, 1, 2\ldots$, multiply both sides of equation (12.63) by $\cos n\theta$ and integrate from 0 to π, the orthogonality of the cosine functions in $[0, \pi]$ gives, for $n = 0, 1, 2\ldots$

$$p_n = \frac{\varepsilon_n}{\pi} \sum_{\substack{m=1 \\ m+n \text{ odd}}}^{\infty} \left(\frac{2m}{m^2 - n^2} \right) q_m = \frac{\varepsilon_n}{\pi} \sum_{\substack{m=1 \\ m+n \text{ odd}}}^{\infty} s_{mn} q_m \tag{12.64}$$

Similarly, for $m = 1, 2, 3\ldots$, multiply both sides of the equation by $\sin m\theta$ and integrate from 0 to π, the orthogonality of the sine functions in $[0, \pi]$ indicates, for $m = 1, 2, 3\ldots$

$$q_m = \frac{2}{\pi} \sum_{\substack{n=0 \\ m+n \text{ odd}}}^{\infty} \left(\frac{2m}{m^2 - n^2} \right) p_n = \frac{2}{\pi} \sum_{\substack{n=0 \\ m+n \text{ odd}}}^{\infty} s_{mn} p_n \tag{12.65}$$

where $s_{mn} = 2m\big/\left(m^2 - n^2\right)$. The identities of trigonometric integrals used in the derivation earlier are included in the Appendix E at the end of this dissertation. Based on these two equalities in the form of infinite series, we can derive out the following lemma,

Lemma If for $0 \le \theta \le \pi$, $\varepsilon(\theta) = \sum_{n=0}^{\infty} p_n \cos n\theta - \sum_{m=1}^{\infty} q_m \sin m\theta = 0$, then for the same $0 \le \theta \le \pi$, $\varepsilon(\theta) = \sum_{n=0}^{\infty} (p_n - \frac{\varepsilon_n}{\pi} \sum_{\substack{m=1 \\ m+n \text{ odd}}}^{\infty} s_{mn} q_m) \cos n\theta = 0$. Also, in the same range, $\varepsilon(\theta) = \sum_{m=1}^{\infty} (q_m - \frac{2}{\pi} \sum_{\substack{n=0 \\ m+n \text{ odd}}}^{\infty} s_{mn} p_n) \sin m\theta = 0$.

Dimensionless modulus of complex number $\varepsilon(\theta)$ in the lemma, $\left|\varepsilon(\theta)\right|$, could be taken as a residual function for the model studied.

6.2.2.3 The boundary conditions in terms of residues

Three dimensionless residues of displacement and stress are defined below

$$\varepsilon_w\left(\theta\right) = \left| w^{(\mathrm{T})}(r,\theta) - w^{(\mathrm{ff})}(r,\theta) - w^{(\mathrm{S})}(r,\theta) - w_1^{(\mathrm{S})}(r,\theta) \right| \quad -\pi \le \theta \le 0 \qquad (12.66)$$

$$\underline{\varepsilon}_\tau\left(\theta\right) = \left| \tau_{rz}^{(\mathrm{T})}(a,\theta) - \tau_{rz}^{(\mathrm{ff})}(a,\theta) - \tau_{rz}^{(\mathrm{S})}(a,\theta) - \tau_{1rz}^{(\mathrm{S})}(a,\theta) \right| \big/ \mu k \quad -\pi \le \theta \le 0 \qquad (12.67)$$

$$\overline{\varepsilon}_\tau\left(\theta\right) = \left| \tau_{rz}^{(\mathrm{ff})}(a,\theta) + \tau_{rz}^{(\mathrm{S})}(a,\theta) + \tau_{1rz}^{(\mathrm{S})}(a,\theta) \right| \big/ \mu k \qquad 0 \le \theta \le \pi \qquad (12.68)$$

they actually could be thought of as the dimensionless residues of boundary condition equations (12.52), (12.53), and (12.54), respectively.

All of the boundary conditions in Eqns (12.55)*, (12.56)*, and (12.57)* are of the form as in Eqn. (12.63), so for the same range $0 \le \theta \le \pi$,

(I) Eqn (12.55) above is of the form $\sum\left[\left(e_n(ka)-c_n(ka)\right)\cos n\theta - f_n(ka)\sin n\theta\right]=0$. By the Lemma, the residue of the displacement continuity boundary condition on the surface $\underline{L}$ of the lower semi-circular cavity could be described as $\varepsilon_w(\theta)=\left|\sum_{n=0}^{\infty}\varepsilon(n)_w \cos n\theta\right|=0$ so that $\varepsilon(n)_w=0$, for n=0,1,2,3,…, where

$$
\begin{aligned}
\varepsilon(n)_w &= \left(a_{0,n}+E_n^*-C_n\right)\mathrm{J}_n(ka)+E_n\mathrm{H}_n^{(1)}(ka)\\
&\quad -\frac{\varepsilon_n}{\pi}\sum_{\substack{m=1\\ m+n\ \text{odd}}}^{\infty} s_{mn}\left[\left(b_{0,m}+F_m^*\right)\mathrm{J}_m(ka)+F_m\mathrm{H}_m^{(1)}(ka)\right]=0
\end{aligned}
\tag{12.69}
$$

Using Eqn.(12.61) to eliminate the C_n in (12.69), the first two terms of the equation becomes,

$$
\begin{aligned}
&=-\left[\left(a_{0,n}+E_n^*\right)\mathrm{J}_n(ka)-E_n\left(\mathrm{H}_n^{(1)}(ka)-2\frac{\mathrm{H}_n^{(1)\prime}(ka)}{\mathrm{J}_n'(ka)}\mathrm{J}_n(ka)\right)\right]\\
&=-\left[\left(a_{0,n}+E_n^*\right)\mathrm{J}_n(ka)-E_n\frac{\mathrm{H}_n^{(1)}(ka)\mathrm{J}_n'(ka)-2\mathrm{H}_n^{(1)\prime}(ka)\mathrm{J}_n(ka)}{\mathrm{J}_n'(ka)}\right]\\
&=-\left[\left(a_{0,n}+E_n^*\right)\mathrm{J}_n(ka)+E_n\frac{\frac{2\mathrm{i}}{\pi ka}+\mathrm{H}_n^{(1)\prime}(ka)\mathrm{J}_n(ka)}{\mathrm{J}_n'(ka)}\right]
\end{aligned}
$$

where Wronskian $W\left(\mathrm{J}_n(ka),\mathrm{H}_n^{(1)}(ka)\right)=\mathrm{J}_n(ka)\mathrm{H}_n^{(1)\prime}(ka)-\mathrm{J}_n'(ka)\mathrm{H}_n^{(1)}(ka)=\frac{2\mathrm{i}}{\pi ka}$ has been used, the displacement residue term $\varepsilon_w(\theta)=\left|\sum_{n=0}^{\infty}\varepsilon(n)_w\cos n\theta\right|=0$ now takes the form

$$\varepsilon(n)_w = \left(a_{0,n} + E_n^*\right)\mathrm{J}_n\left(ka\right) + E_n \frac{\dfrac{2\mathrm{i}}{\pi ka} + \mathrm{H}_n^{(1)\prime}(ka)\mathrm{J}_n\left(ka\right)}{\mathrm{J}_n'(ka)}$$
$$+\frac{\varepsilon_n}{\pi}\sum_{\substack{m=1\\ m+n\ \mathrm{odd}}}^{\infty} s_{mn}\left[\left(b_{0,m} + F_m^*\right)\mathrm{J}_m\left(ka\right) + F_m \mathrm{H}_m^{(1)}\left(ka\right)\right] = 0 \tag{12.69}^*$$

(II) Eqn (12.56) above is of the form $\sum\left[\left(e_n'(ka) - c_n'(ka)\right)\cos n\theta - f_n'(ka)\sin n\theta\right] = 0$, By the Lemma, $\underline{\varepsilon}_\tau\left(\theta\right) = \left|\sum_{n=0}^{\infty}\underline{\varepsilon}(n)_\tau \cos n\theta\right| = 0$ represents the residue of the traction-free boundary condition on the surface $\underline{L}$ of the lower semi-circular cavity, so that $\underline{\varepsilon}(n)_\tau = 0$, for n=0,1,2,…, where

$$\underline{\varepsilon}(n)_\tau = \left(a_{0,n} + E_n^* - C_n\right)\mathrm{J}_n'\left(ka\right) + E_n \mathrm{H}_n^{(1)\prime}\left(ka\right)$$
$$-\frac{\varepsilon_n}{\pi}\sum_{\substack{m=1\\ m+n\ \mathrm{odd}}}^{\infty} s_{mn}\left[\left(b_{0,m} + F_m^*\right)\mathrm{J}_m'\left(ka\right) + F_m \mathrm{H}_m^{(1)\prime}\left(ka\right)\right] = 0 \tag{12.70}$$

Eqn. (12.72) plus (12.70) together gives

$$C_n \mathrm{J}_n'\left(ka\right) = 2\left[\left(a_{0,n} + E_n^*\right)\mathrm{J}_n'\left(ka\right) + E_n \mathrm{H}_n^{(1)\prime}\left(ka\right)\right]$$
$$= -\frac{2\varepsilon_n}{\pi}\sum_{\substack{m=1\\ m+n\ \mathrm{odd}}}^{\infty} s_{mn}\left[\left(b_{0,m} + F_m^*\right)\mathrm{J}_m'\left(ka\right) + F_m \mathrm{H}_m^{(1)\prime}\left(ka\right)\right] \tag{12.71}$$

which is also found from Eqn.(12.61) above. Utilizing Eqn.(12.71), C_n can be eliminated from Eqn.(12.70) to revise the zero residue term as

$$\underline{\varepsilon}(n)_\tau = \left(a_{0,n} + E_n^*\right)\mathrm{J}_n'\left(ka\right) + E_n \mathrm{H}_n^{(1)\prime}\left(ka\right)$$
$$+\frac{\varepsilon_n}{\pi}\sum_{\substack{m=1\\ m+n\ \mathrm{odd}}}^{\infty} s_{mn}\left[\left(b_{0,m} + F_m^*\right)\mathrm{J}_m'\left(ka\right) + F_m \mathrm{H}_m^{(1)\prime}\left(ka\right)\right] = 0 \tag{12.70}^*$$

Then from Eqns (12.72) and (12.70) it is clear that $\overline{\varepsilon}(n)_\tau = \underline{\varepsilon}(n)_\tau$, meaning that the residue term at the upper circular surface $\overline{L}$ is identical to that on the lower circular surface $\underline{L}$. So hitherto the stress residue terms are written as $\varepsilon(n)_\tau = \overline{\varepsilon}(n)_\tau = \underline{\varepsilon}(n)_\tau$, without the upper or lower bar.

(III) Eqn. (12.57) above is of the form $\sum\left[e_n'(ka)\cos n\theta + f_n'(ka)\sin n\theta\right] = 0$. According to the Lemma, $\overline{\varepsilon}_\tau\left(\theta\right) = \left|\sum_{n=0}^{\infty}\overline{\varepsilon}(n)_\tau \cos n\theta\right| = 0$ is the residue of the traction-free boundary condition on the surface $\overline{L}$ of the upper semi-circular cavity, so that $\overline{\varepsilon}(n)_\tau = 0$, for n=0,1,2,…, where

$$\begin{aligned}\overline{\varepsilon}(n)_\tau &= \left(a_{0,n} + E_n^*\right)\mathrm{J}_n'\left(ka\right) + E_n\mathrm{H}_n^{(1)\prime}\left(ka\right)\\ &\quad + \frac{\varepsilon_n}{\pi}\sum_{\substack{m=1\\ m+n\ \text{odd}}}^{\infty} s_{mn}\left[\left(b_{0,m} + F_m^*\right)\mathrm{J}_m'\left(ka\right) + F_m\mathrm{H}_m^{(1)\prime}\left(ka\right)\right] = 0\end{aligned} \tag{12.72}$$

Alternatively, by means of the orthogonality of the sine functions in $[0,\pi]$:

(I)*

$$\begin{aligned}&\left(b_{0,m} + F_m^*\right)\mathrm{J}_m\left(ka\right) + F_m\mathrm{H}_m^{(1)}\left(ka\right)\\ &= \frac{2}{\pi}\sum_{\substack{n=0\\ m+n\ \text{odd}}}^{\infty} s_{mn}\left[\left(a_{0,n} + E_n^* - C_n\right)\mathrm{J}_n\left(ka\right) + E_n\mathrm{H}_n^{(1)}\left(ka\right)\right] \qquad (12.73)\\ &= -\frac{2}{\pi}\sum_{\substack{n=0\\ m+n\ \text{odd}}}^{\infty} s_{mn}\left[\left(a_{0,n} + E_n^*\right)\mathrm{J}_n\left(ka\right) + E_n\frac{\frac{2\mathrm{i}}{\pi ka} + \mathrm{H}_n^{(1)\prime}(ka)\mathrm{J}_n\left(ka\right)}{\mathrm{J}_n'(ka)}\right]\end{aligned}$$

(II)*

$$\begin{aligned}&\left(b_{0,m}+F_m^*\right)\mathrm{J}_m'\left(ka\right)+F_m\mathrm{H}_m^{(1)\prime}\left(ka\right)\\&=\frac{2}{\pi}\sum_{\substack{n=0\\m+n\ odd}}^{\infty}s_{mn}\left[\left(a_{0,n}+E_n^*-C_n\right)\mathrm{J}_n'\left(ka\right)+E_n\mathrm{H}_n^{(1)\prime}\left(ka\right)\right]\\&=-\frac{2}{\pi}\sum_{\substack{n=0\\m+n\ odd}}^{\infty}s_{mn}\left[\left(a_{0,n}+E_n^*\right)\mathrm{J}_n'\left(ka\right)+E_n\mathrm{H}_n^{(1)\prime}\left(ka\right)\right]\end{aligned} \tag{12.74}$$

Eqn (12.74) is then identical to Eqn.(12.75), after eliminating the C_n 's.

(III)*

$$\begin{aligned}&\left(b_{0,m}+F_m^*\right)\mathrm{J}_m'\left(ka\right)+F_m\mathrm{H}_m^{(1)\prime}\left(ka\right)\\&=-\frac{2}{\pi}\sum_{\substack{n=0\\m+n\ \mathrm{odd}}}^{\infty}s_{mn}\left[\left(a_{0,n}+E_n^*\right)\mathrm{J}_n'\left(ka\right)+E_n\mathrm{H}_n^{(1)\prime}\left(ka\right)\right]\end{aligned} \tag{12.75}$$

6.2.2.4 Expressing boundary conditions in terms of A_n and B_n 's

Substitution of Eqns (12.44) through (12.47) into those boundary condition equations can lead to all equations in terms of the coefficients A_n and B_n 's separately by even or odd subscripts, instead of E_n and F_n 's. Eqns. (12.71), (12.69)*, (12.75) are chosen to make the resultant governing equations banded and pivoting for all unknowns.

From Eqn.(12.71), we have

Even:

$$C_{2n}\mathrm{J}_{2n}'\left(ka\right) = 2\left[\left(a_{0,2n}+\hat{A}_{2n}^*\right)\mathrm{J}_{2n}'\left(ka\right)+\hat{A}_{2n}\mathrm{H}_{2n}^{(1)\prime}\left(ka\right)\right] \tag{12.76}$$

Odd:

$$C_{2n+1}\mathrm{J}_{2n+1}'\left(ka\right) = 2\left[\left(a_{0,2n+1}+\hat{B}_{2n+1}^*\right)\mathrm{J}_{2n+1}'\left(ka\right)+\hat{B}_{2n+1}\mathrm{H}_{2n+1}^{(1)}{}'\left(ka\right)\right] \tag{12.77}$$

From Eqn.(12.69)*,

Even:

$$\left(a_{0,2n}+\hat{A}^*_{2n}\right)\mathrm{J}_{2n}\left(ka\right)+\hat{A}_{2n}\frac{\dfrac{2\mathrm{i}}{\pi ka}+\mathrm{H}^{(1)\prime}_{2n}(ka)\mathrm{J}_{2n}\left(ka\right)}{\mathrm{J}'_{2n}(ka)}$$
$$=-\frac{\varepsilon_n}{\pi}\sum_{m=0}^{\infty}s_{2m+1,2n}\left[\left(b_{0,2m+1}+\hat{A}^*_{2m+1}\right)\mathrm{J}_{2m+1}(ka)+\hat{A}_{2m+1}\mathrm{H}^{(1)}_{2m+1}(ka)\right] \tag{12.78}$$

Odd:

$$\left(a_{0,2n+1}+\hat{B}^*_{2n+1}\right)\mathrm{J}_{2n+1}\left(ka\right)+\hat{B}_{2n+1}\frac{\dfrac{2\mathrm{i}}{\pi ka}+\mathrm{H}^{(1)}_{2n+1}{}'(ka)\mathrm{J}_{2n+1}(ka)}{\mathrm{J}'_{2n+1}(ka)}$$
$$=-\frac{2}{\pi}\sum_{m=1}^{\infty}s_{2m,2n+1}\left[\left(b_{0,2m}+\hat{B}^*_{2m}\right)\mathrm{J}_{2m}(ka)+\hat{B}_{2m}\mathrm{H}^{(1)}_{2m}(ka)\right] \tag{12.79}$$

From Eqn.(12.75),

Even:

$$\left(b_{0,2m}+\hat{B}^*_{2m}\right)\mathrm{J}'_{2m}(ka)+\hat{B}_{2m}\mathrm{H}^{(1)\prime}_{2m}(ka)$$
$$=-\frac{2}{\pi}\sum_{n=0}^{\infty}s_{2m,2n+1}\left[\left(a_{0,2n+1}+\hat{B}^*_{2n+1}\right)\mathrm{J}'_{2n+1}(ka)+\hat{B}_{2n+1}\mathrm{H}^{(1)}_{2n+1}{}'(ka)\right] \tag{12.80}$$

Odd:

$$\left(b_{0,2m+1}+\hat{A}^*_{2m+1}\right)\mathrm{J}'_{2m+1}(ka)+\hat{A}_{2m+1}\mathrm{H}^{(1)}_{2m+1}{}'(ka)$$
$$=-\frac{2}{\pi}\sum_{n=0}^{\infty}s_{2m+1,2n}\left[\left(a_{0,2n}+\hat{A}^*_{2n}\right)\mathrm{J}'_{2n}(ka)+\hat{A}_{2n}\mathrm{H}^{(1)\prime}_{2n}(ka)\right] \tag{12.81}$$

Similarly, by substituting equations (12.39), (12.48), and (12.49), we can express the boundary condition equations (12.78) through (12.81) in terms of A_n and B_n separately. The detail elimination procedures are omitted here for briefness. The resultant set of infinite linear equations is called 'governing equations' in this chapter and represented in detail in the next sub-section. Solving them first for the evaluation of A_n, B_n and A^*_n, B^*_n, and then plugging them to Eqns. (12.76) and (12.77) leads to C_n.

6.2.2.5 Governing equations in terms of A_n and B_n separately

Equations in terms of A_n:

$$\begin{cases} \sum_{m=0}^{\infty} \boldsymbol{U^{+}_{nm}} A_m = \boldsymbol{r_{2n}} \\ \sum_{m=0}^{\infty} \boldsymbol{V^{+}_{nm}} A_m = \boldsymbol{t_{2n+1}} \end{cases} \tag{12.82}$$

in which the upper and lower sub-equations are derived from (12.78) and (12.81), respectively. And,

$$\begin{aligned} \boldsymbol{U^{+}_{nm}} = & (-1)^n P^{+}_{2n,m} \mathrm{J}_{2n}\left(ka\right) + (-1)^n \frac{\frac{2\mathrm{i}}{\pi ka} + \mathrm{H}^{(1)\prime}_{2n}(ka)\mathrm{J}_{2n}\left(ka\right)}{\mathrm{J}'_{2n}(ka)} \delta_{2n,m} \\ & + \frac{\varepsilon_n}{\pi} \sum_{l=0}^{\infty} s_{2l+1,2n} (-1)^l \mathrm{J}_{2l+1}\left(ka\right) P^{+}_{2l+1,m} + \operatorname{mod}_2(m) \frac{\varepsilon_n}{\pi} s_{m,2n} (-1)^{\frac{m-1}{2}} \mathrm{H}^{(1)}_m\left(ka\right) \end{aligned} \tag{12.83}$$

$$\boldsymbol{r_{2n}} = -a_{0,2n} \mathrm{J}_{2n}\left(ka\right) - \frac{\varepsilon_n}{\pi} \sum_{m=0}^{\infty} s_{2m+1,2n} \mathrm{J}_{2m+1}\left(ka\right) b_{0,2m+1} \tag{12.84}$$

$$\begin{aligned} \boldsymbol{V^{+}_{nm}} = & (-1)^n P^{+}_{2n+1,m} \mathrm{J}'_{2n+1}\left(ka\right) + (-1)^n \mathrm{H}^{(1)\prime}_{2n+1}\left(ka\right) \delta_{2n+1,m} \\ & + \frac{2}{\pi} \sum_{l=0}^{\infty} s_{2n+1,2l} (-1)^l P^{+}_{2l,m} \mathrm{J}'_{2l}\left(ka\right) + \left(1 - \operatorname{mod}_2(m)\right) \frac{2}{\pi} s_{2n+1,m} (-1)^{\frac{m}{2}} \mathrm{H}^{(1)\prime}_m\left(ka\right) \end{aligned} \tag{12.85}$$

$$\boldsymbol{t_{2n+1}} = -b_{0,2n+1} \mathrm{J}'_{2n+1}\left(ka\right) - \frac{2}{\pi} \sum_{m=0}^{\infty} s_{2n+1,2m} \mathrm{J}'_{2m}\left(ka\right) a_{0,2m} \tag{12.86}$$

with $\operatorname{mod}_2(m) = \begin{cases} 1 \text{ , when } m \text{ is odd} \\ 0 \text{ , when } m \text{ is even} \end{cases}$, and $\delta_{nm} = \begin{cases} 1 \text{ , when } n = m \\ 0 \text{ , when } n \neq m \end{cases}$ is the Kronecker delta function.

Equations in terms of B_n :

$$\begin{cases} \sum_{m=1}^{\infty} \boldsymbol{U^{-}_{nm}} B_m = \boldsymbol{r_{2n+1}} \\ \sum_{m=1}^{\infty} \boldsymbol{V^{-}_{nm}} B_m = \boldsymbol{t_{2n}} \end{cases} \tag{12.87}$$

in which the upper and lower sub-equations are derived from (12.79) and (12.80), respectively. And,

$$\begin{aligned}\boldsymbol{U_{nm}^-} &= (-1)^n P_{2n+1,m}^- \mathrm{J}_{2n+1}(ka) + (-1)^n \frac{\dfrac{2\mathrm{i}}{\pi ka} + \mathrm{H}_{2n+1}^{(1)\prime}(ka)\mathrm{J}_{2n+1}(ka)}{\mathrm{J}_{2n+1}'(ka)}\delta_{2n+1,m} \\ &- \frac{2}{\pi}\sum_{l=0}^{\infty} s_{2l,2n+1}(-1)^l \mathrm{J}_{2l}(ka) P_{2l,m}^- - \left(1-\mathrm{mod}_2(m)\right)\frac{2}{\pi} s_{m,2n+1}(-1)^{\frac{m}{2}} \mathrm{H}_m^{(1)}(ka)\end{aligned} \tag{12.88}$$

$$\boldsymbol{r_{2n+1}} = -a_{0,2n+1}\mathrm{J}_{2n+1}(ka) - \frac{2}{\pi}\sum_{m=1}^{\infty} s_{2m,2n+1}\mathrm{J}_{2m}(ka) b_{0,2m} \tag{12.89}$$

$$\begin{aligned}\boldsymbol{V_{nm}^-} &= -(-1)^n P_{2n,m}^- \mathrm{J}_{2n}'(ka) - (-1)^n \mathrm{H}_{2n}^{(1)\prime}(ka)\delta_{2n,m} \\ &+ \frac{2}{\pi}\sum_{l=0}^{\infty} s_{2n,2l+1}(-1)^l P_{2l+1,m}^- \mathrm{J}_{2l+1}'(ka) + \mathrm{mod}_2(m)\frac{2}{\pi} s_{2n,m}(-1)^{\frac{m-1}{2}} \mathrm{H}_m^{(1)\prime}(ka)\end{aligned} \tag{12.90}$$

$$\boldsymbol{t_{2n}} = -b_{0,2n}\mathrm{J}_{2n}'(ka) - \frac{2}{\pi}\sum_{m=0}^{\infty} s_{2n,2m+1}\mathrm{J}_{2m+1}'(ka) a_{0,2m+1} \tag{12.91}$$

6.2.2.6 Truncation of infinite governing linear equations

This sub-section demonstrates how these two sets of infinite linear equations (12.82) and (12.87) are truncated and solved in details. First we are intended to make sure the order number of the first subscript *m* of s_{mn} to be larger than the second one *n*. That is because if we just simply set the order number identical, we could not ensure the numerical precision of the Fourier Cosine/Sine Expansion of Eqns. (12.64) and (12.65). Therefore, all of the summation including the s_{mn} term are set to a higher order number $2\times\mathrm{NUM}+1$. Here NUM is an integral constant that specifies the truncated row number of coefficient matrices.

First set includes the two equations with respect to A_m

$$\begin{cases} \sum_{m=0}^{2\text{NUM}+1} \boldsymbol{U}_{\boldsymbol{nm}}^{\boldsymbol{+}} A_m = \boldsymbol{r}_{\boldsymbol{2n}} \\ \sum_{m=0}^{2\text{NUM}+1} \boldsymbol{V}_{\boldsymbol{nm}}^{\boldsymbol{+}} A_m = \boldsymbol{t}_{\boldsymbol{2n+1}} \end{cases} \quad (n=0,1,\ldots,\text{NUM};\ m=0,1,\ldots,2\times\text{NUM}+1) \tag{12.92}$$

which could be combined to one single set of linear equations,

$$[QA]_{2\times\text{NUM}+2,2\times\text{NUM}+2}\{A\}_{2\times\text{NUM}+2} = \{RA\}_{2\times\text{NUM}+2} \tag{12.92*}$$

where NUM represents the order number for each sub-equation. So the combined coefficient matrix [QA] is a $(2\times\text{NUM}+2)$ by $(2\times\text{NUM}+2)$ scale square matrix. It is an even-determined set of linear equations and could be solved accurately by any common methods given [QA] is not over ill-conditioned for that method.

The second set is with respect to B_m

$$\begin{cases} \sum_{m=1}^{2\text{NUM}+1} \boldsymbol{U}_{\boldsymbol{nm}}^{\boldsymbol{-}} B_m = \boldsymbol{r}_{\boldsymbol{2n+1}} \\ \sum_{m=1}^{2\text{NUM}+1} \boldsymbol{V}_{\boldsymbol{nm}}^{\boldsymbol{-}} B_m = \boldsymbol{t}_{\boldsymbol{2n}} \end{cases} \quad (n=0,1,\ldots,\text{NUM};\ m=1,\ldots,2\times\text{NUM}+1) \tag{12.93}$$

or expressed in its matrix form as,

$$[QB]_{2\times\text{NUM}+2,2\times\text{NUM}+1}\{B\}_{2\times\text{NUM}+1} = \{RB\}_{2\times\text{NUM}+2} \tag{12.93*}$$

So the combined coefficient matrix [QB] is a $(2\times\text{NUM}+2)$ by $(2\times\text{NUM}+1)$ scale non-square matrix. It is an over-determined linear equation set and could be solved by Least Square Method.

However, since $\boldsymbol{t}_{\boldsymbol{0}} = 0$ and $\boldsymbol{V}_{\boldsymbol{0,m}}^{\boldsymbol{-}} = 0$, the $\text{NUM}+2$ row of equation set (12.93)* is actually a zero line and should be crossed out. Hence Eqn.(12.93) becomes an even-determined linear equation set.

$$\begin{cases} \sum_{m=1}^{2\text{NUM}+1} \boldsymbol{U}^{-}_{\boldsymbol{nm}} B_m = \boldsymbol{r}_{\boldsymbol{2n+1}} \quad (n=0,1,\ldots,\ \text{NUM}) \\ \sum_{m=1}^{2\text{NUM}+1} \boldsymbol{V}^{-}_{\boldsymbol{nm}} B_m = \boldsymbol{t}_{\boldsymbol{2n}} \quad (n=1,2,\ldots,\ \text{NUM}) \end{cases} \quad (m=1,\ldots,\ 2\times\text{NUM}+1) \qquad (12.94)$$

and

$$\left[QB\right]_{2\times\text{NUM}+1,2\times\text{NUM}+1}\left\{B\right\}_{2\times\text{NUM}+1} = \left\{RB\right\}_{2\times\text{NUM}+1} \qquad (12.94)^*$$

After solving the infinite linear equations (12.92)* and (12.94)*, we can substitute the set of A_n and B_n ($n = 0, 1, 2, 3, \ldots$; $B_0 = 0$) into Eqn. (12.39) and find out coefficients A_n^* and B_n^*. Then E_n, F_n and E_n^*, F_n^* could be computed out per Eqn. (12.50) and (12.51). Thus all the unknowns required for the calculation of the total wave field are obtained.

6.3 Numerical Results of Displacement Amplitudes

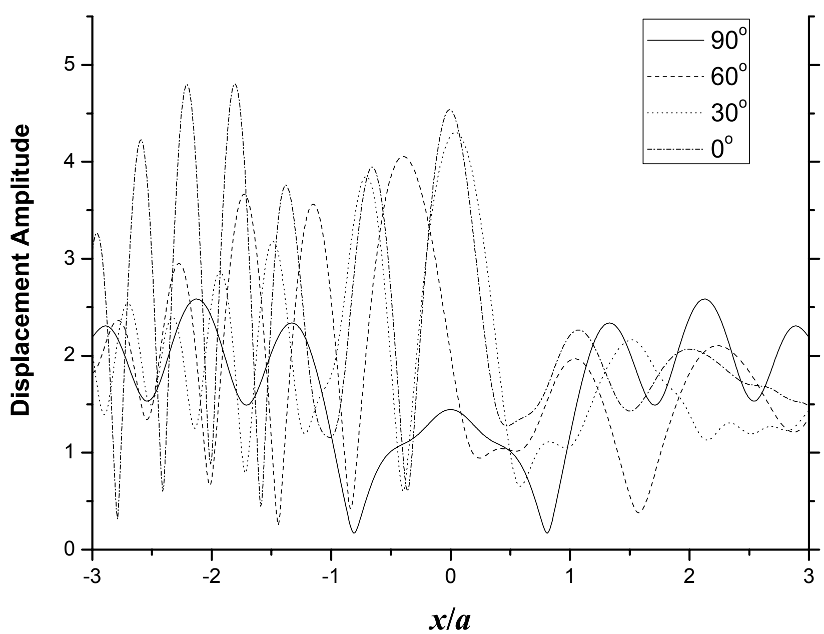

Fig. 6-5 DISPLACEMENT AMPLITUDES ON THE GROUND SURFACE FOR η=3, d/a=2, AND γ= 90°, 60°, 30°, 0°

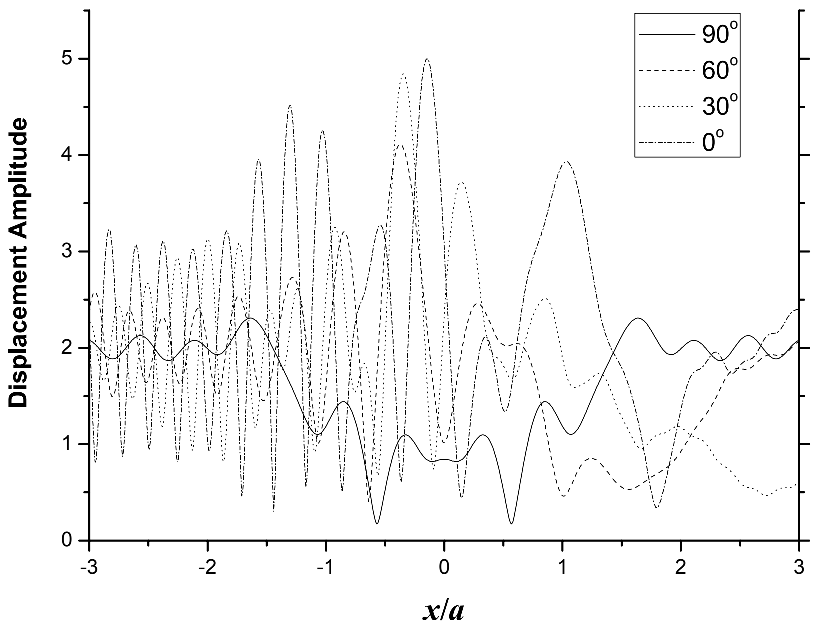

Fig. 6-6 DISPLACEMENT AMPLITUDES ON THE GROUND SURFACE FOR η=5, d / a =2, AND γ= 90°, 60°, 30°, 0°

Although the infinite series have to be truncated when solving this problem by computer, the displacement amplitudes converge as the truncation order increases. Certainly we cannot implement a infinitely large order of series on digital computers, in addition the series will overflow at some high order due to the limitation of machine precision and algorithm of computing special functions; however, a good deal of meaningful and accurate solutions still can be achieved for a wide range of initial conditions by truncation of infinite series to finite ones. Fig. 6-5 and Fig. 6-6 show the displacement amplitudes on the ground surface for various angles of incident waves. Fig. 6-7 shows the comparison of displacement amplitudes by the two methods presented in this and the previous section.

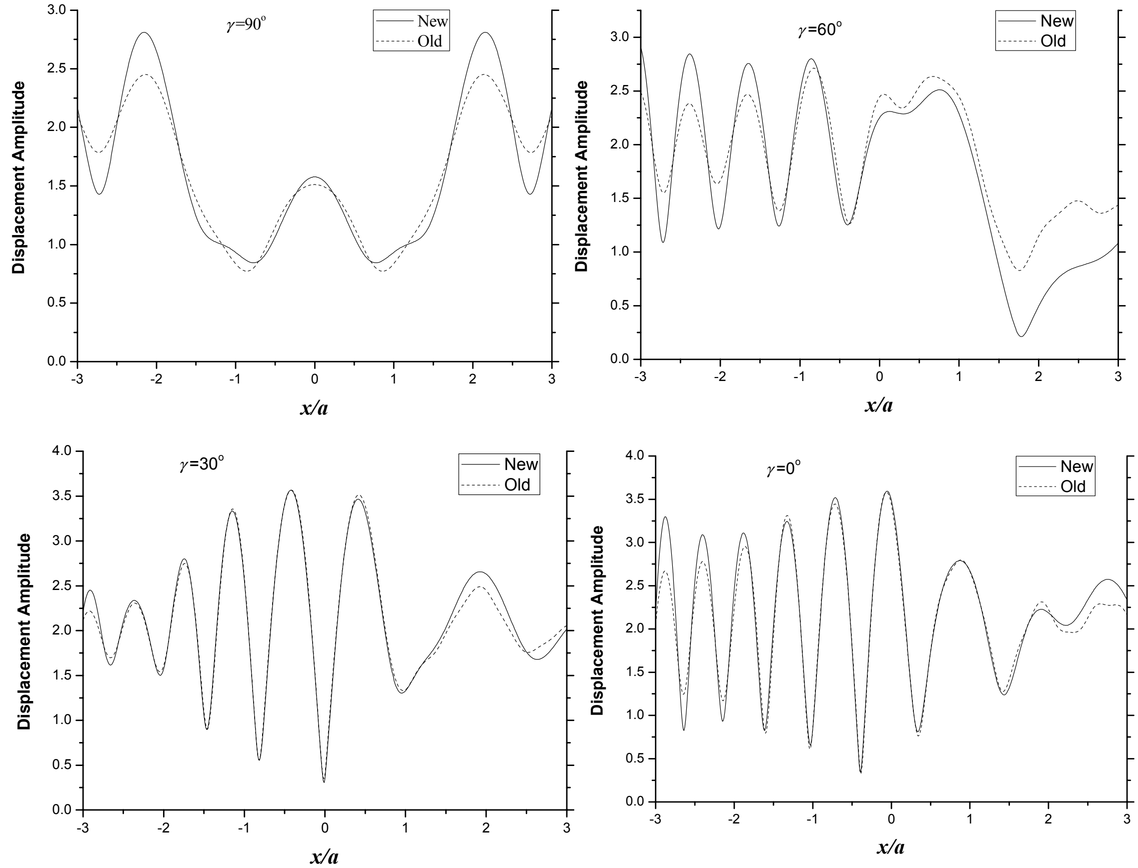

Fig. 6-7 COMPARISON OF DISPLACEMENT AMPLITUDES ON THE GROUND SURFACE BY COSINE HALF-RANGE TRANSFROM METHOD AND AUXILIARY FUNCTION METHOD FOR η=3, d/a=4, γ= 90°, 60°, 30°, 0°

6.4 Accuracy of Solutions

The dimensionless parameters of the stress and displacement residues along boundarier $\overline{L}$ and $\underline{L}$ to be used in subsequent figures are defined earlier in equations (12.66) till (12.68). Since the stress residual errors on the free flat ground surface Γ and tunnel horizontal ground surface L equal zero strictly by setting the wave functions, they are not discussed here.

The dimensionless frequency η for this chapter is defined as ratio of the diameter of cavity $2a$ and wavelength of incident wave λ

$$\eta = \frac{2a}{\lambda} = \frac{ka}{\pi} = \frac{\omega a}{\pi c_\beta} \tag{12.95}$$

The aforementioned improved cosine half-range expansion method in this section is based on minimizing the residues of various boundary conditions (12.69) through (12.72). Fig. 6-8 and Fig. 6-9 are the residues for the same conditions as Fig. 6-5, i.e., η=3, d/a=2, and γ= 90°, 60°, 30°, 0°.

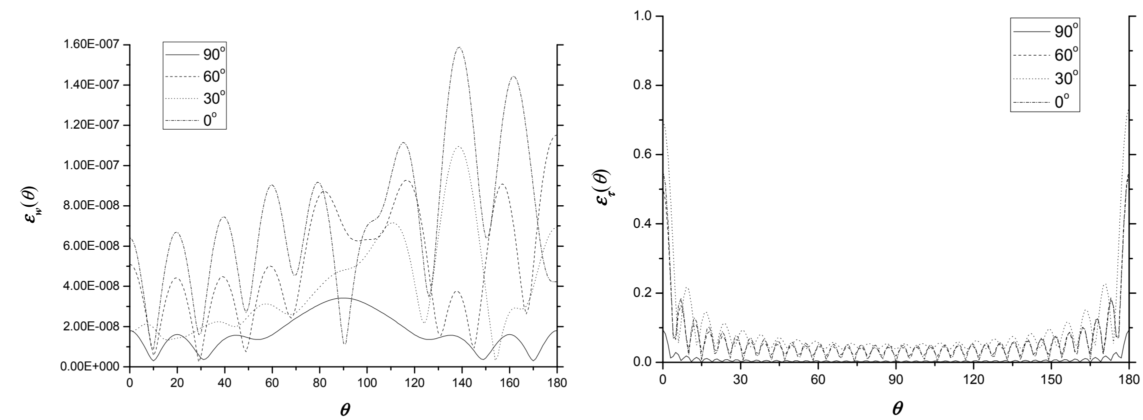

Fig. 6-8 DISPLACEMENT AND STRESS RESIDUES ON THE LOWER SEMI-CIRCULAR $\underline{L}$ FOR η=3, d/a=2, AND γ= 90°, 60°, 30°, 0°

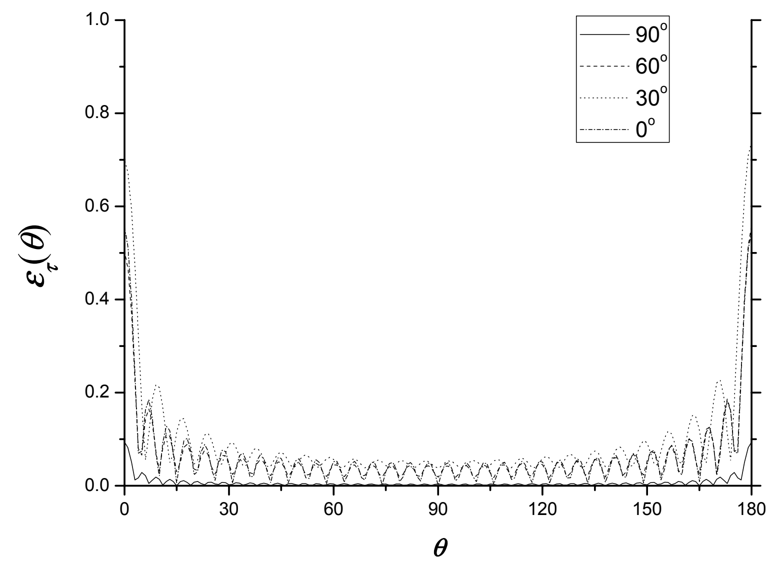

Fig. 6-9 STRESS RESIDUES ON THE UPPER SEMI-CIRCULAR $\overline{L}$ FOR η=3, d/a=2, AND γ= 90°, 60°, 30°, 0°

Fig. 6-10 shows the comparison of displacement amplitude on the ground surface above a full- or semi-circular cavity. It is evident that those two displacement amplitude curves are very close in the range of $x/a \in [-1,1]$, where is exactly the region right above the cavity. This is quite reasonable since the upper shape of either case is the same circular-arc, and horizontally incident SH-waves could not nearly feel the existence of the lower shape of the cavities. As the dimensionless frequency η increases, the wavelength decreases, the displacement amplitudes are supposed to agree with each other even better, as the Fig. 6-10 illustrates.

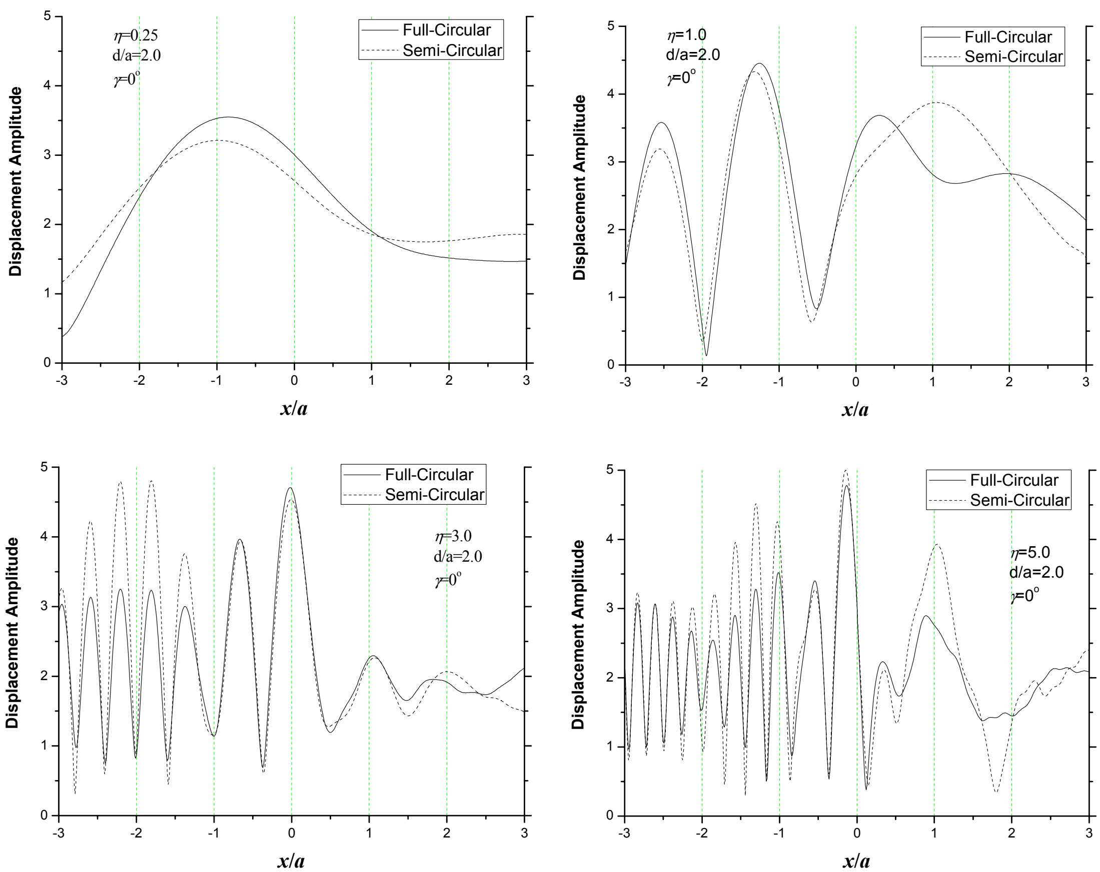

Fig. 6-10 GROUND SURFACE DISPLACEMENT AMPLITUDES FOR FULL- OR SEMI-CYLINDRICAL CAVITIES FOR η=0.25, 1, 3, 5

6.5 Case Study

The subsequent case studies are based on the same definition of displacement and stress residual errors and displacement amplitude on the ground surface as equation (9.17). Each case may be uniquely defined by three parameters: dimensionless frequency η of incident SH-waves, the ratio of buried depth and half-width of cavity d/a, and angle of incidence γ.

The cases studied in this section are for η=1.0, 3.0, 5.0, or 10.0; d/a=2.0 or 5.0; γ=90^{o}, 60^{o}, 30^{o}, 0^{o}. At first, stress and displacement residues are calculated according to equations (12.66) ~ (12.68); then figures of steady-state ground motion (i.e., displacement) are present; At last, ground displacement spectrum with respect to frequency of both sem-cylindrical and full-cylindrical cavities for the same initial conditions are compared and analyzed.

6.5.1 Accuracy of Solutions

Accuracy of solutions is checked by plotting stress or displacement residual errors along the boundaries on which governing equations are based. The figures below from Fig. 6-11 till Fig. 6-17 are still calculated by equations (12.66) to (12.68), but the computation method adopted here in this section 6.5 is the auxiliary function method. Thus the overshooting phenomena at two rims of the tunnel are the same as what we see in the paper by Yuan and Liao (1996) as metioned in Chapter 3. The three n's listed in the legend of those residue plots are the truncated order adopted in the series.

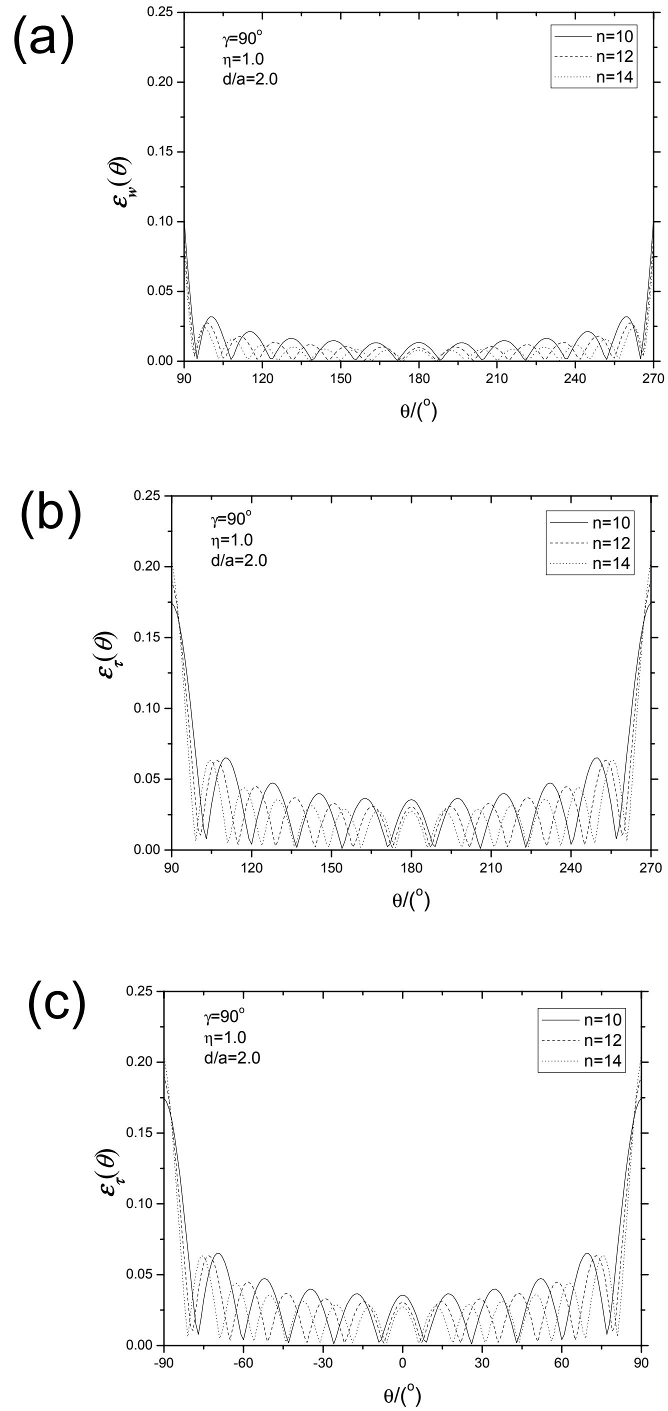

(a) Disp residue on $\underline{L}$ (b) Stress residue on $\underline{L}$ (c) Stress residue on $\overline{L}$

Fig. 6-11 RESIDUES FOR η=1 and d/a=**2**

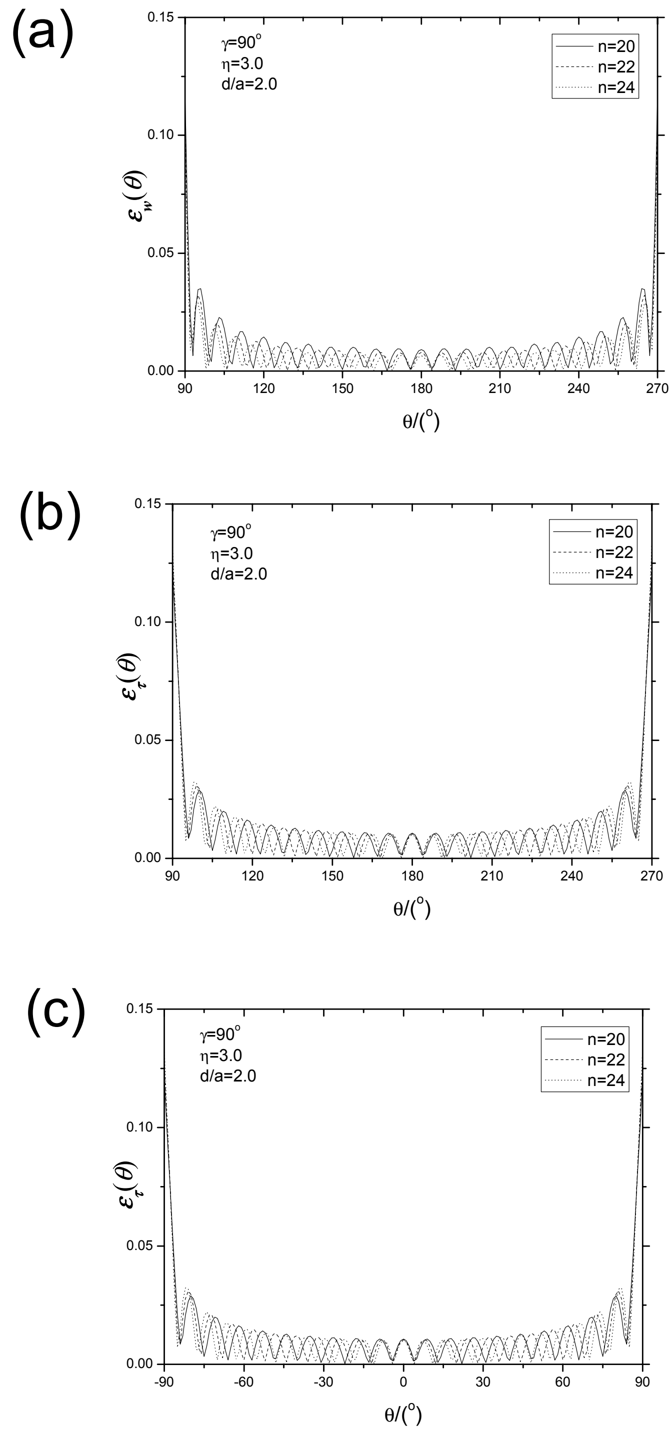

(a) Disp residue on $\underline{L}$ (b) Stress residue on $\underline{L}$ (c) Stress residue on $\overline{L}$

Fig. 6-12 RESIDUES FOR η=3 and d/a=2

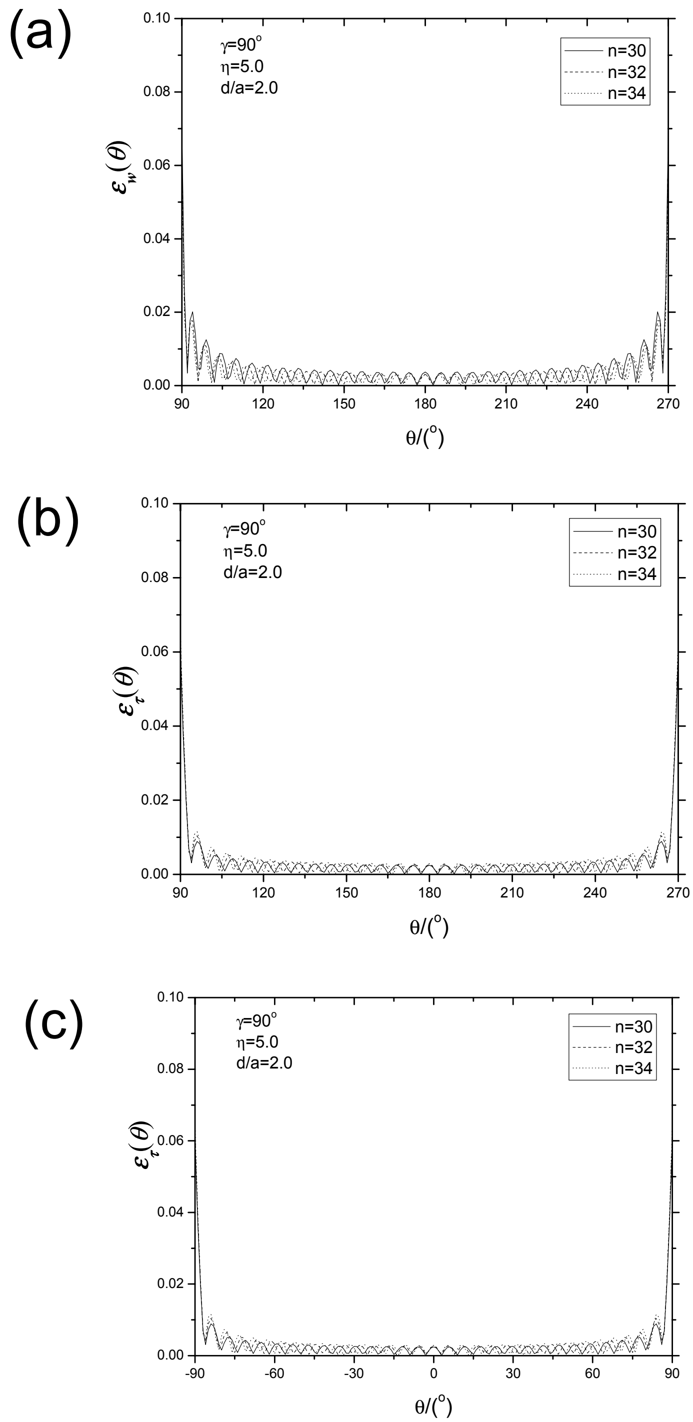

(a) Disp residue on $\underline{L}$ (b) Stress residue on $\underline{L}$ (c) Stress residue on $\overline{L}$

Fig. 6-13 RESIDUES FOR η=5 and d/a=2

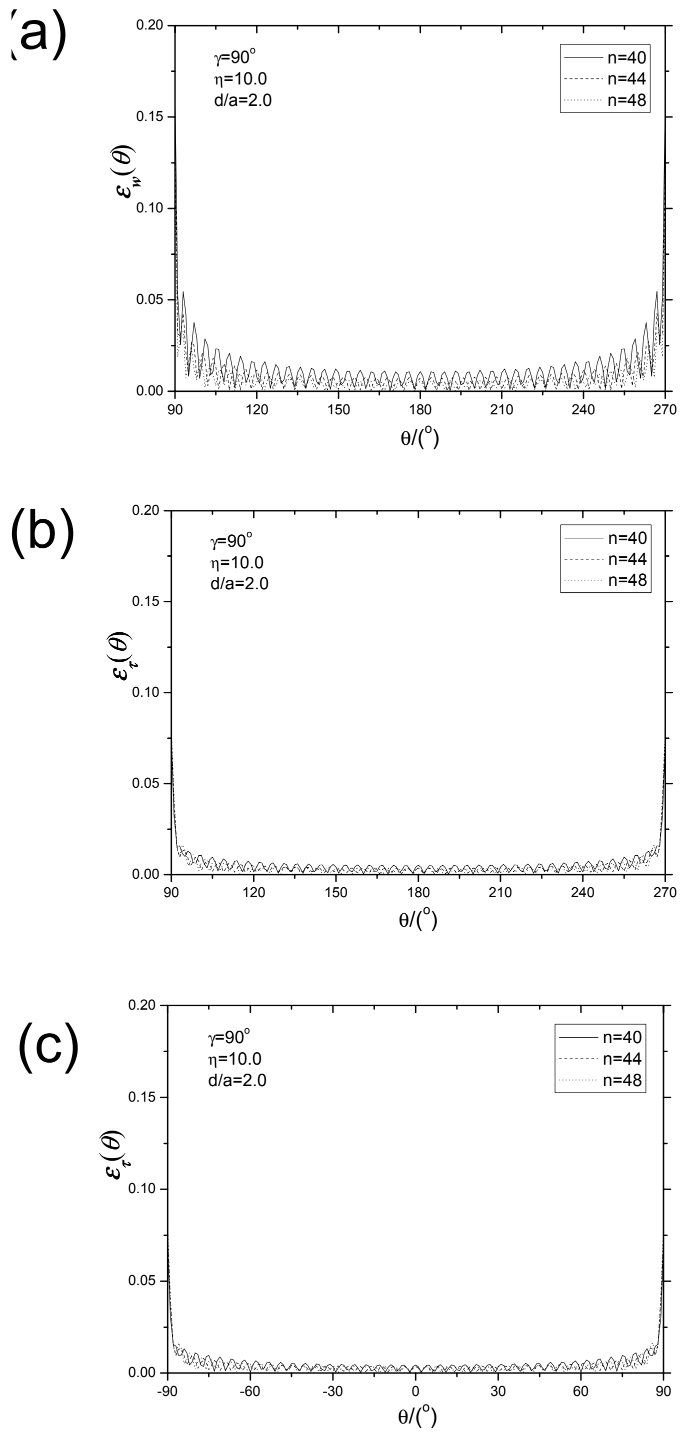

(a) Disp residue on $\underline{L}$ (b) Stress residue on $\underline{L}$ (c) Stress residue on $\overline{L}$

Fig. 6-14 RESIDUES FOR η=10 and d/a=**2**

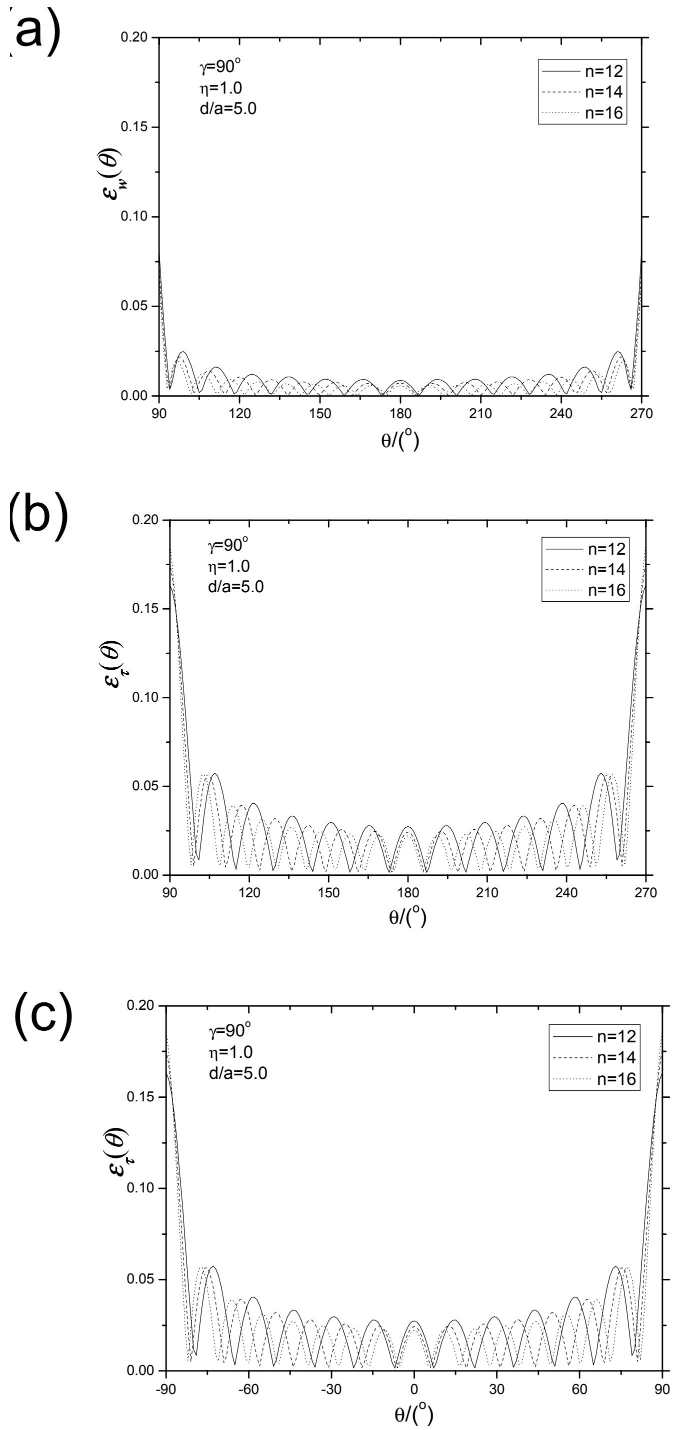

(a) Disp residue on $\underline{L}$ (b) Stress residue on $\underline{L}$ (c) Stress residue on $\overline{L}$

Fig. 6-15 RESIDUES FOR η=1 AND d/a=5

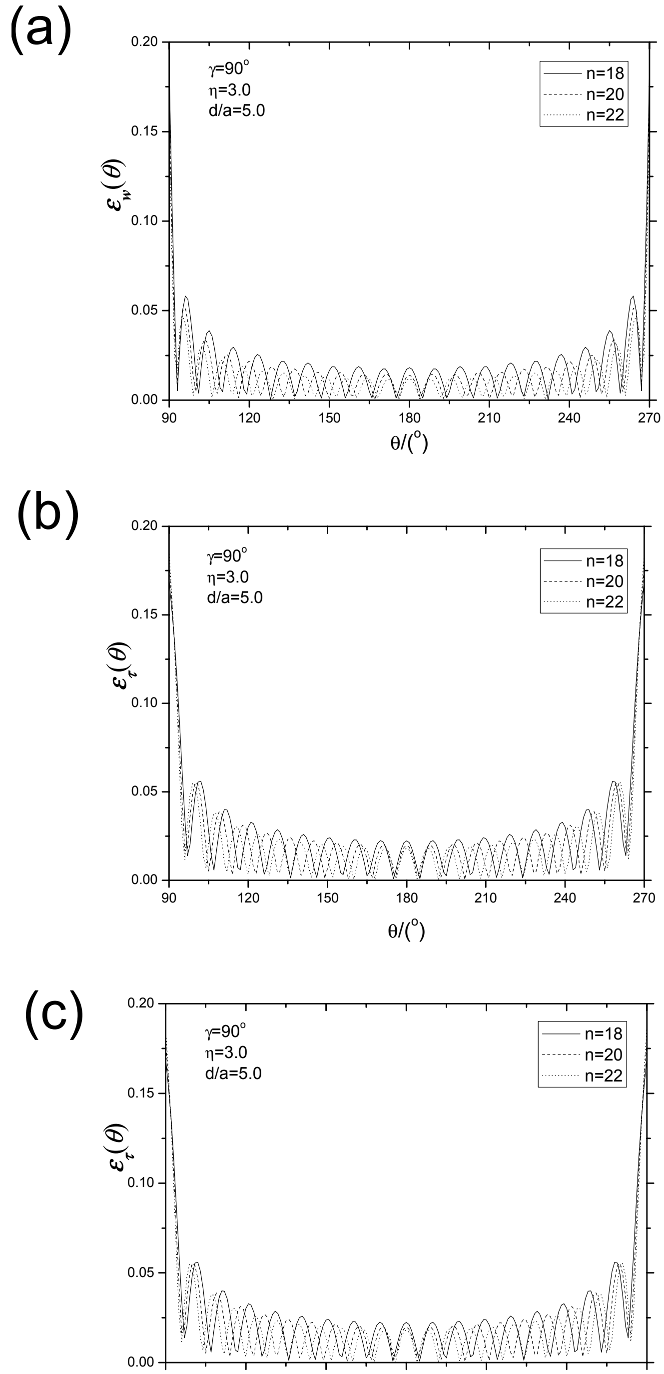

(a) Disp residue on $\underline{L}$ (b) Stress residue on $\underline{L}$ (c) Stress residue on $\overline{L}$

Fig. 6-16 RESIDUES FOR η=3 AND d/a=5

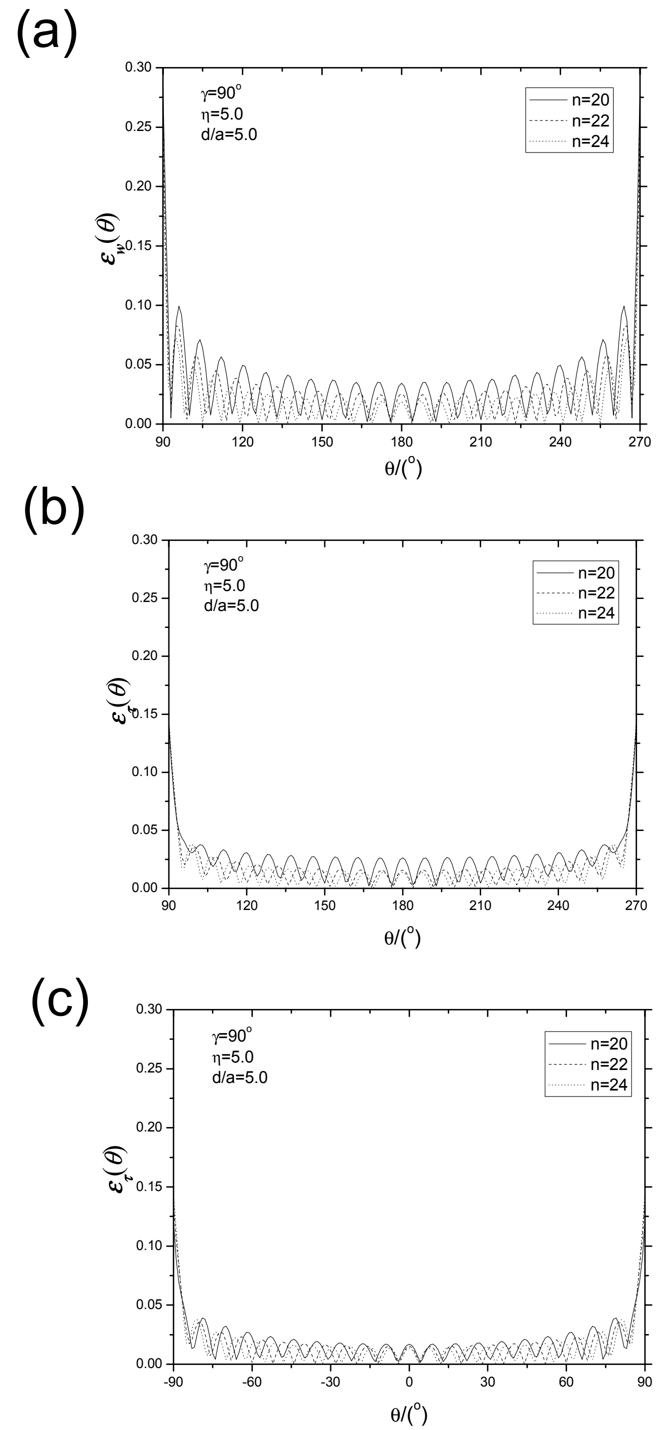

(a) Disp residue on $\underline{L}$ (b) Stress residue on $\underline{L}$ (c) Stress residue on $\overline{L}$

Fig. 6-17 RESIDUES FOR η=5 AND d/a=5

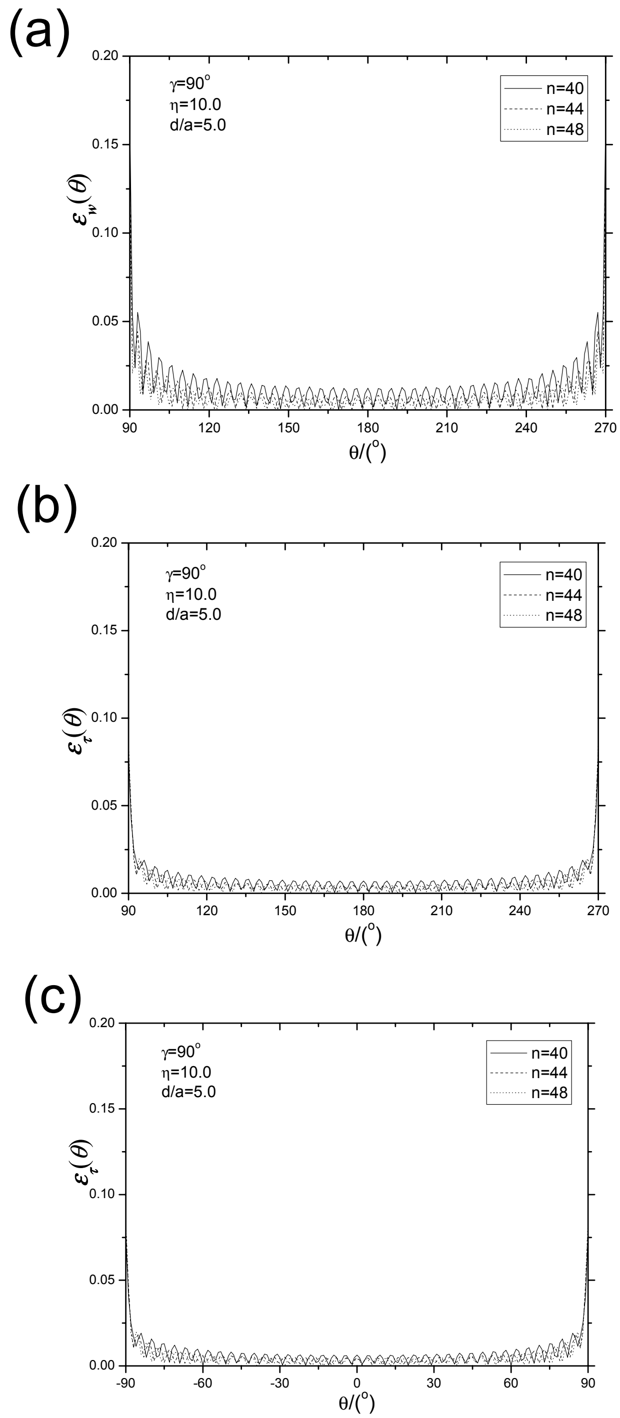

(a) Disp residue on $\underline{L}$ (b) Stress residue on $\underline{L}$ (c) Stress residue on $\overline{L}$

Fig. 6-18 RESIDUES FOR η=10 AND d/a=5

6.5.2 Ground Displacement Amplitudes

Dimensionless displacement amplitude is defined same as prevous chapters.

$$|w| = \left\{ \left[\mathrm{Re}(w) \right]^2 + \left[\mathrm{Im}(w) \right]^2 \right\}^{1/2} \qquad (r, \theta) \in \Gamma \tag{12.96}$$

Fig. 6-19 and Fig. 6-20 show the steady-state displacement response on the ground surface for different dimensionless frequency η=1, 3, 5, and 10, depth-width ratio d/a=2 or 5, and angles of incidence γ=90°, 60°, 30°, and 0°.

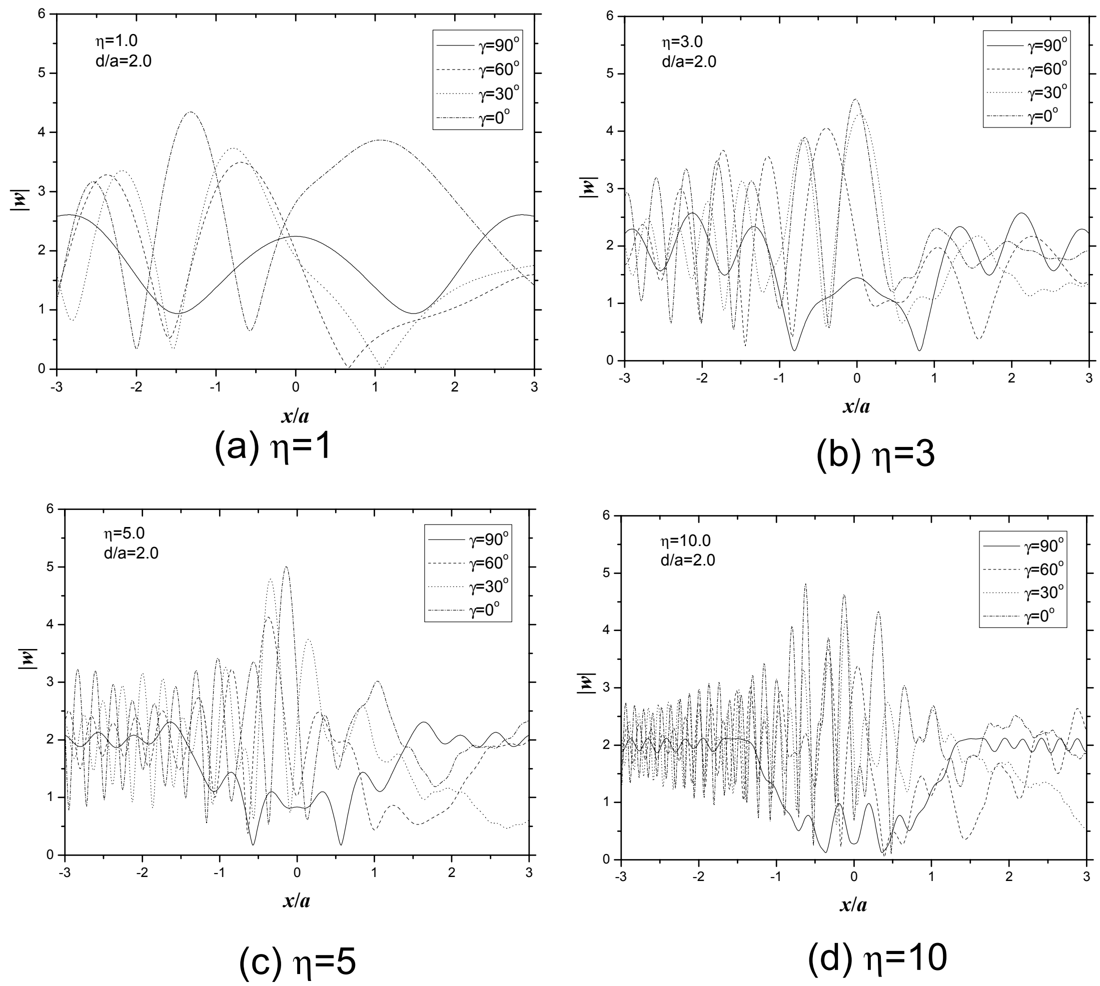

FIG. 6-19 GROUND DISPLACEMENT FOR η=1, 3, 5, 10, γ=90°, 60°, 30°, 0°, d/a=2.0

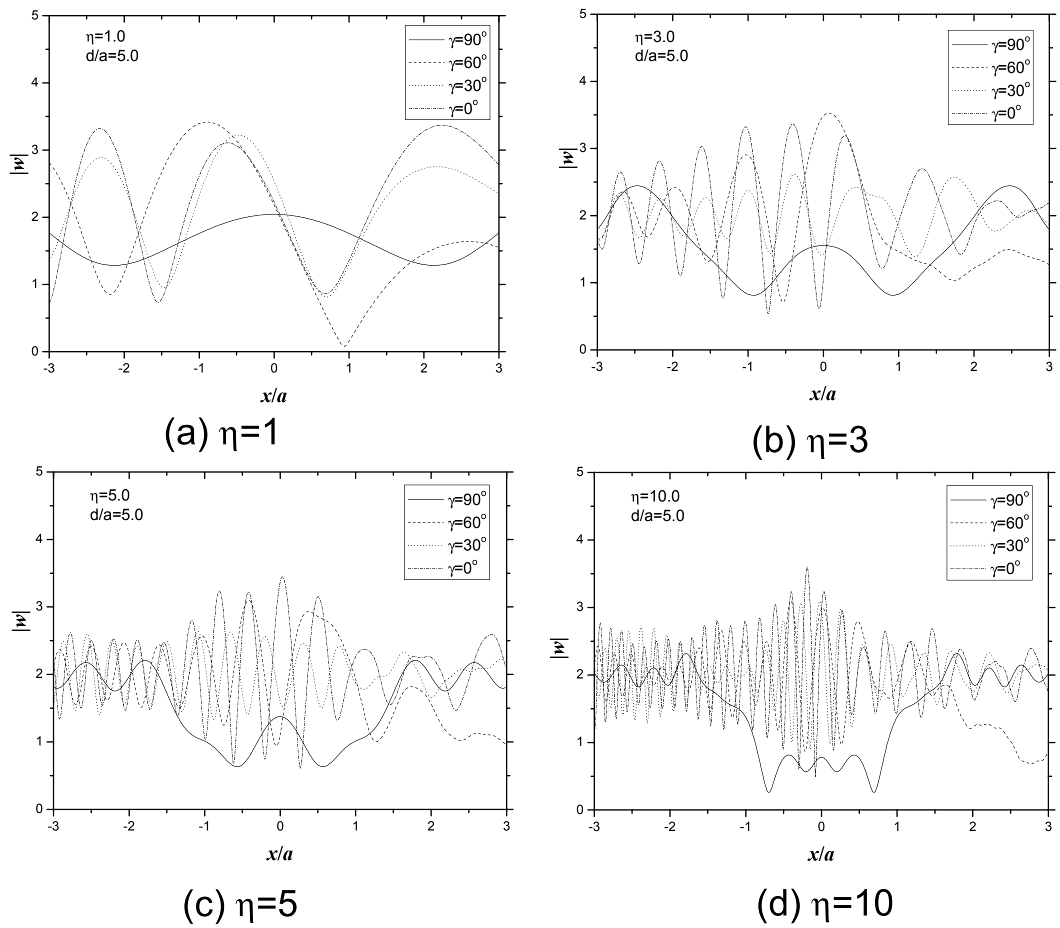

Fig. 6-20 GROUND DISPLACEMENT FOR η=1, 3, 5, 10, γ=90$^{\mathrm{O}}$, 60$^{\mathrm{O}}$, 30$^{\mathrm{O}}$, 0$^{\mathrm{O}}$, d/a=5.0

A deamplified region can be observed to be located right above the cavity for vertical incidecnce. At this case, the hollow semi-cylindrical cavity is functioned as a scatterer blocking the path of energy transfer. The width of this deamplified region becomes wider when d/a goes deeper.

6.5.3 Comparison of Displacement Amplitude Spectrum for Full- or Semi- Cylindrical Cavities at Three Points

This section discusses displacement amplitude in the frequency-domain. In the following figures 6-21 to 6-24, the range of frequency η is $(0,5]$, d/a equals 2 or 5, and only vertical ($\gamma = 90^{\circ}$) or grazing incidence ($\gamma = 0^{\circ}$) are considered. Two rims (left and right) and top point at the crown of the cavity are investigated (see Fig. 6-1 for details). Note that the incidence waves are coming from deep left as shown in Fig. 6-2.

For vertical incidence cases, the response of left and right rims must be identical because of the symmetry. For grazing incidence cases, the response at the left rim is amplified and, to the contrary, the response at the right rim is deamplified because the screening effect of the cavity.

Full- or semi- cylindrical cross-section have similar spectrum curve at the top point. For the two rim points, for vertical incidence cases, full-cylidrical cavity deserves similar but negligible more fluctuations. But for grazing incidence, the left rim of the full-cylindrical cavity has larger response than semi-cylindircal cavity's; and the right rim of the full-cylindrical cavity has smaller response than semi-cylindircal cavity's.

6.6 Conclusions

The objective of this section is originally to figure out why there are always overshoots at the two rims of stress or displacement residue figures (ex. Fig. 6-8~Fig. 6-9), the same phenomenon exists for the semi-circular or shallow hill model by auxiliary-function method. Those two rims should not have stress singularity since they are analogous to the vertexes of a wedge (Lee and Sherif, 1996) whose interior angle is 270o and this kind of points are proven to have explicit closed-form analytical solutions to stress and displacement for any interior angle (Sanchez-Sesma, 1985; MacDonald, 1902). Achenbach (1970) also pointed out that the stress is not singular for interior angles of wedge less than π but is singular for interior angles larger than π. So far, only the displacement residues are reduced to a tiny value (roughly valued 10-7) and uniform in the whole range (ex. Fig. 6-8), but stress residues still has problem. This result might prove the validity of Achenbach's conclusion to some extent.

(a)

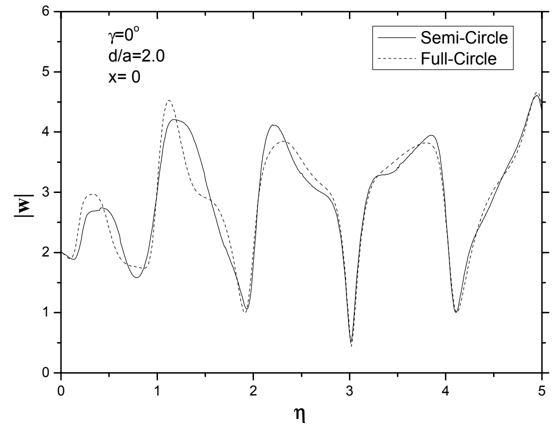

(b)

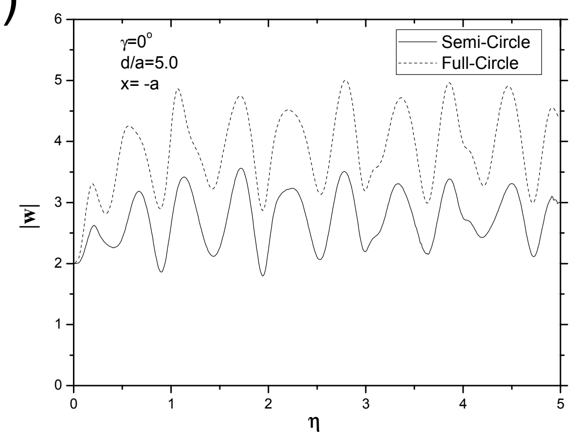

(c)

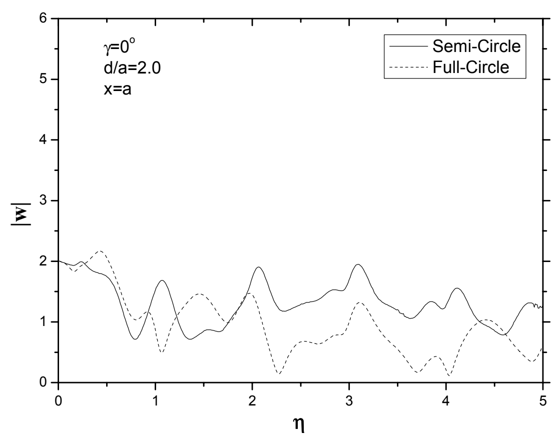

(a) top (b) left rim (c) right rim

Fig. 6-21 Disp Amp Spec for d/a = 2 and γ=0°

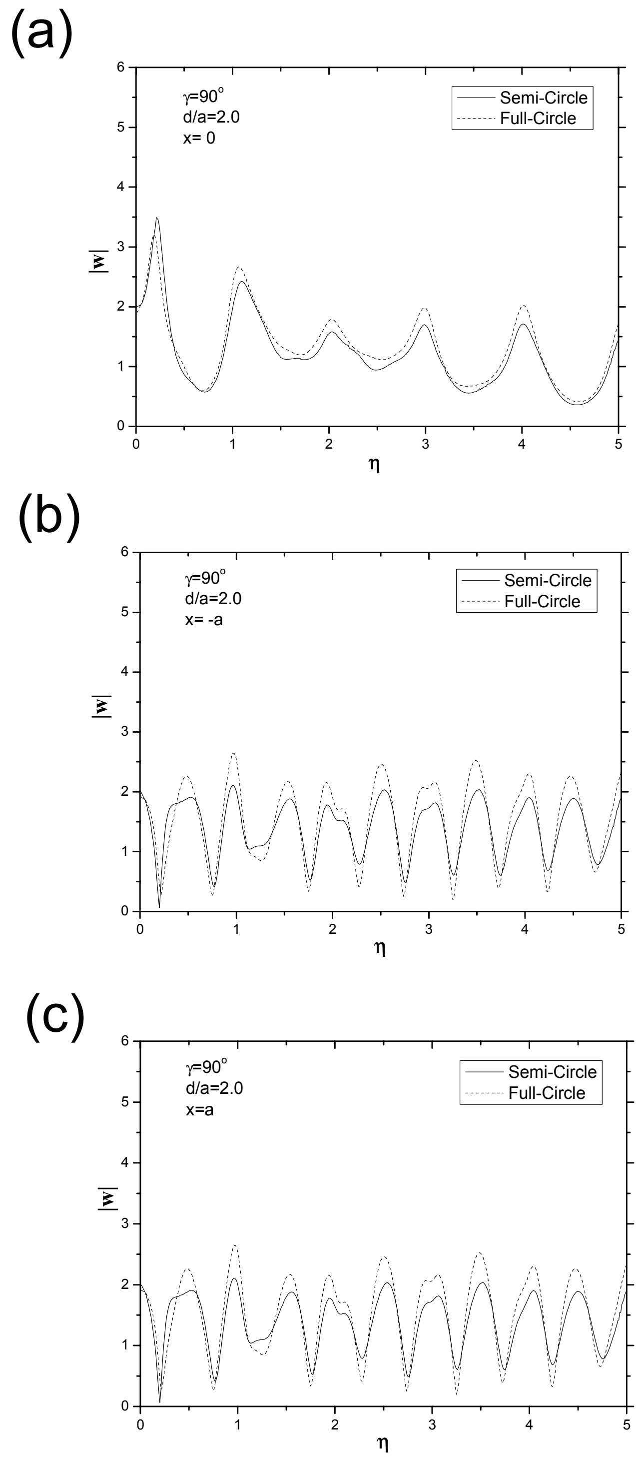

(a) top (b) left rim (c) right rim

Fig. 6-22 Disp Amp Spec for d/a = 2 and γ=90°

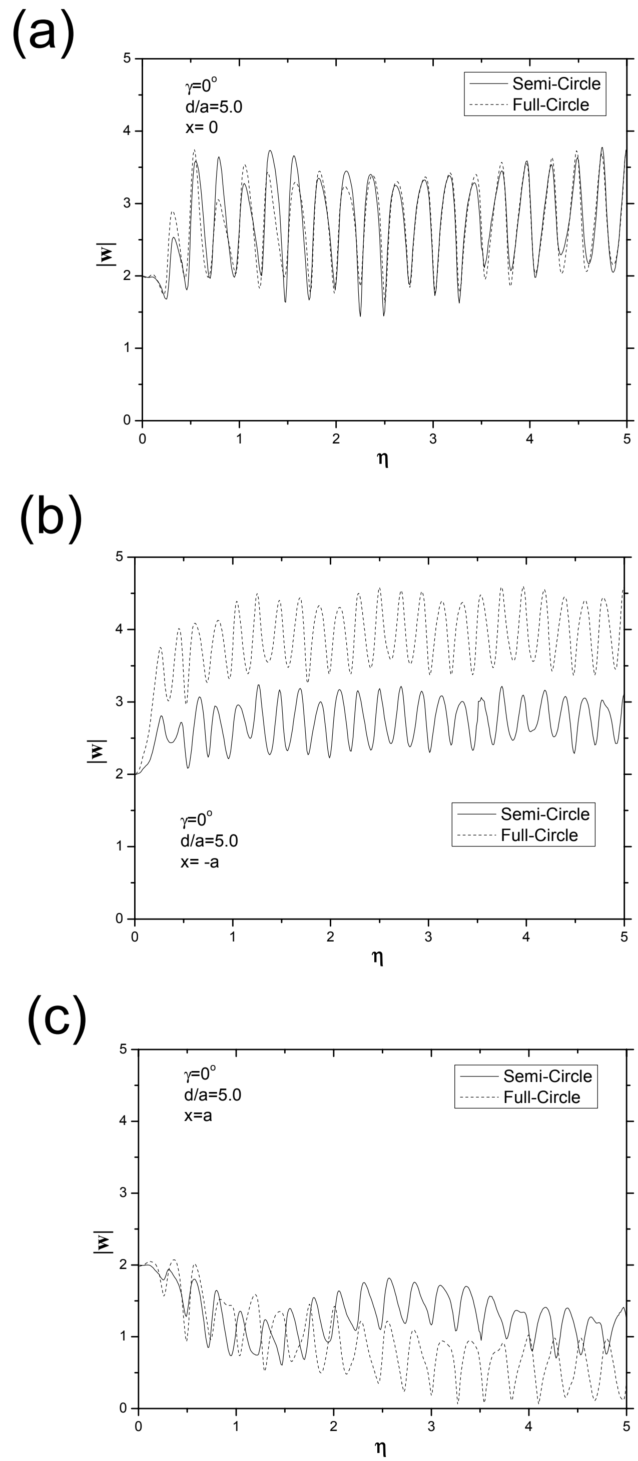

(a) top (b) left rim (c) right rim

Fig. 6-23 Disp Amp Spec for d/a = 5 and γ=0°

(a)

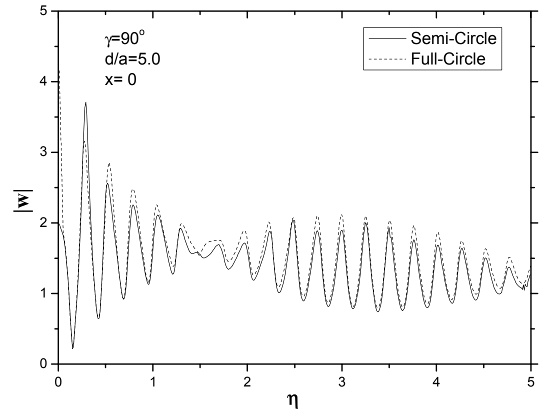

(b)

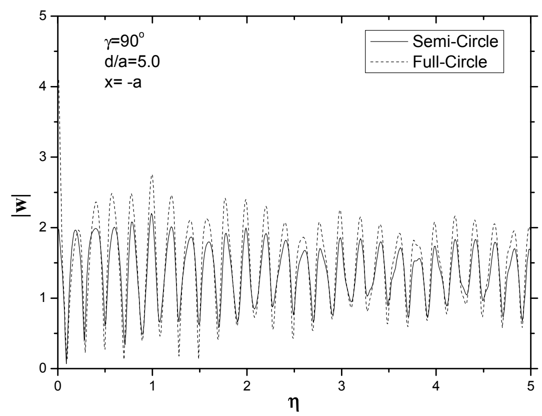

(c)

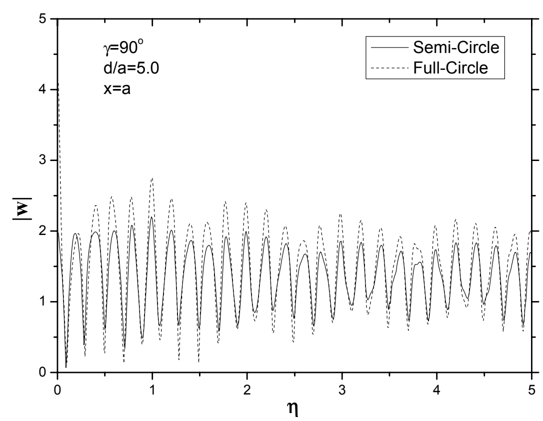

(a) top (b) left rim (c) right rim

Fig. 6-24 Disp Amp Spec for d/a = 5 and γ=90°

During research, we found that this model incorporates characters of both simplicity and complexity. To be simple, it could be thought of as an extension of full-circular cavity model; to be complex, it is featured by a mixed boundary (stress and displacement continuous boundary at one half; zero-stress boundary at the other half). That makes it ideal to be a benchmark model for mixed-boundary problems.

A variety of analytical methods are used to this model by authors: Image method, Large arc approximation (Lee and Cao, 1989), Auxiliary function method, Cosine half-range expansion, Chebyshev series expansion, and Discrete cosine transform. In those methods, the first two are regarding how to satisfy the traction-free boundary condition on the flat ground surface. Image method, which is adopted in this chapter, is an exact approach, not based on (physical) approximations such as large arc approximation. On the other hand, while large arc approximation is an approximation method, it has been widely used for solving half-space models subjected to incident P-, SV-, or Rayleigh waves (Lee and Cao, 1989; Cao and Lee, 1989,1990; Todorovska and Lee, 1990,1991; Lee and Karl, 1992,1993). Auxiliary function method, Cosine half-range expansion, Chebyshev series expansion and discrete Cosine transform are concerning the mathematical approaches on how to apply the mixed boundary conditions. Ideally, if all those methods are formulated correctly, similar results should be yielded by whichever method. However, comparisons show apparent difference for quite a few cases. More methods for mixed-boundary problems, either analytical or numerical, could be applied to this model and made comparisons to validate the correctness and accuracies of their results.

Chapter 7

SOIL-STRUCTURE INTERACTION:

A FOUNDATIONLESS SHEAR BEAM

The ensuing last four chapters deal with Soil-Structure Interaction (SSI) models. One of the earliest SSI model was proposed by Luco (1969). The structure is actually a single degree-of-freedom object on the basis of approximation that the semi-cylindrical foundation is rigid. An extensive study by Trifunac (1972) offers arbitrarily oblique incident angles to Luco's model as well as more detailed analysis on the mechanism of interaction. Wong and Trifunac (1974b) generalized this study further to elliptical cross-section foundation cases which accounts for either shallow or deep foundations depending on how the major and minor axis of the elliptical cross-section are placed. The interaction among adjacent multiple structures has also been studied by Wong and Trifunac (1975), with each of those buildings erecting on a rigid semi-circular foundation. Those solutions make up the existing analytical solutions of Soil-Structure Interaction for incident plane SH-waves to the author's knowledge.

All these solutions are based on a same assumption, the foundation is rigid. Todorovska et al (2001) provided a solution for a 2-D dike supported on a flexible segmental annulus foundation. For most of high-rise buildings, this rigid foundation assumption is true due to the relative flexibility of the superstructures; but as for enormous amount of single or low-rise buildings, this assumption will lose its effectiveness. The advantage of this assumption is it makes the boundary conditions of the superstructure, especially the interface of superstructure and foundation, become quite easy to be dealt with. On the other hand, the drawback of this assumption is that it results in the superstructure actually vibrates like a single degree-of-freedom pole. That makes few valuable conclusions on the dynamic response of the superstructure could be retrieved. In this chapter and Chapter 9, we put our stress on the response of superstructure by assuming nonexistence or flexibility of the foundations. Chapter 8 holds this rigid foundation assumption but extend the study of Trifunac (1972) from two-dimensional semicircular cross-section foundation to shallow circular-arc ones.

7.1 Mathematical Model and Wave Functions

The model studied in this chapter is an elastic rectangular shear beam (also referred as structure or building afterwards) placed directly on a homogeneous, perfectly elastic, and isotropic half-space without foundations, as depicted in Fig. 7-1. A bound of parallel harmonic incident SH-waves impinge on the model from the deep earth by angel γ with respect to the horizontal axis. The width and height of the wall are $2a$ and d, respectively. A Cartesian coordinate system has been set up with origin at the midpoint of the structure along its bottom interface Γ with the half-space. The Lamé constants of the wall and half-space are $\mu_{\mathrm{B}}, C_{\beta_{\mathrm{B}}}$ and μ, C_β, respectively.

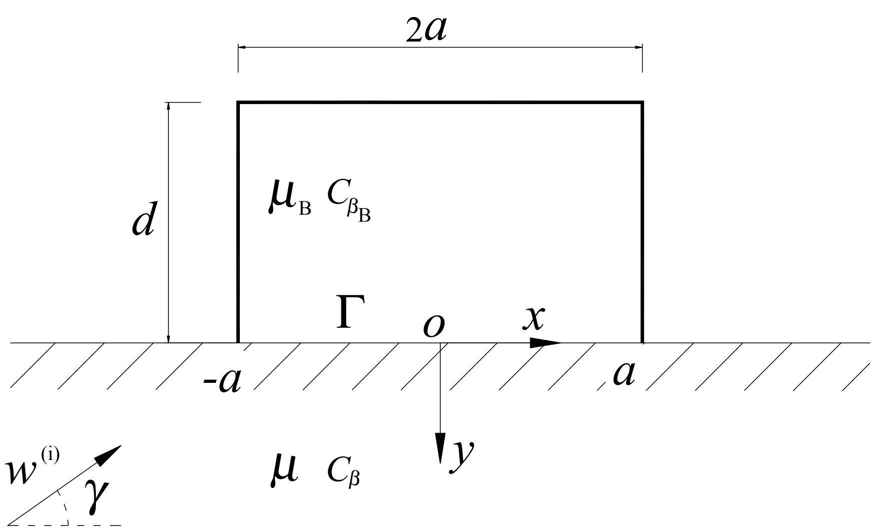

Fig. 7-1 A NON-FOUNDATION SHEAR BEAM MODEL

7.1.1 Wave field in the half-space

The incident and reflected waves could be written as follows

$$w^{(\mathrm{i})}(x, y)=\exp\left[\mathrm{i}\left(k_x x-k_y y\right)\right]=\exp\left[\mathrm{i}k_\beta\left(x\cos\gamma-y\sin\gamma\right)\right] \tag{13.1}$$

$$w^{(\mathrm{r})}(x, y)=\exp\left[\mathrm{i}\left(k_x x+k_y y\right)\right]=\exp\left[\mathrm{i}k_\beta\left(x\cos\gamma+y\sin\gamma\right)\right] \tag{13.2}$$

they comprise the free-field, where k_β represents wave number of half-space medium. The integral representation of scatted wave field due to the existence of the structure in the half-space is written as

$$w^{(\mathrm{S})}(x,y)=\frac{1}{2\pi}\int_{-\infty}^{\infty}W^{\mathrm{S}}(k)\exp(-\mathrm{i}kx+\mathrm{i}\zeta y)\,\mathrm{d}k \tag{13.3}$$

where, $k_x = k_\beta \cos\gamma$, $k_y = k_\beta \sin\gamma$, represent the components of k_β on the *x*- and *y*-axes, respectively. And,

$$\zeta=\sqrt{k_\beta^2-k^2} \tag{13.4}$$

$$W^{\mathrm{S}}(k)=\int_{-\infty}^{\infty}w^{\mathrm{S}}(x,0)\,\mathrm{e}^{\mathrm{i}kx}\mathrm{d}x \tag{13.5}$$

Equations (13.3) and (13.5) are the inverse and forward Fourier transforms, respectively.

7.1.2 Wave Field within the Flexible Shear beam

The total transmitted field within the structure could be represented with a summation of parallel-plate waveguide modes

$$w^{(\mathrm{B})}(x,y)=\sum_{m=0}^{\infty}B_m\cos\left[a_m(x+a)\right]\cos\left[\xi_m(y+d)\right] \tag{13.6}$$

where, for m = 0, 1, 2, …

$$\xi_m=\sqrt{k_{\mathrm{B}}^2-a_m^2} \tag{13.7}$$

$$a_m=\frac{m\pi}{2a} \tag{13.8}$$

7.1.3 Boundary Conditions

Traction-free boundary condition equations along the outer boundaries of the structure are

$$\mu_{\mathrm{B}}\frac{\partial w^{(\mathrm{B})}}{\partial x}=0 \quad \text{at} \quad x=\pm a,\ -d\le y\le 0 \tag{13.9}$$

$$\mu_{\mathrm{B}}\frac{\partial w^{(\mathrm{B})}}{\partial y}=0 \quad \text{at} \quad y=-d,\ -a\le x\le a \tag{13.10}$$

These two boundary conditions are satisfied automatically. For detail explanation please review APPENDIX C at the end of this dissertation.

The stress and displacement continuity equations at y = 0, $-a \le x \le a$ could be summarized as follows,

- Displacement continuity:

$$w^{\mathrm{i+r}} + w^{\mathrm{S}}\Big|_{y=0} = w^{\mathrm{B}}\Big|_{y=0},\ |x| \le a \tag{13.11}$$

- Stress continuity:

$$\mu \frac{\partial}{\partial y}\left(w^{\mathrm{i+r}} + w^{\mathrm{S}}\right)\Big|_{y=0} = \mu \frac{\partial w^{\mathrm{S}}}{\partial y}\Big|_{y=0} = \begin{cases} \mu_{\mathrm{B}} \dfrac{\partial w^{\mathrm{B}}}{\partial y}\Big|_{y=0} & , \quad |x| \le a \\ 0 & , \quad |x| > a \end{cases} \tag{13.12}$$

Then, after substituting Eq. (13.3) into Eq. (13.12), it is obtained that

$$\frac{\mathrm{i}\mu}{2\pi}\int_{-\infty}^{\infty} \zeta \cdot W^{\mathrm{S}}(k)\mathrm{e}^{-\mathrm{i}kx+\mathrm{i}\zeta y}\mathrm{d}k\Big|_{y=0} = \begin{cases} -\mu_{\mathrm{B}} \sum\limits_{m=0}^{\infty} \xi_m B_m \cos\left[a_m(x+a)\right]\sin\left[\xi_m(y+d)\right]\Big|_{y=0} & , \quad |x| \le a \\ 0 & , \quad |x| > a \end{cases}$$

. eliminate variable y by set it equal zero,

$$\frac{\mathrm{i}\mu}{2\pi}\int_{-\infty}^{\infty} \zeta \cdot W^{s}(k)\mathrm{e}^{-\mathrm{i}kx}\mathrm{d}k = \begin{cases} -\mu_{\mathrm{B}} \sum\limits_{m=0}^{\infty} \xi_m B_m \cos\left[a_m(x+a)\right]\sin\left(\xi_m d\right) & , \quad |x| \le a \\ 0 & , \quad |x| > a \end{cases}$$

Making forward Fourier transform on both sides of the above equation, we get

$$\mathrm{i}\mu\zeta W^{s}(k) = -\mu_{\mathrm{B}} \sum_{m=0}^{\infty} \xi_m B_m \sin\left(\xi_m d\right)\int_{-a}^{a} \cos\left[a_m(x+a)\right]\mathrm{e}^{\mathrm{i}kx}\mathrm{d}x$$

After integration (see Appendix A for details), we get

$$W^{\mathrm{S}}(k)=\frac{\mu_{\mathrm{B}}}{\mu\zeta}\sum_{m=0}^{\infty}\frac{\xi_m B_m \sin(\xi_m d)k}{k^2-(m\pi/2a)^2}\left[(-1)^m \mathrm{e}^{\mathrm{i}ka}-\mathrm{e}^{-\mathrm{i}ka}\right]$$

$$=\frac{\mu_{\mathrm{B}}}{\mu}\sum_{m=0}^{\infty}\frac{\xi_m B_m \sin(\xi_m d)}{\sqrt{k_\beta^2-k^2}}ka^2F_m(ka) \tag{13.13}$$

where,

$$F_m(ka)=\frac{(-1)^m \mathrm{e}^{\mathrm{i}ka}-\mathrm{e}^{-\mathrm{i}ka}}{(ka)^2-(m\pi/2)^2} \tag{13.14}$$

Substituting Eqns. (13.1) through (13.3) and Eq. (13.6) into displacement continuity boundary condition equation (13.11),

$$2\mathrm{e}^{\mathrm{i}k_\beta\cos\gamma x}+\frac{1}{2\pi}\int_{-\infty}^{\infty}W^s(k)\mathrm{e}^{-\mathrm{i}kx}\mathrm{d}k=\sum_{m=0}^{\infty}B_m\cos\left[\frac{m\pi}{2a}(x+a)\right]\cos(\xi_m d)$$

substituting Eq. (13.13) into the above equation,

$$2\mathrm{e}^{\mathrm{i}k_\beta\cos\gamma x}+\frac{\mu_{\mathrm{B}}}{2\pi\mu}\sum_{m=0}^{\infty}\xi_m B_m\sin(\xi_m d)\int_{-\infty}^{\infty}\frac{ka^2F_m(ka)\mathrm{e}^{-\mathrm{i}kx}}{\sqrt{k_\beta^2-k^2}}\mathrm{d}k=\sum_{m=0}^{\infty}B_m\cos\left[\frac{m\pi}{2a}(x+a)\right]\cos(\xi_m d)$$

To determine the coefficient B_m, we make $\int_{-a}^{a}(\bullet)\times\cos\left[a_n(x+a)\right]\mathrm{d}x$ on both sides of the above equation. Three terms of this equation were elaborated separately as below

- For the first term,

$$\int_{-a}^{a}2\mathrm{e}^{\mathrm{i}k_\beta\cos\gamma x}\cos\left[\frac{n\pi}{2a}(x+a)\right]\mathrm{d}x=2\int_{-a}^{a}\mathrm{e}^{\mathrm{i}k_x x}\cos\left[\frac{n\pi}{2a}(x+a)\right]\mathrm{d}x$$
$$=2\frac{(-1)^n\mathrm{e}^{\mathrm{i}k_x a}-\mathrm{e}^{-\mathrm{i}k_x a}}{k_x^2-(n\pi/2a)^2}(-k_x\mathrm{i})=-2\mathrm{i}k_x a^2F_n(k_x a)$$

- For the second term,

$$\frac{\mu_{\mathrm{B}}}{2\pi\mu}\sum_{m=0}^{\infty}\xi_m B_m \sin\left(\xi_m d\right)\cdot\int_{-\infty}^{\infty}\frac{ka^2 F_m\left(ka\right)}{\sqrt{k_\beta^2-k^2}}\left\{\int_{-a}^{a}\cos\left[a_n\left(x+a\right)\right]\mathrm{e}^{-\mathrm{i}kx}\mathrm{d}x\right\}\mathrm{d}k$$

$$=\frac{\mathrm{i}\mu_{\mathrm{B}}}{2\pi\mu}\sum_{m=0}^{\infty}\xi_m B_m \sin\left(\xi_m d\right)\int_{-\infty}^{\infty}\frac{\left(ka\right)^2 F_m\left(ka\right)}{\sqrt{k_\beta^2-k^2}}\frac{\left[(-1)^n\,\mathrm{e}^{-\mathrm{i}ka}-\mathrm{e}^{\mathrm{i}ka}\right]}{\left[\left(ka\right)^2-\left(n\pi/2\right)^2\right]}\mathrm{d}k$$

$$=\frac{\mathrm{i}\mu_{\mathrm{B}}}{2\pi\mu}\sum_{m=0}^{\infty}\xi_m B_m \sin\left(\xi_m d\right)\int_{-\infty}^{\infty}\frac{\left(ka\right)^2 F_m\left(ka\right)}{\sqrt{k_\beta^2-k^2}}F_n\left(-ka\right)a^2\mathrm{d}k=\frac{\mathrm{i}\mu_{\mathrm{B}}}{2\pi\mu}\sum_{m=0}^{\infty}\xi_m B_m \sin\left(\xi_m d\right)I_{mn}a^2$$

where,

$$I_{mn}=\int_{-\infty}^{\infty}\frac{\left(ka\right)^2}{\sqrt{k_\beta^2-k^2}}F_m\left(ka\right)F_n\left(-ka\right)\mathrm{d}k \tag{13.15}$$

Please refer to Appendix B for the evaluation of I_{mn}.

- For the third term,

$$\sum_{m=0}^{\infty}B_m\cos\left(\xi_m d\right)\int_{-a}^{a}\cos\left[\frac{m\pi}{2a}\left(x+a\right)\right]\cos\left[\frac{n\pi}{2a}\left(x+a\right)\right]\mathrm{d}x=\varepsilon_m aB_m\cos\left(\xi_m d\right)=\varepsilon_n aB_n\cos\left(\xi_n d\right)$$

in which, $\varepsilon_0=2$, $\varepsilon_n=1$, (n = 1, 2, 3, …), and

$$\int_{-a}^{a}\cos\left[\frac{m\pi}{2a}\left(x+a\right)\right]\cos\left[\frac{n\pi}{2a}\left(x+a\right)\right]\mathrm{d}x=\begin{cases}0 & , \quad m\neq n\\ a & , \quad m=n\neq 0\\ 2a & , \quad m=n=0\end{cases}$$

based on the orthogonality of trigonometric functions.

In conclusion, Eq. (13.11) could be derived as,

$$-2\mathrm{i}k_x a^2 F_n\left(k_x a\right)+\frac{\mathrm{i}\mu_{\mathrm{B}}}{2\pi\mu}\sum_{m=0}^{\infty}\xi_m B_m\sin\left(\xi_m d\right)I_{mn}a^2=\varepsilon_n aB_n\cos\left(\xi_n d\right)$$

Moving the terms including unknown B_m to the left side,

$$\frac{\mathrm{i}\mu_{\mathrm{B}}}{2\pi\mu}\sum_{m=0}^{\infty}\xi_m \sin\left(\xi_m d\right) I_{mn} a B_m - \varepsilon_n \cos\left(\xi_n d\right) B_n = 2\mathrm{i}k_x a F_n\left(k_x a\right) \tag{13.16}$$

in which, n = 0, 1, 2, 3, …

Eqn. (13.16) could also be further simplified to the following infinite linear equation,

$$\sum_{m=0}^{\infty}\left[CB_{nm}\right]\left\{B_m\right\} = \left[BR_n\right] \tag*{(13.16)*}$$

in which,

$$CB_{nm} = \frac{\mathrm{i}a\mu_{\mathrm{B}}}{2\pi\mu}\xi_m \sin\left(\xi_m d\right) I_{nm} - \delta_{nm}\varepsilon_n \cos\left(\xi_n d\right) \tag{13.17}$$

$$BR_n = 2\mathrm{i}k_x a F_n\left(k_x a\right) \tag{13.18}$$

and δ_{mn} is the Kronecker Delta,

$$\delta_{mn} = \begin{cases} 1 & \text{for} \quad m = n \\ 0 & \text{for} \quad m \neq n \end{cases} \tag{13.19}$$

Note that for vertical incidence cases, i.e., when γ=90°, k_x=0, the RHS of (13.16)* must be a zero vector. After truncation of this infinite simultaneous linear equation, a series of coefficients B_m could be obtained.

7.2 Numerical Computation of Displacement Amplitudes

After solving the infinite linear equations (13.16), we can substitute the set of B_n (n = 1, 2, 3, …) into Eqn. (13.13) and get the $W^{\mathrm{S}}\left(k\right)$. Then plugging $W^{\mathrm{S}}\left(k\right)$ into Eqn.(13.3), namely taking the inverse Fourier transform on $W^{\mathrm{S}}\left(k\right)$, the expression of scattered field should be,

$$w^{(\mathrm{S})}(x,y)=\frac{1}{2\pi}\int_{-\infty}^{\infty}W^{\mathrm{S}}\left(k\right)\cdot\exp\left(-\mathrm{i}kx+\mathrm{i}\zeta y\right)\mathrm{d}k$$
$$=\frac{\mu_{\mathrm{B}}}{2\pi\mu}\sum_{m=0}^{\infty}B_m\xi_m\sin\left(\xi_m d\right)\int_{-\infty}^{\infty}\frac{ka^2F_m\left(ka\right)}{\sqrt{k_\beta^2-k^2}}\exp\left(-\mathrm{i}kx+\mathrm{i}\zeta y\right)\mathrm{d}k \tag{13.20}$$
$$=\frac{\mu_{\mathrm{B}}}{2\pi\mu}\sum_{m=0}^{\infty}B_m\xi_m\sin\left(\xi_m d\right)\int_{-\infty}^{\infty}\frac{\left(-1\right)^m\mathrm{e}^{\mathrm{i}ka}-\mathrm{e}^{-\mathrm{i}ka}}{\left(k^2-a_m^2\right)\zeta}k\exp\left(-\mathrm{i}kx+\mathrm{i}\zeta y\right)\mathrm{d}k$$

This equation should be applicable to evaluate either near-zone and/or far-zone scattered field. To the earthquake engineering's interest, we want to find the displacement field on the verge of this model, i.e., the left and right sides, and the top of the structure, associated with the flat ground surface in the neighborhood of this structure.

Park et al (1993) used a simplified method, "Stationary phase approximation (Graf, 1975)", on the basis of supposed self-cancelling oscillations of the integrand away from critical points, could be used to derive a simple asymptotic expansion expression of far-zone scattered field under the polar coordinate system $\left(r,\theta_s\right)$ as follows (here $\theta_s=\arcsin\left(x/r\right)$, $r=\sqrt{x^2+y^2}$)

$$w^{\mathrm{S}}\left(r,\theta_s\right)=\sqrt{k_\beta/2\pi r}\exp\left[\mathrm{i}\left(k_\beta r-\pi/4\right)\right]\cos\theta_s\cdot W^{\mathrm{S}}\left(-k_\beta\sin\theta_s\right)$$

$$=\sqrt{\frac{k_\beta}{2\pi r}}\exp\left[\mathrm{i}\left(k_\beta r-\frac{\pi}{4}\right)\right]\frac{\mu_{\mathrm{B}}\cos\theta_s}{\mu\sqrt{k_\beta^2-k_\beta^2\sin^2\theta_s}}\sum_{m=0}^{\infty}\frac{\left(-1\right)^m\exp\left(-\mathrm{i}k_\beta a\sin\theta_s\right)-\exp\left(\mathrm{i}k_\beta a\sin\theta_s\right)}{\left(k_\beta\sin\theta_s\right)^2-a_m^2}B_m\xi_m\sin\left(\xi_m d\right)\left(-k_\beta\sin\theta_s\right)$$

$$=-\sqrt{\frac{k_\beta}{2\pi r}}\exp\left[\mathrm{i}\left(k_\beta r-\frac{\pi}{4}\right)\right]\frac{\mu_{\mathrm{B}}}{\mu}\sin\theta_s\sum_{m=0}^{\infty}B_m\xi_m\sin\left(\xi_m d\right)\frac{\left(-1\right)^m\exp\left(-\mathrm{i}k_\beta a\sin\theta_s\right)-\exp\left(\mathrm{i}k_\beta a\sin\theta_s\right)}{\left(k_\beta\sin\theta_s\right)^2-a_m^2}$$

$$=-a^2\sqrt{\frac{k_\beta}{2\pi r}}\exp\left[\mathrm{i}\left(k_\beta r-\frac{\pi}{4}\right)\right]\frac{\mu_{\mathrm{B}}}{\mu}\sin\theta_s\sum_{m=0}^{\infty}B_m\xi_m\sin\left(\xi_m d\right)F_m\left(-k_\beta a\sin\theta_s\right) \tag{13.21}$$

In principle, equation (13.21) is an asymptotic expansion of Fourier integral in equation (13.20). It approaches the accurate solution of equation (13.20) when r approaches infinity. Thus this equation could be used to evaluate far-zone scattered field for different cases. However, we could not find how to determine whether this approximation is applicable for a specific r in relevant literatures. The only thing we know is that, the wave field calculated by this method must not be applied in the region fairly close to the structure; however, unfortunately, near-zone is exactly what we are interested in. Therefore, for our interested region, the solution by this method could only be taken as an approximate and reference solution to the accurate solution.

In order to find this "accurate solution", the Fourier integral in equation (13.20) has to be evaluated first. Because of the complexity of the integrand, it could only be computed numerically. The detail analysis and attempt are presented as follow.

Since we only have interest in the displacement amplitudes on the ground surface, we could just set y in the integral formula equal zero. Thus equation (13.20) could be rewritten as

$$w^s\left(x,0\right)=\frac{\mu_{\mathrm{B}}}{2\pi\mu}\sum_{m=0}^{\infty}B_m\xi_m\sin\left(\xi_m d\right)T\left(m,x\right) \tag{13.22}$$

in which,

$$T\left(m,x\right)=\int_{-\infty}^{\infty}R\left(m,k\right)\exp\left(-\mathrm{i}kx\right)\mathrm{d}k \tag{13.23}$$

$$R\left(m,k\right)=\frac{\left(-1\right)^m\mathrm{e}^{\mathrm{i}ka}-\mathrm{e}^{-\mathrm{i}ka}}{\left(k^2-a_m^2\right)\sqrt{k_\beta^2-k^2}}k=\frac{ka^2F_m\left(ka\right)}{\sqrt{k_\beta^2-k^2}} \tag{13.24}$$

Since $\int_{-\infty}^{\infty}f(x)\mathrm{d}x=\int_0^{\infty}\left[f(x)+f(-x)\right]\mathrm{d}x$, we could expand eqn (13.23) in the half-infinite interval as

$$\begin{aligned}T\left(m,x\right)&=\int_0^{\infty}\left[R\left(m,k\right)\exp\left(-\mathrm{i}kx\right)+R\left(m,-k\right)\exp\left(\mathrm{i}kx\right)\right]\mathrm{d}k\\&=\int_0^{\infty}R1\left(m,k\right)\cos\left(kx\right)\mathrm{d}k+\mathrm{i}\cdot\int_0^{\infty}R2\left(m,k\right)\sin\left(kx\right)\mathrm{d}k\end{aligned} \tag{13.25}$$

where,

$$R1\left(m,k\right)=R\left(m,-k\right)+R\left(m,k\right) \tag{13.26}$$

$$R2(m,k) = R(m,-k) - R(m,k) \tag{13.27}$$

Deriving the above two equations further by Euler formula,

$$R1(m,k) = \frac{2\mathrm{i}\sin(ka)\left[(-1)^m + 1\right]k}{\left(k^2 - a_m^2\right)\sqrt{k_\beta^2 - k^2}} = \begin{cases} \dfrac{4\mathrm{i}\sin(ka)k}{\left(k^2 - a_m^2\right)\sqrt{k_\beta^2 - k^2}}, & m \text{ even} \\ 0 & , m \text{ odd} \end{cases} \tag{13.28}$$

$$R2(m,k) = \frac{2\cos(ka)\left[1 - (-1)^m\right]k}{\left(k^2 - a_m^2\right)\sqrt{k_\beta^2 - k^2}} = \begin{cases} 0 & , m \text{ even} \\ \dfrac{4\cos(ka)k}{\left(k^2 - a_m^2\right)\sqrt{k_\beta^2 - k^2}}, & m \text{ odd} \end{cases} \tag{13.29}$$

To simplify the integrand of (13.25) from complex to real, we split equations (13.28) and (13.29) into two sets of cases that k larger or less than k_β,

◎ If $k_\beta > k$,

- When *m* are even,

$$\left\{ \begin{array}{c} R1(m,k) = \dfrac{4k\sin(ka)}{\left(k^2 - a_m^2\right)\sqrt{k_\beta^2 - k^2}}\mathrm{i} \\ R2(m,k) = 0 \end{array} \right\} \Rightarrow \quad T(m,x) = \mathrm{i}\int_?^? \frac{4k\sin(ka)}{\left(k^2 - a_m^2\right)\sqrt{k_\beta^2 - k^2}}\cos(xk)\,\mathrm{d}k$$

- When *m* are odd,

$$\left\{ \begin{array}{c} R1(m,k) = 0 \\ R2(m,k) = \dfrac{4k\cos(ka)}{\left(k^2 - a_m^2\right)\sqrt{k_\beta^2 - k^2}} \end{array} \right\} \Rightarrow \quad T(m,x) = \mathrm{i}\int_?^? \frac{4k\cos(ka)}{\left(k^2 - a_m^2\right)\sqrt{k_\beta^2 - k^2}}\sin(xk)\,\mathrm{d}k$$

◎ Else if $k > k_\beta$,

- When *m* are even,

$$\left\{\begin{matrix} R1(m,k)=\dfrac{4k\sin(ka)}{\left(k^2-a_m^2\right)\sqrt{k^2-k_\beta^2}} \\ R2(m,k)=0 \end{matrix}\right\} \Rightarrow \quad T(m,x)=\int_?^? \frac{4k\sin(ka)}{\left(k^2-a_m^2\right)\sqrt{k^2-k_\beta^2}}\cos(xk)\,\mathrm{d}k$$

- When m are odd,

$$\left\{\begin{matrix} R1(m,k)=0 \\ R2(m,k)=\dfrac{-4\mathrm{i}k\cos(ka)}{\left(k^2-a_m^2\right)\sqrt{k^2-k_\beta^2}} \end{matrix}\right\} \Rightarrow \quad T(m,x)=\int_?^? \frac{4k\cos(ka)}{\left(k^2-a_m^2\right)\sqrt{k^2-k_\beta^2}}\sin(xk)\,\mathrm{d}k$$

 Else if $k_\beta = k$,

- Singularities of this integral

 End if

Thus, integration (13.25) could be derived as,

· When m are even,

$$T(m,x)=\int_0^\infty R1(m,k)\cos(xk)\,\mathrm{d}k=\int_0^{k_\beta} R1(m,k)\cos(xk)\,\mathrm{d}k+\int_{k_\beta}^\infty R1(m,k)\cos(xk)\,\mathrm{d}k$$

$$=\mathrm{i}\int_0^{k_\beta}\frac{4k\sin(ak)}{\left(k^2-a_m^2\right)\sqrt{k_\beta^2-k^2}}\cos(xk)\,\mathrm{d}k+\int_{k_\beta}^\infty\frac{4k\sin(ak)}{\left(k^2-a_m^2\right)\sqrt{k^2-k_\beta^2}}\cos(xk)\,\mathrm{d}k \quad (13.30)$$

· When m are odd,

$$T(m,x)=\mathrm{i}\int_0^\infty R2(m,k)\sin(xk)\,\mathrm{d}k=\mathrm{i}\int_0^{k_\beta} R2(m,k)\sin(xk)\,\mathrm{d}k+\mathrm{i}\int_{k_\beta}^\infty R2(m,k)\sin(xk)\,\mathrm{d}k$$

$$=\mathrm{i}\int_0^{k_\beta}\frac{4k\cos(ak)}{\left(k^2-a_m^2\right)\sqrt{k_\beta^2-k^2}}\sin(xk)\,\mathrm{d}k+\int_{k_\beta}^\infty\frac{4k\cos(ak)}{\left(k^2-a_m^2\right)\sqrt{k^2-k_\beta^2}}\sin(xk)\,\mathrm{d}k \quad (13.31)$$

Then, after combining the sine and cosine terms in the above two equations, we could conclude the integral (13.25) further briefly as follows,

$$T\left(m,x\right)=\mathrm{Re}\left(T\right)+\mathrm{i}\cdot\mathrm{Im}\left(T\right) \tag{13.32}$$

where $\mathrm{Re}\left(T\right)$ and $\mathrm{Im}\left(T\right)$ denote the real and imaginary part of integral $T\left(m,x\right)$, and,

$$\mathrm{Re}\left(T\right)=\begin{cases} IRP+IRM\,, & m \text{ even} \\ IRP-IRM\,, & m \text{ odd} \end{cases} \tag{13.33}$$

$$\mathrm{Im}\left(T\right)=\begin{cases} IIP+IIM\,, & m \text{ even} \\ IIP-IIM\,, & m \text{ odd} \end{cases} \tag{13.34}$$

, together with,

$$IRP=\int_{k_\beta}^{\infty}\frac{2k\sin\left[\left(a+x\right)k\right]}{\left(k^2-a_m^2\right)\sqrt{k^2-k_\beta^2}}\mathrm{d}k \tag{13.35}$$

$$IRM=\int_{k_\beta}^{\infty}\frac{2k\sin\left[\left(a-x\right)k\right]}{\left(k^2-a_m^2\right)\sqrt{k^2-k_\beta^2}}\mathrm{d}k \tag{13.36}$$

$$IIP=\int_{0}^{k_\beta}\frac{2k\sin\left[\left(a+x\right)k\right]}{\left(k^2-a_m^2\right)\sqrt{k_\beta^2-k^2}}\mathrm{d}k \tag{13.37}$$

$$IIM=\int_{0}^{k_\beta}\frac{2k\sin\left[\left(a-x\right)k\right]}{\left(k^2-a_m^2\right)\sqrt{k_\beta^2-k^2}}\mathrm{d}k \tag{13.38}$$

From equation (13.23) all along to (13.32), we separate the complex integrand of equation (13.23) into its real and imaginary parts. All four integrals from equation (13.35) through (13.38) are univariate integrals with real integrands and integration variables within their respective intervals. They are all of the form

$$\tilde{f}\left(\omega\right)=\int_{a}^{b\text{ or }+\infty}f\left(x\right)\sin\left(\omega x\right)\mathrm{d}x \tag{13.39}$$

which is a standard Fourier sine transform and ω is the oscillatory factor which determines the oscillation level. a and b are finite constants. Nevertheless, due to the co-existence of oscillator sine functions and singularities at $k = k_\beta$ and a_m, those four improper integrals are still hard to be numerically computed directly. By depicting the integrand functions within each integration interval in Fig. 7-2, we can tell those two integrands (Eqns. (13.35) and (13.36)) are slowly converging and highly oscillatory. The input parameters are $k_\beta = 4.5$, $a = 1$, $x = -2$, $m = 2$, and $a_m = \pi$.

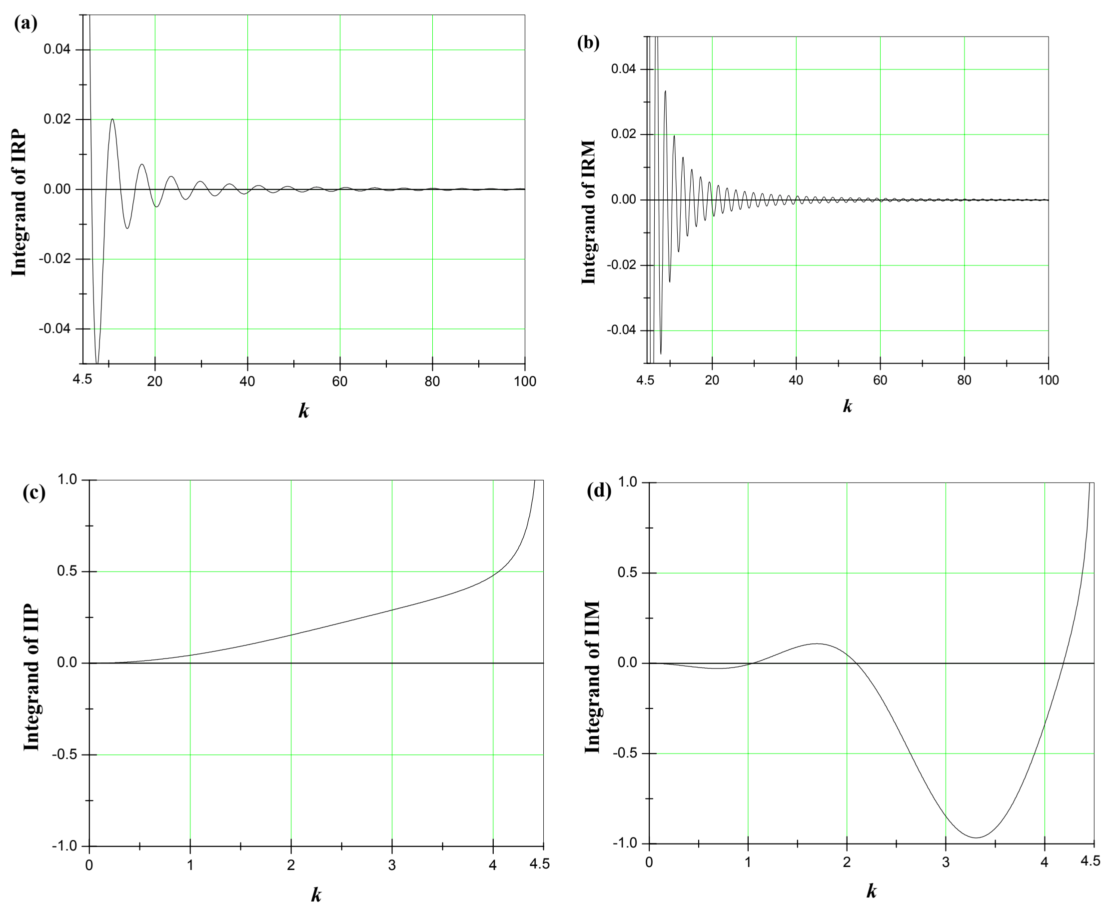

Fig. 7-2 INTEGRAND DIAGRAMS OF FOUR INTEGRATIONS (13.35) THROUGH (13.38)

For the sake of making the converging trend of curves more clearly, the vertical axes of Fig. 7-2 has been limited to a relatively low value. In fact, the curve segments in the neighborhood of $k = k_\beta$ are far out of these limitations. We can see that the singularity $k = a_m$ (equals π for this case) is not noticeable; however, the other singularity $k = k_\beta$ really is. Fortunately this singularity is of apparent (removable) type. That is the other reason why we split the interval at this singular point, since numerical end-point correction techniques of QUADPACK routines could also be applied to this singularity.

Thus, singularity $k = k_\beta$ has to be removed first. We adopt the same method as (Ghosh 1995), in which first the singular point is isolated by a small region, and then the singularity within this region is removed by variable replacement. According to our trial calculation, numerical integration on Eqns. (13.35) through (13.38) will evoke the displacement result oscillating, though it looks much simpler than Eqns. (13.30) and (13.31). As for the stress cases, similar phenomena happen, and we will discuss it later on the reason regarding stress oscillatory in Appendix D. Thus Eqns. (13.30) and (13.31) are adopted to remove the singularity.

The integrating range of the real and imaginary parts of $T(m,x)$ are of the form $\int_{k_\beta}^{\infty}(\bullet)\,\mathrm{d}k$ and $\int_{0}^{k_\beta}(\bullet)\,\mathrm{d}k$, respectively. Splitting the integrating range as below

$$\int_{k_\beta}^{\infty}(\bullet)\,\mathrm{d}k = \int_{k_\beta}^{k_\beta+\delta}(\bullet)\,\mathrm{d}k + \int_{k_\beta+\delta}^{\infty}(\bullet)\,\mathrm{d}k \tag{13.40}$$

$$\int_{0}^{k_\beta}(\bullet)\,\mathrm{d}k = \int_{0}^{k_\beta-\delta}(\bullet)\,\mathrm{d}k + \int_{k_\beta-\delta}^{k_\beta}(\bullet)\,\mathrm{d}k \tag{13.41}$$

where δ is a small real constant. In my FORTRAN program, it is set to be 0.1. Then solve integration $\int_{k_\beta+\delta}^{\infty}(\bullet)\,\mathrm{d}k$ and $\int_{0}^{k_\beta-\delta}(\bullet)\,\mathrm{d}k$ by QUADPACK subroutine DQAWF (handling Fourier sine/cosine transform) and DQAWO (handling integration of $\cos(\omega x)f(x)$ or $\sin(\omega x)f(x)$ over a finite interval), respectively. For the other two finite-range integration, $\int_{k_\beta}^{k_\beta+\delta}(\bullet)\,\mathrm{d}k$ and $\int_{k_\beta-\delta}^{k_\beta}(\bullet)\,\mathrm{d}k$, replacing the integration variable k by u as following procedures and treating the resulting integrations (13.42) through (13.45) below by

DQAGS (1-D globally adaptive integrator using interval subdivision and extrapolation). First taking the real part of $T(m,x)$, when m is even, as an example:

$$\int_{k_\beta}^{\infty}\frac{4k\sin(ak)}{\left(k^2-a_m^2\right)\sqrt{k^2-k_\beta^2}}\cos(xk)\,\mathrm{d}k=\int_{k_\beta}^{\infty}\frac{f_1(k)}{\sqrt{k^2-k_\beta^2}}\mathrm{d}k=\int_{k_\beta}^{k_\beta+\delta}\frac{f_1(k)}{\sqrt{k^2-k_\beta^2}}\mathrm{d}k+\int_{k_\beta+\delta}^{\infty}\frac{f_1(k)}{\sqrt{k^2-k_\beta^2}}\mathrm{d}k$$

where,

$$f_1(k)=\frac{4k\sin(ak)}{k^2-a_m^2}\cos(xk)$$

Let,

$$u=\sqrt{k^2-k_\beta^2}\text{ , and }\frac{\mathrm{d}u}{\sqrt{u^2+k_\beta^2}}=\frac{\mathrm{d}k}{\sqrt{k^2-k_\beta^2}}$$

Then,

$$\int_{k_\beta}^{k_\beta+\delta}\frac{f_1(k)}{\sqrt{k^2-k_\beta^2}}\mathrm{d}k=\int_0^{\sqrt{2k_\beta\delta+\delta^2}}\frac{4\sin\left(a\sqrt{k_\beta^2+u^2}\right)\cos\left(x\sqrt{k_\beta^2+u^2}\right)}{k_\beta^2-a_m^2+u^2}\mathrm{d}u \tag{13.42}$$

Similarly, for the real part of $T(m,x)$ when m is odd,

$$\int_{k_\beta}^{\infty}\frac{4k\cos(ak)}{\left(k^2-a_m^2\right)\sqrt{k^2-k_\beta^2}}\sin(xk)\,\mathrm{d}k=\int_{k_\beta}^{\infty}\frac{f_2(k)}{\sqrt{k^2-k_\beta^2}}\mathrm{d}k=\int_{k_\beta}^{k_\beta+\delta}\frac{f_2(k)}{\sqrt{k^2-k_\beta^2}}\mathrm{d}k+\int_{k_\beta+\delta}^{\infty}\frac{f_2(k)}{\sqrt{k^2-k_\beta^2}}\mathrm{d}k$$

where,

$$f_2(k)=\frac{4k\cos(ak)}{k^2-a_m^2}\sin(xk)$$

and,

$$\int_{k_\beta}^{k_\beta+\delta}\frac{f_2(k)}{\sqrt{k^2-k_\beta^2}}\mathrm{d}k=\int_0^{\sqrt{2k_\beta\delta+\delta^2}}\frac{4\cos\left(a\sqrt{k_\beta^2+u^2}\right)\sin\left(x\sqrt{k_\beta^2+u^2}\right)}{k_\beta^2-a_m^2+u^2}\mathrm{d}u \tag{13.43}$$

Using the same method, for the imaginary part of $T(m,x)$ when m is even or odd,

$$\int_0^{k_\beta} \frac{4k\sin(ak)}{\left(k^2-a_m^2\right)\sqrt{k_\beta^2-k^2}}\cos(xk)\,\mathrm{d}k = \int_0^{k_\beta} \frac{f_1(k)}{\sqrt{k_\beta^2-k^2}}\,\mathrm{d}k = \int_0^{k_\beta-\delta} \frac{f_1(k)}{\sqrt{k_\beta^2-k^2}}\,\mathrm{d}k + \int_{k_\beta-\delta}^{k_\beta} \frac{f_1(k)}{\sqrt{k_\beta^2-k^2}}\,\mathrm{d}k$$

Let,

$$u=\sqrt{k_\beta^2-k^2}\ \text{, and}\ \frac{\mathrm{d}u}{\sqrt{k_\beta^2-u^2}} = \frac{-\mathrm{d}k}{\sqrt{k_\beta^2-k^2}}$$

Then,

$$\int_{k_\beta-\delta}^{k_\beta} \frac{f_1(k)}{\sqrt{k_\beta^2-k^2}}\,\mathrm{d}k = \int_0^{\sqrt{2k_\beta\delta-\delta^2}} \frac{4\sin\left(a\sqrt{k_\beta^2-u^2}\right)\cos\left(x\sqrt{k_\beta^2-u^2}\right)}{k_\beta^2-a_m^2-u^2}\,\mathrm{d}u \tag{13.44}$$

$$\int_0^{k_\beta} \frac{4k\cos(ak)}{\left(k^2-a_m^2\right)\sqrt{k_\beta^2-k^2}}\sin(xk)\,\mathrm{d}k = \int_0^{k_\beta} \frac{f_2(k)}{\sqrt{k_\beta^2-k^2}}\,\mathrm{d}k = \int_0^{k_\beta-\delta} \frac{f_2(k)}{\sqrt{k_\beta^2-k^2}}\,\mathrm{d}k + \int_{k_\beta-\delta}^{k_\beta} \frac{f_2(k)}{\sqrt{k_\beta^2-k^2}}\,\mathrm{d}k$$

and,

$$\int_{k_\beta-\delta}^{k_\beta} \frac{f_2(k)}{\sqrt{k_\beta^2-k^2}}\,\mathrm{d}k = \int_0^{\sqrt{2k_\beta\delta-\delta^2}} \frac{4\cos\left(a\sqrt{k_\beta^2-u^2}\right)\sin\left(x\sqrt{k_\beta^2-u^2}\right)}{k_\beta^2-a_m^2-u^2}\,\mathrm{d}u \tag{13.45}$$

Using QUADPACK routines, despite the displacement continuity condition is not satisfied at the interface Γ, the displacement amplitudes converge as the truncation order increases. Furthermore, the converged series expansion displacement amplitude solutions produced by QUADPACK routines coincided with the solutions by Stationary Phase Approximation. Fig. 7-3 shows the superposition comparison of displacement amplitudes between those two methods. The displacements on the left and right sides of the structure are not plotted. Fig. 7-4 is two 3D plot of displacement amplitudes by the two methods for the same initial conditions.

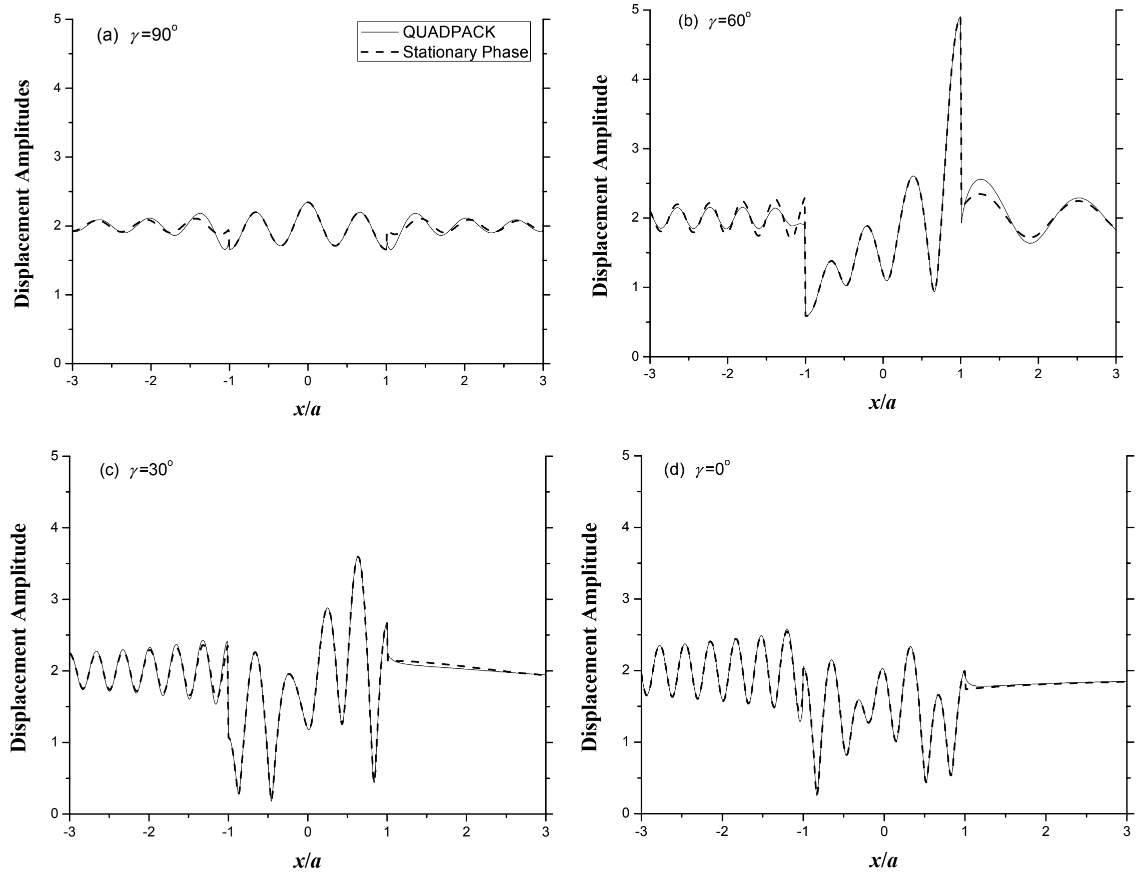

Fig. 7-3 DISPLACEMENT AMPLITUDES AROUND THE STRUCTURE FOR k_β=10, a/d=1.0, μ_B/μ=1.0, k_b/k=1.0, AND γ= 90°, 60°, 30°, 0°

Although Eqns. (13.35)~(13.38) looks much simpler than Eqns. (13.30) and (13.31), after integrated using QUADPACK, displacement amplitudes curves of the latter are relatively smoother than the former's. It might be because the former approach needs four numerical integrations for one-time evaluation of $T(m,x)$ but the latter only needs two steps. By reducing the times of numerical evaluations of quadrature by half, the unsteady properties of displacement amplitude results are also reduced for some extent. For stress amplitudes on the two sides of the common interface Γ, there are alike phenomena. Please refer to Fig. 7-7 and Fig. 7-8 for detail. Therefore, all the plots shown in this report, except Fig. 7-7, are actually computed from Eqns (13.30), (13.31) or (13.58). Fig. 7-5 below shows two examples of calculated displacement amplitudes on the two sides of the interface Γ between the structure (denoted as "Upper Disp Amp") and half-space (denoted as “Lower Disp Amp”). We can tell that there are still distinct gaps for this continuous boundary condition but the “vibration periods” are nearly the same. Thus the numerical displacement amplitudes in the half-space are not reliable.

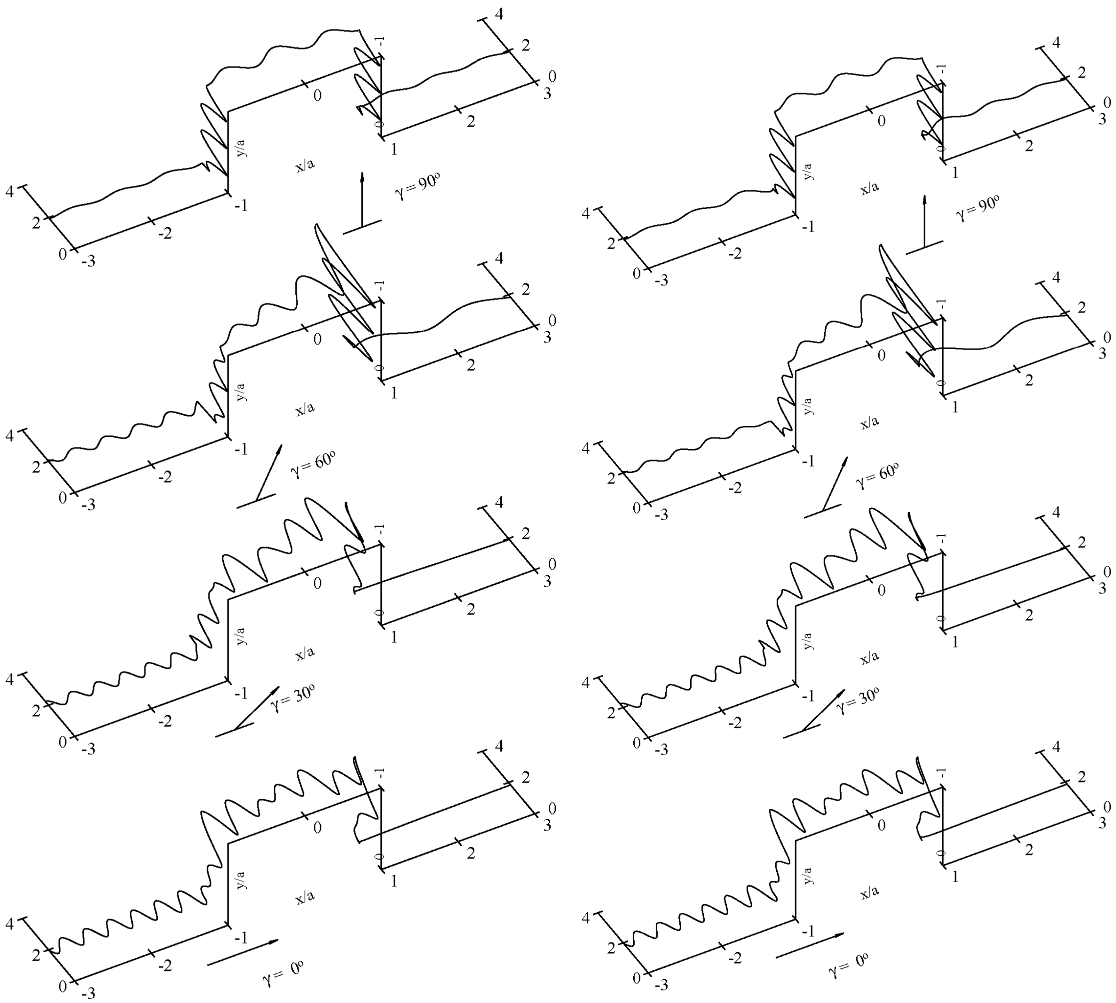

(a) Stationary Phase Approximation (b) QUADPACK Fourier Integral

Fig. 7-4 3-D DISPLACEMENT AMPLITUDES FOR k_β=10, μ_B/μ=1.0, AND γ= 90°, 60°, 30°, 0°

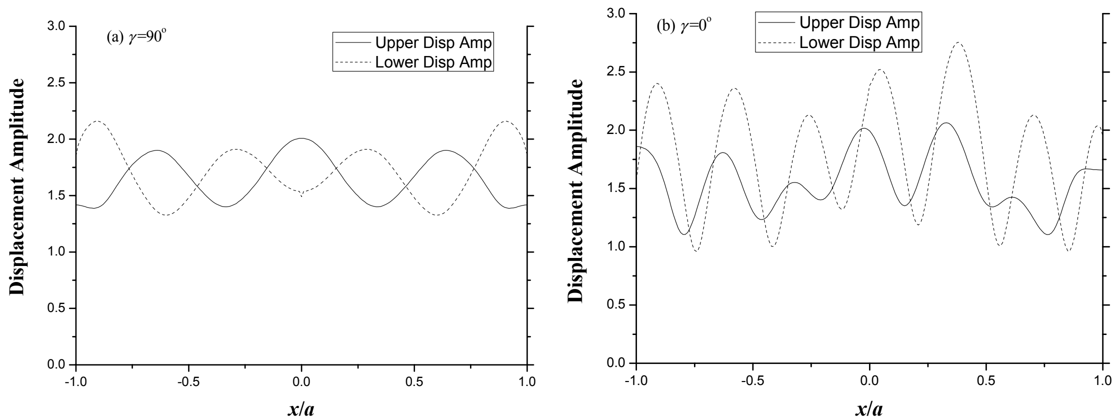

Fig. 7-5 DISPLACEMENT AMPLITUDES ON Γ FOR k_β=10, μ_{B}/μ=1.0, k_b/k=1.0, AND γ= 90° (VERTICAL), 0° (HORIZONTAL)

7.3 Check of Boundary Condition Satisfaction

The stress continuity boundary condition along the common interface Γ of structure and half-space is studied in this section. The derivation is much similar to the preceding section.

The stress of the structure and half-space are

$$\tau_{zy}^{(b)}(x,0)=\mu_{\mathrm{B}}\left.\frac{\partial w^{(b)}}{\partial y}\right|_{y=0}=-\mu_{\mathrm{B}}\sum_{m=0}^{\infty}\xi_m B_m\cos\left[a_m(x+a)\right]\sin(\xi_m d) \tag{13.46}$$

$$\tau_{zy}^{(s)}(x,0)=\mu\left.\frac{\partial w^{(s)}}{\partial y}\right|_{y=0}=\frac{\mathrm{i}\mu}{2\pi}\int_{-\infty}^{\infty}\zeta W^s(k)\exp(-\mathrm{i}kx)\,\mathrm{d}k \tag{13.47}$$

Substituting Eqn. (13.13) into (13.47),

$$\tau_{zy}^{(s)}(x,0)=\frac{\mathrm{i}\mu_{\mathrm{B}}}{2\pi}\sum_{m=0}^{\infty}\xi_m B_m\sin(\xi_m d)P(m,x) \tag{13.48}$$

in which,

$$P(m,x)=\int_{-\infty}^{\infty}Q(m,k)\exp(-\mathrm{i}kx)\,\mathrm{d}k \tag{13.49}$$

$$Q(m,k) = \frac{(-1)^m \mathrm{e}^{\mathrm{i}ka} - \mathrm{e}^{-\mathrm{i}ka}}{k^2 - a_m^2} k = ka^2 F_m(ka) \tag{13.50}$$

Similarly, change the quadrature interval of Eqn.(13.49) to half-infinite range,

$$P(m,x) = \int_0^\infty \left[Q(m,k)\exp(-\mathrm{i}kx) + Q(m,-k)\exp(\mathrm{i}kx) \right] \mathrm{d}k$$

$$= \int_0^\infty Q1(m,k)\cos(kx)\,\mathrm{d}k + \mathrm{i}\cdot\int_0^\infty Q2(m,k)\sin(kx)\,\mathrm{d}k \tag{13.51}$$

where,

$$Q1(m,k) = Q(m,-k) + Q(m,k) \tag{13.52}$$

$$Q2(m,k) = Q(m,-k) - Q(m,k) \tag{13.53}$$

Deriving the above two equations further by Euler formula,

$$Q1(m,k) = \frac{2\mathrm{i}\sin(ka)\left[(-1)^m + 1\right]k}{k^2 - a_m^2} = \begin{cases} \dfrac{4\mathrm{i}\sin(ka)k}{k^2 - a_m^2}, & m \text{ even} \\ 0 & , m \text{ odd} \end{cases} \tag{13.54}$$

$$Q2(m,k) = \frac{2\cos(ka)\left[1 - (-1)^m\right]k}{k^2 - a_m^2} = \begin{cases} 0 & , m \text{ even} \\ \dfrac{4\cos(ka)k}{k^2 - a_m^2}, & m \text{ odd} \end{cases} \tag{13.55}$$

Therefore,

$$P(m,x) = \begin{cases} \mathrm{i}\displaystyle\int_0^\infty \frac{4k\sin(ka)}{k^2 - a_m^2}\cos(kx)\,\mathrm{d}k, & m \text{ even} \\ \mathrm{i}\displaystyle\int_0^\infty \frac{4k\cos(ka)}{k^2 - a_m^2}\sin(kx)\,\mathrm{d}k, & m \text{ odd} \end{cases} \tag{13.56}$$

So $P(m,x)$ is actually an imaginary number. Eliminating the imaginary units out then Eqn. (13.48) becomes

$$\tau_{zy}^{(\mathrm{S})}\left(x,0\right)=-\frac{\mu_{\mathrm{B}}}{2\pi}\sum_{m=0}^{\infty}\xi_m B_m \sin\left(\xi_m d\right)P^*\left(m,x\right) \tag{13.57}$$

where,

$$P^*\left(m,x\right)=\begin{cases}\int_0^{\infty}\frac{4k\sin\left(ak\right)}{k^2-a_m^2}\cos\left(xk\right)\mathrm{d}k, & m \text{ even}\\ \int_0^{\infty}\frac{4k\cos\left(ak\right)}{k^2-a_m^2}\sin\left(xk\right)\mathrm{d}k, & m \text{ odd}\end{cases} \tag{13.58}$$

Or, combining sine and cosine terms together, we got

$$P^*\left(m,x\right)=\begin{cases}\int_0^{\infty}\frac{2k}{k^2-a_m^2}\sin\left[\left(a+x\right)k\right]\mathrm{d}k+\int_0^{\infty}\frac{2k}{k^2-a_m^2}\sin\left[\left(a-x\right)k\right]\mathrm{d}k, & m \text{ even}\\ \int_0^{\infty}\frac{2k}{k^2-a_m^2}\sin\left[\left(a+x\right)k\right]\mathrm{d}k-\int_0^{\infty}\frac{2k}{k^2-a_m^2}\sin\left[\left(a-x\right)k\right]\mathrm{d}k, & m \text{ odd}\end{cases} \tag{13.59}$$

Comparing Eqns. (13.58) and (13.59) with (13.30)~(13.31) and (13.35)~(13.38), we can see that the only difference between those integrands is that displacement integrands have one additional term $\sqrt{k^2-k_\beta^2}$ or $\sqrt{k_\beta^2-k^2}$ in their denominators.

Similarly as Eqn.(9.17), the stress τ_{zy} could be characterized by the normalized stress amplitude $|\tau|$, for the region of building and half-space, respectively given by

$$\left|\tau^{(\mathrm{B})}\right|=\left|\tau_{zy}^{(\mathrm{B})}\right|/\mu k_\beta=\frac{\mu_{\mathrm{B}}}{\mu k_\beta}\left|\sum_{m=0}^{\infty}\xi_m B_m\cos\left[a_m\left(x+a\right)\right]\sin\left(\xi_m d\right)\right| \tag{13.60}$$

$$\left|\tau^{(\mathrm{S})}\right|=\left|\tau_{zy}^{(\mathrm{S})}\right|/\mu k_\beta=\frac{\mu_{\mathrm{B}}}{2\pi\mu k_\beta}\left|\sum_{m=0}^{\infty}\xi_m B_m\sin\left(\xi_m d\right)P^*\left(m,x\right)\right| \tag{13.61}$$

Same as the case of displacement, Eqn. (13.59) looks simpler than (13.58) but brings much stronger oscillation into the stress amplitude curves. That is because the integrals of Eqn. (13.59)actually converge much slower than those of (13.58). For detail reason, please refer to Appendix D. Thus in Fig. 7-6 and Fig.

7-7, under the same initial conditions as Fig. 7-5, the curves are computed by Eqn. (13.58) and (13.59) using QUADPACK Fourier integral routines DQAWF, respectively. In Fig. 7-6 those two curves almost completely match each other, except in the regions adjacent to two rims ($x/a=\pm 1$) and the midpoint ($x/a=0$) of common interface Γ. As for Fig. 7-7, integral solutions in the half-space (denoted as "Lower Stress Amp") are much more unstable than Fig. 7-6.

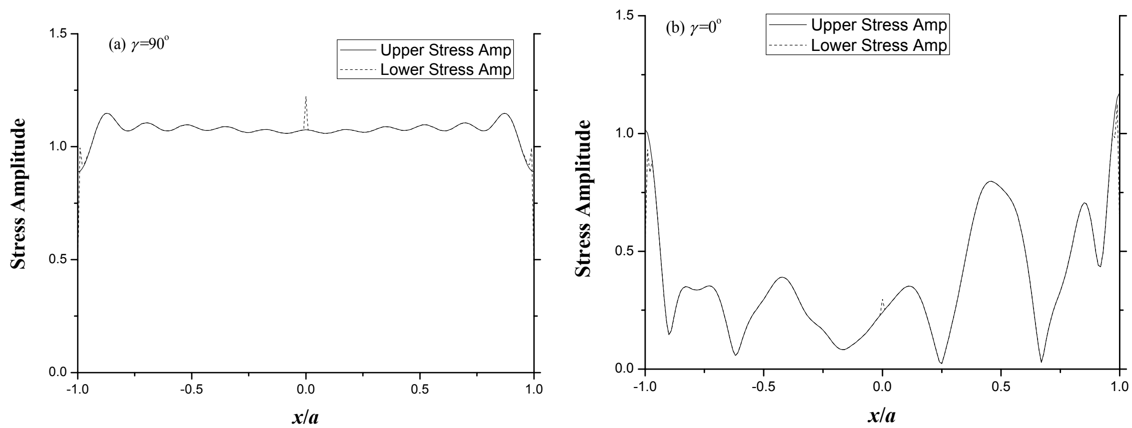

Fig. 7-6 STRESS AMPLITUDES ON Γ FOR k_β=10, a/d=1.0, μ_B/μ=1.0, k_b/k=1.0, γ= 90° (VERTICAL) OR 0° (HORIZONTAL), CALCULATING BASED ON INTEGRALS (13.58)

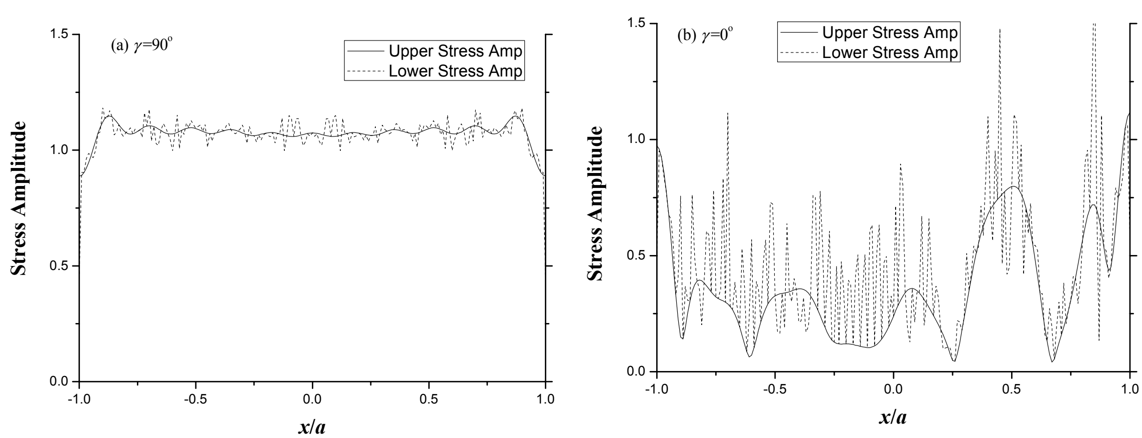

Fig. 7-7 STRESS AMPLITUDES ON Γ FOR k_β=10, a/d=1.0, μ_B/μ=1.0, k_b/k=1.0, γ= 90° (VERTICAL) OR 0° (HORIZONTAL), CALCULATING BASED ON INTEGRALS (13.59)

In summary, along common interface Γ, stress continuity is satisfied but displacement continuity not. Derivative procedures are very alike. The resultant Fourier integrals are alike too, except the term $\sqrt{k_\beta^2 - k^2}$. QUADPACK routines return much more error flags when calculating stress amplitudes than calculating displacement amplitudes; however, the continuity checking results is to the contrast. If there are no error in our derivation and programming, the convergence of displacement series (13.22) must have problem.

Stress ratio along the interface also has been calculated, either from structure equation (13.46) or from half-space equation (13.57), which are plotted in Fig. 7-8 and Fig. 7-9, respectively. They all look the same. Stress ratio are defined as below

$$\kappa_\gamma = \tau_{zy,\gamma} / \tau_{zy,\text{normal incidence}} \tag{13.62}$$

in which the numerator denotes the shear stress for incidence angle equals γ, and the 'normal incidence' in the denominator means $\gamma = 90^{\circ}$.

$$\text{Stress ratio amplitude} = \left|\kappa_\gamma\right| = \left[\operatorname{Re}^2(\kappa_\gamma) + \operatorname{Im}^2(\kappa_\gamma)\right]^{1/2} \tag{13.63}$$

$$\text{Stress ratio phase} = \text{Phase}(\kappa_\gamma) = \tan^{-1}\left[\operatorname{Im}(\kappa_\gamma) / \operatorname{Re}(\kappa_\gamma)\right] \tag{13.64}$$

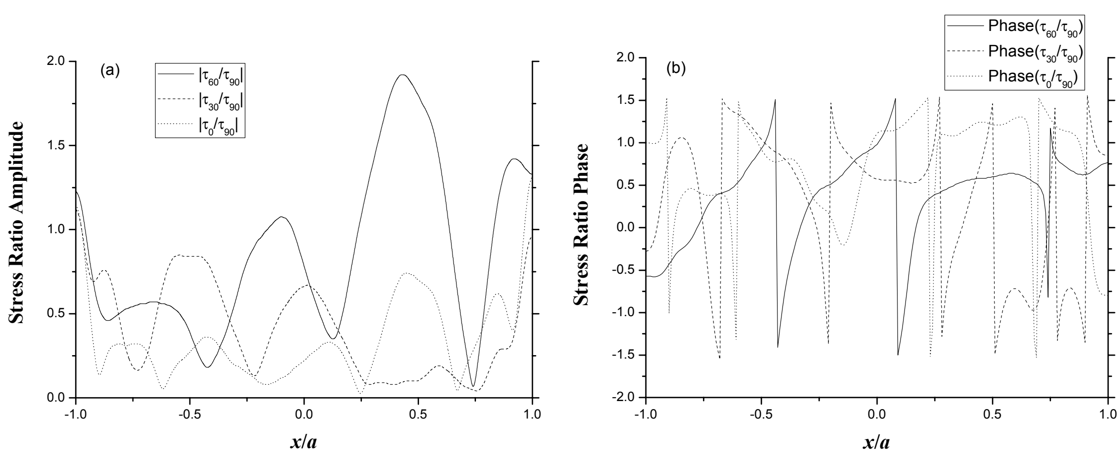

Fig. 7-8 STRESS RATIO ON Γ FOR k_β=10, a/d=1.0, μ_B/μ=1.0, k_b/k=1.0, AND γ= 60°, 30°, 0°, CALCULATING BASED ON STRUCTURE STRESS EQUATION (13.40)

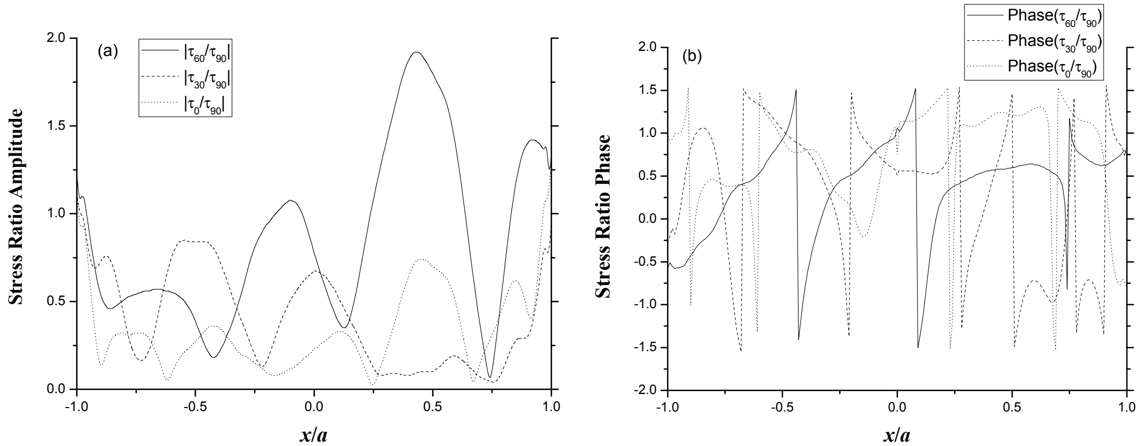

Fig. 7-9 STRESS RATIO ON Γ FOR k_β=10, a/d=1.0, μ_B/μ=1.0, k_b/k=1.0, AND γ= 60°, 30°, 0°, CALCULATING BASED ON HALF-SPACE STRESS EQUATION (13.50)

Chapter 8

SOIL-STRUCTURE INTERACTION:

A SHEAR BEAM WITH A SHALLOW RIGID CYLINDRICAL FOUNDATION

The model studied in this chapter is a further extension on which Luco and Trifunac studied much earlier. Luco (1969) first studied the similar model with the exception that the foundation is semi-cylindrical and SH-wave considered is plane and vertically incident. Trifunac (1972) extended the angle of incident plane SH-waves to oblique cases and provided quite careful analysis and valuable conclusions after investigating the numerical results.

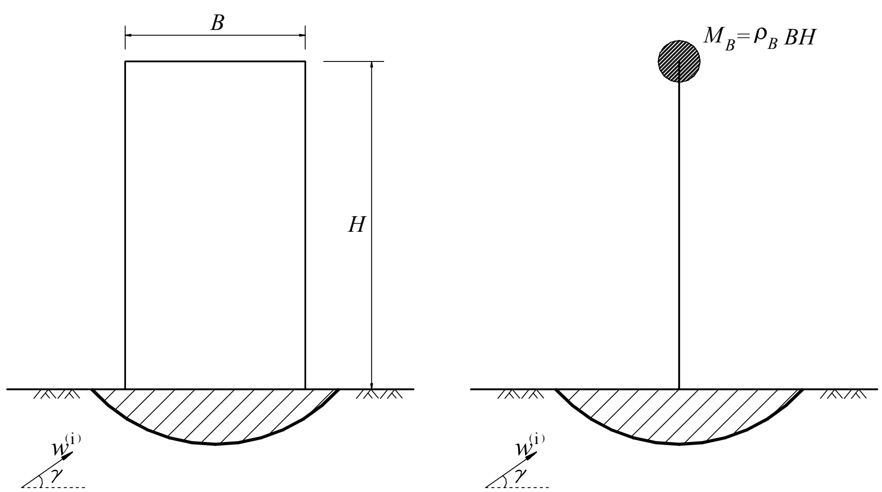

Fig. 8-1 SINGLE-DEGREE-OF-FREEDOM OSCILLATOR SSI SYSTEM

The foundations investigated in this chapter are in shallow cylindrical configuration so as to represent more general cases. Two types of incident SH-waves, plane or cylindrical, are examined. As illustrated in Fig. 8-1, by the assumption of perfectly rigidity of foundation, the contribution of the higher modes of vibration to the building response is ignored automatically. The building (shear beam) can be replaced by an equivalent single degree of freedom (SDOF) oscillator (or called Inverted Pendulum system) in the horizontal translation. The realizations of SDOF oscillator in practice might be some cantilever structures that have a large portion of total mass of the building concentrated near the top, such as water tower or bridge pier.

8.1 Incident Plane SH-Waves

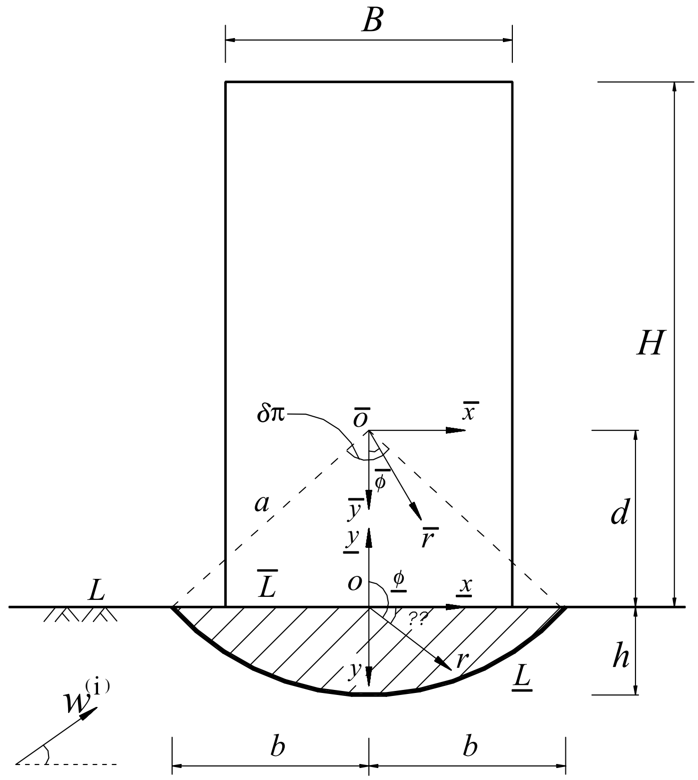

Fig. 8-2 A SHEAR BEAM WITH A RIGID SHALLOW CYLINDRICAL FOUNDATION

An elastic homogeneous shear beam (also referred to as 'building' or 'structure' in the subsequent sections) with cross-section dimension of B by H sitting on a movable shallow circular rigid foundation radius a embedded in a isotropic, homogeneous and elastic half-space, as illustrated in Fig. 8-2. This model is a two-dimensional plane strain problem so that it could be viewed as having infinite depth in the out-of-plane direction. A band of parallel harmonic incident anti-plane SH-waves excite the model from the deep earth at an incidence angel γ with respect to the horizontal axis. The perpendicular distance between the circular center and ground surface is d. The angle of this segment of circular arc is $\delta\pi$. Depth of embedment and half-width of the rigid foundation are h and b, respectively. It is obvious that $\delta\pi = 2\arccos(d/a)$. The material constants of half-space and building, namely rigidity and shear wave velocity, are respectively denoted by μ, C_β and $\mu_{\mathrm{B}}, C_{\beta_{\mathrm{B}}}$. The contacts between the soil and foundation and building are assumed to be welded, implying no slippage between them would happen but the foundation is removable.

8.1.1 Wave Field in the Half-Space

Differential wave equation (8.1) should be satisfied for *w* which is assumed to be the total anti-plane wave field within the half-space after scattered by this rigid foundation. In addition, the following two boundary conditions must be satisfied

$$\tau_{\theta z}|_L = 0 \quad \text{at} \qquad r > b,\ \theta = 0, \pi \tag{14.1}$$

$$w|_{\underline{L}} = w_0 \mathrm{e}^{\mathrm{i}\omega t} \quad \text{at} \quad \bar{r} = a,\ \bar{\phi} \in [-\frac{\delta\pi}{2}, \frac{\delta\pi}{2}] \tag{14.2}$$

where w_0 is the unknown movement of the rigid foundation.

Similar derivation of free-field wave field is given in Chapter 2, hence only final expression is restated here for convenience

$$w^{(\mathrm{ff})}(r,\theta) = w^{(\mathrm{i})} + w^{(\mathrm{r})} = \sum_{n=0}^{\infty} a_n^{(\mathrm{f})} \mathrm{J}_n(kr)\cos n\theta \tag{14.3}$$

$$w^{(\mathrm{ff})}(\bar{r},\bar{\phi}) = \sum_{m=-\infty}^{\infty} \bar{a}_m^{(\mathrm{f})} \mathrm{J}_m(k\bar{r})\mathrm{e}^{\mathrm{i}m\bar{\phi}} \tag{14.4}$$

in which, for $n = 0,1,2,\cdots$; $m = 0,\pm1,\pm2,\cdots$

$$a_n^{(\mathrm{f})} = 2\varepsilon_n \mathrm{i}^n \cos n\gamma \tag{14.5}$$

$$\bar{a}_m^{(\mathrm{f})} = 2\cos(kd\sin\gamma - m\gamma) \tag{14.6}$$

The wave field in the half-space scattered and diffracted in the presence of the foundation is

$$w^{(\mathrm{S})}(r,\theta)=\sum_{n=0}^{\infty}A_n \mathrm{H}_n^{(1)}\left(kr\right)\cos n\theta \tag{14.7}$$

where, the A_n 's are a set of complex unknowns to be determined by boundary conditions. Like the scattered waves due to shallow cylindrical canyon, traction-free boundary condition Eqn.(14.1) is satisfied automatically. And after applying Graf's formula (8.26), the scattered wave $w^{(\mathrm{S})}$ could be transformed to the upper coordinate $\left(\overline{r},\overline{\phi}\right)$

$$w^{(\mathrm{S})}(\overline{r},\overline{\phi})=\sum_{m=-\infty}^{\infty}\overline{A}_m \mathrm{H}_m^{(1)}\left(k\overline{r}\right)\mathrm{e}^{\mathrm{i}m\overline{\phi}} \tag{14.8}$$

in which,

$$\overline{A}_m=\sum_{n=-\infty}^{\infty}\underline{A}_n \mathrm{J}_{n+m}(kd)=\sum_{n=0}^{\infty}\frac{A_n}{2}(-\mathrm{i})^n\left[\mathrm{J}_{m+n}(kd)+\mathrm{J}_{m-n}(kd)\right] \tag{14.9}$$

The derivation of the scattered wave is the same as equations (11.8) through (11.12) for shallow cylindrical canyons.

8.1.2 Displacement Continuity between Soil and Foundation

The boundary conditions at the interface of foundation and half-space

$$\left(w^{(\mathrm{ff})}+w^{(\mathrm{S})}\right)\Big|_{\overline{r}=a}=w^{(\mathrm{R})}=w_0\mathrm{e}^{-\mathrm{i}\omega t} \tag{14.10}$$

Substituting expressions into this equation,

$$\overline{A}_0\mathrm{H}_0^{(1)}\left(ka\right)+\overline{a}_0\mathrm{J}_0\left(ka\right)=w_0 \tag{14.11}$$

for $n=\pm1,\pm2,\pm3,\ldots$

$$\overline{A}_n\mathrm{H}_n^{(1)}\left(ka\right)+\overline{a}_n\mathrm{J}_n\left(ka\right)=0 \tag{14.12}$$

In summary,

$$\bar{A}_n = \begin{cases} \dfrac{w_0 - \bar{a}_0^{(\mathrm{f})} \mathrm{J}_0(ka)}{\mathrm{H}_0^{(1)}(ka)}, \text{ for } n=0 \\ -\dfrac{\bar{a}_n^{(\mathrm{f})} \mathrm{J}_n(ka)}{\mathrm{H}_n^{(1)}(ka)}, \text{ for } n=\pm 1, \pm 2, \pm 3, ... \end{cases} \tag{14.13}$$

So $\bar{A}_n$ for $n \neq 0$ are solved already but $\bar{A}_0$ still keeps unknown due to undetermined w_0.

8.1.3 Response of the Building

Since the foundation is rigid and every particle at any horizontal cross-section of the structure parallel to the half-space surface must have the same antiplane motion w_0, the motion of the shear beam is independent of coordinate *x* and could be represented as $w_{\mathrm{B}} = w_{\mathrm{B}}(y)\ \mathrm{e}^{-\mathrm{i}\omega t}$, which must satisfy the following ordinary differential equation,

$$\frac{\mathrm{d}^2 w_{\mathrm{B}}}{\mathrm{d}y^2} + k_{\mathrm{B}}^2 w_{\mathrm{B}} = 0 \tag{14.14}$$

whose general solution is

$$w_{\mathrm{B}}(y) = E \cos k_{\mathrm{B}} y + F \sin k_{\mathrm{B}} y \tag{14.15}$$

where E and F are two constants to be determined. With that, the building is simplified to a single degree-of-freedom (SDOF) oscillator or a uniform shear beam. The top and bottom boundary conditions of the structure are

$$w_{\mathrm{B}}\big|_{y=0} = w^{(\mathrm{R})} = w_0 \mathrm{e}^{-\mathrm{i}\omega t} \tag{14.16}$$

$$\tau_{yz}\big|_{y=-H} = \mu_{\mathrm{B}} \frac{\partial w_{\mathrm{B}}}{\partial y}\bigg|_{y=-H} = 0 \tag{14.17}$$

Substitution of Eqn. (14.15) into (14.16) and (14.17) leads to the building motion expression (with $E = w_0$ and $F = -w_0 \tan k_{\mathrm{B}} H$)

$$w_{\mathrm{B}}(y)=w_0\left(\cos k_{\mathrm{B}}y-\tan k_{\mathrm{B}}H\sin k_{\mathrm{B}}y\right)=\frac{w_0}{\cos k_{\mathrm{B}}H}\cos k_{\mathrm{B}}(y+H) \tag{14.18}$$

So the shear stress along the interface of building and foundation could be derived as

$$\tau_{yz}\Big|_{y=0}=\mu_{\mathrm{B}}\frac{\partial w_{\mathrm{B}}(y)}{\partial y}\Bigg|_{y=0}=-w_0\mu_{\mathrm{B}}k_{\mathrm{B}}\tan k_{\mathrm{B}}H \tag{14.19}$$

The force of building acting on the foundation per unit length is

$$f_{\mathrm{B}}=-w_0\mu_{\mathrm{B}}k_{\mathrm{B}}B\tan k_B H \tag{14.20}$$

8.1.4 Kinetic Equation of Foundation

As pointed out by Luco (1969), displacement of the foundation w_0 can be determined by the kinetic equation for the rigid foundation

$$M_{\mathrm{f}}\ddot{w}_{\mathrm{f}}=-\left(f_{\mathrm{s}}+f_{\mathrm{B}}\right)\mathrm{e}^{-\mathrm{i}\omega t} \tag{14.21}$$

where M_{f} is the mass of the rigid foundation per unit length in the *z* axis, and f_{s} denotes the action of half-space soil on the foundation. w_{f} represents the displacement function of rigid foundation in terms of time factor *t*, i.e., $w_{\mathrm{f}}=w_{\mathrm{f}}(t)=w_0\mathrm{e}^{-\mathrm{i}\omega t}$.

$$M_{\mathrm{f}}=\frac{\rho_{\mathrm{f}}a^2}{2}\left(\delta\pi-\sin\delta\pi\right) \tag{14.22}$$

$$f_{\mathrm{s}}=a\int_{-\delta\pi/2}^{\delta\pi/2}\tau_{\overline{r}z}\big|_{\overline{r}=a}\,\mathrm{d}\overline{\phi}=\mu ka\sum_{n=-\infty}^{\infty}\left(\overline{a}_n^{(\mathrm{f})}\mathrm{J}'_n\left(ka\right)+\overline{A}_n\mathrm{H}_n^{(1)\prime}\left(ka\right)\right)\int_{-\delta\pi/2}^{\delta\pi/2}\mathrm{e}^{\mathrm{i}n\overline{\phi}}\,\mathrm{d}\overline{\phi} \tag{14.23}$$

$$\ddot{w}_{\mathrm{f}}=-w_0\omega^2\mathrm{e}^{-\mathrm{i}\omega t} \tag{14.24}$$

and the definite integral could be solved explicitly,

$$\int_{-\delta\pi/2}^{\delta\pi/2}\mathrm{e}^{\mathrm{i}n\overline{\phi}}\,\mathrm{d}\overline{\phi}=\begin{cases}\delta\pi & ,\ n=0\\ -\dfrac{\mathrm{i}\mathrm{e}^{\mathrm{i}n\overline{\phi}}}{n}\Bigg|_{-\delta\pi/2}^{\delta\pi/2}=\dfrac{2\sin\dfrac{n\delta\pi}{2}}{n} & ,\ n\neq 0\end{cases} \tag{14.25}$$

So f_{s} could be rewritten as

$$f_{\mathrm{s}} = \mu ka \left[\begin{array}{l} \sum\limits_{\substack{n=-\infty \\ n\neq 0}}^{\infty} \dfrac{2\sin\dfrac{n\delta\pi}{2}}{n} \left(\overline{a}_n^{(\mathrm{f})} \mathrm{J}_n'\left(ka\right) + \overline{A}_n \mathrm{H}_n^{(1)\prime}\left(ka\right) \right) \\ + \delta\pi \left(\overline{a}_0^{(\mathrm{f})} \mathrm{J}_0'\left(ka\right) + \overline{A}_0 \mathrm{H}_0^{(1)\prime}\left(ka\right) \right) \end{array} \right] \tag{14.26}$$

and the formula for f_{B} is given above in Eqn. (14.20). Therefore, the displacement of the rigid foundation w_0 is solvable and could be simplified as,

$$w_0 = \frac{ -\dfrac{2\mathrm{i}}{\pi ka} \sum\limits_{n=-\infty}^{\infty} \dfrac{\overline{a}_n^{(\mathrm{f})} \xi_n}{\mathrm{H}_n^{(1)}\left(ka\right)} }{ \dfrac{ka}{2} \left(1 - \dfrac{\sin\delta\pi}{\delta\pi} \right) \left(\dfrac{M_{\mathrm{f}}}{M_{\mathrm{s}}} + \dfrac{M_{\mathrm{B}}}{M_{\mathrm{s}}} \dfrac{\tan k_{\mathrm{B}} H}{k_{\mathrm{B}} H} \right) + \dfrac{\mathrm{H}_1^{(1)}\left(ka\right)}{\mathrm{H}_0^{(1)}\left(ka\right)} } \tag{14.27}$$

in which,

$$\xi_n = \begin{cases} 1 & \text{, when } n=0 \\ \sin\dfrac{n\delta\pi}{2} \Big/ \dfrac{n\delta\pi}{2} & \text{, when } n \neq 0 \end{cases} \tag{14.28}$$

During the simplification procedure, equalities

$$M_{\mathrm{s}} = \frac{\rho a^2}{2} \left(\delta\pi - \sin\delta\pi \right) \tag{14.29}$$

$$\omega^2 = \frac{\mu k^2 a^2}{2M_{\mathrm{s}}} \left(\delta\pi - \sin\delta\pi \right) \tag{14.30}$$

and following Wronskians formula (Abramowitz and Stegun, 1972) has been used

$$W\left\{ \mathrm{J}_p\left(z\right), \mathrm{H}_p^{(1)}\left(z\right) \right\} = \mathrm{J}_p\left(z\right) \mathrm{H}_p^{(1)\prime}\left(z\right) - \mathrm{J}_p'\left(z\right) \mathrm{H}_p^{(1)}\left(z\right) = \frac{2\mathrm{i}}{\pi z} \tag{14.31}$$

If we set $\delta\pi = \pi$ in Eqn. (14.27), apparently $d = 0$ and center $\overline{O}$ overlaps with point O. Since $\mathrm{J}_0(0) = 1$ and $\mathrm{J}_n(0) = 0$ for any other integer order n, either positive or negative.

$$\overline{a}_n^{(\mathrm{f})} = 2\cos n\gamma \tag{14.32}$$

With that, Eqn. (14.27) could be reduced into the following expression for semi-cylindrical foundation cases

$$w_0 = \frac{-\dfrac{4\mathrm{i}}{\pi ka\mathrm{H}_0^{(1)}(ka)}}{\dfrac{ka}{2}\left[\dfrac{\tan k_{\mathrm{B}}H}{k_{\mathrm{B}}H}\dfrac{M_{\mathrm{B}}}{M_{\mathrm{s}}}+\dfrac{M_{\mathrm{f}}}{M_{\mathrm{s}}}\right]+\dfrac{\mathrm{H}_1^{(1)}(ka)}{\mathrm{H}_0^{(1)}(ka)}} \tag{14.33}$$

which is in agreement with the corresponding formula in the previous work (Trifunac, 1971).

8.1.5 Torsional Displacement

Trifunac (1982) provided a method on how to exactly determinate rocking and torsional motion of ground surface from known translational components of ground motion at the same location. For our problem, since the system is excited by incident anti-plane SH waves; besides anti-plane displacement, torsional motions of foundation and soil around axis y also exist. The formula of this rotational component of motion is present by Lee and Trifunac (1985).

$$\psi(r,\theta) = -\frac{1}{2}\frac{\partial w}{\partial x} = -\frac{\cos\theta}{2}\frac{\partial w}{\partial r}+\frac{\sin\theta}{2r}\frac{\partial w}{\partial \theta} \tag{14.34}$$

where w is the displacement field of half-space so that $w = w^{(\mathrm{ff})}+w^{(\mathrm{S})}$. Therefore,

$$w^{(\mathrm{ff})}+w^{(\mathrm{S})} = \begin{cases} w(r,\theta) = \displaystyle\sum_{n=0}^{\infty}\left[a_n^{(\mathrm{f})}\mathrm{J}_n(kr)+A_n\mathrm{H}_n^{(1)}(kr)\right]\cos n\theta \\ w(\overline{r},\overline{\phi}) = \displaystyle\sum_{m=-\infty}^{\infty}\left[\overline{a}_m^{(\mathrm{f})}\mathrm{J}_m(k\overline{r})+\overline{A}_m\mathrm{H}_m^{(1)}(k\overline{r})\right]\mathrm{e}^{\mathrm{i}m\overline{\phi}} \end{cases} \tag{14.35}$$

$$\psi(r,\theta) = -\frac{\cos\theta}{2}\frac{\partial w}{\partial r} = -\frac{k\cos\theta}{2}\sum_{n=0}^{\infty}\left[a_n^{(\mathrm{f})}\mathrm{J}_n'(kr)+A_n\mathrm{H}_n^{(1)\prime}(kr)\right]\cos n\theta \tag{14.36}$$

For oblique incident waves, we only discuss the torsional motion on the ground surface $L+\overline{L}$, thus θ equals 0 or π, and Eqn.(14.34) can be simplified to the following equation after normalized by coefficient $\lambda/\pi = 2/k$.

$$\left|\xi(r,\theta)\right|=\left|\frac{\lambda\psi}{\pi}\right|=\left|\cos\theta\sum_{n=0}^{\infty}\left[a_n^{(\mathrm{f})}\mathrm{J}_n'\left(kr\right)+A_n\mathrm{H}_n^{(1)\prime}\left(kr\right)\right]\cos n\theta\right| \quad \left(r,\theta\right)\in L+\overline{L} \qquad (14.37)$$

For vertical incident waves, there must be no anti-plane rotational motions due to symmetry of the whole model. But this formula needs coefficients A_n, which involves the resolution of infinite linear equation (14.9), and that induces the convergence of rotational motion results not as good as we thought. So we apply the upper coordinate $\left(\overline{r},\overline{\phi}\right)$ to accomplish this procedure.

$$\left|\xi(r,\theta)\right|=\left|\frac{\lambda\psi}{\pi}\right|=\frac{1}{2}\left|\sum_{n=-\infty}^{\infty}\left\{\begin{aligned}&\left[\overline{a}_n^{(\mathrm{f})}\mathrm{J}_{n-1}\left(k\overline{r}\right)+\overline{A}_n\mathrm{H}_{n-1}^{(1)}\left(k\overline{r}\right)\right]\mathrm{e}^{\mathrm{i}(n-1)\overline{\phi}}\\&+\left[\overline{a}_n^{(\mathrm{f})}\mathrm{J}_{n+1}\left(k\overline{r}\right)+\overline{A}_n\mathrm{H}_{n+1}^{(1)}\left(k\overline{r}\right)\right]\mathrm{e}^{\mathrm{i}(n+1)\overline{\phi}}\end{aligned}\right\}\right| \quad \left(r,\theta\right)\in L+\overline{L} \qquad (14.38)$$

This formula converges much better than Eqn(14.37). For low frequency incident waves, at which only a few terms needed to make series converged, the results from those two formulae agree well. That proves the effectiveness of equation (14.38).

8.1.6 Numerical Computation of Displacement Amplitudes

First we verify the correctness of the numerical results through a simple way: comparing the results from semi-cylindrical foundation case and shallow cylindrical foundation case under the same condition. That is basically identical to compare formulae (14.27) and (14.33) numerically. The two examples are represented in Fig. 8-3 with the initial condition shown in the legends. It is clearly that the two curves match with each other perfectly.

3-dimensional plots are presented in order to provide an overall insight on the correlation of ground surface displacement amplitude and various initial conditions: angle of incidence, $M_\mathrm{f}/M_\mathrm{s}$, $M_\mathrm{B}/M_\mathrm{s}$, $k_\mathrm{B}H/kb$, and depth-width ratio of foundation h/b.

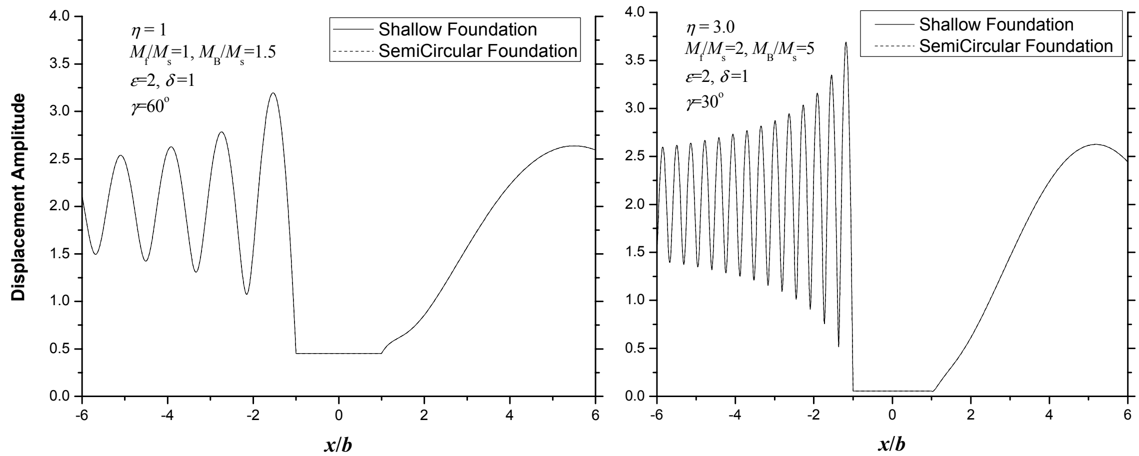

Fig. 8-3 VERIFICATION OF PLANE INCIDENCE BY COMPARING WITH THE SEMI-CIRCULAR FOUNDATION RESULTS

Assuming $\left|w_0^{\mathrm{e}}\right|$ as the envelope of the rigid foundation displacement w_0, then we have

$$\left|w_0^{\mathrm{e}}\right| = \left|\left[\mathrm{J}_0^2(ka)+\mathrm{Y}_0^2(ka)\right]\sum_{n=-\infty}^{\infty}\frac{\overline{a}_n^{(\mathrm{f})}\xi_n}{\mathrm{H}_n^{(1)}(ka)}\right| \tag{14.39}$$

where $\mathrm{J}_0(\cdot)$ and $\mathrm{Y}_0(\cdot)$ represent the first and second kind of Bessel function with order 0. Equation (14.39) is obtained in the case of equivalence and elimination of the $\frac{ka}{2}\left(1-\frac{\sin\delta\pi}{\delta\pi}\right)\left(\frac{M_{\mathrm{f}}}{M_{\mathrm{s}}}+\frac{M_{\mathrm{B}}}{M_{\mathrm{s}}}\frac{\tan k_{\mathrm{B}}H}{k_{\mathrm{B}}H}\right)$ and the real part of $\frac{\mathrm{H}_1^{(1)}(ka)}{\mathrm{H}_0^{(1)}(ka)}$ in the denominator of (14.27).

And then (14.39) is the quotient of original numerator $\frac{2\mathrm{i}}{\pi ka}\sum_{n=-\infty}^{\infty}\frac{\overline{a}_n^{(\mathrm{f})}\xi_n}{\mathrm{H}_n^{(1)}(ka)}$ and imaginary part of $\frac{\mathrm{H}_1^{(1)}(ka)}{\mathrm{H}_0^{(1)}(ka)}$. Another Wronskians formula (Abramowitz and Stegun, 1972) has been used here for simplification

$$W\left\{\mathrm{J}_p(z),\mathrm{Y}_p(z)\right\} = \mathrm{J}_{p+1}(z)\mathrm{Y}_p(z)-\mathrm{J}_p(z)\mathrm{Y}_{p+1}(z) = \frac{2}{\pi z} \tag{14.40}$$

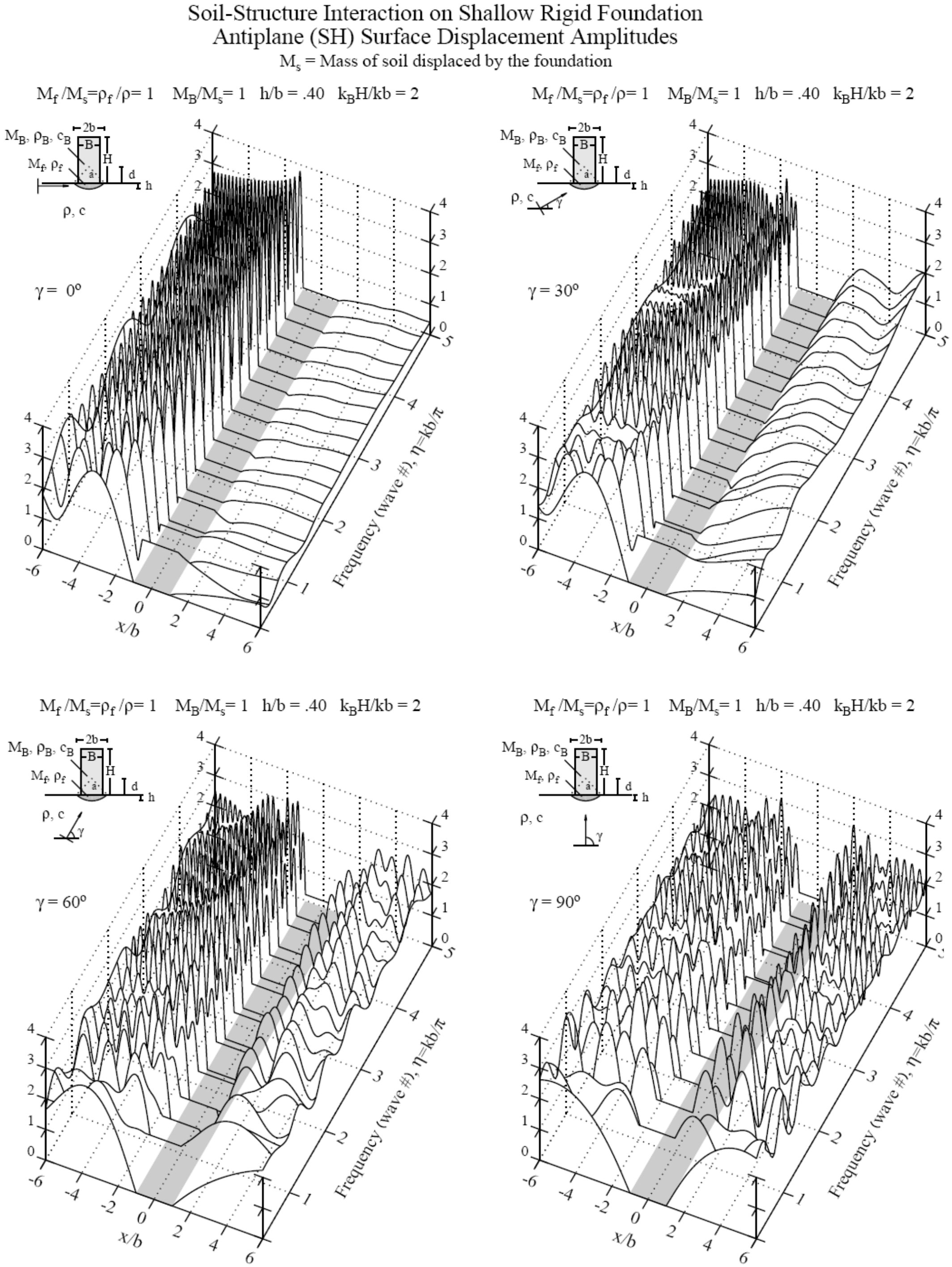

Fig. 8-4 3-D GROUND SURFACE DISPLACEMENT FOR $M_{\mathrm{f}}/M_{\mathrm{s}}=1$, $M_{\mathrm{B}}/M_{\mathrm{s}}=1$, $h/b=0.4$, $k_{\mathrm{B}}H/kb=2$, **AND** γ **= 90°, 60°, 30°, 0°**

Soil-Structure Interaction on Shallow Rigid Foundation
Antiplane (SH) Surface Displacement Amplitudes
M_s = Mass of soil displaced by the foundation

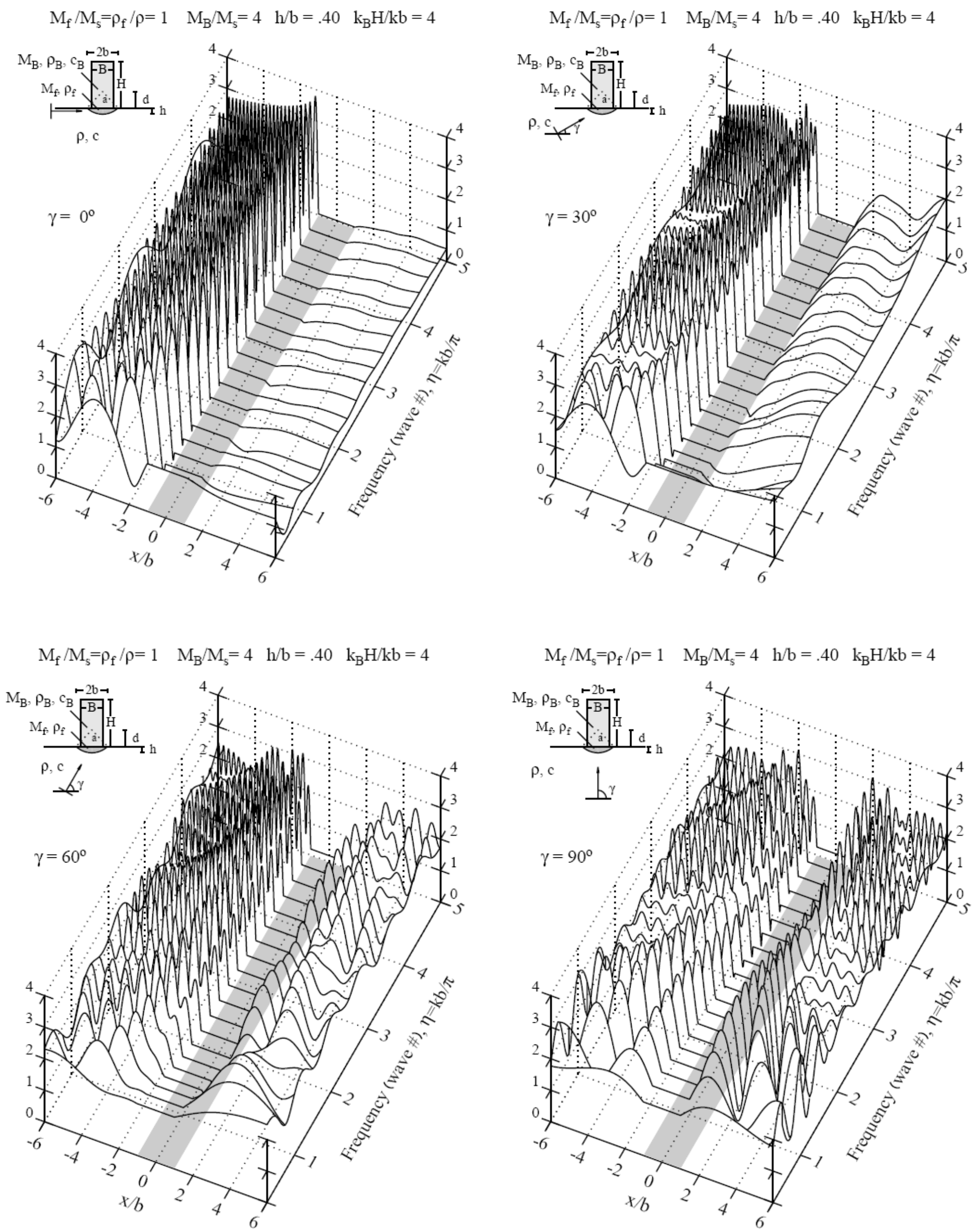

Fig. 8-5 3-D GROUND SURFACE DISPLACEMENT FOR $M_f/M_s = 1$, $M_B/M_s = 4$, $h/b = 0.4$, $k_B H/kb = 4$, **AND** γ **= 90°, 60°, 30°, 0°**

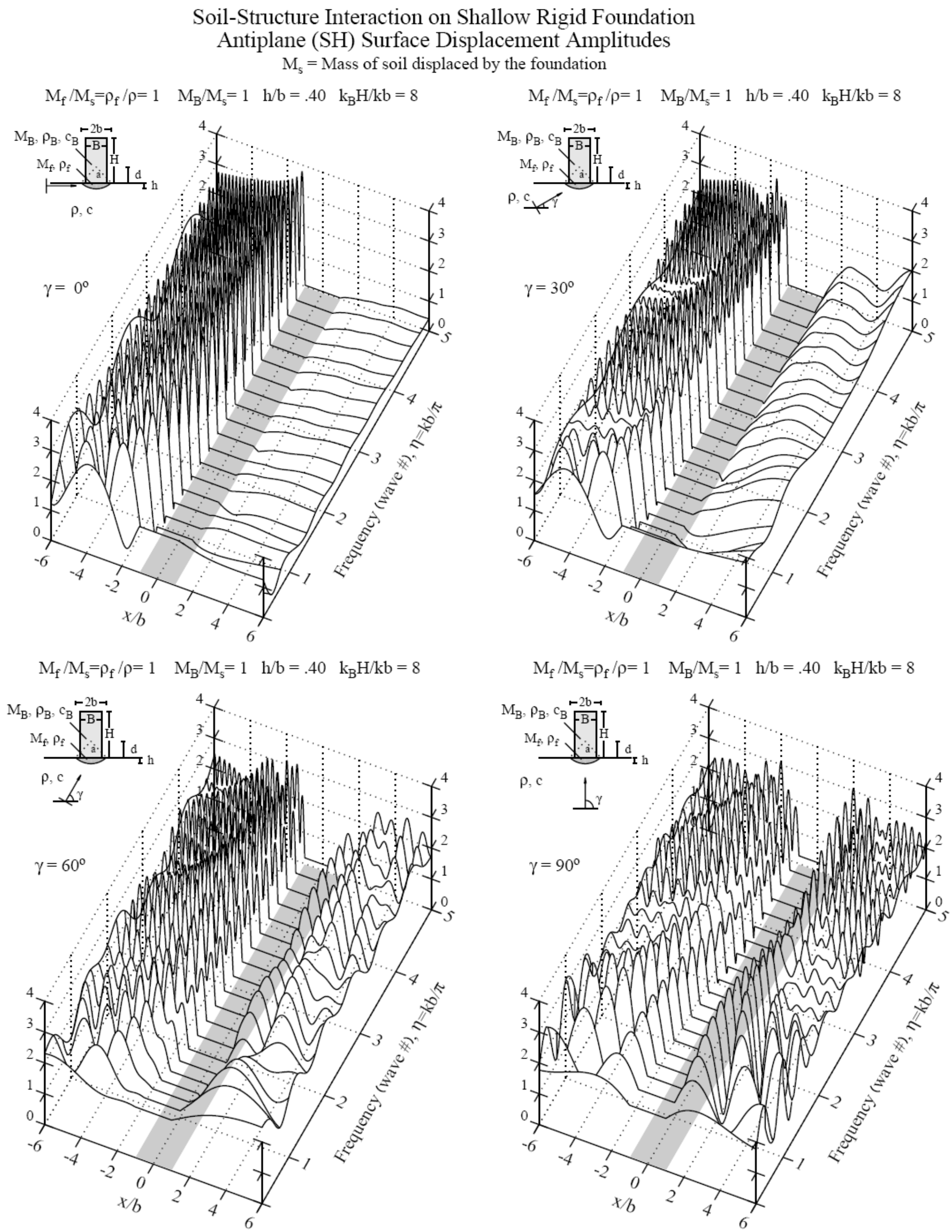

Fig. 8-6 3-D GROUND SURFACE DISPLACEMENT FOR $M_{\mathrm{f}}/M_{\mathrm{s}}=1$, $M_{\mathrm{B}}/M_{\mathrm{s}}=1$, $h/b=0.4$, $k_{\mathrm{B}}H/kb=8$, **AND** γ **= 90º, 60º, 30º, 0º**

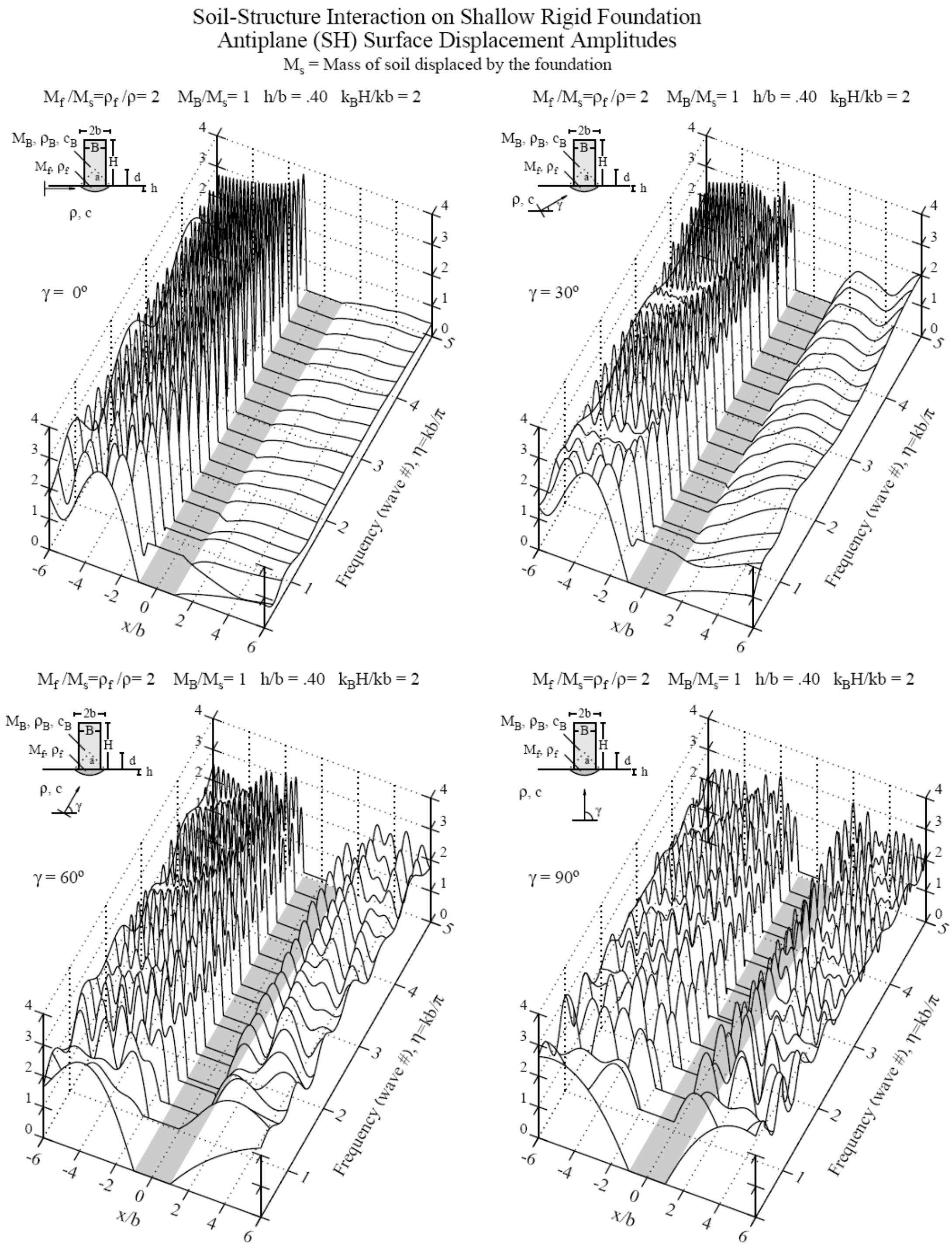

Fig. 8-7 3-D GROUND SURFACE DISPLACEMENT FOR $M_{\mathrm{f}}/M_{\mathrm{s}} = 2$, $M_{\mathrm{B}}/M_{\mathrm{s}} = 1$, $h/b = 0.4$, $k_{\mathrm{B}}H/kb = 2$, **AND** γ **= 90º, 60º, 30º, 0º**

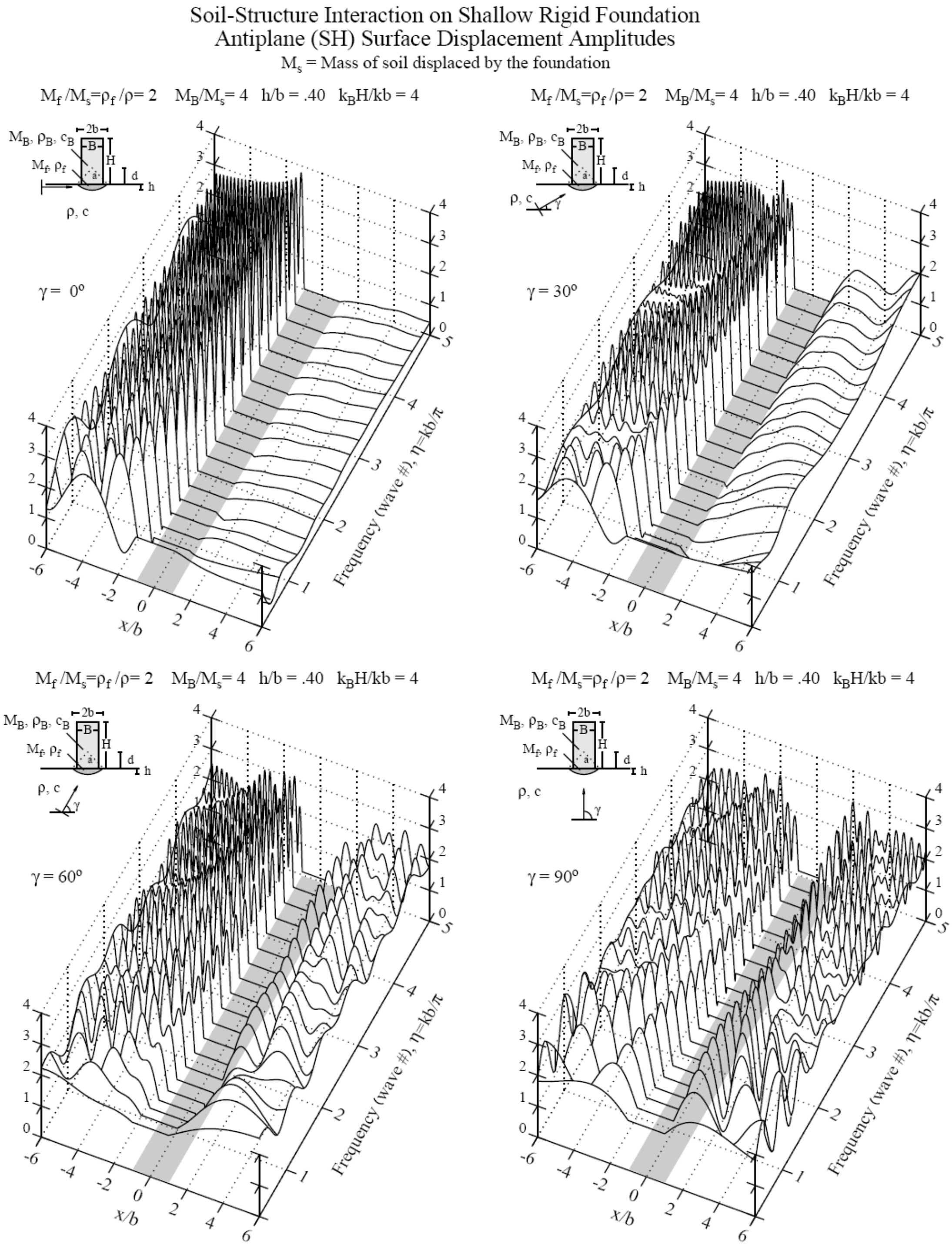

Fig. 8-8 3-D GROUND SURFACE DISPLACEMENT FOR $M_f/M_s = 2$, $M_B/M_s = 4$, $h/b = 0.4$, $k_B H/kb = 4$, **AND** γ **= 90°, 60°, 30°, 0°**

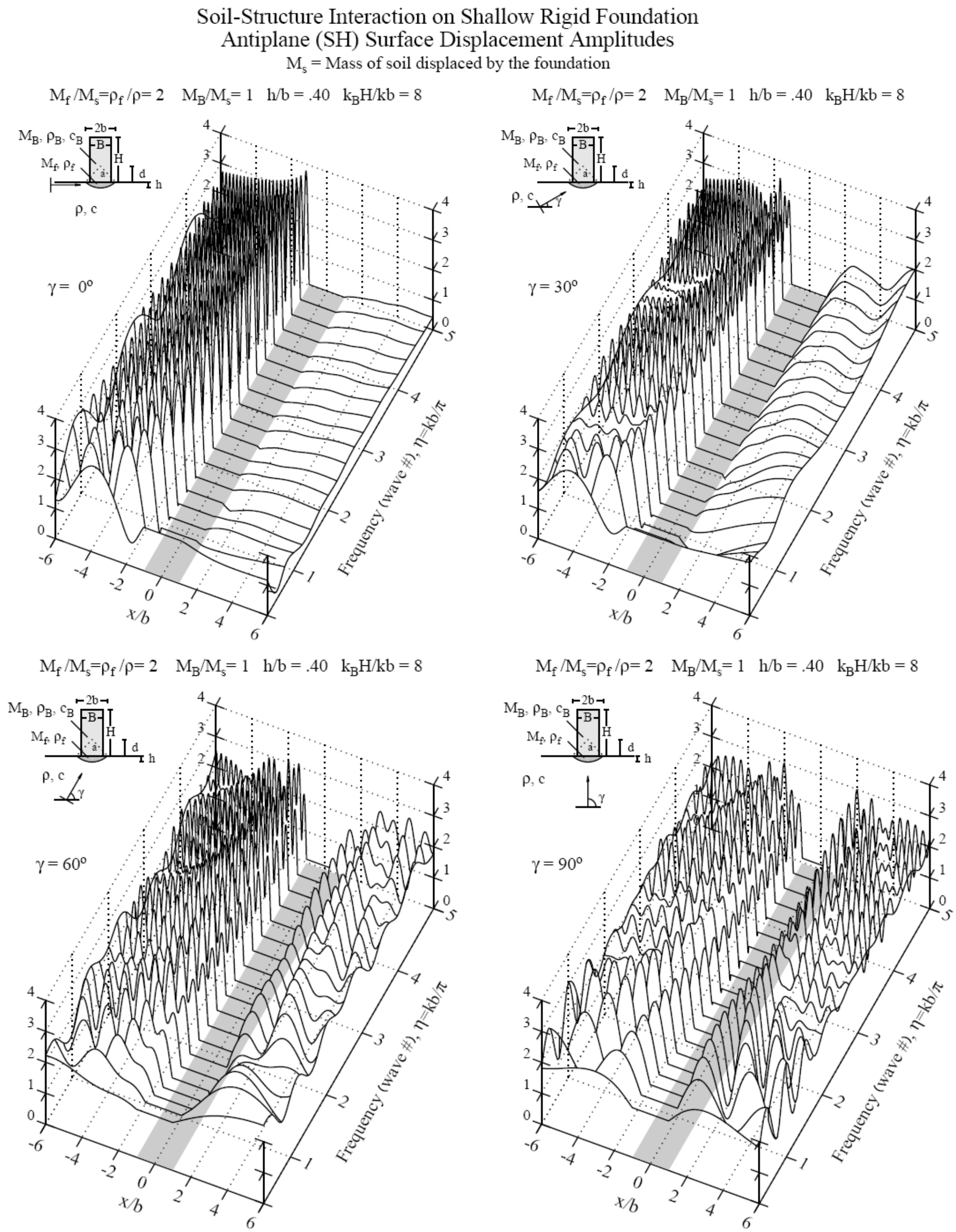

Fig. 8-9 3-D GROUND SURFACE DISPLACEMENT FOR $M_f/M_s = 2$, $M_B/M_s = 1$, $h/b = 0.4$, $k_B H/kb = 8$, **AND** γ **= 90°, 60°, 30°, 0°**

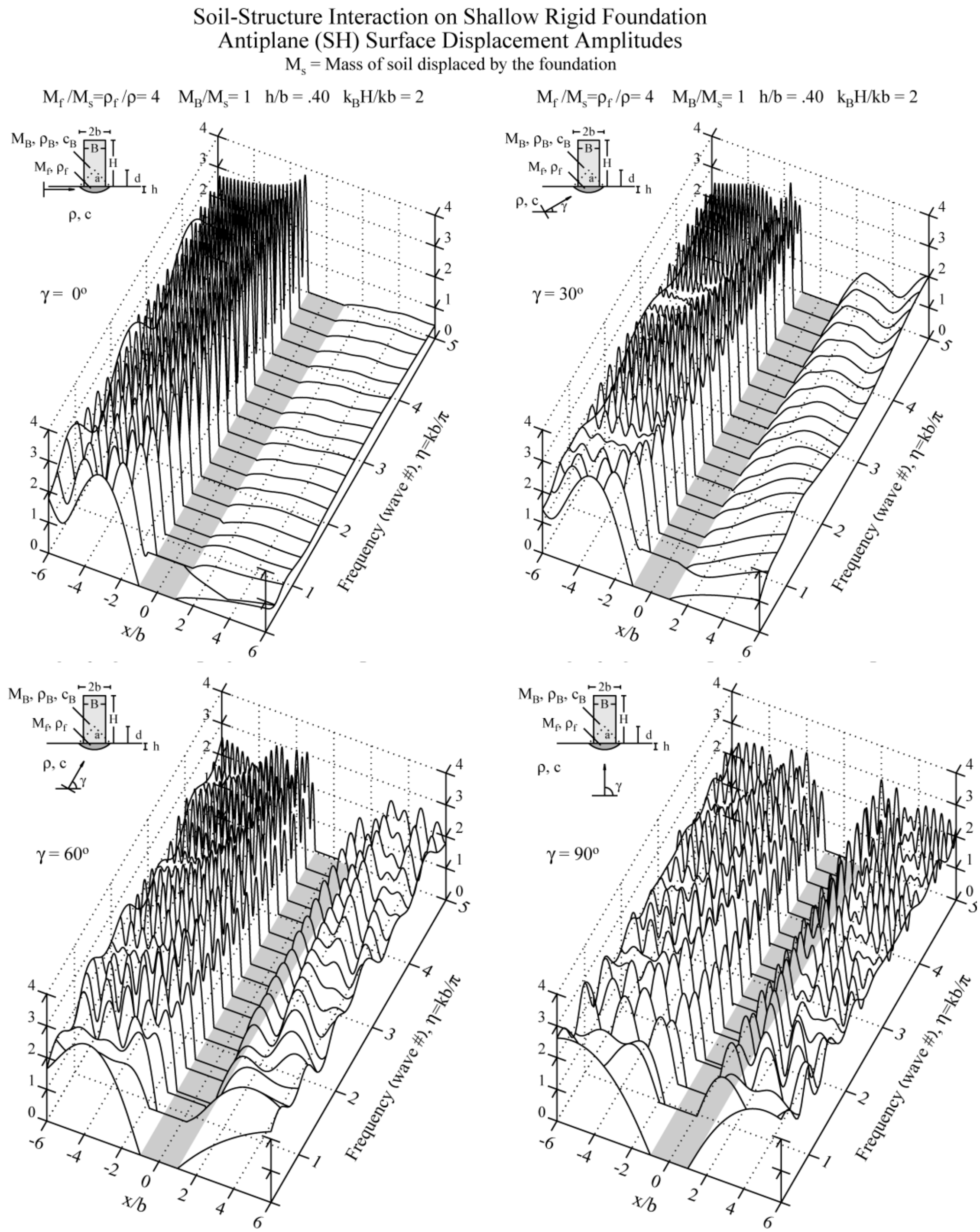

Fig. 8-10 3-D GROUND SURFACE DISPLACEMENT FOR $M_f/M_s=4$, $M_B/M_s=1$, $h/b=0.4$, $k_BH/kb=2$, **AND** γ **= 90º, 60º, 30º, 0º**

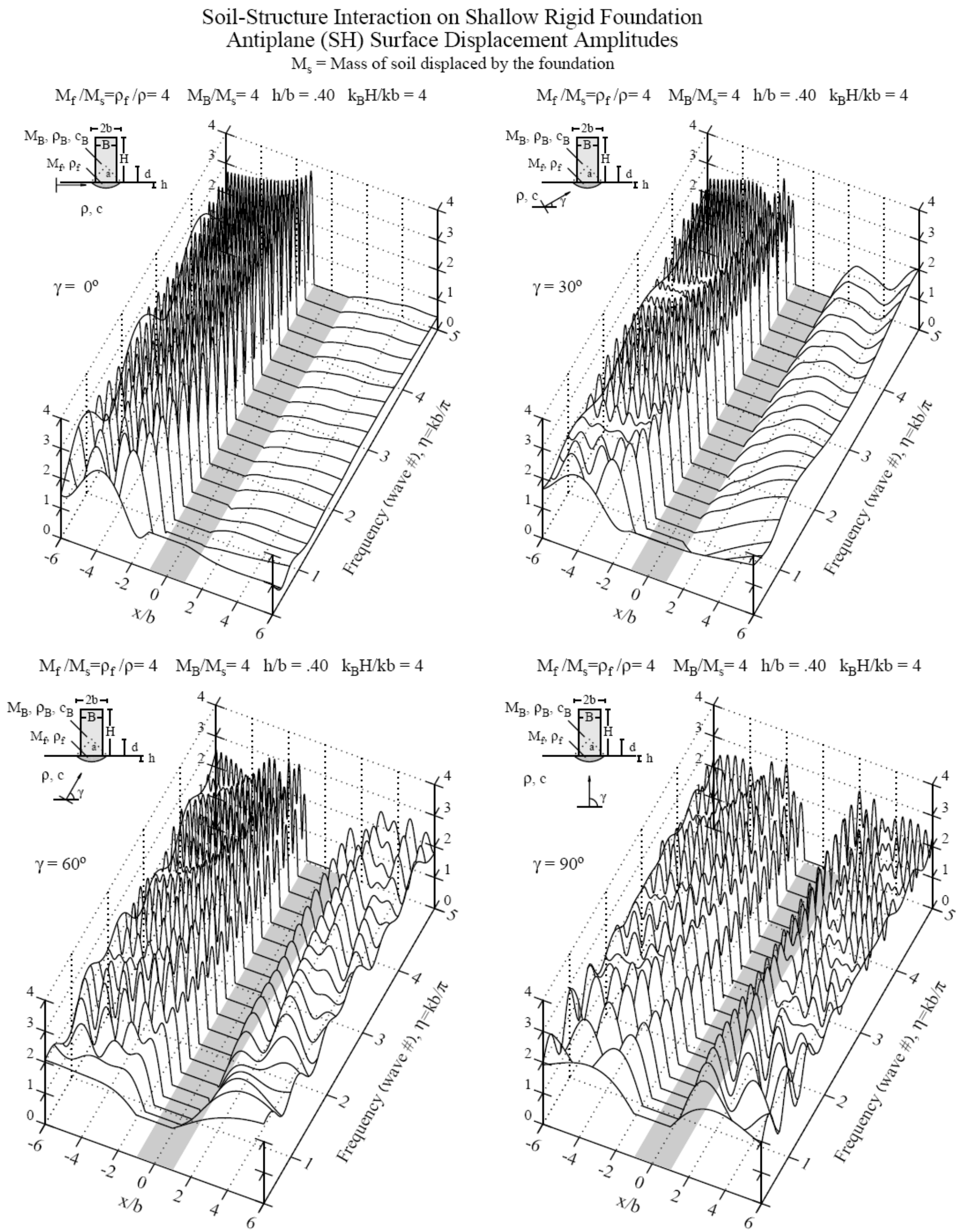

Fig. 8-11 3-D GROUND SURFACE DISPLACEMENT FOR $M_f/M_s = 4$, $M_B/M_s = 4$, $h/b = 0.4$, $k_B H/kb = 4$, **AND** γ **= 90º, 60º, 30º, 0º**

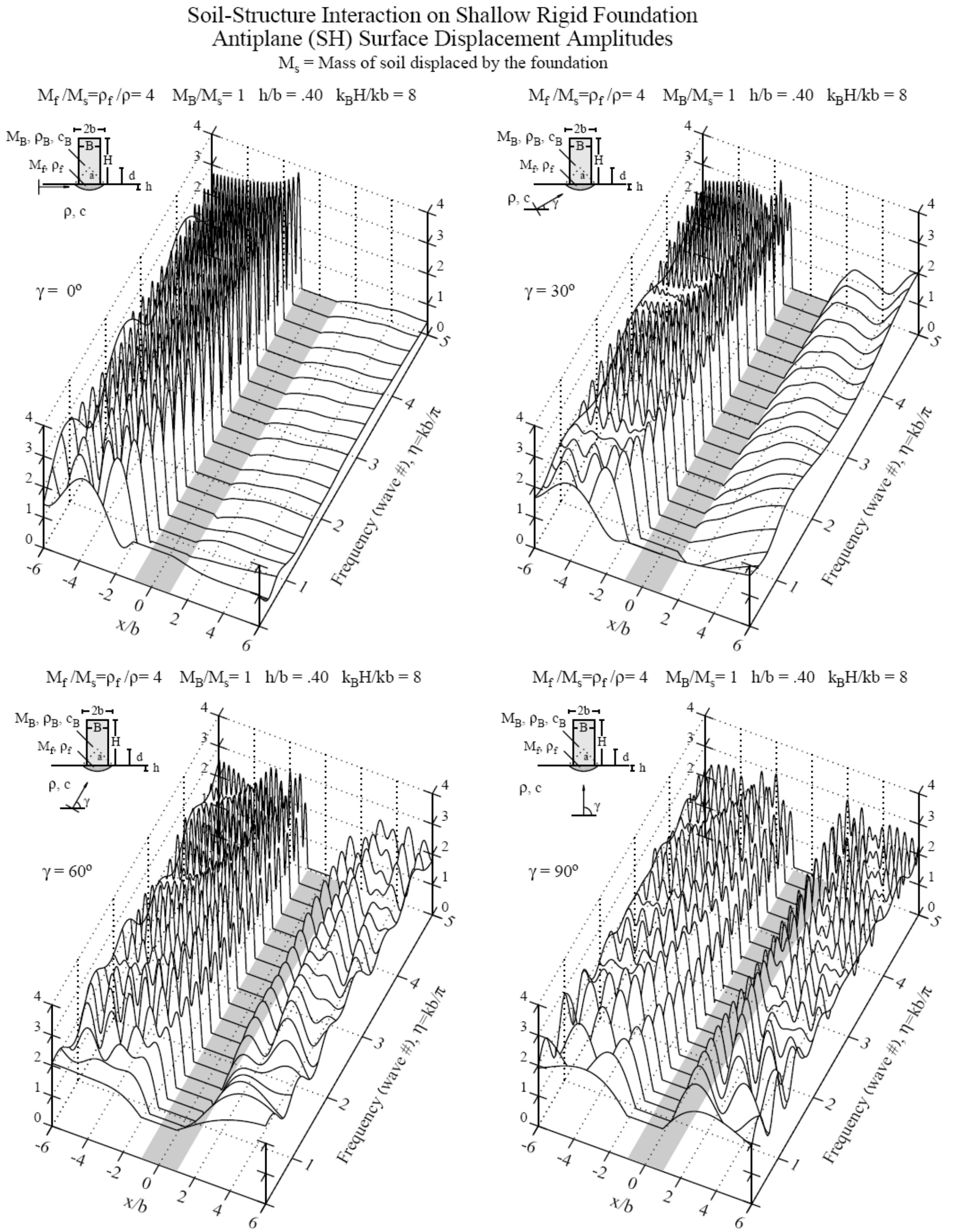

Fig. 8-12 3-D GROUND SURFACE DISPLACEMENT FOR $M_{\mathrm{f}}/M_{\mathrm{s}}=4$, $M_{\mathrm{B}}/M_{\mathrm{s}}=1$, $h/b=0.4$, $k_{\mathrm{B}}H/kb=8$, **AND** γ **= 90°, 60°, 30°, 0°**

As shown in Fig. 8-4 through Fig. 8-12, the existence of rigid foundation has considerable restraining effect on the ground motion. This effect turns into strong screening effect when the incident waves impinge on model horizontally.

The backbone curve of w_0 could be understood as the displacement of rigid foundation whose density is identical to that of the surrounding soil. By setting $M_\mathrm{B}/M_\mathrm{s}=0$ and $M_\mathrm{f}/M_\mathrm{s}=1$

$$w_0^* = w_0\Big|_{\substack{\frac{M_\mathrm{B}}{M_\mathrm{s}}=0 \\ \frac{M_\mathrm{f}}{M_\mathrm{s}}=1}} = \frac{-\dfrac{2\mathrm{i}}{\pi ka}\displaystyle\sum_{n=-\infty}^{\infty}\frac{\overline{a}_n^{(\mathrm{f})}\xi_n}{\mathrm{H}_n^{(1)}(ka)}}{\dfrac{ka}{2}\left(1-\dfrac{\sin\delta\pi}{\delta\pi}\right)+\dfrac{\mathrm{H}_1^{(1)}(ka)}{\mathrm{H}_0^{(1)}(ka)}} \tag{14.41}$$

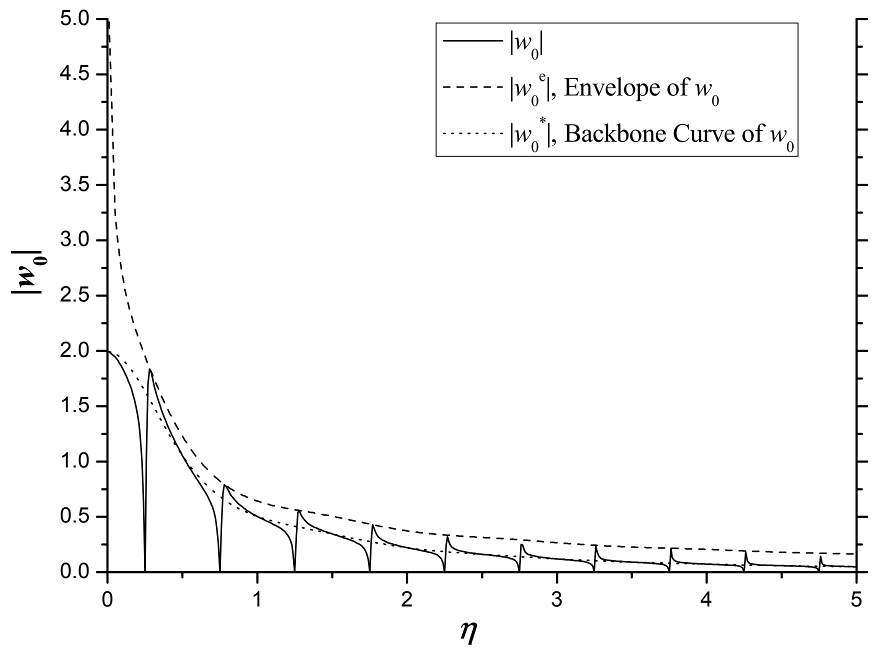

Fig. 8-13 ENVELOPE AND BACKBONE CURVE PLOT FOR DISPLACEMENT AMPLITUDE SPECTRUM $M_\mathrm{f}/M_\mathrm{s}=1$, $M_\mathrm{B}/M_\mathrm{s}=1$, $h/b=1$, $k_\mathrm{B}H/kb=2$, $\gamma = 45^\circ$

It needs to be noted that when we assemble free-field and scattered wave field to the total motion on the ground surface, $w = w^{(\mathrm{ff})} + w^{(\mathrm{S})}$, here $w^{(\mathrm{ff})}$ needs to be calculated by its original formula (8.5) and (8.6) to prevent numerical drift when x/a becomes large. Similarly, $w^{(\mathrm{S})}$ also should be computed from its originally defined formula (14.7) to ensure the traction-free boundary condition (14.1) on the ground surface, in that $w^{(S)}$ defined in coordinate system $(\bar{r},\bar{\phi})$ as Eqn.(14.8), although transformed from (14.7), not necessarily satisfy boundary condition (14.1). In fact, numerical results prove that for incident SH line source which are represented in the following separate paper; but for incident plane SH-waves, traction-free boundary condition is satisfied pretty well for either upper or lower coordinate systems. However, utilization of Eqn.(14.7) involves resolution of infinite linear equation (14.9), which may induce more errors into the ground displacement results. And we tried several cases when frequencies are relatively low (for example, $\eta < 2$) and numerical resolutions converge, both of those approaches give out the same ground surface displacement results. Therefore, all the numerical results involving scattered waves $w^{(S)}$ present here in this section were still calculated based on Eqn.(14.8).

8.1.7 Traction-Free Boundary Condition on the Ground Surface

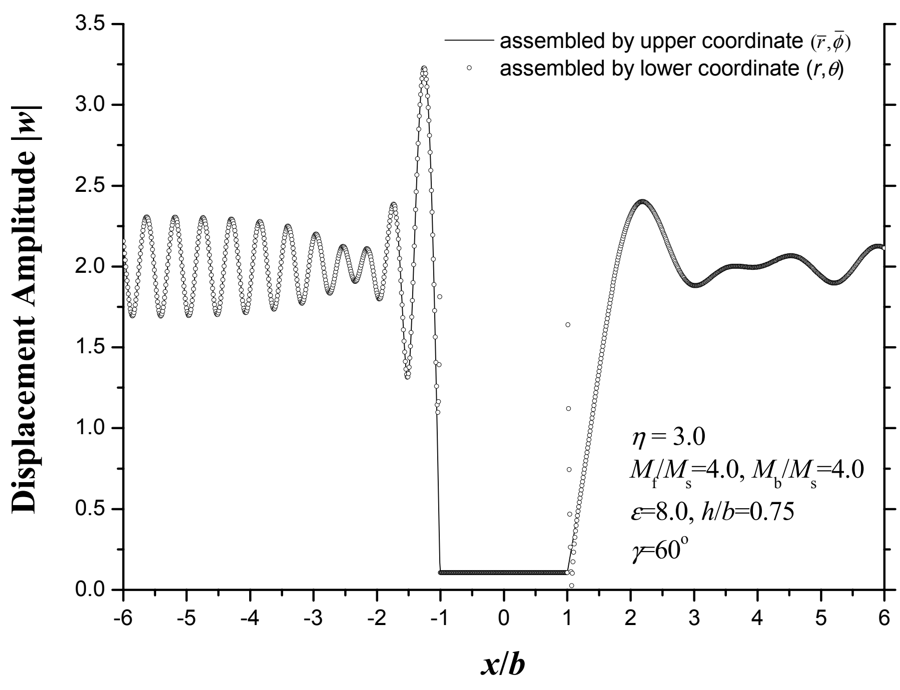

Fig. 8-14 DISPLACEMENT AMPLITUDE PLOT FOR $\eta = 3$, $M_f/M_s = 4$, $M_B/M_s = 4$, $h/b = 0.75$, $k_B H/kb = 8$, γ= 60° ASSEMBLED BY DIFFERENT COORDINATES

The outer surface of half-space L must have no normal stress on it, which has been satisfied by the form of scattered waves equation (14.7) defined in the coordinate system (r,θ). However, the scattered wave that we applied to satisfy continuity boundary condition on circular-arc $\underline{L}$ and determine the ground surface displacement amplitudes is based on the upper polar coordinate system $(\overline{r},\overline{\phi})$. That means the scattered wave function based on coefficients $\{\overline{A}_n\}$ may not satisfy the traction-free boundary condition strictly. Therefore, an alternative way is to solve out coefficients $\{A_n\}$ from $\{\overline{A}_n\}$ by equation (14.9) and then calculate ground surface displacement amplitudes based on $\{A_n\}$. This approach could ensure the validities of both boundary conditions.

However, due to various numerical errors induced by floating-point arithmetic and round-off, especially by Graf's formula (8.26), it is better to use coefficients $\{\overline{A}_n\}$ from coordinate system $(\overline{r},\overline{\phi})$ rather than $\{A_n\}$ and (r,θ) to avoid larger errors, which would cause divergence and drifting of displacement amplitude results. Depending on our trials, the latter method could only calculate for the cases of h/b larger than 0.5 and η up to 4.0; in comparison, the former method do not have apparent limitation for h/b and can calculate for the cases of η at least up to 10.0. For the cases when both methods capable, displacement amplitude results agree well. Thus we adopt upper coordinate $(\overline{r},\overline{\phi})$ and its corresponding coefficients $\{\overline{A}_n\}$ to compute all the results illustrated in the subsequent plots, if not specified.

8.2 Incident Cylindrical SH-Waves

The model shown in Fig. 8-15 for this section is exactly the same as the one discussed in the last section, as illustrated in Fig. 8-2. The only difference is the excitation source, which is changed to a SH-wave point (line) source located at O' with radial distance and incident angle with respect to horizontal axis equal R and γ, respectively. All the other notations are same as Fig. 8-2.

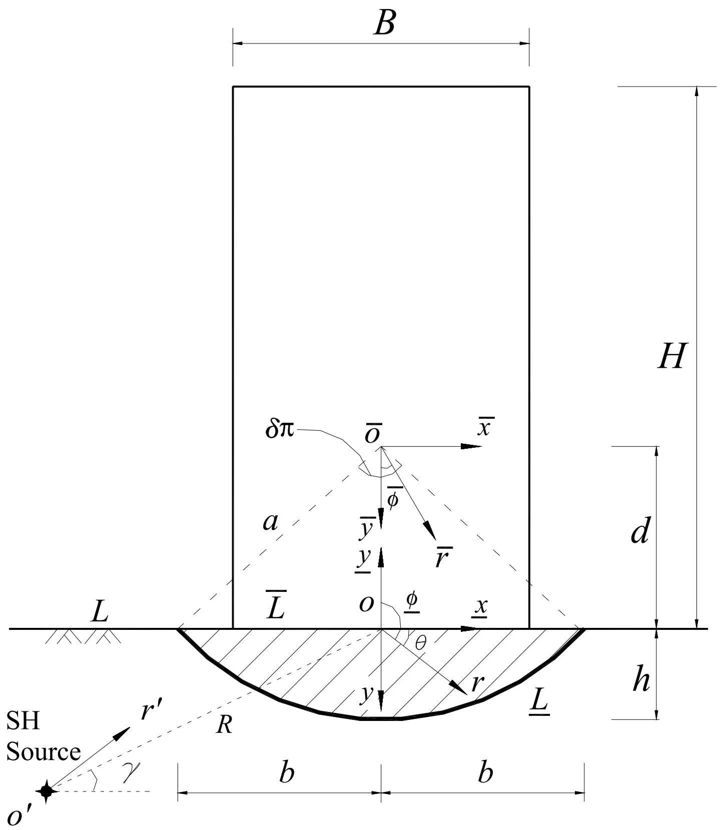

Fig. 8-15 SOIL-STRUCTURE INTERACTION SUBJECTED TO INCIDENT CYLINDICAL SH-WAVES

All the stress and displacement boundary conditions are also same as plane incident SH-wave cases. The incident point-source SH-waves with unit amplitude could be expressed

$$w_{o'}^{(i)}(r') = \frac{\mathrm{H}_0^{(1)}\left(kr'\right)}{\left|\mathrm{H}_0^{(1)}\left(kR\right)\right|} \tag{14.42}$$

and the free-field motion field in absence of any variation of topography is represented as follows for polar coordinate systems (r,θ) and $(\bar{r},\bar{\phi})$, which has been derived in details in section 2.2.2 in Chapter 2.

$$w^{(\mathrm{ff})}(r,\theta) = w^{(\mathrm{i})} + w^{(\mathrm{r})} = \sum_{n=0}^{\infty} a_n^{(\mathrm{f})} \mathrm{J}_n(kr)\cos n\theta \tag{14.43}$$

$$w^{(\mathrm{ff})}(\bar{r},\bar{\phi}) = \sum_{m=-\infty}^{\infty} \bar{a}_m^{(\mathrm{f})} \mathrm{J}_m(k\bar{r})\mathrm{e}^{\mathrm{i}m\bar{\phi}} \tag{14.44}$$

where for $n = 0,1,2,\cdots$; $m = 0,\pm1,\pm2,\cdots$

$$a_n^{(\mathrm{f})} = 2\varepsilon_n(-1)^n \frac{\mathrm{H}_n^{(1)}(kR)}{\left|\mathrm{H}_0^{(1)}(kR)\right|}\cos n\gamma \tag{14.45}$$

$$\begin{aligned}\bar{a}_m^{(\mathrm{f})} &= \sum_{n=0}^{\infty} \varepsilon_n \mathrm{i}^n \frac{\mathrm{H}_n^{(1)}(kR)}{\left|\mathrm{H}_0^{(1)}(kR)\right|}\cos n\gamma\left[\mathrm{J}_{m+n}(kd) + \mathrm{J}_{m-n}(kd)\right] \\ &= \frac{\mathrm{i}^m}{\left|\mathrm{H}_0^{(1)}(kR)\right|}\left[\mathrm{H}_m^{(1)}(k\underline{R})\mathrm{e}^{-\mathrm{i}m\underline{\gamma}} + \mathrm{H}_m^{(1)}(k\bar{R})\mathrm{e}^{-\mathrm{i}m\bar{\gamma}}\right]\end{aligned} \tag{14.46}$$

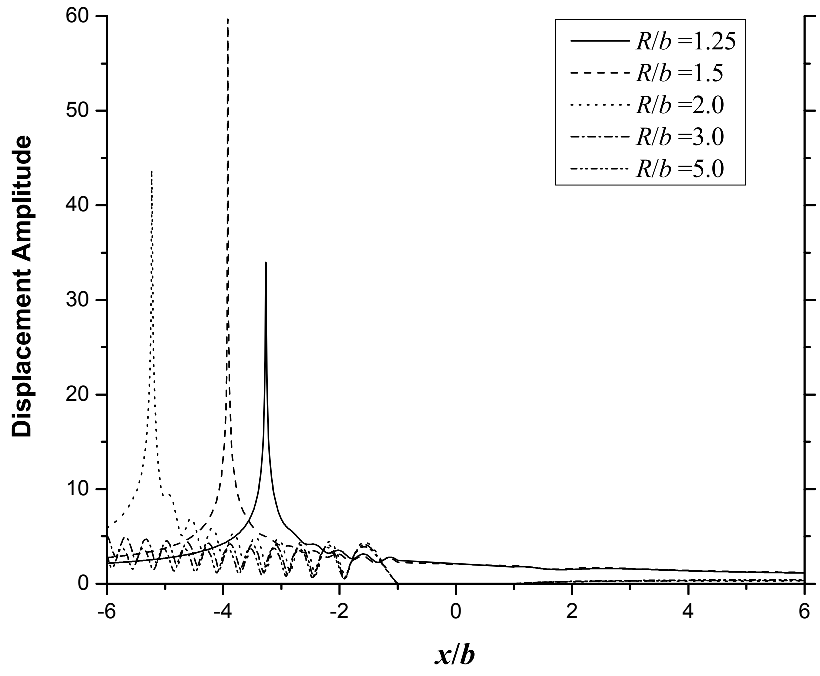

Fig. 8-16 SURFACE DISPLACEMENT AMPLITUDE FOR $\eta = 3.0$, $M_\mathrm{f}/M_\mathrm{s} = 2.0$, $M_\mathrm{B}/M_\mathrm{s} = 5.0$, $k_\mathrm{B}H/kb = 2$, ν=0.25, $\delta\pi = 0^\circ$ **AND** $R/b = 1.25$, 1.5, 2.0, 3.0, 5.0

Expressions of the scattered wave in polar coordinate systems (r,θ) and $(\overline{r},\overline{\phi})$ are also same as equations (14.7) and (14.8), respectively. Thus the remaining derivation procedures are equivalent to the corresponding portions of the plane incident SH-wave cases. Therefore those steps are not repeated here.

To investigate the correlation of displacement and stress responses on the ground surface and shear beam with the location of SH-wave source, Fig. 8-16 is plotted above. Note that one more argument, radial distance between source focus and midpoint of foundation on the ground surface R, is added in the intial conditions. Fig. 8-17 shows the effectiveness of envelope and backbone curve equations (14.39) and (14.41) on cylindrical incident wave cases.

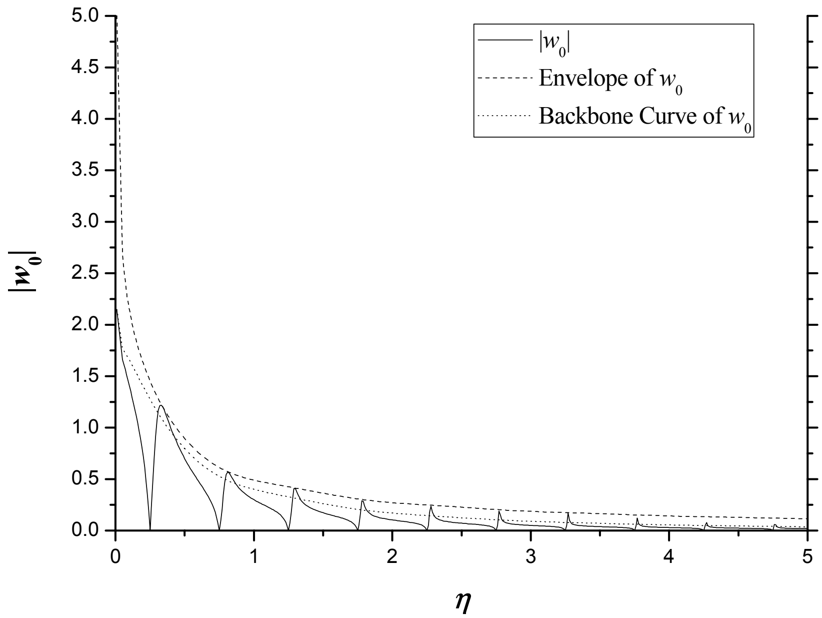

Fig. 8-17 ENVELOPE AND BACKBONE CURVE PLOT FOR DISPLACEMENT AMPLITUDE SPECTRUM $M_{\rm f}/M_{\rm s}=2$, $M_{\rm B}/M_{\rm s}=5$, $h/b=0.451$, $k_{\rm B}H/kb=2$, $R/a=2$, γ **= 90º**

Fig. 8-18 and Fig. 8-19 are the displacement amplitude diagrams for different R. When the point source is excessively close to the foundation, say R = 1.25b, as the black line in the above figure, the resultant displacement curve might not converge. That's why the disp amplitudes of the two rim points of the foundation are not equal while supposed to. Some subsequent figures have the same phenomena also. The red curve represents the case when R=2.0b, the convergence is much better.

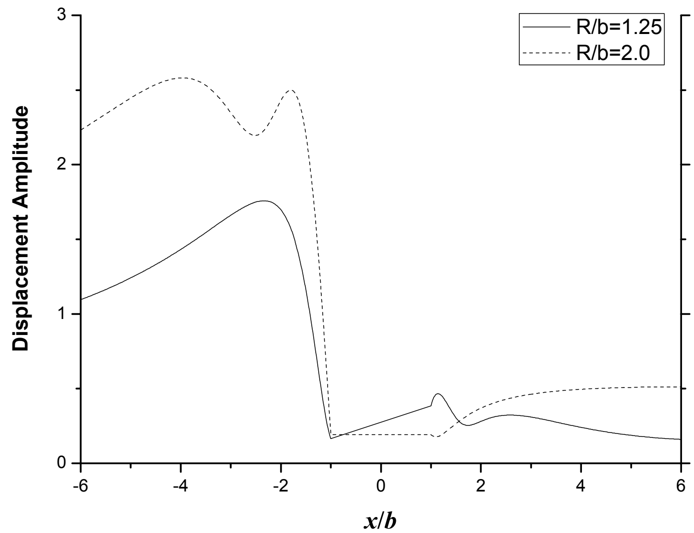

Fig. 8-18 GROUND SURFACE DISPLACEMENT FOR $\eta = 1$; $M_f / M_s = 1$; $M_B / M_s = 1.5$; $k_B H / kb = 2$; δ=0.5; $\gamma = 45^o$; R/b **=1.25 OR 2.0**

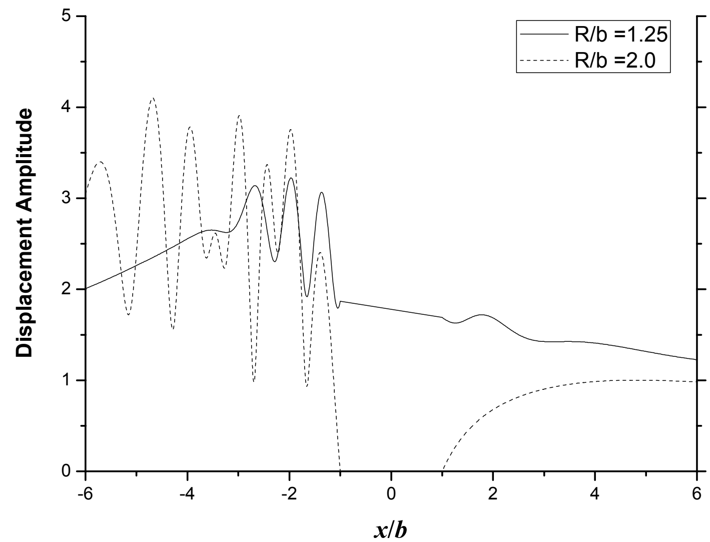

Fig. 8-19 GROUND SURFACE DISPLACEMENT FOR $\eta = 3$; $M_f / M_s = 2$; $M_B / M_s = 5$; $k_B H / kb = 2$; δ=0.25; $\gamma = 30^o$; R/b **=1.25 OR 2.0**

Chapter 9

SOIL-STRUCTURE INTERACTION: A SHEAR BEAM WITH A FLEXIBLE ELASTIC SEMI-CYLINDRICAL FOUNDATION

Similar to previous two chapters, the foundation in most of SSI research papers is either neglected or simplified as a rigid body that moves as a whole. As a juncture connecting superstructure and ground, the way by which we simplify the model of foundation is crucial to the effectiveness and accuracy of numerical results. Almost every building has a foundation so as to transfer upper loads to the soil below evenly with adequate settlement. And except some tower or mast structures, most of engineering structures ought not to be mathematically over-simplified to a single degree-of-freedom dynamic system. Therefore, a mathematical model with a flexible foundation appears to have high significance in SSI research.

9.1 A Rectangular Shear beam with A Flexible Semi-Circular Foundation

The model studied in this chapter is a two-dimensional rectangular shear beam (also referred to as building afterwards) erected on a semi-circular foundation of radius a embedded on a half-space, as illustrated in Fig. 9-1. All materials here are homogeneous, elastic, and isotropic. A train of parallel harmonic incident SH-wave excites the model from the deep earth at an incidence angel γ with respect to the horizontal axis. The width and height of the structure are $2a$ and h, respectively. A Cartesian coordinate system (x, y) and a corresponding polar coordinate system (r, θ) have been defined with origin at the center of the semi-circular foundation. Another Cartesian coordinate system (x_1, y_1) is located at the left verge of the shear beam, foundation, and half-space. The material constants, namely shear modulus and wave speed, of the building, foundation, and half-space are respectively denoted by $\mu_{\mathrm{B}}, C_{\beta_{\mathrm{B}}}$, $\mu_{\mathrm{f}}, C_{\beta_{\mathrm{f}}}$ and μ, C_{β} .

9.1.1 Wave Field in the Half-Space

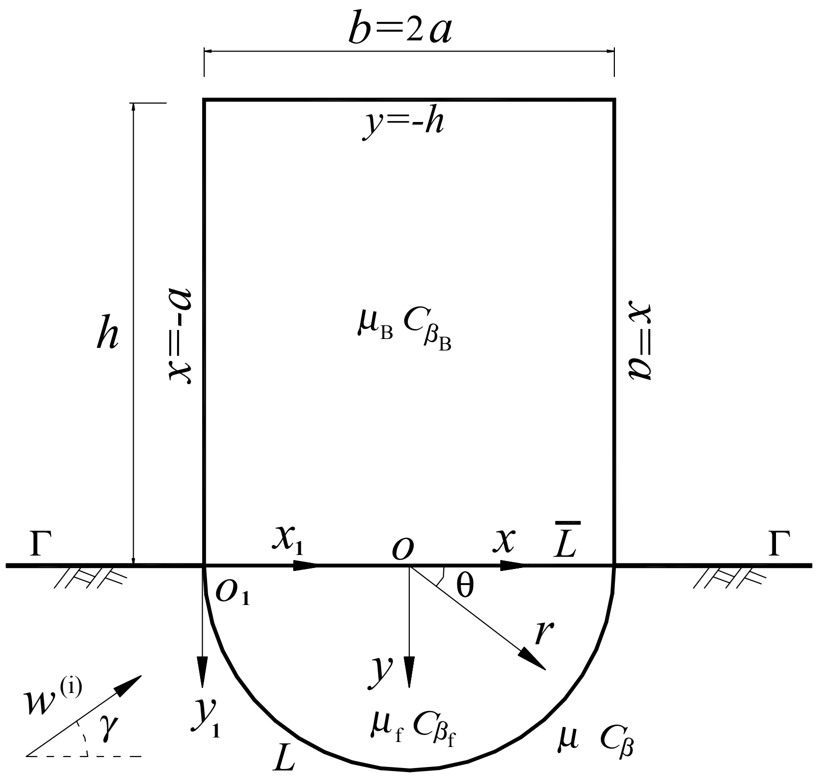

Fig. 9-1 A SHEAR BEAM WITH A FLEXIBLE SEMI-CYLINDRICAL FOUNDATION

The free-field standing wave field in the half-space is given by

$$w^{(\mathrm{ff})}(r,\theta) = w^{(\mathrm{i})} + w^{(\mathrm{r})} = \sum_{n=0}^{\infty} a_{0,n} \mathrm{J}_n(kr)\cos n\theta \tag{15.1}$$

where for n=0, 1, 2…

$$a_{0,n} = 2\varepsilon_n \mathrm{i}^n \cos n\gamma \tag{15.2}$$

The wave field in the half-space scattered and diffracted in the presence of the foundation is

$$w^{(\mathrm{S})}(r,\theta)=\sum_{n=0}^{\infty}A_n\mathrm{H}_n^{(1)}(kr)\cos n\theta \tag{15.3}$$

9.1.2 Wave Field within the Shear beam

Same as what we assumed in Chapter 7, the total transmitted field within the structure could be represented as a summation of parallel-plate waveguide modes, of the (same) harmonic frequency ω, wave speed C_{β_B}, and wave number $k_\mathrm{B}=\omega/C_{\beta_\mathrm{B}}$. For $-a\le x\le a$, $-h\le y\le 0$,

$$w^{(\mathrm{B})}(x,y)=\sum_{m=0}^{\infty}B_m\cos\left[a_m(x+a)\right]\cos\left[\xi_m(y+h)\right] \tag{15.4}$$

where for m=0, 1, 2…

$$a_m=\frac{m\pi}{2a}=\frac{m\pi}{b},\qquad \xi_m=\sqrt{k_\mathrm{B}^2-a_m^2} \tag{15.5}$$

are respectively the wave numbers in the x and y directions of the waves in the structure, and B_m the amplitude of the mth mode. It will be seen below that each mode of the wave field will satisfy the zero stress boundary conditions on both the left and right sides, $x=\pm a$, and the top side, $y=-h$, of the structure.

9.1.3 Wave Field within the Foundation

The transmitted field within the semi-circular foundation could be represented with a Fourier-Bessel series, of the (same) harmonic frequency ω, wave speed β_f and wave number $k_\mathrm{f}=\omega/\beta_\mathrm{f}$

$$w^{(\mathrm{F})}(r,\theta)=\sum_{n=0}^{\infty}\mathrm{J}_n(k_\mathrm{f}r)\left(C_n\cos n\theta+D_n\sin n\theta\right), \tag{15.6}$$

where C_n and D_n are two sets of complex constants to be determined. Only the Bessel functions of the first kind $\mathrm{J}_n(\cdot)$ for n=0, 1, 2… are used as the waves are finite everywhere inside the foundation, including the origin ($r=0$). Since the foundation is semi-circular in shape, the range of θ is between 0 and π (half-range), which means that the trigonometric sine and cosine functions are not mutually orthogonal (they are orthogonal only in the full range 0 to 2π). In fact, in the half-range 0 to π, where the half-space ($y>0$) is, the cosine functions are orthogonal, and hence all sine functions can be expressed in terms of the cosine functions.

Here the same expansion as Chapter 3 is also applied in this approach to express sine function in terms of the cosine functions in both ranges $[-\pi,0]$ and $[0,\pi]$: with $\varepsilon_0=1$, $\varepsilon_n=2$ for n >0, and for m = 1,2,3…

$$\sin m\theta = \mp\sum_{m+n\text{ odd}} \boldsymbol{s}_{mn}\cos n\theta = \begin{cases} -\dfrac{2m}{\pi}\displaystyle\sum_{\substack{n=0\\ m+n\text{ odd}}}^{\infty}\dfrac{\varepsilon_n}{m^2-n^2}\cos n\theta, & -\pi\le\theta\le 0 \\ +\dfrac{2m}{\pi}\displaystyle\sum_{\substack{n=0\\ m+n\text{ odd}}}^{\infty}\dfrac{\varepsilon_n}{m^2-n^2}\cos n\theta, & 0\le\theta\le\pi \end{cases} \tag{15.7}$$

with

$$\boldsymbol{s}_{mn} = \frac{2\varepsilon_n m}{\pi\left(m^2-n^2\right)} \tag{15.8}$$

The clause "*m*+*n* odd" in the summation means that when m is even, only the odd n terms are used in the summation, and vice versa. Note that with the sine function being an odd function ($\sin(-\theta)=-\sin(\theta)$), the corresponding cosine function expansion is also defined to be equal in absolute value but of opposite sign on either side of the axis θ=0.

Thus Eqn. (15.6) can be rewritten as, for $y>0$, namely $-\pi\le\theta\le\pi$

$$w^{(\mathrm{F})}(r,\theta) = \sum_{n=0}^{\infty}\left[C_n \mathrm{J}_n(k_\mathrm{f} r) + \sum_{\substack{m=0\\ m+n\text{ odd}}}^{\infty}\boldsymbol{s}_{mn}\mathrm{J}_m(k_\mathrm{f} r)D_m\right]\cos n\theta\,, \tag{15.9}$$

in terms of merely the cosine functions.

9.1.4 Boundary Conditions

The traction-free boundary conditions on the flat ground surface are automatically satisfied by the free-field waves $w^{(\mathrm{ff})}$ and the scattered waves $w^{(\mathrm{S})}$ because of

$$\mu \frac{\partial w^{(\mathrm{S})}}{\partial \theta}\bigg|_{\theta=0,\pi} = -\sum_{n=0}^{\infty} n A_n \mathrm{H}_n^{(1)}(kr)\sin n\theta \bigg|_{\theta=0,\pi} \equiv 0 \tag{15.10}$$

The traction-free boundary condition equations at the outer boundaries of the building are

$$\begin{aligned} \mu_{\mathrm{B}} \frac{\partial w^{(\mathrm{B})}}{\partial x} &= 0 \ \text{ at } \ x = \pm a, \ -h \le y \le 0 \\ \mu_{\mathrm{B}} \frac{\partial w^{(\mathrm{B})}}{\partial y} &= 0 \ \text{ at } \ y = -h, \ -a \le x \le a \end{aligned} \tag{15.11}$$

These two boundary conditions are also satisfied automatically.

The stress and displacement continuity equations along the semi-circular interface $\underline{L}$ ($r = a$, $0 \le \theta \le \pi$) are:

· Displacement continuity:

$$w^{(\mathrm{ff})} + w^{(\mathrm{S})}\Big|_{r=a} = w^{(\mathrm{F})}\Big|_{r=a}, 0 \le \theta \le \pi \tag{15.12}$$

· Stress continuity:

$$\mu \frac{\partial}{\partial r}\left(w^{(\mathrm{ff})} + w^{(\mathrm{S})}\right)\bigg|_{r=a} = \mu_{\mathrm{f}} \frac{\partial w^{(\mathrm{F})}}{\partial r}\bigg|_{r=a}, 0 \le \theta \le \pi \tag{15.13}$$

Substitution of Eqns. (15.1), (15.3), and (15.9) into Eqns.(15.12) and (15.13) leads to the following two boundary condition equations, for n = 0, 1, 2, 3…

$$\begin{Bmatrix} \mathrm{J}_n(ka) \\ \mathrm{J}_n'(ka) \end{Bmatrix} a_{0,n} + \begin{Bmatrix} \mathrm{H}_n^{(1)}(ka) \\ \mathrm{H}_n^{(1)\prime}(ka) \end{Bmatrix} A_n = \begin{Bmatrix} \mathrm{J}_n(k_{\mathrm{f}}a) \\ \kappa \mathrm{J}_n'(k_{\mathrm{f}}a) \end{Bmatrix} C_n + \sum_{\substack{m=1 \\ n+m \text{ odd}}}^{\infty} \begin{Bmatrix} \mathrm{J}_m(k_{\mathrm{f}}a) \\ \kappa \mathrm{J}_m'(k_{\mathrm{f}}a) \end{Bmatrix} \boldsymbol{s}_{mn} D_m \tag{15.14}$$

where material property ratio $\kappa = \dfrac{\mu_{\mathrm{f}} k_{\mathrm{f}}}{\mu k}$ in the equation for the stress boundary condition.

The stress and displacement continuity equations on the flat interface $\overline{L}$ between foundation and building at $y=0$, $-a \le x \le a$, $\theta = 0,\ \pi$ could be summarized as follows

· Displacement continuity:

$$w^{(\mathrm{F})}\Big|_{y=0} = w^{(\mathrm{B})}\Big|_{y=0}, \qquad |x| \le a \tag{15.15}$$

· Stress continuity:

$$\mu_{\mathrm{f}} \frac{\partial w^{(\mathrm{F})}}{\partial y}\bigg|_{y=0} = \mu_{\mathrm{B}} \frac{\partial w^{(\mathrm{B})}}{\partial y}\bigg|_{y=0}, \qquad |x| \le a \tag{15.16}$$

To apply these two boundary conditions at y=0, first transform Eqn. (15.7) from polar coordinate (r,θ) for $\theta = 0,\ \pi$ to Cartesian coordinate (x, y) for $y = 0$. With $\theta = 0$, and $r = x$ at $y = 0$, for $0 \le x \le a$

$$\begin{gathered} w^{(\mathrm{F})}(x,y)\Big|_{y=0} = \sum_{n=0}^{\infty} C_n \mathrm{J}_n(k_{\mathrm{f}} x) \\ \mu_{\mathrm{f}} \frac{\partial w^{(\mathrm{F})}}{\partial y}\bigg|_{y=0} = \mu_{\mathrm{f}} \frac{\partial w^{(\mathrm{F})}}{\partial \theta}\bigg|_{\theta=0} = \mu_{\mathrm{f}} \sum_{n=0}^{\infty} n D_n \mathrm{J}_n(k_{\mathrm{f}} x) \end{gathered} \tag{15.17}$$

With $\theta = \pi$, and $r = -x$ at $y = 0$, so with $\cos n\pi = (-1)^n$, $\mathrm{J}_n(-z) = (-1)^n \mathrm{J}_n(z)$, for $-a \le x \le 0$:

$$\begin{gathered} w^{(\mathrm{F})}(x,y)\Big|_{y=0} = \sum_{n=0}^{\infty} C_n \mathrm{J}_n(-k_{\mathrm{f}} x)(-1)^n = \sum_{n=0}^{\infty} C_n \mathrm{J}_n(k_{\mathrm{f}} x) \\ \mu_{\mathrm{f}} \frac{\partial w^{(\mathrm{F})}}{\partial y}\bigg|_{y=0} = \mu_{\mathrm{f}} \frac{\partial w^{(\mathrm{F})}}{\partial \theta}\bigg|_{\theta=\pi} = \mu_{\mathrm{f}} \sum_{n=0}^{\infty} n D_n \mathrm{J}_n(-k_{\mathrm{f}} x)(-1)^n = \mu_{\mathrm{f}} \sum_{n=1}^{\infty} n D_n \mathrm{J}_n(k_{\mathrm{f}} x) \end{gathered} \tag{15.18}$$

So that for $-a \le x \le a$, at $y = 0$, over the whole flat surface of the foundation,

$$\begin{aligned} w^{(\mathrm{F})}(x,y)\Big|_{y=0} &= \sum_{n=0}^{\infty} C_n \mathrm{J}_n(k_\mathrm{f} x) = \sum_{n=0}^{\infty} C_n \mathrm{J}_n(k_\mathrm{f}(x_1 - b/2)) \\ \mu_\mathrm{f} \frac{\partial w^{(\mathrm{F})}(x,y)}{\partial y}\Bigg|_{y=0} &= \mu_\mathrm{f} \sum_{n=1}^{\infty} n D_n \mathrm{J}_n(k_\mathrm{f} x) = \mu_\mathrm{f} \sum_{n=1}^{\infty} n D_n \mathrm{J}_n(k_\mathrm{f}(x_1 - b/2)) \end{aligned} \tag{15.19}$$

Substituting them into boundary conditions in Eqn (15.18),

$$\sum_{m=0}^{\infty} \mathrm{J}_m(k_\mathrm{f} x) C_m = \sum_{m=0}^{\infty} \cos(\xi_m h) \cos\left[a_m(x+a)\right] B_m \tag{15.20}$$

$$\sum_{m=1}^{\infty} m \mathrm{J}_m(k_\mathrm{f} x) D_m = \frac{-\mu_\mathrm{B}}{\mu_\mathrm{f}} \sum_{m=0}^{\infty} \xi_m \sin(\xi_m h) \cos\left[a_m(x+a)\right] B_m \tag{15.21}$$

These two equations can be separated into the following two sets of equations respectively by index m is even or odd.

$$\begin{cases} \displaystyle\sum_{m=0}^{\infty} \mathrm{J}_{2m}(k_\mathrm{f} x) C_{2m} = \sum_{m=0}^{\infty} (-1)^m \cos(\xi_{2m} h) \cos(a_{2m} x) B_{2m} \\ \displaystyle\sum_{m=0}^{\infty} \mathrm{J}_{2m+1}(k_\mathrm{f} x) C_{2m+1} = \sum_{m=0}^{\infty} (-1)^{m+1} \cos(\xi_{2m+1} h) \sin(a_{2m+1} x) B_{2m+1} \end{cases}, \tag{15.22}$$

$$\begin{cases} \displaystyle\sum_{m=0}^{\infty} 2m \mathrm{J}_{2m}(k_\mathrm{f} x) D_{2m} = \frac{\mu_\mathrm{B}}{\mu_\mathrm{f}} \sum_{m=0}^{\infty} (-1)^{m+1} \xi_{2m} \sin(\xi_{2m} h) \cos(a_{2m} x) B_{2m} \\ \displaystyle\sum_{m=0}^{\infty} (2m+1) \mathrm{J}_{2m+1}(k_\mathrm{f} x) D_{2m+1} = \frac{\mu_\mathrm{B}}{\mu_\mathrm{f}} \sum_{m=0}^{\infty} (-1)^m \xi_{2m+1} \sin(\xi_{2m+1} h) \sin(a_{2m+1} x) B_{2m+1} \end{cases} \tag{15.23}$$

Equations (15.20) and (15.21) can be expressed in (x_1, y_1) for $0 \le x_1 \le b = 2a$

$$\sum_{m=0}^{\infty} C_m \mathrm{J}_m(k_\mathrm{f}(x_1 - b/2)) = \sum_{m=0}^{\infty} B_m \cos(\xi_m h) \cos(\frac{m\pi}{b} x_1) \tag{15.24}$$

$$\frac{-\mu_\mathrm{f}}{\mu_\mathrm{B}} \sum_{m=1}^{\infty} m D_m \mathrm{J}_m(k_\mathrm{f}(x_1 - b/2)) = \sum_{m=0}^{\infty} B_m \xi_m \sin(\xi_m h) \cos(\frac{m\pi}{b} x_1) \tag{15.25}$$

Correspondingly equations (15.22) and (15.23) can be rewritten a

$$\begin{cases} \sum_{m=0}^{\infty} C_{2m} \mathrm{J}_{2m}\left(k_{\mathrm{f}}(x_1 - b/2)\right) = \sum_{m=0}^{\infty} B_{2m} \cos\left(\xi_{2m} h\right) \cos(\frac{2m\pi}{b} x_1) \\ \sum_{m=0}^{\infty} C_{2m+1} \mathrm{J}_{2m+1}\left(k_{\mathrm{f}}(x_1 - b/2)\right) = \sum_{m=0}^{\infty} B_{2m+1} \cos\left(\xi_{2m+1} h\right) \cos\left(\frac{(2m+1)\pi}{b} x_1\right) \end{cases} \tag{15.26}$$

$$\begin{cases} \frac{-\mu_{\mathrm{f}}}{\mu_{\mathrm{B}}} \sum_{m=1}^{\infty} 2mD_{2m} \mathrm{J}_{2m}\left(k_{\mathrm{f}}(x_1 - b/2)\right) = \sum_{m=0}^{\infty} B_{2m} \xi_{2m} \sin\left(\xi_{2m} h\right) \cos(\frac{2m\pi}{b} x_1) \\ \frac{-\mu_{\mathrm{f}}}{\mu_{\mathrm{B}}} \sum_{m=0}^{\infty} \left(2m+1\right) D_{2m+1} \mathrm{J}_{2m+1}\left(k_{\mathrm{f}}(x_1 - b/2)\right) = \sum_{m=0}^{\infty} B_{2m+1} \xi_{2m+1} \sin\left(\xi_{2m+1} h\right) \cos\left(\frac{(2m+1)\pi}{b} x_1\right) \end{cases} \tag{15.27}$$

Comparison of the above four equations shows that odd and even terms of (15.24) and (15.25) are independent and can be dealt with separately. Although written in summations of index from 0 to infinity, those series have to be truncated into a finite number of terms to be calculated in reality. Thus the right-hand-side of equations (15.24) and (15.25) can be thought of as finite cosine Fourier expansions over the left-hand-side functions.

For an arbitrary function $f\left(x\right)$ defined for $x = 0,1,...,N$, assuming $f\left(-x\right) = f\left(x\right)$ for $x = 1,2,...,N-1$, thus now $f(x)$ is an even function for $x = -(N-1),...,-1,0,1,...,N$ and has period $2N$. Then this modified $f(x)$ can be expanded in a series of cosine terms alone by the orthogonality of cosine on those discrete points (Hamming, 1962).

$$f\left(x\right) = \frac{a_0}{2} + \sum_{m=1}^{N-1} a_m \cos(\frac{m\pi}{N} x) + \frac{a_N}{2} \cos(\pi x) \tag{15.28}$$

where,

$$a_m = \frac{1}{N} \sum_{p=1-N}^{N} f\left(p\right) \cos(\frac{m\pi}{N} p) = \frac{2}{N} \left[\frac{f(0)}{2} + \sum_{p=1}^{N-1} f\left(p\right) \cos(\frac{m\pi}{N} p) + \frac{f(N)}{2} (-1)^m \right] \tag{15.29}$$

In other words, for this chapter, the essence of discrete cosine expansion is to evaluate $N+1$ equally spaced points of the L.H.S. of equations (15.24) and (15.25) along the interface $\overline{L}$ and then, based on those points, interpolate and reproduce the continuous series expression of the L.H.S. function. If we take equation (15.24) as an example, first we truncate both sides of the series into N terms. i.e.,

$$\sum_{n=0}^{N} C_n \mathrm{J}_n\left(k_{\mathrm{f}}(x_1 - b/2)\right) = \sum_{m=0}^{N} B_m \cos\left(\xi_m h\right) \cos(\frac{m\pi}{b} x_1) \tag{15.30}$$

Then we assume the L.H.S. of the equation as a function $f(x_1)$, so

$$f(x_1) = \sum_{n=0}^{N} C_n \mathrm{J}_n\left(k_\mathrm{f}(x_1 - b/2)\right) \tag{15.31}$$

and evaluate $N+1$ equally spaced points on $\overline{L}$ for x_1 ranging from 0 to $b=2a$, i.e.,

$$x_{1p} = \frac{pb}{N} \quad (p = 0,1,\ldots,N) \tag{15.32}$$

So,

$$B_m \cos(\xi_m h) = \begin{cases} \dfrac{2}{N}\left[\dfrac{f(0)}{2} + \displaystyle\sum_{p=1}^{\infty} f(x_{1p})\cos\left(\dfrac{m\pi x_{1p}}{b}\right) + \dfrac{(-1)^m}{2} f(0)\right] & , \quad \text{when } m = 1,2,\ldots,\ N-1 \\ \dfrac{1}{N}\left[\dfrac{f(0)}{2} + \displaystyle\sum_{p=1}^{\infty} f(x_{1p})\cos\left(\dfrac{m\pi x_{1p}}{b}\right) + \dfrac{(-1)^m}{2} f(0)\right] & , \quad \text{when } m = 0 \text{ or } N \end{cases} \tag{15.33}$$

after a set of simplification, we get

$$B_m \cos(\xi_m h) = \frac{\hat{\varepsilon}_m}{N}\sum_{n=0}^{N} U_{mn} C_n \tag{15.34}$$

where, $\hat{\varepsilon}_m = \begin{cases} 2, \text{ when } m = 1,2,\ldots,\ N-1 \\ 1, \text{ when } m = 0 \text{ or } N \end{cases}$, and

$$U_{mn} = \frac{(-1)^n + (-1)^m}{2} \mathrm{J}_n\left(\frac{k_\mathrm{f} b}{2}\right) + \sum_{p=1}^{N-1} \cos\left(\frac{m\pi}{N} p\right) \mathrm{J}_n\left(\frac{k_\mathrm{f} b}{2}\frac{(2p-N)}{N}\right) \tag{15.35}$$

Likewise, for equation (15.25), we obtained,

$$B_m \xi_m \sin(\xi_m h) = -\frac{\mu_\mathrm{f}}{\mu_\mathrm{B}}\frac{\hat{\varepsilon}_m}{N}\sum_{n=0}^{N} V_{mn} D_n \tag{15.36}$$

where,

$$V_{mn} = nU_{mn} = n\left[\frac{(-1)^n + (-1)^m}{2} \mathrm{J}_n\left(\frac{k_\mathrm{f} b}{2}\right) + \sum_{p=1}^{N-1} \cos\left(\frac{m\pi}{N} p\right) \mathrm{J}_n\left(\frac{k_\mathrm{f} b}{2}\frac{(2p-N)}{N}\right)\right] \tag{15.37}$$

Similarly we can apply discrete cosine expansion on the left-hand-side of equation (15.25). Thus in summary it can be obtained that, for $m = 0,1,...,N$

$$B_m \cos\left(\xi_m h\right) = \frac{\hat{\varepsilon}_m}{N} \sum_{n=0}^{N} U_{mn} C_n \tag{15.38}$$

$$B_m \xi_m \sin\left(\xi_m h\right) = -\frac{\mu_\mathrm{f}}{\mu_\mathrm{B}} \frac{\hat{\varepsilon}_m}{N} \sum_{n=0}^{N} V_{mn} D_n \tag{15.39}$$

where, $\hat{\varepsilon}_m = \begin{cases} 2, \text{ when } m = 1,2,..., N-1 \\ 1, \text{ when } m = 0 \text{ or } N \end{cases}$, and

$$U_{mn} = \frac{(-1)^m + (-1)^n}{2} \mathrm{J}_n\left(k_\mathrm{f} a\right) + \sum_{p=1}^{N-1} \cos\left(\frac{m\pi}{N} p\right) \mathrm{J}_n\left(k_\mathrm{f} a(\frac{2p}{N} - 1)\right) \tag{15.40}$$

$$V_{mn} = nU_{mn} = n\left[\frac{(-1)^m + (-1)^n}{2} \mathrm{J}_n\left(k_\mathrm{f} a\right) + \sum_{p=1}^{N-1} \cos\left(\frac{m\pi}{N} p\right) \mathrm{J}_n\left(k_\mathrm{f} a(\frac{2p}{N} - 1)\right)\right] \tag{15.41}$$

(for $n, m = 0,1,...,N$)

9.1.5 Elimination of Variables

Since indices *m* and *n* both range from 0 to *N*, the coefficients of the R.H.S. of equations (15.38) and (15.39) make up two square matrices. By numerically calculating the inverse of them, i.e., $[P_{nm}] = [U_{mn}]^{-1}$ and $[Q_{nm}] = [V_{mn}]^{-1}$, the explicit expressions of C_n and D_n in terms of B_m could be obtained as below. When inverting the matrix $[V_{mn}]$, element $V_{0,0}$ should be first changed to 1 instead of 0, otherwise matrix $[V_{mn}]$ will be a singular matrix due to the zero column when $n = 0$.

$$C_n = N \sum_{m=0}^{N} \frac{P_{nm} \cos\left(\xi_m h\right)}{\hat{\varepsilon}_m} B_m \tag{15.42}$$

$$D_n = -\hat{\mu} N \sum_{m=0}^{N} \frac{Q_{nm} \xi_m \sin\left(\xi_m h\right)}{\hat{\varepsilon}_m} B_m \tag{15.43}$$

with the shear modulus ratio $\hat{\mu} = \mu_\mathrm{B} / \mu_\mathrm{f}$. For $n = 0,1,2\ldots$

Substitution of Eqns (15.42) and (15.43) into (15.14) leads to

$$\begin{Bmatrix} \mathrm{J}_n(ka) \\ \mathrm{J}'_n(ka) \end{Bmatrix} a_{0,n} + \begin{Bmatrix} \mathrm{H}_n^{(1)}(ka) \\ \mathrm{H}_n^{(1)\prime}(ka) \end{Bmatrix} A_n = N \begin{Bmatrix} \mathrm{J}_n(k_\mathrm{f} a) \\ \kappa \mathrm{J}'_n(k_\mathrm{f} a) \end{Bmatrix} \sum_{m=0}^{N} \frac{P_{nm}\cos(\xi_m h)}{\hat{\varepsilon}_m} B_m$$
$$- \hat{\mu} N \sum_{\substack{m=1 \\ n+m \text{ odd}}}^{N} \begin{Bmatrix} \mathrm{J}_m(k_\mathrm{f} a) \\ \kappa \mathrm{J}'_m(k_\mathrm{f} a) \end{Bmatrix} \boldsymbol{s}_{mn} \left(\sum_{l=0}^{N} \frac{Q_{ml}\xi_l \sin(\xi_l h)}{\hat{\varepsilon}_l} B_l \right) \tag{15.44}$$

On switching *m* and *l,* Eqn (15.44) becomes

$$\begin{Bmatrix} \mathrm{J}_n(ka) \\ \mathrm{J}'_n(ka) \end{Bmatrix} a_{0,n} + \begin{Bmatrix} \mathrm{H}_n^{(1)}(ka) \\ \mathrm{H}_n^{(1)\prime}(ka) \end{Bmatrix} A_n = \sum_{m=0}^{N} \begin{Bmatrix} \mathcal{J}_{nm}(k_\mathrm{f} a) \\ \kappa \mathcal{J}_{nm}{}'(k_\mathrm{f} a) \end{Bmatrix} B_m \tag{15.45}$$

where for $z = k_\mathrm{f} a$, *n*, *m*=0,1,2…, *N*

$$\mathcal{J}_{nm}(z) = \frac{N}{\hat{\varepsilon}_m} \left\{ P_{nm}\cos(\xi_m h)\mathrm{J}_n(z) - \hat{\mu}\xi_m \sin(\xi_m h) \sum_{\substack{l=1 \\ n+l \text{ odd}}}^{N} \mathrm{J}_l(z)\boldsymbol{s}_{ln} Q_{lm} \right\} \tag{15.46}$$

is a new defined set of sums of ***"scaled"*** Bessel functions to be used with the building coefficients B_m , that resulted from the displacement continuity boundary condition, and for *n*, *m*=0,1,2…, *N*

$$\mathcal{J}'_{nm}(z) = \frac{N}{\hat{\varepsilon}_m} \left\{ P_{nm}\cos(\xi_m h)\mathrm{J}'_n(z) - \hat{\mu}\xi_m \sin(\xi_m h) \sum_{\substack{l=1 \\ n+l \text{ odd}}}^{N} \mathrm{J}'_l(z)\boldsymbol{s}_{ln} Q_{lm} \right\} \tag{15.47}$$

is the corresponding set of derivatives of sums of ***"scaled"*** Bessel functions resulting from the stress continuity boundary condition.

Equation (15.45) is solvable for two sets of unknowns in two sets of equations. For better convergence, B_m 's are chosen to be eliminated first to get a set of equations with only respect to A_n 's. From the first line of equation (15.45),

$$\{B_m\} = [\mathcal{J}_{mn}]\{\mathrm{J}_n(ka)a_{0,n} + \mathrm{H}_n^{(1)}(ka)A_n\} \tag{15.48}$$

where, $[\mathscr{I}_{mn}]=[\mathscr{J}_{nm}]^{-1}$ and the braces here denote the L.H.S. of the equation is a column vector. So equation (15.48) could be expressed explicitly as, for m=0,1,2,…,N

$$B_m = \sum_{n=0}^{N} \mathscr{I}_{mn} \left[\mathrm{J}_n(ka) a_{0,n} + \mathrm{H}_n^{(1)}(ka) A_n \right] \tag{15.49}$$

Substitute it into the second line of (15.45), we obtain

$$\mathrm{J}_n'(ka) a_{0,n} + \mathrm{H}_n^{(1)\prime}(ka) A_n = \kappa \sum_{m=0}^{N} \mathscr{Z}_{nm} \left[\mathrm{J}_m(ka) a_{0,m} + \mathrm{H}_m^{(1)}(ka) A_m \right] \tag{15.50}$$

in which, $\mathscr{Z}_{nm} = \sum_{l=0}^{N} \mathscr{J}_{nl}' \mathscr{I}_{lm}$ is the element of matrix $[\mathscr{Z}]=[\mathscr{J}'][\mathscr{I}]$. Equation can be further simplified to

$$\sum_{m=0}^{N} \mathscr{G}_{nm} A_m = \mathscr{g}_n \tag{15.51}$$

where, for n, m =0,1,2…,N

$$\begin{aligned} \mathscr{G}_{nm} &= \delta_{nm} H_n^{(1)\prime}(ka) - \kappa \mathscr{Z}_{nm} H_m^{(1)}(ka) \\ \mathscr{g}_n &= \sum_{m=0}^{N} \left[\kappa \mathscr{Z}_{nm} \mathrm{J}_m(ka) - \delta_{nm} \mathrm{J}_n'(ka) \right] a_{0,m} \end{aligned} \tag{15.52}$$

and $\delta_{nm}=1$ when $n=m$ and $\delta_{nm}=0$ otherwise. After calculating the $\{A_m\}$ (m = 0, 1, 2 …, N) from Eqn(15.51), Eqn (15.49) can be used to calculate the $\{B_m\}$ from $\{A_n\}$. Their substitution into (15.42) and (15.43) leads to the solutions of C_m, D_m for m = 0, 1, 2, 3… , N from that of B_m.

9.1.6 Iterative Method

Traditional way of resolving the governing linear equation system (15.14), (15.38), and (15.39) are given in the preceding section 9.1.5. The governing equations are reduced to solving an infinite linear system equation system (15.51) in terms of a unknown vector $\{A_n\}$ only. However, the coefficient matrix $\mathscr{G}_{nm}$ is extremely ill-conditioned after truncation, partially because $\{A_n\}$ associated with a rapid increasing function $\mathrm{H}_n^{(1)}(ka)$. That makes $\{A_n\}$ diverge when index n increases by means of direct linear-system-solving methods. This section provides an alternative way to solve the unknown coefficients without inverting the 'ill-conditioned' matrix but constructing a series of approximated solutions self-correctingly converges to the exact solution of the governing equation.

The following iterative algorithim is designed exclusively for this model and equation set. For our experience, the resultant linear equations in each iterative step have to be solved and stabilized with the help of Tikhonov Regularization method (Please read subsequent Section 9.2 in this chapter for reference), the common solver including Pivoting Gaussian Elimination, Singular Value decomposition (SVD), or Linear Least Square method (LLS) does not work for this particular problem.

First we summarize the four unknown coefficient vectors as follows:

$\{A_n\}$ coefficients of Hankel functions of waves in the half-space;

$\{B_n\}$ coefficients of the Building wave functions;

$\{C_n\}$ coefficients of the Bessel cosine functions;

$\{D_n\}$ coefficients of the Bessel sine functions.

and repeat the original boundary condition equations below:

$$\begin{Bmatrix} \mathrm{J}_n(ka) \\ \mathrm{J}'_n(ka) \end{Bmatrix} a_{0,n} + \begin{Bmatrix} \mathrm{H}_n^{(1)}(ka) \\ \mathrm{H}_n^{(1)\prime}(ka) \end{Bmatrix} A_n = \begin{Bmatrix} \mathrm{J}_n(k_\mathrm{f} a) \\ \kappa \mathrm{J}'_n(k_\mathrm{f} a) \end{Bmatrix} C_n + \sum_{\substack{m=1 \\ n+m \text{ odd}}}^{\infty} \begin{Bmatrix} \mathrm{J}_m(k_\mathrm{f} a) \\ \kappa \mathrm{J}'_m(k_\mathrm{f} a) \end{Bmatrix} \boldsymbol{s}_{mn} D_m \tag{15.14}$$

$$\sum_{n=0}^{N} \cos(\xi_n h) \cos\left[a_n\left(x_p + a\right)\right] B_n = \sum_{n=0}^{N} \mathrm{J}_n\left(k_\mathrm{f} x_p\right) C_n \tag{15.38}$$

$$\sum_{n=1}^{N} n \mathrm{J}_n\left(k_\mathrm{f} x_p\right) D_n = -\hat{\mu} \sum_{n=0}^{N} \xi_n \sin(\xi_n h) \cos\left[a_n\left(x_p + a\right)\right] B_n \tag{15.39}$$

where, $\hat{\mu} = \dfrac{\mu_{\mathrm{B}}}{\mu_{\mathrm{f}}}$, $x_p = x_{1p} - a$, $x_{1p} = \dfrac{p}{N} 2a$. Here subscripts p, n = 0, 1, …, N.

Eqn (15.38) and (15.39) are equivalent to uniformly picking up N+1 points along the horizontal interface between building and foundation and then evaluating the displacement and stress boundary condition at those points. Because there are also N+1 unknowns, those eqns are determinable.

They can be solved by iteration procedures in the following:

First we outline the iterative scheme as this:

$$\boxed{\begin{array}{l}
\text{Initialize } \left\{D_n^{(0)}\right\} = \left\{0\right\}; \\
\text{Do} \left\{\begin{array}{l}
\text{substitute } \left\{D_n^{(k)}\right\} \text{ into (9.14) and solve for } \left\{A_n^{(k)}\right\} \text{ and } \left\{C_n^{(k)}\right\} \\
\text{substitute } \left\{C_n^{(k)}\right\} \text{ into (9.38) and solve for } \left\{B_n^{(k)}\right\} \\
\text{substitute } \left\{C_n^{(k)}\right\} \text{ into (9.39) and solve for } \left\{D_n^{(k+1)}\right\} \text{ in next iteration}
\end{array}\right\}_{k \text{ is iteration \#}} \\
\text{while a terminal condition is satisfied or a prescribed max number of iteration is reached}
\end{array}} \tag{15.53}$$

Apparently there is nothing special here but the basic procedures of iterative method. In our computation, the iteration is commonly repeated until a prescribed maximum number of iteration is reached, because the terminal criterion is not easy to be properly assumed without sufficient trials. Moreover, we adopted running iteration by prescribed number because this iteration scheme converges fast. Now we elaborate this scheme in detail:

Step (0):

Assume $\{D_m\} = \{0\}$ in eqn (15.14) as the initial guess and solves $\{A_n^{(0)}\}$ and $\{C_n^{(0)}\}$ there

Plug step (0) $\{C_m^{(0)}\}$ into eqn (15.38) to solve for $\{B_m^{(0)}\}$ and then $\{D_m^{(0)}\}$ from eqn (15.39)

Step (1):

Plug Step (1) $\{D_m^{(0)}\}$ into eqn (15.14) and solves $\{A_n^{(1)}\}$ and $\{C_n^{(1)}\}$ there

Plug step (1) $\{C_m^{(1)}\}$ into eqn (15.38) to solve for $\{B_m^{(1)}\}$ and then $\{D_m^{(1)}\}$ from eqn (15.39)

…After *k* steps, the cumulative solutions are

$$A_n \approx A_n^{(k)};\ B_n \approx B_n^{(k)};\ C_n \approx C_n^{(k)};\ D_n \approx D_n^{(k)}.$$

Then, **Step (*k*+1):**

Plug Step (*k*) $\{D_m^{(k)}\}$ into (15.14) and solves $\{A_n^{(k+1)}\}$ and $\{C_n^{(k+1)}\}$ there

Plug step (*k*+1) $\{C_m^{(k+1)}\}$ into (15.38) to compute $\{B_m^{(k+1)}\}$ and then $\{D_m^{(k+1)}\}$ from (15.39)

For each step after step (2), check convergence by comparing the results with the ones in the previous step. Continue if necessary.

To illustrate the procedures in more detail:

Step (0):

From eqn (15.14):

$$-\begin{Bmatrix} \mathrm{H}_n^{(1)}(ka) \\ \mathrm{H}_n^{(1)\prime}(ka) \end{Bmatrix} A_n + \begin{Bmatrix} \mathrm{J}_n(k_\mathrm{f}a) \\ \kappa \mathrm{J}_n'(k_\mathrm{f}a) \end{Bmatrix} C_n = \begin{Bmatrix} \mathrm{J}_n(ka) \\ \mathrm{J}_n'(ka) \end{Bmatrix} a_{0,n}$$

$$\Rightarrow \begin{bmatrix} -\mathrm{H}_n^{(1)}(ka) & \mathrm{J}_n(k_\mathrm{f}a) \\ -\mathrm{H}_n^{(1)\prime}(ka) & \kappa \mathrm{J}_n'(k_\mathrm{f}a) \end{bmatrix} \begin{Bmatrix} A_n \\ C_n \end{Bmatrix} = \begin{Bmatrix} \mathrm{J}_n(ka) \\ \mathrm{J}_n'(ka) \end{Bmatrix} a_{0,n}$$

$$\Rightarrow \begin{Bmatrix} A_n \\ C_n \end{Bmatrix} = \begin{bmatrix} \kappa \mathrm{J}_n'(k_\mathrm{f}a) & -\mathrm{J}_n(k_\mathrm{f}a) \\ \mathrm{H}_n^{(1)\prime}(ka) & -\mathrm{H}_n^{(1)}(ka) \end{bmatrix} \begin{Bmatrix} \mathrm{J}_n(ka) \\ \mathrm{J}_n'(ka) \end{Bmatrix} \frac{a_{0,n}}{d_n}$$

where $d_n = \mathrm{H}_n^{(1)\prime}(ka)\mathrm{J}_n(k_\mathrm{f}a) - \kappa \mathrm{H}_n^{(1)}(ka)\mathrm{J}_n'(k_\mathrm{f}a)$ is the determinant of the matrix. So the 0-step iterative results for $\{A_n\}$ and $\{B_n\}$ are

$$
\begin{cases}
A_n^{(0)} = \left[\kappa \mathrm{J}'_n\left(k_\mathrm{f}a\right)\mathrm{J}_n\left(ka\right) - \mathrm{J}_n\left(k_\mathrm{f}a\right)\mathrm{J}'_n\left(ka\right)\right]\dfrac{a_{0,n}}{d_n} \\
C_n^{(0)} = \left[\mathrm{H}_n^{(1)\prime}\left(ka\right)\mathrm{J}_n\left(ka\right) - \mathrm{H}_n^{(1)}\left(ka\right)\mathrm{J}'_n\left(ka\right)\right]\dfrac{a_{0,n}}{d_n}
\end{cases}
\tag{15.54}
$$

Substitute $C_n^{(0)}$ into eqn (15.38), then solving $C_n^{(0)}$ from linear eqn (15.38) for p=0,1,…,N

$$
\sum_{n=0}^{N}\cos\left(\xi_n h\right)\cos\left[\varsigma_n\left(x_p+a\right)\right]B_n^{(0)} = \sum_{n=0}^{N}\mathrm{J}_n\left(k_\mathrm{f}x_p\right)C_n^{(0)}
\tag{15.55}
$$

And substitution of $B_m^{(0)}$ into eqn (15.39) leads to the simultaneous linear equations with regard to $D_n^{(0)}$

$$
\sum_{n=1}^{N} n\mathrm{J}_n\left(k_\mathrm{f}x_p\right)D_n^{(0)} = -\hat{\mu}\sum_{n=0}^{N}\xi_n\sin\left(\xi_n h\right)\cos\left[\varsigma_n\left(x_p+a\right)\right]B_n^{(0)}
\tag{15.56}
$$

……

Step (k+1): k=1, 2, …, *N*-1

From eqn (15.14):

$$
\begin{bmatrix} -\mathrm{H}_n^{(1)}\left(ka\right) & \mathrm{J}_n\left(k_\mathrm{f}a\right) \\ -\mathrm{H}_n^{(1)\prime}\left(ka\right) & \kappa\mathrm{J}'_n\left(k_\mathrm{f}a\right)\end{bmatrix}
\begin{Bmatrix} A_n^{(k+1)} \\ C_n^{(k+1)} \end{Bmatrix}
= \begin{Bmatrix} \mathrm{J}_n\left(ka\right) \\ \mathrm{J}'_n\left(ka\right) \end{Bmatrix} a_{0,n}
- \sum_{\substack{m=1 \\ n+m \text{ odd}}}^{N} \begin{Bmatrix} \mathrm{J}_m\left(k_\mathrm{f}a\right) \\ \kappa\mathrm{J}'_m\left(k_\mathrm{f}a\right) \end{Bmatrix} \boldsymbol{s}_{mn} D_m^{(k)} \Rightarrow
$$

$$
\begin{Bmatrix} A_n^{(k+1)} \\ C_n^{(k+1)} \end{Bmatrix}
= \begin{bmatrix} \kappa\mathrm{J}'_n\left(k_\mathrm{f}a\right) & -\mathrm{J}_n\left(k_\mathrm{f}a\right) \\ \mathrm{H}_n^{(1)\prime}\left(ka\right) & -\mathrm{H}_n^{(1)}\left(ka\right)\end{bmatrix}
\begin{Bmatrix} \mathrm{J}_n\left(ka\right) \\ \mathrm{J}'_n\left(ka\right) \end{Bmatrix} \frac{a_{0,n}}{d_n}
- \frac{1}{d_n}\begin{bmatrix} \kappa\mathrm{J}'_n\left(k_\mathrm{f}a\right) & -\mathrm{J}_n\left(k_\mathrm{f}a\right) \\ \mathrm{H}_n^{(1)\prime}\left(ka\right) & -\mathrm{H}_n^{(1)}\left(ka\right)\end{bmatrix}
\begin{Bmatrix} \displaystyle\sum_{\substack{m=1 \\ n+m \text{ odd}}}^{N} \mathrm{J}_m\left(k_\mathrm{f}a\right)\boldsymbol{s}_{mn}D_m^{(k)} \\ \kappa \displaystyle\sum_{\substack{m=1 \\ n+m \text{ odd}}}^{N} \mathrm{J}'_m\left(k_\mathrm{f}a\right)\boldsymbol{s}_{mn}D_m^{(k)} \end{Bmatrix}
$$

where $d_n = \mathrm{H}_n^{(1)\prime}(ka)\mathrm{J}_n(k_\mathrm{f}a) - \kappa\mathrm{H}_n^{(1)}(ka)\mathrm{J}'_n(k_\mathrm{f}a)$ is the determinant of the matrix.

$$\begin{cases} A_n^{(k+1)} = A_n^{(0)} - \dfrac{\kappa}{d_n}\left[\mathrm{J}_n'\left(k_\mathrm{f}a\right) \sum_{\substack{m=1 \\ n+m \text{ odd}}}^{N} \mathrm{J}_m\left(k_\mathrm{f}a\right) \boldsymbol{s}_{mn} D_m^{(k)} - \mathrm{J}_n\left(k_\mathrm{f}a\right) \sum_{\substack{m=1 \\ n+m \text{ odd}}}^{N} \mathrm{J}_m'\left(k_\mathrm{f}a\right) \boldsymbol{s}_{mn} D_m^{(k)} \right] \\ C_n^{(k+1)} = C_n^{(0)} - \dfrac{1}{d_n}\left[\mathrm{H}_n^{(1)\prime}\left(ka\right) \sum_{\substack{m=1 \\ n+m \text{ odd}}}^{N} \mathrm{J}_m\left(k_\mathrm{f}a\right) \boldsymbol{s}_{mn} D_m^{(k)} - \kappa \mathrm{H}_n^{(1)}\left(ka\right) \sum_{\substack{m=1 \\ n+m \text{ odd}}}^{N} \mathrm{J}_m'\left(k_\mathrm{f}a\right) \boldsymbol{s}_{mn} D_m^{(k)} \right] \end{cases} \tag{15.57}$$

In which $A_n^{(0)}$ and $C_n^{(0)}$ is shown in eqn (15.54). Substitute $C_n^{(k+1)}$ into eqn (15.38), then

$$\sum_{n=0}^{N} \cos\left(\xi_n h\right) \cos\left[\varsigma_n\left(x_p + a\right)\right] B_n^{(k+1)} = \sum_{n=0}^{N} \mathrm{J}_n\left(k_\mathrm{f} x_p\right) C_n^{(k+1)} \tag{15.58}$$

And substitution of $B_m^{(k+1)}$ into eqn (3) leads to the simultaneous linear equations with regard to $D_n^{(k+1)}$

$$\sum_{n=1}^{N} n \mathrm{J}_n\left(k_\mathrm{f} x_p\right) D_n^{(k+1)} = -\hat{\mu} \sum_{n=0}^{N} \xi_n \sin\left(\xi_n h\right) \cos\left[\varsigma_n\left(x_p + a\right)\right] B_n^{(k+1)} \tag{15.59}$$

9.1.7 Case Study

The authors have tested many ways to get the matrix better conditioned or other ways to set up the equations in order to solve the model, but the best results for this model hitherto is obtained using Finite Cosine expansion plus iterative method plus Tikhonov regularization. For the limited solutions we gained (roughly $\eta < 2.3$), all the boundary conditions are well-matched, but the displacement amplitude diagram is not symmetric for vertical incidence case. That does not obey the common sense, but is reasonable for the iteration algorithm we used. Therefore, only one case is studied in this section with all the boundary condition verification presented.

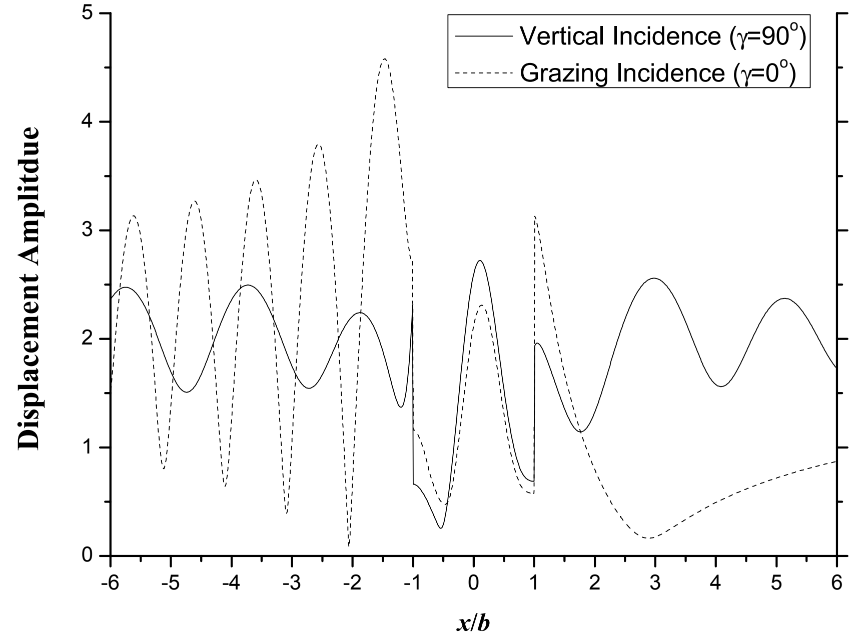

Fig. 9-2 GROUND SURFACE DISPLACEMENT AMPLITUDE FOR $\eta = 1$, $h/b = 1/3$, $\mu_f/\mu_B = 1.5$, $\mu_f/\mu = 1.5$, $k_f/k_B = 2$, $k_f/k = 3$, $\gamma = 90^o$ and 0^o

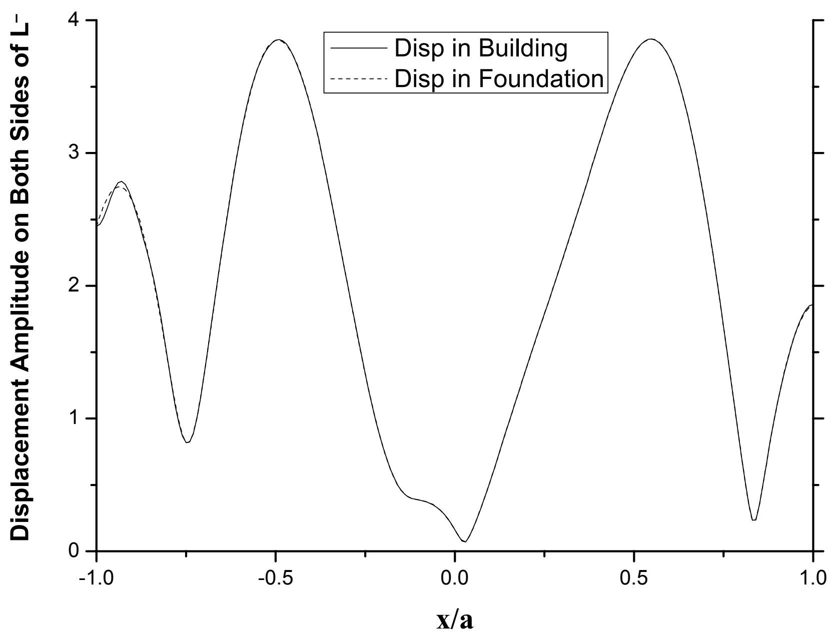

Fig. 9-3 DISPLACEMENT AMPLITUDE ON BOTH SIDES OF $\overline{L}$ **FOR** $\eta = 1$, $h/b = 1/3$, $\mu_f/\mu_B = 1.5$, $\mu_f/\mu = 1.5$, $k_f/k_B = 2$, $k_f/k = 3$, $\gamma = 90^o$

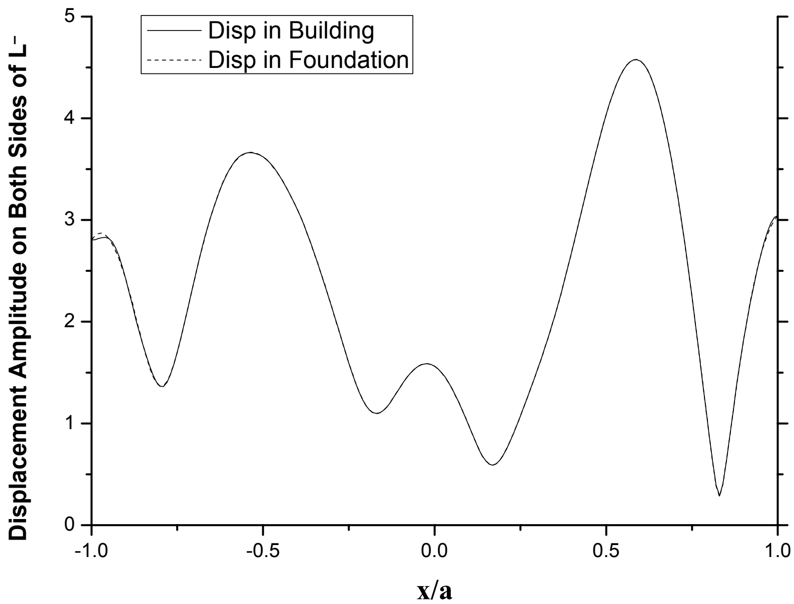

Fig. 9-4 DISPLACEMENT AMPLITUDE ON BOTH SIDES OF $\overline{L}$ **FOR** $\eta = 1$, $h/b = 1/3$,

$\mu_{\mathrm{f}}/\mu_{\mathrm{B}} = 1.5$, $\mu_{\mathrm{f}}/\mu = 1.5$, $k_{\mathrm{f}}/k_{\mathrm{B}} = 2$, $k_{\mathrm{f}}/k = 3$, $\gamma = 0^{\circ}$

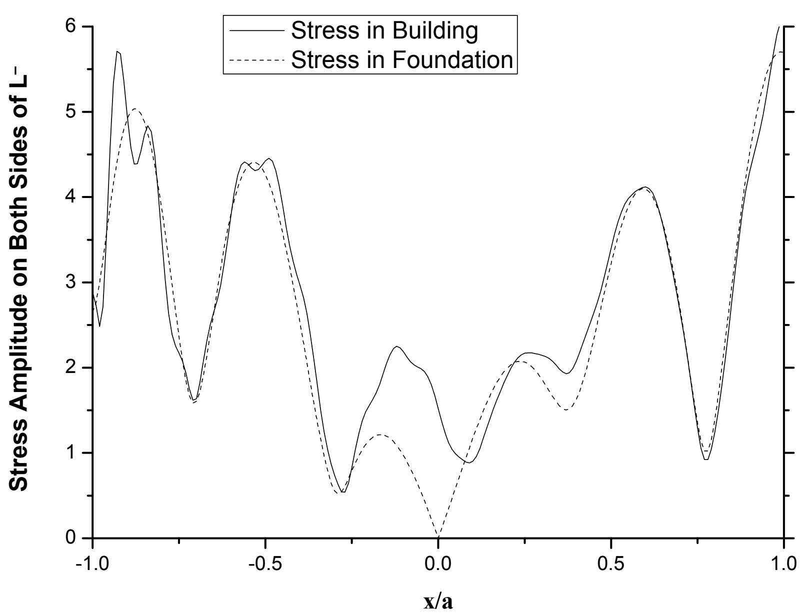

Fig. 9-5 STRESS AMPLITUDE ON BOTH SIDES OF $\overline{L}$ **FOR** $\eta = 1$, $h/b = 1/3$,

$\mu_{\mathrm{f}}/\mu_{\mathrm{B}} = 1.5$, $\mu_{\mathrm{f}}/\mu = 1.5$, $k_{\mathrm{f}}/k_{\mathrm{B}} = 2$, $k_{\mathrm{f}}/k = 3$, $\gamma = 90^{\circ}$

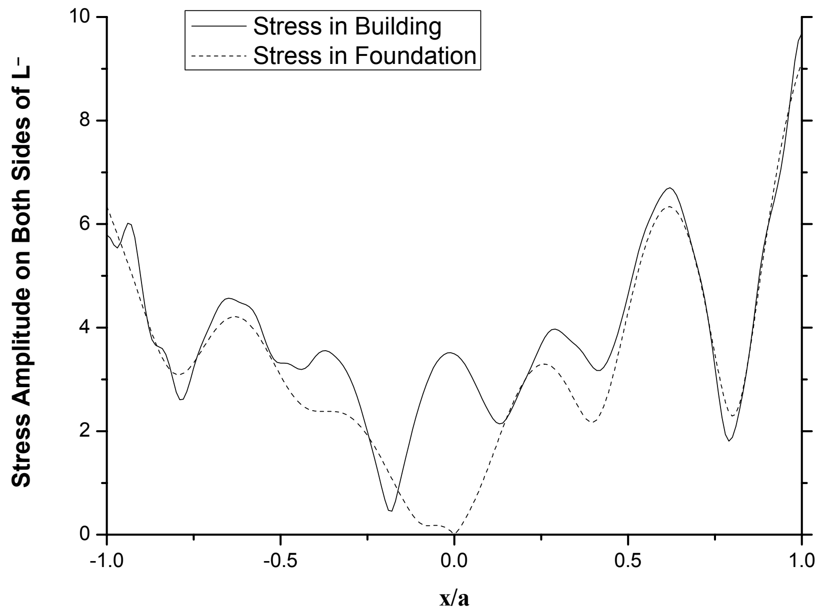

Fig. 9-6 STRESS AMPLITUDE ON BOTH SIDES OF $\overline{L}$ **FOR** $\eta = 1$, $h/b = 1/3$,

$\mu_f/\mu_B = 1.5$, $\mu_f/\mu = 1.5$, $k_f/k_B = 2$, $k_f/k = 3$, $\gamma = 0^o$

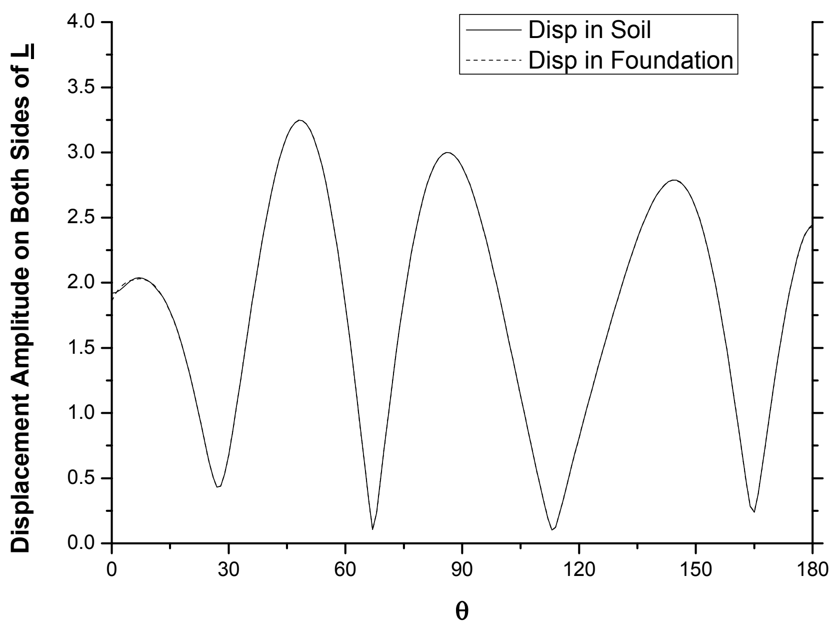

Fig. 9-7 DISPLACEMENT AMPLITUDE ON BOTH SIDES OF $\underline{L}$ **FOR** $\eta = 1$, $h/b = 1/3$,

$\mu_f/\mu_B = 1.5$, $\mu_f/\mu = 1.5$, $k_f/k_B = 2$, $k_f/k = 3$, $\gamma = 90^o$

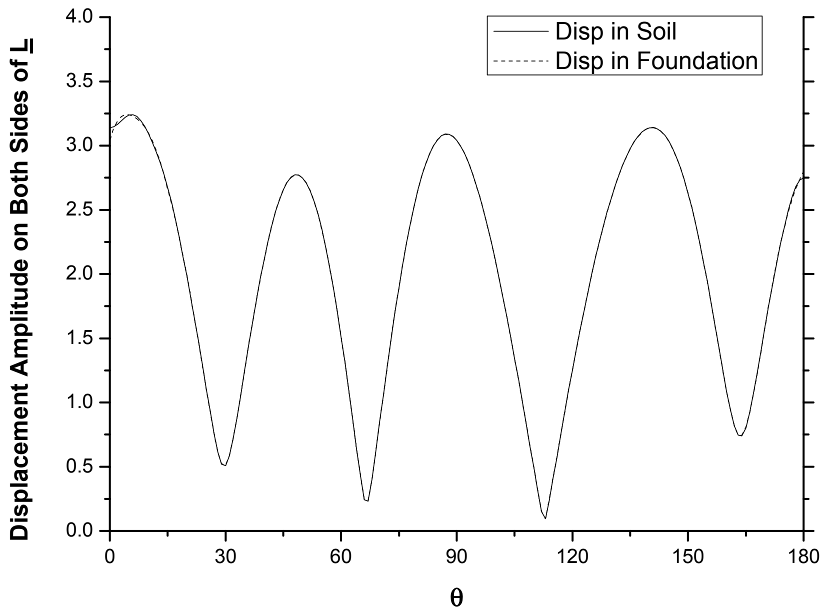

Fig. 9-8 DISPLACEMENT AMPLITUDE ON BOTH SIDES OF $\underline{L}$ **FOR** $\eta=1$, $h/b=1/3$, $\mu_{\mathrm{f}}/\mu_{\mathrm{B}}=1.5$, $\mu_{\mathrm{f}}/\mu=1.5$, $k_{\mathrm{f}}/k_{\mathrm{B}}=2$, $k_{\mathrm{f}}/k=3$, $\gamma=0^{\mathrm{o}}$

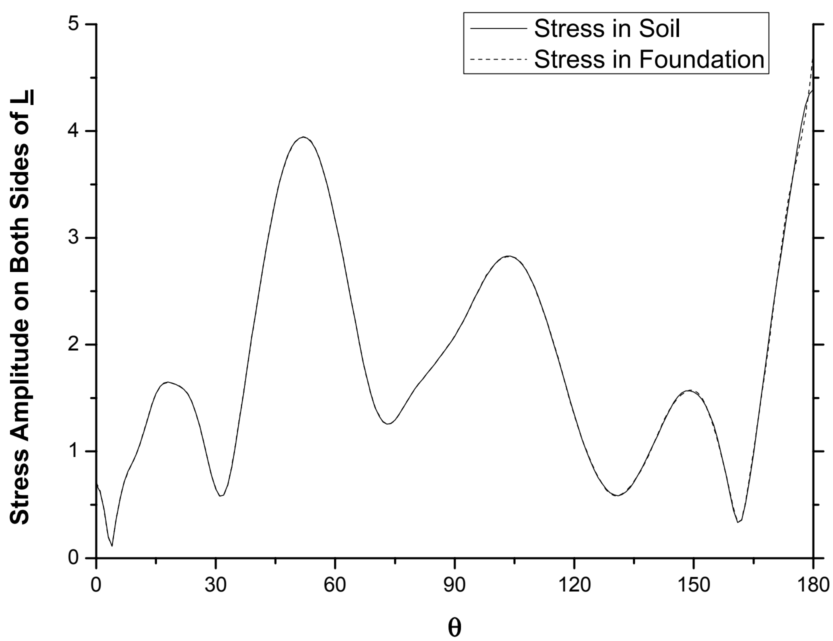

Fig. 9-9 STRESS AMPLITUDE ON BOTH SIDES OF $\underline{L}$ **FOR** $\eta=1$, $h/b=1/3$, $\mu_{\mathrm{f}}/\mu_{\mathrm{B}}=1.5$, $\mu_{\mathrm{f}}/\mu=1.5$, $k_{\mathrm{f}}/k_{\mathrm{B}}=2$, $k_{\mathrm{f}}/k=3$, $\gamma=90^{\mathrm{o}}$

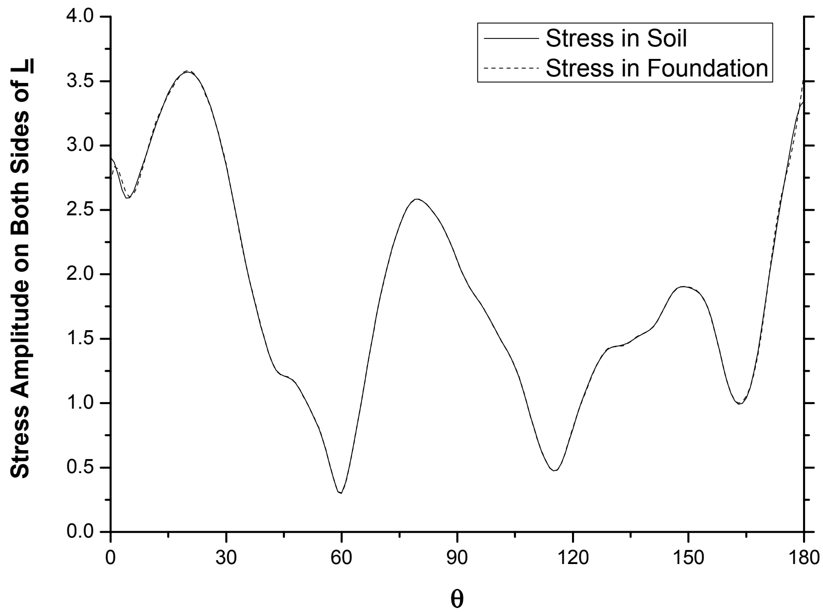

Fig. 9-10 STRESS AMPLITUDE ON BOTH SIDES OF $\underline{L}$ **FOR** $\eta = 1$, $h/b = 1/3$, $\mu_{\mathrm{f}}/\mu_{\mathrm{B}} = 1.5$, $\mu_{\mathrm{f}}/\mu = 1.5$, $k_{\mathrm{f}}/k_{\mathrm{B}} = 2$, $k_{\mathrm{f}}/k = 3$, $\gamma = 0^{\circ}$

9.2 Discrete Ill-Posed Problems

Boundary condition equations derived above seem in good shape and easy to be solved out. However, this mathematical model inherently belongs to ill-posed problems. Ill-posed problems often associate with inverse problems, as opposed to the direct problems; notwithstanding the models discussed here are all direct problems for sure. An inverse problem refers to the process of retrieving model parameter(s) based on the observed data, a formulation of exploring origins by consequences caused by them. Inverse problems are often ill-posed. It was first addressed by Hadamard (1902), who proposed three properties that must be owned by mathematical models to make them well-posed:

1) Existence: A solution exists

2) Uniqueness: The solution is unique

3) Stability: The solution depends continuously on the data, in some reasonable topology.

The third property, stability of the solution or solutions, is often unable to be satisfied firmly in that most of continuum problems must be discretized so as to obtain a numerical solution by digital computers. Therefore, those problems have the potential to be ill-posed or at least ill-conditioned. For those ones that an arbitrary small data perturbation can cause an arbitrarily large perturbation of the solution, Hadamard believed they were "artificial" in respect that those models can not represent the physical system.

The mathematical criteria that categorize linear system of equations or linear least-squares problems into ill-posed problems (Hansen, 1993) are:

1) The singular values of coefficient matrix decay gradually to zero;
2) The ratio between the largest and the smallest nonzero singular vaules is large.

Many research areas of science and engineering can be ended up with solving a set of governing linear equations. The governing equations of linear inverse problems are typically ill-conditioned indicated by large condition numbers. The classical direct or iterative linear equation solvers, e.g. complete or partial pivoting Gaussian elimination, are not feasible for those ill-posed problems.

To obtain a reasonable solution of ill-posed problem, a-priori knowledge such as an assumption on the smoothness or a bound on the norm must be applied to strengthen the constraints of linear equations. This kind of restraints is called regularization. One of the simple regularization algorithms is the least-squares method, in which norm of equation residues is minimized.

Solution methods of inverse problems have intensive application background such as geophysical investigation of minerals or petroleum; nondestructive evaluation of materials or structures; image deblurring. A typical application is to identify parameters of media by boundary measurement. For the application of wave motion theory, inverse problems often arise for detection of invisible boundary profile from backscattering data. The direct wave propagation problems discussed in this dissertation, although multiple fancy algorithms have been used to investigate the underlying physical principle in a mathematical way, are all essentially solved by boundary discretization and method of undetermined coefficients – that is, establishing boundary condition equations; evaluating those equations at discrete points (most likely uniformly distributed) along the boundaries; eliminating unknowns to the least and solving the linear equations.

The evaluation of boundary condition equations at discrete points mentioned above, although are done numerically by digital computers, are somewhat alike as sampling by experimental measurements. And, the numerical errors generated by round-off, truncation of series, and discretization, play the similar role as measurement errors induced by instruments and manipulation. In this sense, the method of undetermined coefficients is analogous to a numerical experiment for identification of parameters (unknown coefficients of wave functions for models in this dissertation), a typical inverse problem. This can help us understand the ill-poseness of the method of Fourier-Bessel wave function expansion. The model discussed in this chapter is deemed by author as a discrete ill-posed problem that regularization method has to be utilized in order to solve the governing equations effectively.

Regularization Tools is a state-of-the-art MATLAB routine package developed by Hansen (1994) on a variety of regularization methods and their auxiliary routines for solving ill-posed inverse problems. This numerical package has been well maintenaced and kept updating (Hansen 2007). The results we obtained in the previous section are computed by this software.

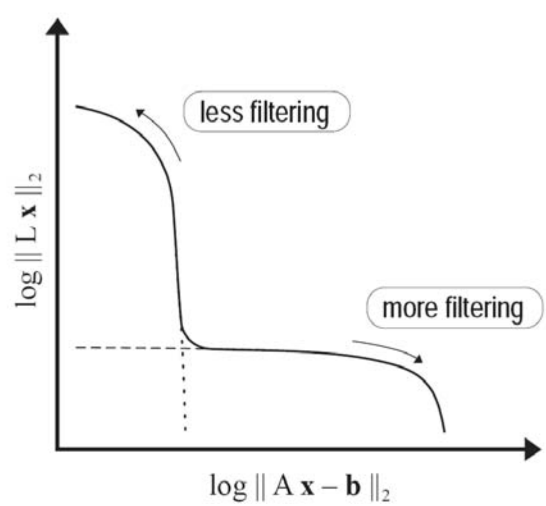

Fig. 9-11 SCHEMATIC PLOT OF THE L-CURVE (ADAPTED FROM HANSEN 1994)

Tikhonov regularization (Tikhonov and Arsenin, 1977) is the most classical regularization method and commonly used in solving ill-posed problems. If we are solving a square linear system $Ax = b$ for $A \in \mathbb{R}^{n \times n}$ or an overdetermined linear system $\min \|Ax - b\|_2$ for $A \in \mathbb{R}^{m \times n}$ with $m > n$, it is essentially a trade-off between fitting the data ($\|Ax - b\|_2$) and reducing a norm of the solution ($\|Lx\|_2$), where L termed as Tikhonov matrix is a linear operator that improves the conditioning of the solution. For example, L can be either chosen as the identity matrix I for solutions with small norms, or as highpass operators for strengthening smoothness of solutions. But how to appropriately control this trade-off mathematically is a puzzle. L-curve analysis (Hansen and O'Leary, 1993; Hansen et al. 2007) makes the regularization algorithm adaptive. For discrete ill-posed problems, when plot $\|Ax - b\|_2$ and $\|Lx\|_2$ in the log-log scale in *x*- and *y*- axes, the curve is commonly in the L-shaped appearance. The L-curve thus shows the trade-off between minimizing the residual norm versus the solution norm, and the L-curve's corner, with the maximum curvature in the log-log scale, is mostly where the optimal parameter locates. It is the criterion to select the optimal regularization parameter. After comparison, these two methods are adopted in this dissertation whereas many more methods are available in Regularization Tools. For conciseness, no cumbersome theory is present herein but only reference books and papers listed in the end of this dissertation.

One of the difficulties for regularization is, not an algorithm is so universal as to be applicable for all the ill-posed problems. It might need more investigation on seek a particular effective algorthim for the model discussed in this chapter.

Chapter 10

SOIL-STRUCTURE INTERACTION:

RIGID-FLEXIBLE COMPOSITE FOUNDATION

In the previous two chapters, the foundation in the model is of one medium either pure rigid or pure flexible foundation. In fact, high-rise buildings are often supported by a deep box foundation or pile-raft composite foundation but not a large volume of concrete like a gravity dam. This kind of box foundation is functioned as a basement or horizontally divided into multiple floors underground. While the box foundation is hollow inside for providing occupancy, the top plate to connect foundation and superstructure has to be of high rigidity to transfer lateral and gravity loads from superstructure to foundation and then to the soil underneath or around.

Besides, for heavy superstructures, the natural rude ground soil commonly cannot provide sufficient carrying capacity and needs to be consolidated, reinforced, or even replaced artificially to improve its deformation, saturation, or settlement quality. This process is called Foundation Treatment or Foundation Improvement. A number of possibilities exist for altering the soil properties, such as: removal or excavation of the unqualified soil and replacement by suitable fill; consolidation by surcharge fills for soft clay foundations; chemical alteration by lime and cement piles; physical stabilization including dynamic compaction or sand compaction piles for loose granular materials; or reinforcement using geotextiles and geogrids, etc. After treated, the characteristics of local soil that surrounds reinforced-concrete foundation, including rigidity and density, are distinctly different from the half-space soil. That is the other possible realization of the flexible foundation we assumed in this chapter.

Fig. 10-1 and Fig. 10-2 are two realizations of the mathematical model of this chapter as shown in Fig. 10-3 and Fig. 10-4, respectively. Fig. 10-1 shows a shearwall-rigid foundation embedded in a half-space with a flexible treated-subgrade in between. Fig. 10-2 represents a shear beam sitting on a pile cap or raft or mat foundation, which collects the upper loads and transfer them to the half-space through multiple piles.

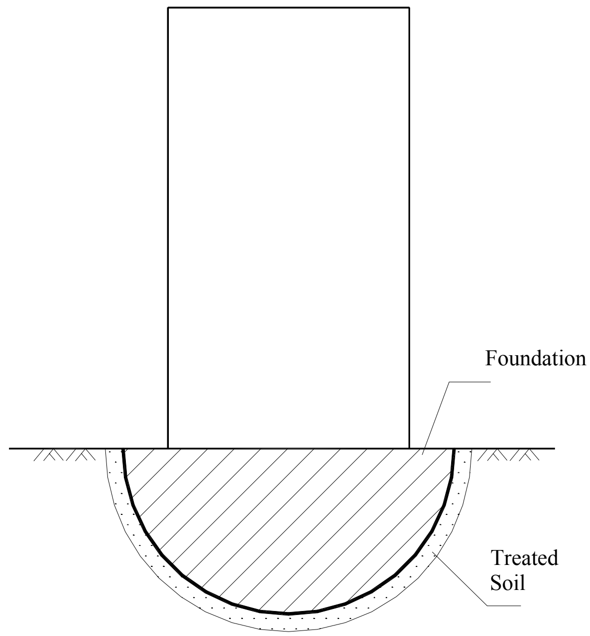

Fig. 10-1 REALIZATION OF RIGID-FLEXIBLE COMPOSITE FOUNDATIONS I

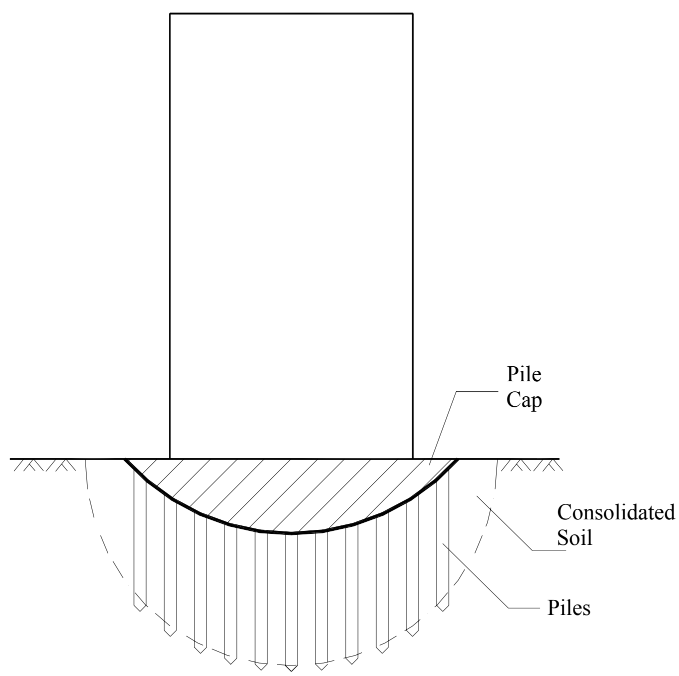

Fig. 10-2 REALIZATION OF RIGID-FLEXIBLE COMPOSITE FOUNDATIONS II

10.1 The Mathematical Model

This chapter studies a model similar to what we discussed in the previous two chapters, but the rigid semi- or shallow rigid foundation is wrapped with an elastic semi-circular flexible foundation radius $\underline{a}$ outside. Correspondingly, the notation of radius of upper rigid foundation is changed to $\overline{a}$. The material constants of half-space soil, building, and flexible foundation, namely rigidity and shear wave velocity, are respectively denoted by μ_s, C_{β_s}; μ_B, C_{β_B}; and μ_f, C_{β_f}. The contacts between the soil and foundation and building are assumed to be welded, no slippage between them would happen but the foundation is removable. For the shallow rigid foundation case (simplified to "shallow case" in the remaining of this chapter), the dimension of the geometry of shallow rigid foundation is characterized by its half-width b on the ground surface and the interior angle of circular arc $\delta\pi = 2\arccos\left(d/\overline{a}\right)$.

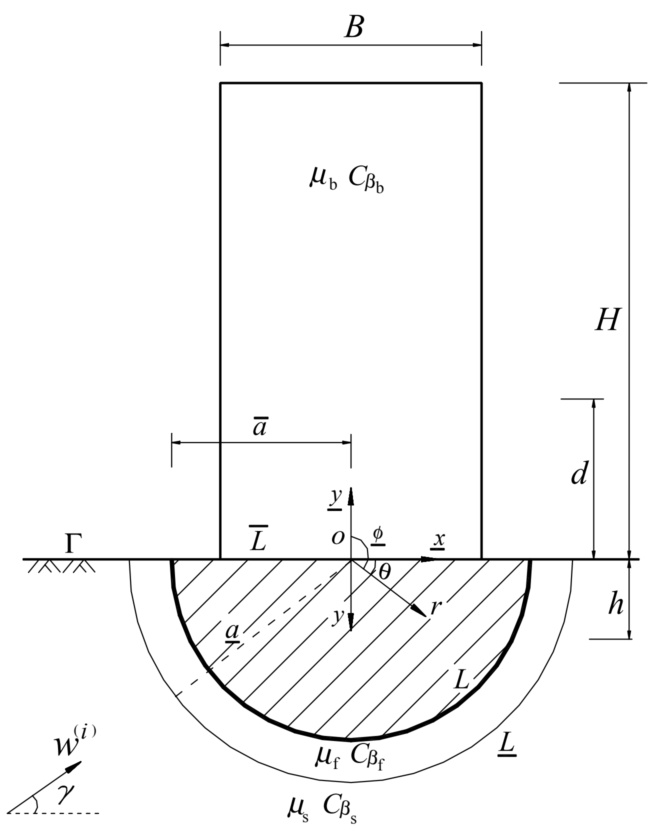

Fig. 10-3 SOIL-STRCUTRE INTERACTION WITH SEMI-CYLINDRICAL FOUNDATION

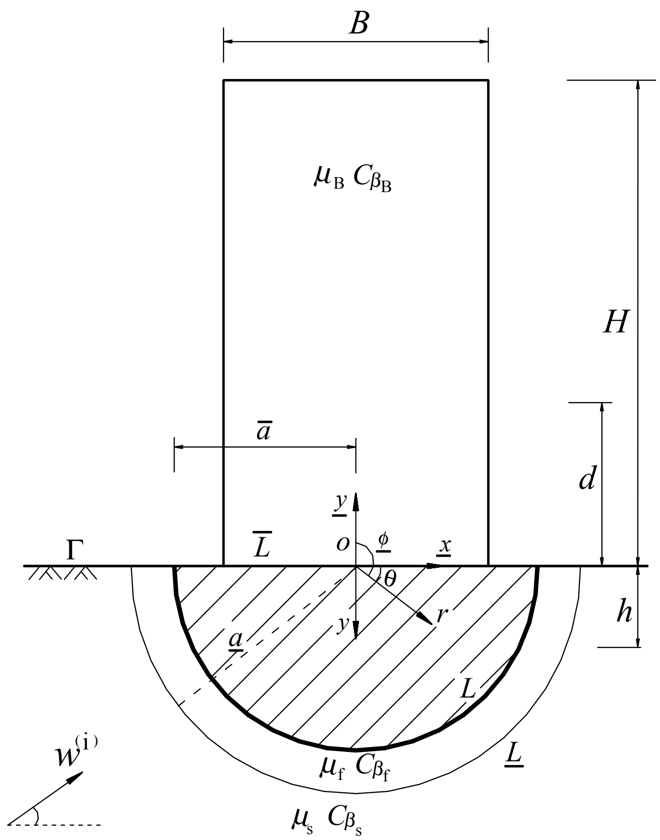

Fig. 10-4 SOIL-STRCUTRE INTERACTION WITH SHALLOW CYLINDRICAL FOUNDATION ENCLOSED BY A SEMI-CYLINDRICAL FOUNDATION

10.2 Wave field in the half-space

The free field wave functions are exactly the same as preceding chapters so that omitted herein. For the semi-circular rigid foundation case, the following traction-free boundary conditions should be satisfied

$$\tau_{\theta z}|_{\bar{L}} = 0 \quad \text{at} \quad r > \underline{a};\ \theta = 0, \pi \tag{16.1}$$

$$w|_{L} = w_0 e^{i\omega t} \quad \text{at} \quad r = \bar{a};\ \theta \in [0, \pi] \tag{16.2}$$

in which, w_0 denotes the unknown movement of the rigid foundation. For shallow rigid foundation case, the following boundary conditions should be satisfied

$$\tau_{\theta z}|_{\Gamma} = 0 \qquad \text{at} \quad r > b; \ \theta = 0, \pi \tag{16.3}$$

$$w|_{L} = w_0 \mathrm{e}^{\mathrm{i}\omega t} \quad \text{at} \quad \overline{r} = \overline{a}; \ \overline{\phi} \in \left[-\frac{\delta\pi}{2}, \frac{\delta\pi}{2}\right] \tag{16.4}$$

The wave field in the half-space scattered and diffracted in the presence of the foundation is written as

$$w^{(\mathrm{S})}(r,\theta) = \sum_{n=0}^{\infty} A_n \mathrm{H}_n^{(1)}\left(k_{\mathrm{s}} r\right) \cos n\theta \tag{16.5}$$

where, the A_n are a set of complex unknowns to be determined by boundary conditions. The stress generated by $w^{(\mathrm{S})}$, for $r > \underline{a}$

$$\tau_{\theta z}^{(\mathrm{S})}(r,\theta) = \frac{\mu_{\mathrm{s}}}{r} \frac{\partial w^{(\mathrm{S})}(r,\theta)}{\partial \theta} = -\frac{\mu_{\mathrm{s}}}{r} \sum_{n=0}^{\infty} n \mathrm{J}_n(k_{\mathrm{s}} r) A_n \sin n\theta \tag{16.6}$$

Since $\theta = 0, \pi$ on the flat boundary $\Gamma + \overline{L}$, traction-free boundary condition equation.(16.3) is satisfied automatically.

For the wave $w^{(\mathrm{F})}$ inside the flexible foundation ($\overline{a} \le r \le \underline{a}$, $0 \le \theta \le \pi$), the expression of the wave function is:

$$w^{(\mathrm{F})}(r,\theta) = \sum_{n=0}^{\infty} \left[C_n^{(1)} \mathrm{H}_n^{(1)}\left(k_{\mathrm{f}} r\right) + C_n^{(2)} \mathrm{H}_n^{(2)}\left(k_{\mathrm{f}} r\right) \right] \cos n\theta \tag{16.7}$$

To applying boundary conditions in other coordinate system, for shallow circular foundation case, the wave function shall be transformed by Graf's formula (8.26) same as used in Chapter 8.

$$w^{(\mathrm{F})}(\underline{r},\underline{\phi}) = \sum_{n=-\infty}^{\infty} \left[\underline{C}_n^{(1)} \mathrm{H}_n^{(1)}\left(k_{\mathrm{f}} \underline{r}\right) + \underline{C}_n^{(2)} \mathrm{H}_n^{(2)}\left(k_{\mathrm{f}} \underline{r}\right) \right] \mathrm{e}^{\mathrm{i}n\underline{\phi}} \tag{16.8}$$

$$w^{(\mathrm{F})}(\overline{r},\overline{\phi}) = \sum_{m=-\infty}^{\infty} \left[\overline{C}_m^{(1)} \mathrm{H}_m^{(1)}\left(k_{\mathrm{f}} \overline{r}\right) + \overline{C}_m^{(2)} \mathrm{H}_m^{(2)}\left(k_{\mathrm{f}} \overline{r}\right) \right] \mathrm{e}^{\mathrm{i}m\overline{\phi}} \tag{16.9}$$

in which, the coefficients are interchangeable, for $l = 1, 2$

$$\underline{C}_0^{(l)} = C_0^{(l)} \tag{16.10}$$

$$\underline{C}_n^{(l)} = \underline{C}_{-n}^{(l)} = \frac{(-\mathrm{i})^n}{2} C_n^{(l)} \quad \text{for} \quad n = 0,1,2,\cdots \tag{16.11}$$

$$\overline{C}_m^{(l)} = \sum_{n=-\infty}^{\infty} \underline{C}_n^{(l)} \mathrm{J}_{n+m}(k_\mathrm{f} d) = \mathrm{J}_m\left(k_\mathrm{f} d\right) C_0^{(l)} + \sum_{n=1}^{\infty} C_n^{(l)} \frac{(-\mathrm{i})^n}{2} \left[\mathrm{J}_{m+n}\left(k_\mathrm{f} d\right) + \mathrm{J}_{m-n}\left(k_\mathrm{f} d\right)\right] \tag{16.12}$$

10.3 Displacement and Stress Continuity between Soil and Flexible Foundation

The boundary conditions at the interface of flexible foundation and half-space (semi-circle $\underline{L}$ as denoted in Figure 1), for $0 \le \theta \le \pi$ and $r = \underline{a}$,

$$w^{(\mathrm{ff})} + w^{(\mathrm{S})}\Big|_{r=\underline{a}} = w^{(\mathrm{F})}\Big|_{r=\underline{a}} \tag{16.13}$$

$$\mu_\mathrm{s} \frac{\partial}{\partial r}\left(w^{(\mathrm{ff})} + w^{(\mathrm{S})}\right)\Big|_{r=\underline{a}} = \mu_\mathrm{f} \frac{\partial w^{(\mathrm{F})}}{\partial r}\Big|_{r=\underline{a}} \tag{16.14}$$

The two equations are able to be reduced to the following discrete equations, for $n = 0,1,2,3,\ldots$

$$a_n^{(f)} \mathrm{J}_n\left(k_\mathrm{s}\underline{a}\right) + A_n \mathrm{H}_n^{(1)}\left(k_\mathrm{s}\underline{a}\right) = C_n^{(1)} \mathrm{H}_n^{(1)}\left(k_\mathrm{f}\underline{a}\right) + C_n^{(2)} \mathrm{H}_n^{(2)}\left(k_\mathrm{f}\underline{a}\right) \tag{16.15}$$

$$a_n^{(f)} \mathrm{J}_n'\left(k_\mathrm{s}\underline{a}\right) + A_n \mathrm{H}_n^{(1)\prime}\left(k_\mathrm{s}\underline{a}\right) = \kappa\left[C_n^{(1)} \mathrm{H}_n^{(1)\prime}\left(k_\mathrm{f}\underline{a}\right) + C_n^{(2)} \mathrm{H}_n^{(2)\prime}\left(k_\mathrm{f}\underline{a}\right)\right] \tag{16.16}$$

These two boundary conditions ensure the effectiveness of seamless between those contingent media on either sides of $\underline{L}$. Here rigidity ratio $\kappa = \dfrac{\mu_\mathrm{f} k_\mathrm{f}}{\mu_\mathrm{s} k_\mathrm{s}}$

10.4 Displacement Continuity between Rigid and Flexible Foundations

The boundary conditions at the interface of rigid and flexible foundations

$$w^{(\mathrm{F})}\left(r,\theta\right)\Big|_{r=\overline{a}} = w^{(\mathrm{R})} = w_0 \mathrm{e}^{-\mathrm{i}\omega t} \tag{16.17}$$

Substituting (16.7) into this equation,

$$C_0^{(1)} \mathrm{H}_0^{(1)}\left(k_\mathrm{f}\overline{a}\right) + C_0^{(2)} \mathrm{H}_0^{(2)}\left(k_\mathrm{f}\overline{a}\right) = w_0 \tag{16.18}$$

for $n = 1,2,3,\ldots$

$$C_n^{(1)}\mathrm{H}_n^{(1)}\left(k_\mathrm{f}\overline{a}\right)+C_n^{(2)}\mathrm{H}_n^{(2)}\left(k_\mathrm{f}\overline{a}\right)=0 \tag{16.19}$$

In summary,

$$C_n^{(2)}=\begin{cases}\dfrac{w_0-C_0^{(1)}\mathrm{H}_0^{(1)}\left(k_\mathrm{f}\overline{a}\right)}{\mathrm{H}_0^{(2)}\left(k_\mathrm{f}\overline{a}\right)}, \text{ for } n=0\\ -\dfrac{\mathrm{H}_n^{(1)}\left(k_\mathrm{f}\overline{a}\right)}{\mathrm{H}_n^{(2)}\left(k_\mathrm{f}\overline{a}\right)}C_n^{(1)}, \text{ for } n=1,2,3,\ldots\end{cases} \tag{16.20}$$

For shallow case, similar to equation (16.17),

$$w^{(\mathrm{F})}\left(\overline{r},\overline{\phi}\right)\Big|_{\overline{r}=\overline{a}}=w^{(\mathrm{R})}=w_0\mathrm{e}^{-\mathrm{i}\omega t} \tag{16.21}$$

and

$$\begin{cases}\overline{C}_0^{(1)}\mathrm{H}_0^{(1)}\left(k_\mathrm{f}\overline{a}\right)+\overline{C}_0^{(2)}\mathrm{H}_0^{(2)}\left(k_\mathrm{f}\overline{a}\right)=w_0\ , \ m=0\\ \overline{C}_m^{(1)}\mathrm{H}_m^{(1)}\left(k_\mathrm{f}\overline{a}\right)+\overline{C}_m^{(2)}\mathrm{H}_m^{(2)}\left(k_\mathrm{f}\overline{a}\right)=0\ , \ m=\pm1,\pm2,\pm3,\ldots\end{cases} \tag{16.22}$$

Such that under this coordinate system $(\overline{r},\overline{\phi})$, we attain the relation below

$$\overline{C}_m^{(2)}=\begin{cases}\dfrac{w_0-\overline{C}_0^{(1)}\mathrm{H}_0^{(1)}\left(k_\mathrm{f}\overline{a}\right)}{\mathrm{H}_0^{(2)}\left(k_\mathrm{f}\overline{a}\right)}, \text{ for } m=0\\ -\dfrac{\overline{C}_m^{(1)}\mathrm{H}_m^{(1)}\left(k_\mathrm{f}\overline{a}\right)}{\mathrm{H}_m^{(2)}\left(k_\mathrm{f}\overline{a}\right)}, \text{ for } m=\pm1,\pm2,\pm3,\ldots\end{cases} \tag{16.23}$$

10.5 Response of the Building

By the same procedures in Chapter 8, the three formulae of displacement and stress response of the SDOF wall above are repeated here for convenience. For $-H\le y\le 0$

$$w_\mathrm{B}(y)=w_0\left(\cos k_\mathrm{B}y-\tan k_\mathrm{B}H\sin k_\mathrm{B}y\right)=\frac{w_0}{\cos k_\mathrm{B}H}\cos k_\mathrm{B}(y+H) \tag{16.24}$$

The shear stress along the interface of wall and foundation is

$$\tau_{yz}\Big|_{y=0} = \mu_{\mathrm{B}} \frac{\partial w_{\mathrm{B}}(y)}{\partial y}\Bigg|_{y=0} = -w_0 \mu_{\mathrm{B}} k_{\mathrm{B}} \tan k_{\mathrm{B}} H \tag{16.25}$$

The force of building acting on the foundation per unit length is

$$f_{\mathrm{B}} = -w_0 \mu_{\mathrm{B}} k_{\mathrm{B}} B \tan k_{\mathrm{B}} H \tag{16.26}$$

10.6 Kinetic Equation of Foundation

The kinetic equation for the semi- (or shallow) rigid foundation is

$$M_{\mathrm{R}} \ddot{w}_{\mathrm{R}} = -\left(f_{\mathrm{f}} + f_{\mathrm{B}}\right) \mathrm{e}^{-\mathrm{i}\omega t} \tag{16.27}$$

where M_{R} is the mass of the rigid foundation per unit depth in the *z* axis, and f_{f} denotes the action of flexible foundation on the rigid foundation. w_{R} represents the displacement function of rigid foundation in terms of time factor *t*, i.e., $w_{\mathrm{R}} = w_{\mathrm{R}}(t) = w_0 \mathrm{e}^{-\mathrm{i}\omega t}$.

$$f_{\mathrm{f}} = \bar{a} \int_0^{\pi} \tau_{rz}\Big|_{r=\bar{a}} \mathrm{d}\theta = \mu_{\mathrm{f}} k_{\mathrm{f}} \bar{a} \sum_{n=0}^{\infty} \left(C_n^{(1)} \mathrm{H}_n^{(1)\prime}\left(k_{\mathrm{f}}\bar{a}\right) + C_n^{(2)} \mathrm{H}_n^{(2)\prime}\left(k_{\mathrm{f}}\bar{a}\right) \right) \int_0^{\pi} \cos n\theta \mathrm{d}\theta \tag{16.28}$$

$$\ddot{w}_{\mathrm{R}} = -w_0 \omega^2 \mathrm{e}^{-\mathrm{i}\omega t} \tag{16.29}$$

and the definite integral could be solved explicitly,

$$\int_0^{\pi} \cos n\theta \mathrm{d}\theta = \begin{cases} \pi\ ,\ n=0 \\ 0\ ,\ n \neq 0 \end{cases} \tag{16.30}$$

So f_{f} could be rewritten as

$$f_{\mathrm{f}} = \mu_{\mathrm{f}} k_{\mathrm{f}} \bar{a} \left[0 + \pi \left(C_0^{(1)} \mathrm{H}_0^{(1)\prime}\left(k_{\mathrm{f}}\bar{a}\right) + C_0^{(2)} \mathrm{H}_0^{(2)\prime}\left(k_{\mathrm{f}}\bar{a}\right) \right) \right] \tag{16.31}$$

and the formula for f_{B} is derived in foregoing section 8.1.3 and shown in Eqn. (14.20). Therefore, the displacement of the rigid foundation w_0 is solvable and could be simplified as,

$$w_0 = P_0 C_0^{(1)} \tag{16.32}$$

in which,

$$P_0 = \frac{\dfrac{4\mathrm{i}}{\pi k_\mathrm{f} \mathrm{H}_0^{(2)}\left(k_\mathrm{f}\overline{a}\right)}}{\dfrac{k_\mathrm{f}\underline{a}^2}{2}\left(\dfrac{M_\mathrm{R}}{M_\mathrm{f}} + \dfrac{M_\mathrm{B}}{M_\mathrm{f}}\dfrac{\tan k_\mathrm{B} H}{k_\mathrm{B} H}\right) + \overline{a}\,\dfrac{\mathrm{H}_1^{(2)}\left(k_\mathrm{f}\overline{a}\right)}{\mathrm{H}_0^{(2)}\left(k_\mathrm{f}\overline{a}\right)}} \tag{16.33}$$

And M_B, M_R, and M_f stand for the mass of building, Rigid foundation, and flexible foundation, respectively. Similarly, ρ_B, ρ_R, and ρ_f denote density of those three media sequentially.

$$M_\mathrm{B} = \rho_\mathrm{B} B H \tag{16.34}$$

$$M_\mathrm{R} = \rho_\mathrm{R} \pi \overline{a}^2 / 2 \tag{16.35}$$

$$M_\mathrm{f} = \rho_\mathrm{f} \pi\, \underline{a}^2 / 2 \tag{16.36}$$

During the simplification procedure, the following Wronskians formula (Abramowitz and Stegun, 1972) has been applied,

$$W\left\{\mathrm{H}_p^{(2)}(z), \mathrm{H}_p^{(1)}(z)\right\} = \mathrm{H}_p^{(2)}(z)\mathrm{H}_p^{(1)\prime}(z) - \mathrm{H}_p^{(2)\prime}(z)\mathrm{H}_p^{(1)}(z) = \frac{4\mathrm{i}}{\pi z} \tag{16.37}$$

For shallow rigid foundation case, the procedures above in this section are conducted in the lower $(\overline{r}, \overline{\phi})$ coordinate system.

$$\begin{aligned} f_\mathrm{f} &= \overline{a}\int_{-\delta\pi/2}^{\delta\pi/2} \tau_{\overline{r}z}\Big|_{\overline{r}=a} d\overline{\phi} = \mu_\mathrm{f} k_\mathrm{f} \overline{a} \sum_{m=-\infty}^{\infty}\left(\overline{C}_m^{(1)}\mathrm{H}_m^{(1)\prime}\left(k_\mathrm{f}\overline{a}\right) + \overline{C}_m^{(2)}\mathrm{H}_m^{(2)\prime}\left(k_\mathrm{f}\overline{a}\right)\right)\int_{-\delta\pi/2}^{\delta\pi/2} \mathrm{e}^{\mathrm{i}m\overline{\phi}}\mathrm{d}\overline{\phi} \\ &= \mu_\mathrm{f} k_\mathrm{f} \overline{a}\left[\begin{aligned} &\sum_{\substack{m=-\infty \\ m\neq 0}}^{\infty} \frac{2}{m}\sin\frac{m\delta\pi}{2}\left(\overline{C}_m^{(1)}\mathrm{H}_m^{(1)\prime}\left(k_\mathrm{f}\overline{a}\right) + \overline{C}_m^{(2)}\mathrm{H}_m^{(2)\prime}\left(k_\mathrm{f}\overline{a}\right)\right) \\ &+\delta\pi\left(\overline{C}_0^{(1)}\mathrm{H}_0^{(1)\prime}\left(k_\mathrm{f}\overline{a}\right) + \overline{C}_0^{(2)}\mathrm{H}_0^{(2)\prime}\left(k_\mathrm{f}\overline{a}\right)\right) \end{aligned}\right] \end{aligned} \tag{16.38}$$

And w_0 for shallow case can be written as

$$w_0 = \frac{\frac{4\mathrm{i}}{\pi k_\mathrm{f}} \sum_{m=-\infty}^{\infty} \frac{\mathrm{sinc}(\frac{m\delta}{2})}{\mathrm{H}_m^{(2)}(k_\mathrm{f}\bar{a})} \bar{C}_m^{(1)}}{\frac{k_\mathrm{f}\underline{a}^2}{2\delta}\left(\frac{M_\mathrm{B}}{M_\mathrm{f}} \frac{\tan k_\mathrm{B} H}{k_\mathrm{B} H} + \frac{M_\mathrm{R}}{M_\mathrm{f}}\right) + \bar{a} \frac{\mathrm{H}_1^{(2)}(k_\mathrm{f}\bar{a})}{\mathrm{H}_0^{(2)}(k_\mathrm{f}\bar{a})}} \tag{16.39}$$

Compared with explicit equation (16.32) for semi-circular case, w_0 for shallow case is expressed implicitly in terms of sum of coefficients $\bar{C}_m^{(1)}$. Also M_R is also altered due to the change of rigid foundation shape. The normalized sinc function, also called "sampling function" in digital signal processing, is adopted here for abbreviation

$$\mathrm{sinc}(t) = \begin{cases} 1 \ , \ t = 0 \\ \frac{\sin(\pi t)}{\pi t}, \ t \neq 0 \end{cases} \tag{16.40}$$

$$M_\mathrm{R} = \frac{\rho_\mathrm{R} \bar{a}^2}{2}(\delta\pi - \sin\delta\pi) \tag{16.41}$$

Comparison of equations of rigid foundation motion, namely (16.32) and (16.39), shows that if we set $\delta = 1$ in Eqn. (14.27), apparently $d = 0$ and center $\bar{O}$ overlaps with O. Since $\mathrm{J}_0(0) = 1$ and $\mathrm{J}_n(0) = 0$ for any other integer order n, either positive or negative. By applying $d = 0$ into equation (16.12), we have $\bar{C}_0^{(1)} = C_0^{(1)}$, and

$$\bar{C}_m^{(1)} = \frac{(-\mathrm{i})^{|m|}}{2} C_{|m|}^{(1)} \text{ when } m \neq 0 \tag{16.42}$$

With that, Eqn. (16.39) could be reduced into (16.32) for semi-circular rigid foundation case.

10.7 Elimination and Solution

First, for the semi-circular rigid foundation case, by combining equations (14.27), (16.15), (16.16), and (14.13), we can derive out the explicit expressions for wave function coefficients A_n and $C_n^{(1)}$ as follows:

$$\begin{Bmatrix} C_n^{(1)} \\ A_n \end{Bmatrix} = \frac{a_n^{(f)}}{Q_n' \mathrm{H}_n^{(1)}(k_\mathrm{s}\underline{a}) - Q_n \mathrm{H}_n^{(1)\prime}(k_\mathrm{s}\underline{a})} \begin{Bmatrix} \dfrac{-2\mathrm{i}}{\pi k_\mathrm{s}\underline{a}} \\ Q_n \mathrm{J}_n{}'(k_\mathrm{s}\underline{a}) - Q_n' \mathrm{J}_n(k_\mathrm{s}\underline{a}) \end{Bmatrix} \tag{16.43}$$

in which, for n=0,1,2,3…

$$Q_n = \frac{\mathrm{H}_n^{(1)}(k_\mathrm{f}\underline{a})\mathrm{H}_n^{(2)}(k_\mathrm{f}\overline{a}) - \mathrm{H}_n^{(2)}(k_\mathrm{f}\underline{a})\mathrm{H}_n^{(1)}(k_\mathrm{f}\overline{a}) + \delta_n \mathrm{H}_n^{(2)}(k_\mathrm{f}\underline{a})P_0}{\mathrm{H}_n^{(2)}(k_\mathrm{f}\overline{a})} \tag{16.44}$$

$$Q_n' = \kappa \left[\frac{\mathrm{H}_n^{(1)\prime}(k_\mathrm{f}\underline{a})\mathrm{H}_n^{(2)}(k_\mathrm{f}\overline{a}) - \mathrm{H}_n^{(2)\prime}(k_\mathrm{f}\underline{a})\mathrm{H}_n^{(1)}(k_\mathrm{f}\overline{a}) + \delta_n \mathrm{H}_n^{(2)\prime}(k_\mathrm{f}\underline{a})P_0}{\mathrm{H}_n^{(2)}(k_\mathrm{f}\overline{a})} \right] \tag{16.45}$$

$$\delta_n = \begin{cases} 1, & n = 0 \\ 0, & n \neq 0 \end{cases} \tag{16.46}$$

$$\kappa = \frac{\mu_\mathrm{f} k_\mathrm{f}}{\mu_\mathrm{s} k_\mathrm{s}} \tag{16.47}$$

Here the δ_n is the unit impulse function and please notice not to be messed up with central angle $\delta\pi$ in this paper, which is given as a constant.

So, as equation (16.43) shows, for semi-circular case, coefficients of wave functions can be solved out explicitly. Next we discuss the governing equation for shallow case.

So in summary, totally we obtained the following 6 sets of equations in terms of 6 (sets of) unknowns, w_0, A_n, $C_n^{(1)}$, $C_n^{(2)}$, $\overline{C}_m^{(1)}$, and $\overline{C}_m^{(2)}$ with subscripts $n = 0, 1, 2, \ldots$ and $m = 0, \pm 1, \pm 2, \ldots$.

$$w_0 = P_0 \sum_{m=-\infty}^{\infty} \frac{\mathrm{sinc}(\frac{m\delta}{2})}{\mathrm{H}_m^{(2)}\left(k_\mathrm{f}\overline{a}\right)} \overline{C}_m^{(1)} \tag{16.48}$$

$$\overline{C}_m^{(2)} = \begin{cases} \dfrac{w_0 - \overline{C}_0^{(1)} \mathrm{H}_0^{(1)}\left(k_\mathrm{f}\overline{a}\right)}{\mathrm{H}_0^{(2)}\left(k_\mathrm{f}\overline{a}\right)}, & \text{for } m = 0 \\ -\dfrac{\overline{C}_m^{(1)} \mathrm{H}_m^{(1)}\left(k_\mathrm{f}\overline{a}\right)}{\mathrm{H}_m^{(2)}\left(k_\mathrm{f}\overline{a}\right)}, & \text{for } m = \pm 1, \pm 2, \pm 3, \ldots \end{cases} \tag{16.49}$$

$$a_n^{(f)}\mathrm{J}_n\left(k_\mathrm{s}\underline{a}\right)+A_n\mathrm{H}_n^{(1)}\left(k_\mathrm{s}\underline{a}\right)=C_n^{(1)}\mathrm{H}_n^{(1)}\left(k_\mathrm{f}\underline{a}\right)+C_n^{(2)}\mathrm{H}_n^{(2)}\left(k_\mathrm{f}\underline{a}\right) \tag{16.50}$$

$$a_n^{(f)}\mathrm{J}_n'\left(k_\mathrm{s}\underline{a}\right)+A_n\mathrm{H}_n^{(1)\prime}\left(k_\mathrm{s}\underline{a}\right)=\kappa\left[C_n^{(1)}\mathrm{H}_n^{(1)\prime}\left(k_\mathrm{f}\underline{a}\right)+C_n^{(2)}\mathrm{H}_n^{(2)\prime}\left(k_\mathrm{f}\underline{a}\right)\right] \tag{16.51}$$

$$\overline{C}_m^{(1)}=\sum_{n=0}^{\infty}D_{mn}C_n^{(1)} \tag{16.52}$$

$$\overline{C}_m^{(2)}=\sum_{n=0}^{\infty}D_{mn}C_n^{(2)} \tag{16.53}$$

where,

$$P_0=\frac{\dfrac{4\mathrm{i}}{\pi k_\mathrm{f}}}{\dfrac{k_\mathrm{f}\underline{a}^2}{2\delta}\left(\dfrac{M_\mathrm{B}}{M_\mathrm{f}}\dfrac{\tan k_\mathrm{B}H}{k_\mathrm{B}H}+\dfrac{M_\mathrm{R}}{M_\mathrm{f}}\right)+\overline{a}\,\dfrac{\mathrm{H}_1^{(2)}\left(k_\mathrm{f}\overline{a}\right)}{\mathrm{H}_0^{(2)}\left(k_\mathrm{f}\overline{a}\right)}} \tag{16.54}$$

$$D_{mn}=\frac{(-\mathrm{i})^n}{2}\left[\mathrm{J}_{m+n}\left(k_\mathrm{f}d\right)+\mathrm{J}_{m-n}\left(k_\mathrm{f}d\right)\right] \tag{16.55}$$

After eliminating w_0, $\overline{C}_m^{(1)}$ and $\overline{C}_m^{(2)}$, we attain the following simplified formula, for $m=0,\pm1,\pm2,\dots$

$$\sum_{n=0}^{\infty}D_{mn}C_n^{(2)}=\sum_{n=0}^{\infty}E_{mn}C_n^{(1)} \tag{16.56}$$

in which, the coefficient matrix on the right-hand-side can be written as equation (16.57)

$$E_{mn}=\begin{cases}\dfrac{P_0}{\mathrm{H}_0^{(2)}\left(k_\mathrm{f}\overline{a}\right)}\displaystyle\sum_{l=-\infty}^{\infty}\frac{\mathrm{sinc}(\frac{\delta l}{2})}{\mathrm{H}_l^{(2)}\left(k_\mathrm{f}\overline{a}\right)}D_{ln}-\dfrac{\mathrm{H}_0^{(1)}\left(k_\mathrm{f}\overline{a}\right)}{\mathrm{H}_0^{(2)}\left(k_\mathrm{f}\overline{a}\right)}D_{0n}, & m=0\\[2ex] -\dfrac{\mathrm{H}_m^{(1)}\left(k_\mathrm{f}\overline{a}\right)}{\mathrm{H}_m^{(2)}\left(k_\mathrm{f}\overline{a}\right)}D_{mn}, & m\neq0\end{cases} \tag{16.57}$$

$C_n^{(1)}$ and $C_n^{(1)}$ can be expressed in terms of A_n by inverting the following coefficient matrix composed of equation (16.50) and (16.51):

$$\begin{bmatrix} \mathrm{H}_n^{(1)}\left(k_{\mathrm{f}}\underline{a}\right) & \mathrm{H}_n^{(2)}\left(k_{\mathrm{f}}\underline{a}\right) \\ \kappa\mathrm{H}_n^{(1)\prime}\left(k_{\mathrm{f}}\underline{a}\right) & \kappa\mathrm{H}_n^{(2)\prime}\left(k_{\mathrm{f}}\underline{a}\right) \end{bmatrix} \begin{Bmatrix} C_n^{(1)} \\ C_n^{(2)} \end{Bmatrix} = \begin{bmatrix} \mathrm{J}_n\left(k\underline{a}\right) & \mathrm{H}_n^{(1)}\left(k\underline{a}\right) \\ \mathrm{J}_n'\left(k\underline{a}\right) & \mathrm{H}_n^{(1)\prime}\left(k\underline{a}\right) \end{bmatrix} \begin{Bmatrix} a_n^{(\mathrm{f})} \\ A_n \end{Bmatrix} \tag{16.58}$$

After inverting matrix in the left-hand-side,

$$\begin{Bmatrix} C_n^{(1)} \\ C_n^{(2)} \end{Bmatrix} = \begin{Bmatrix} G11_n a_n^{(\mathrm{f})} + G12_n A_n \\ G21_n a_n^{(\mathrm{f})} + G22_n A_n \end{Bmatrix} \tag{16.59}$$

Where

$$G11_n = \frac{\pi \mathrm{i} k_{\mathrm{f}}\underline{a}}{4}\left[\mathrm{H}_n^{(2)\prime}\left(k_{\mathrm{f}}\underline{a}\right)\mathrm{J}_n\left(k\underline{a}\right) - \frac{1}{\kappa}\mathrm{H}_n^{(2)}\left(k_{\mathrm{f}}\underline{a}\right)\mathrm{J}_n'\left(k\underline{a}\right)\right] \tag{16.60}$$

$$G12_n = \frac{\pi \mathrm{i} k_{\mathrm{f}}\underline{a}}{4}\left[\mathrm{H}_n^{(2)\prime}\left(k_{\mathrm{f}}\underline{a}\right)\mathrm{H}_n^{(1)}\left(k_{\mathrm{f}}\underline{a}\right) - \frac{1}{\kappa}\mathrm{H}_n^{(2)}\left(k_{\mathrm{f}}\underline{a}\right)\mathrm{H}_n^{(1)\prime}\left(k_{\mathrm{f}}\underline{a}\right)\right] \tag{16.61}$$

$$G21_n = \frac{\pi \mathrm{i} k_{\mathrm{f}}\underline{a}}{4}\left[\frac{1}{\kappa}\mathrm{H}_n^{(1)}\left(k_{\mathrm{f}}\underline{a}\right)\mathrm{J}_n'\left(k\underline{a}\right) - \mathrm{H}_n^{(1)\prime}\left(k\underline{a}\right)\mathrm{J}_n\left(k\underline{a}\right)\right] \tag{16.62}$$

$$G22_n = \frac{\pi \mathrm{i} k_{\mathrm{f}}\underline{a}}{4}\left[\frac{1}{\kappa}\mathrm{H}_n^{(1)}\left(k_{\mathrm{f}}\underline{a}\right)\mathrm{H}_n^{(1)\prime}\left(k_{\mathrm{f}}\underline{a}\right) - \mathrm{H}_n^{(1)\prime}\left(k\underline{a}\right)\mathrm{H}_n^{(1)}\left(k\underline{a}\right)\right] \tag{16.63}$$

Substituting (16.59) into (16.56), we have the following derivation bringing out the governing equations in term of A_n only

$$\sum_{n=0}^{\infty} M_{mn} A_n = R_m \tag{16.64}$$

where,

$$M_{mn} = G22_n D_{mn} - G12_n E_{mn} \tag{16.65}$$

$$R_m = \sum_{n=0}^{\infty}\left(G11_n E_{mn} - G21_n D_{mn}\right) a_n^{(\mathrm{f})} \tag{16.66}$$

Thus by this way, after solving out A_n from (16.64), $C_n^{(1)}$ and $C_n^{(1)}$ can be obtained by substituting A_n into (16.59); and then $\overline{C}_m^{(1)}$ and $\overline{C}_m^{(1)}$ by equations (16.52) and (16.53).

10.8 Numerical Solutions

This section includes numerical solutions and case study of antiplane excitation of SSI system with rigid-flexible foundations. Fig. 10-5 through Fig. 10-10 represent the ground displacement amplitudes of semi-cylindrical foundation enclosed in a concentric semi-cylindircal flexible ring. The overshooting displacements existing between the two foundations ($\overline{a} \le x \le \underline{a}$) on the ground surface is quite noticeable. In the author's opinion, this phenomenon is not because of numerical errors, but the massive shear stress and displacement generated by the narrorw band sandwiched by three media (rigid foundation; flexible foundation, half-space soil). The first three plots are for $\overline{a}/\underline{a} = 1.1$, and the next three are for $\overline{a}/\underline{a} = 1.5$. As we can tell, the thickness of the soft ring doesn't have too much influence on the ground displacement amplitude.

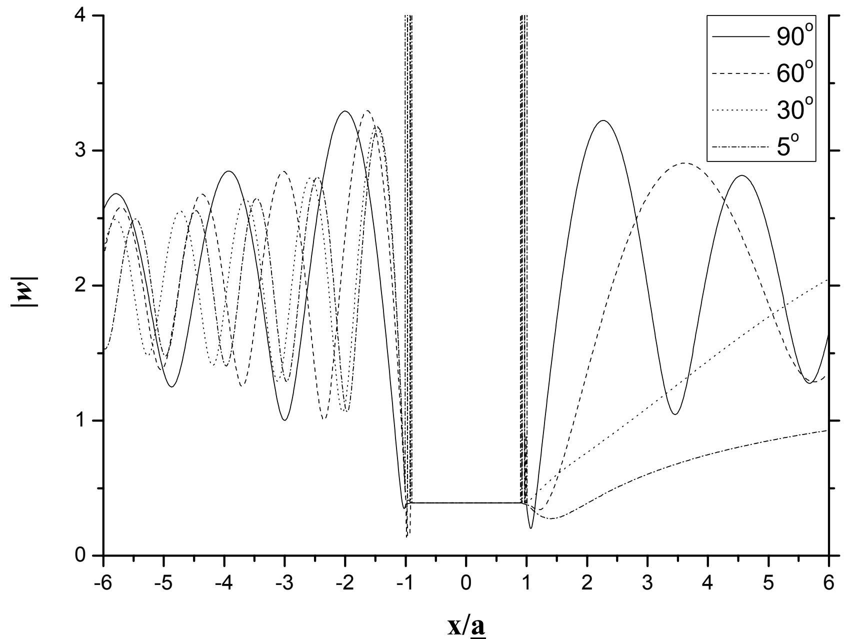

Fig. 10-5 GROUND SURFACE DISPLACEMENT FOR $\eta = 1$, $M_R/M_f = 2$, $M_B/M_f = 4$, $M_s/M_f = 1.5$, $\overline{a}/\underline{a} = 1.1$, $k_B H/kb = 4$, $\kappa = 4$, **AND** γ **= 85°, 60°, 30°, 5°**

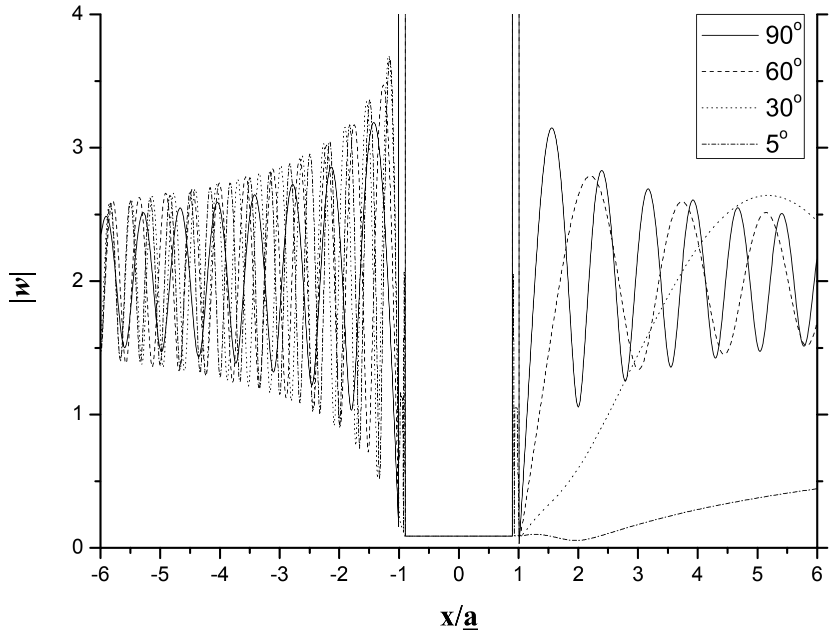

Fig. 10-6 GROUND SURFACE DISPLACEMENT FOR $\eta = 3$, $M_{\mathrm{R}}/M_{\mathrm{f}} = 2$, $M_{\mathrm{B}}/M_{\mathrm{f}} = 4$, $M_{\mathrm{s}}/M_{\mathrm{f}} = 1.5$, $\overline{a}/\underline{a} = 1.1$, $k_{\mathrm{B}}H/kb = 4$, $\kappa = 4$, **AND** $\gamma = 85^{\circ}, 60^{\circ}, 30^{\circ}, 5^{\circ}$

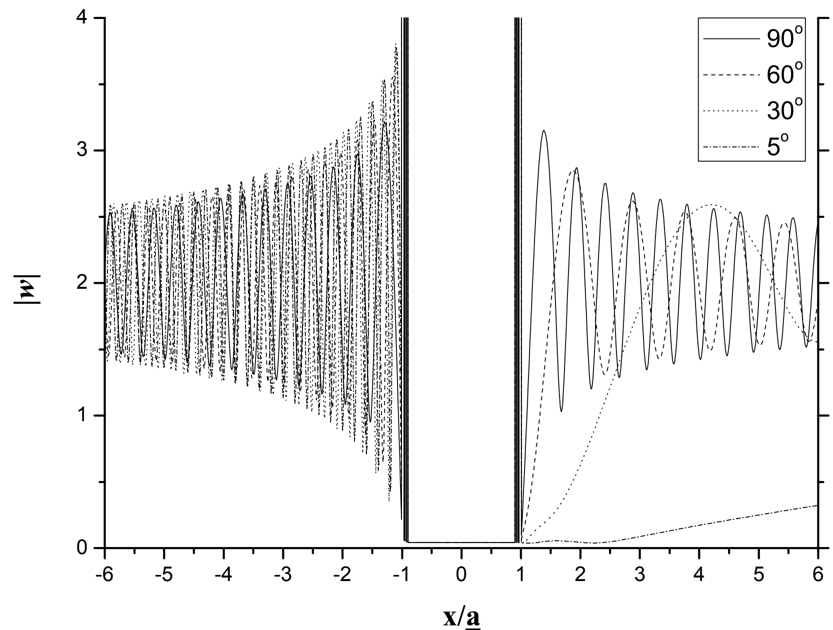

Fig. 10-7 GROUND SURFACE DISPLACEMENT FOR $\eta = 5$, $M_{\mathrm{R}}/M_{\mathrm{f}} = 2$, $M_{\mathrm{B}}/M_{\mathrm{f}} = 4$, $M_{\mathrm{s}}/M_{\mathrm{f}} = 1.5$, $\overline{a}/\underline{a} = 1.1$, $k_{\mathrm{B}}H/kb = 4$, $\kappa = 4$, **AND** $\gamma = 85^{\circ}, 60^{\circ}, 30^{\circ}, 5^{\circ}$

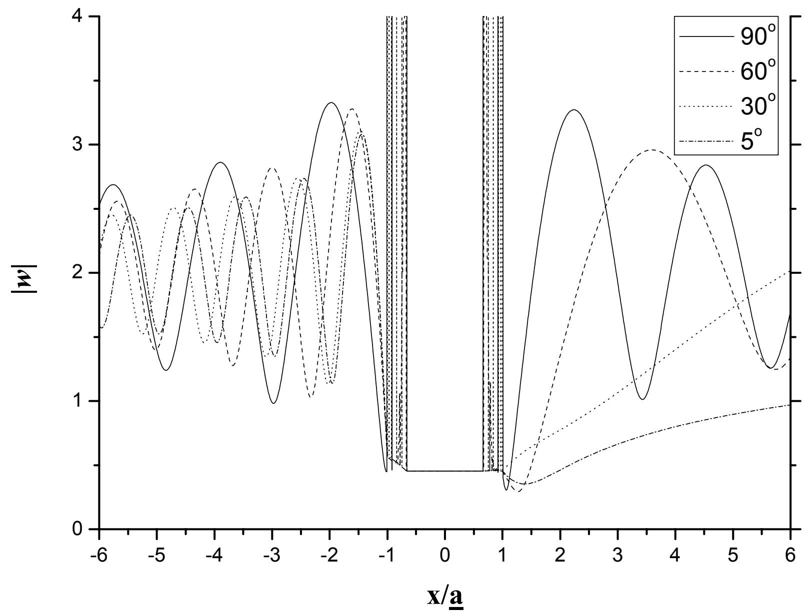

Fig. 10-8 GROUND SURFACE DISPLACEMENT FOR $\eta = 1$, $M_R/M_f = 2$, $M_B/M_f = 4$, $M_s/M_f = 1.5$, $\bar{a}/\underline{a} = 1.5$, $k_B H/kb = 4$, $\kappa = 4$, **AND** γ **= 85°, 60°, 30°, 5°**

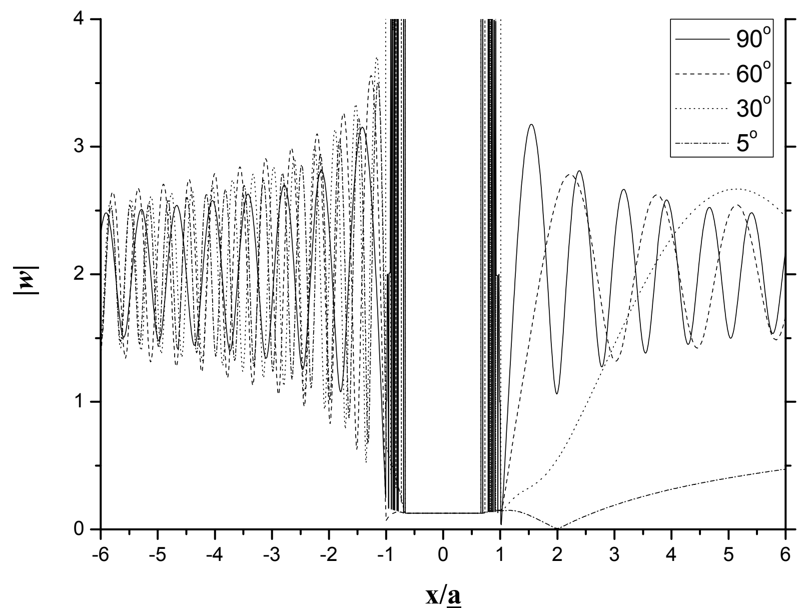

Fig. 10-9 GROUND SURFACE DISPLACEMENT FOR $\eta = 3$, $M_R/M_f = 2$, $M_B/M_f = 4$, $M_s/M_f = 1.5$, $\bar{a}/\underline{a} = 1.5$, $k_B H/kb = 4$, $\kappa = 4$, **AND** γ **= 85°, 60°, 30°, 5°**

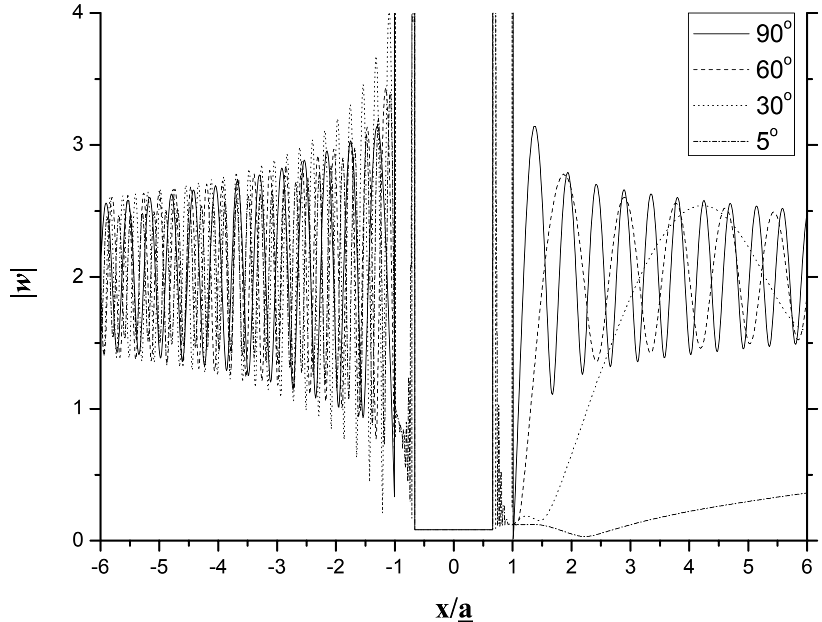

Fig. 10-10 GROUND SURFACE DISPLACEMENT FOR $\eta = 5$, $M_R/M_f = 2$, $M_B/M_f = 4$, $M_s/M_f = 1.5$, $\overline{a}/\underline{a} = 1.5$, $k_B H/kb = 4$, $\kappa = 4$, **AND** γ **= 85°, 60°, 30°, 5°**

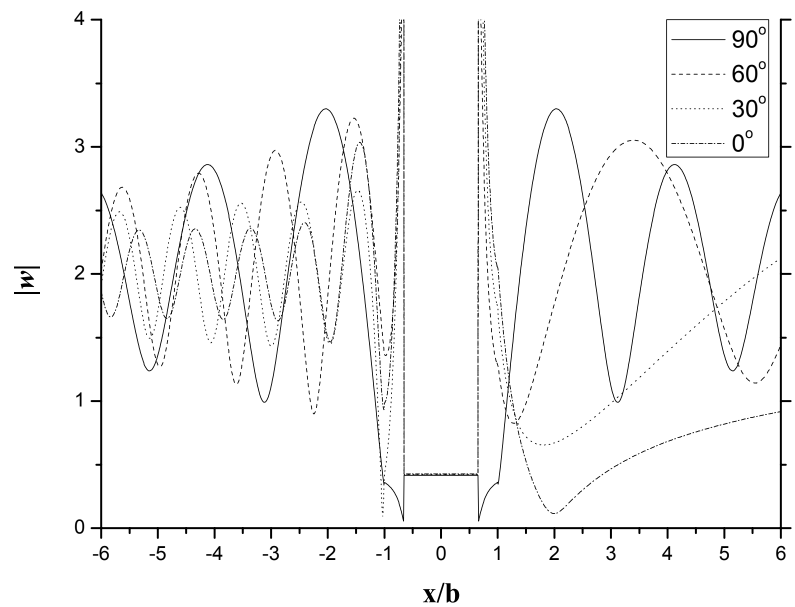

Fig. 10-11 GROUND SURFACE DISPLACEMENT FOR $\eta = 1$, $M_R/M_f = 2$, $M_B/M_f = 4$, $M_s/M_f = 1.5$, $\overline{a}/\underline{a} = 1.5$, $h/b = 0.85$, $k_B H/kb = 2$, $\kappa = 2$, **AND** γ **= 90°, 60°, 30°, 0°**

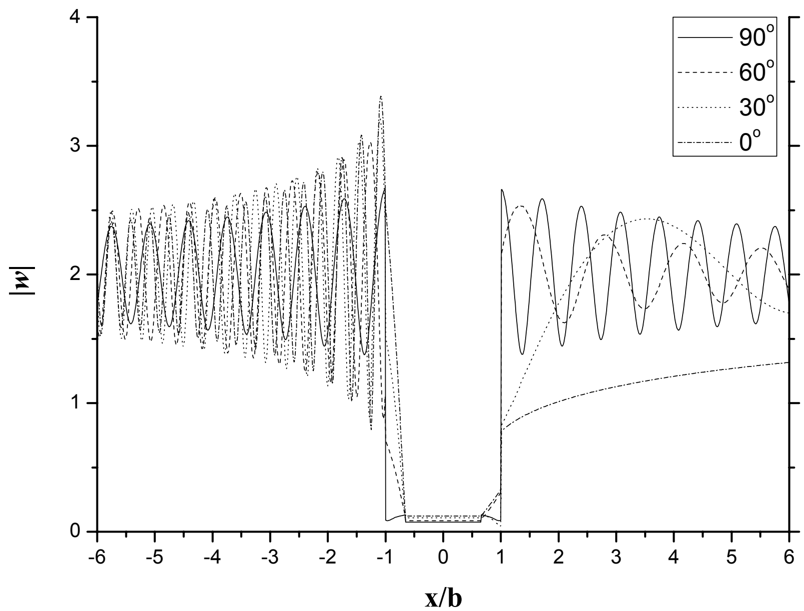

Fig. 10-12 GROUND SURFACE DISPLACEMENT FOR $\eta = 3$, $M_R/M_f = 2$, $M_B/M_f = 4$, $M_s/M_f = 1.5$, $\overline{a}/\underline{a} = 1.5$, $h/b = 0.85$, $k_B H/kb = 2$, $\kappa = 2$, **AND** γ **= 90°, 60°, 30°, 0°**

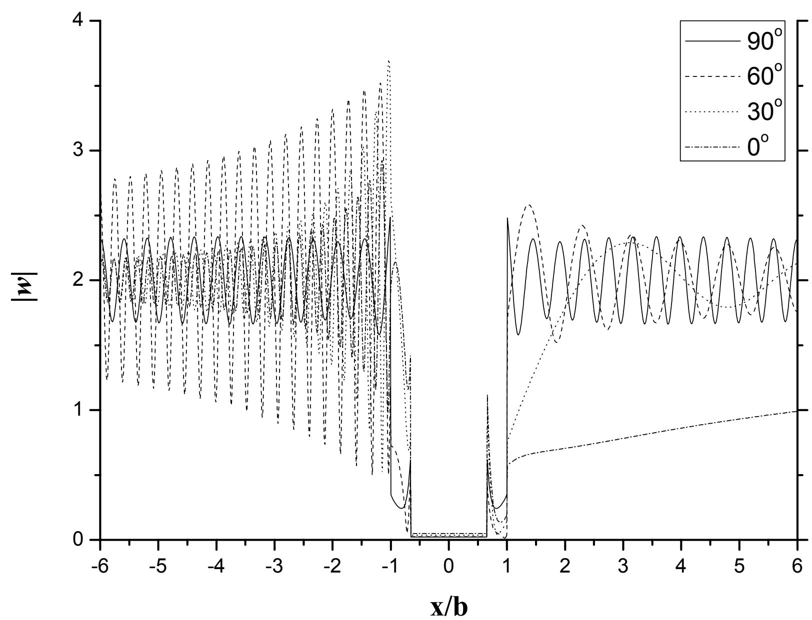

Fig. 10-13 GROUND SURFACE DISPLACEMENT FOR $\eta = 5$, $M_R/M_f = 2$, $M_B/M_f = 4$, $M_s/M_f = 1.5$, $\overline{a}/\underline{a} = 1.5$, $h/b = 0.85$, $k_B H/kb = 2$, $\kappa = 2$, **AND** γ **= 90°, 60°, 30°, 0°**

Comparison of these displacement amplitude plots and the ones in Chapter 8, in which only one rigid foundation, shows that the flexible (soft) interlayer ring has the effect of diminishing the ground displacement amplitude. Same for the composite foundation plots shown in Fig. 10-11 to Fig. 10-13, the soft flexible foundation to some extend reduces the ground motion near the model we examined.

Chapter 11

REMARKS AND CONCLUSIONS

Two-dimensional analytical models have been employed in this dissertation to investigate the steady-state response of engineering structures during soil-foundation-structure interaction or near-field ground motion, under the excitation of incident plane SH-waves. Those two-dimensional models appear to be diverse but share a few similarities. First, all the boundaries are in linear or circular for the purpose of construction of analytical wave functions to represent the wave field divided by those boundaries. Free or continuity boundary conditions are then formulated. In this manner all the models studied are circular or rectangular cylinders, from a three-dimensional point of view. Other common geometric coordinate systems ever used by other researchers such as elliptical and parabolic ones are not studied in this dissertation.

Secondly, only the simplest kind of body wave, SH-wave - either plane or cylindrical, is discussed. Without loss of generality, the intention of this dissertation emphasizes on the diversity of configurations of models and mathematical techniques to solving wave propagation problems with application in earthquake engineering. Other body waves or surface waves such as P- or SV-waves, bringing on wave mode conversion when reflected or refracted at boundaries separating dissimilar media, involve more numerous and complex boundary conditions, thus are not discussed in this dissertation. However, some of the mathematical techniques successfully applied for SH-waves can be used for P or SV-wave incident cases. According to superposition principle, the steady-state theory and results for incident harmonic waves are easy to be expanded to solve transient response for time-varying incidence.

Finally, all present models are solved based on wave function expansion method. Through the construction of wave functions in various regions, clear understanding of physical concepts can be achieved. In addition, we solve those analytical solutions for the same purpose of providing accurate reference criteria for various approximate numerical or other analytical methods. Numerical errors are inevitable for any methods, including analytical methods, except a few extremely theoretical and nonobjective models such as the semi-cylindrical valley with a concentric line source inside as shown in Fig. 5-19. However, one of the advantages of analytical methods over numerical methods is the error of analytical solutions is quantitative and precisely estimable. On the contrary, the error of numerical methods most likely could only be roughly assessed in the scale of magnitude order, owing to the indetermination aroused by additional artificial assumptions such as meshing procedure when performing finite element analysis (FEA).

GLOSSARY

a	characteristic dimension of the scatterer studied (commonly radius or half-width)
$\overline{a}$	radius of the shallow circular rigid foundation
$\underline{a}$	radius of the semi-circular flexible foundation
A_n	complex constants
b	half-width of the foundation
B	width of the building
C_{β_b}	shear wave velocity in the building
C_{β_f}	shear wave velocity in the flexible foundation
C_{β_s} or C_β	shear wave velocity in the soil
d	distance between the center of the circular-arc and the half-space surface
f_F	force per unit length acting on the rigid foundation from the flexible foundaton
f_b	force per unit length acting on the building
h	height of the rigid foundation
H	height of the building (shear beam)
$\mathrm{H}_p^{(1)}(x)$, $\mathrm{H}_p^{(2)}(x)$	Hankel function of the first or second kind with argument x and order p
i	imaginary unit
j, l, m, n	subscripts used for sequence number

$\mathrm{J}_p(x)$	Bessel function of the first kind with argument x and order p
k_b	wave number in the soil, $k_\mathrm{b} = \omega / C_{\beta_\mathrm{b}}$
k_f	wave number in the foundation, $k_\mathrm{f} = \omega / C_{\beta_\mathrm{f}}$
k_s or k	wave number in the soil, $k_\mathrm{s} = \omega / C_{\beta_\mathrm{s}}$
M_b	mass of building per unit length
M_f	mass of foundation per unit length
M_s	mass of soil in place of foundation per unit length
γ	angle of incidence for SH-waves
w_0	amplitude of the displacement of the foundation
w	amplitude of the displacement of the total wave field in the soil
$w^{(\mathrm{ff})}$	amplitude of the displacement of the free wave field in the half-space soil
$w^{(\mathrm{B})}$	amplitude of the displacement of wave field in the building
$w^{(\mathrm{F})}$	amplitude of the displacement of wave field in the flexible foundation
$w^{(\mathrm{R})}$ or w_R	amplitude of the displacement of wave field in the rigid foundation
$w^{(\mathrm{S})}$	amplitude of the displacement of scattered wave field in the soil
$w^{(\mathrm{T})}$	amplitude of the displacement of transmitted wave field in a certain medium
η	dimensionless frequency of the incident SH waves

μ_{b}	shear modulus (rigidity) of the building
μ_{f}	shear modulus (rigidity) of the flexible foundation
μ_{s} or μ	shear modulus (rigidity) of the soil
ρ_{b}	density of the building
ρ_{f}	density of the flexible foundation
ρ_{R}	density of the rigid foundation
ρ_{s} or ρ	density of the soil
ω	circular frequency of the incident SH waves
$\delta\pi$	interior angle of the circular sector of the foundation
δ_n	unit impulse function

BIBLIOGRAPHY

1. Abramowitz, M., and Stegun, I. A. (1972). *Handbook of mathematical functions, with formulas, graphs, and mathematical tables*, Dover Publications, Inc., New York, N.Y.

2. Achenbach, J. D. (1970). *Shear Waves in an Elastic Wedge*, International Journal of Solids and Structures, 6(4), 379-388.

3. Bowman, J. J., Senior, T. B. A., and Uslenghi, P. L. E. (1969). *Electromagnetic and Acoustic Scattering by Simple Shapes*, North-Holland Publishing Company, Amsterdam, Netherlands

4. Cao, H., and Lee, V. W. (1989). *Scattering of Plane SH Waves by Circular Cylindrical Canyons with Variable Depth-to-Width Ratio*, European Journal of Earthquake Engineering, III(2), 29-37.

5. Cao, H., and Lee, V. W. (1990). *Scattering and Diffraction of Plane P Waves by Circular Cylindrical Canyons with Variable Depth-to-Width Ratio*, International Journal of Soil Dynamics and Earthquake Engineering, 9(3), 141-150.

6. Davis, P. J., and Rabinowitz, P. (1984). *Methods of Numerical Integration*, 2nd edition, Academic Press Inc.

7. Eom, H. J. (2001). *Wave Scattering Theory: A Series Approach Based on the Fourier Transformation*, Springer-Verlag, Heidelberg.

8. Fang, Hsai-Yang (1991). *Foundation Engineering Handbook*, 2nd edition, Van Nostrand Reinhold, New York, N.Y.

9. Geli, L., Bard, P.-Y., and Jullien, B. (1988). *The Effect of Topography on Earthquake Ground Motion*: *A Review and New Results*, Bulletin of the Seismological Society of America, 78(1), 42-63.

10. Ghosh, T. K. (1995). *Diffraction of Plane and Surface Waves by Three-Dimensional Cylindrical, Sub-Surface Cavities in an Elastic Half Space*, Ph.D. degree Dissertation, University of Southern California, Civil Eng. Dept., 151-152

11. Graff, K. F. (1975). *Wave Motion in Elastic Solids*, Ohio State University Press, Dover Publications, Inc., New York, N.Y., 65-68.

12. Hadamard, J. (1902). *Sur les problèmes aux dérivées partielles et leur signification physique*. Princeton University Bulletin, 13, 49-52.

13. Hamming, R. W. (1962). *Numerical Methods for Scientists and Engineers*, McGraw-Hill Book Company, Inc., New York, N.Y.

14. Hansen, Per Christian, and O'Leary, D.P. (1993). *The Use of the L-Curve in the Regularization of Discrete Ill-Posed Problems*, SIAM Journal on Scientific Computing, 14(6), 1487-1503.

15. Hansen, Per Christian. (1994). *Regularization Tools: A Matlab package for analysis and solution of discrete ill-posed problems*, Numerical Algorithms, 6(1), 1-35.

16. Hansen, Per Christian. (1998). *Rank-Deficient and Discrete Ill-Posed Problems*: *Numerical Aspects of Linear Inversion*, SIAM, Philadelphia, P.A.

17. Hansen, Per Christian. (2007). *Regularization Tools version 4.0 for Matlab 7.3*, Numerical Algorithms, 46(2), 189-194.

18. Hansen, P. C., Jensen, T. K., and Rodriguez, G. (2007). *An Adaptive Pruning Algorithm for the Discrete L-Curve Criterion*, Journal of Computational and Applied Mathematics, 198(2), 483-492.

19. Harrington, R. F. (1968). *Field Computation by Moment Methods*, MacMillan, New York, N.Y.

20. Hayir, A., Todorovska, M. I., and Trifunac, M. D. (2001). *Antiplane Response of a Dike with Flexible Soil-Structure Interface to Incident SH Waves*, Soil Dynamics and Earthquake Engineering, 21(7), 603-613.

21. Housner, G. W. (1957) *Interaction of Buildings and Ground during an Earthquake*, Bulletin of the Seismological Society of America, 47(3), 179-186.

22. Jeremić, B., Kunnath S., and Xiong, F. (2004) *Influence of Soil-Foundation-Structure Interaction on Seismic Response of the I-880 Viaduct*, Engineering Structures, 26(3), 391-402.

23. Kolymbas, D. (2005). *Tunnelling and Tunnel Mechanics – A Rational Approach to Tunnelling*, Springer-Verlag, Berlin, Germany.

24. Kirsch, Andreas (1996). *An Introduction to the Mathematical Theory of Inverse Problems*, Springer-Verlag, New York, N.Y.

25. Lamb, Horace (1904). *On the Propagation of Tremors over the Surface of an Elastic Solid*, Philosophical Transactions of the Royal Society of London. Series A, 1-42.

26. Lee, V. W. (1977). *On Deformations Near Circular Underground Cavity Subjected to Incident Plane SH-Waves*, Proceedings of the Application of Computer Methods in Engineering Conference, Los Angeles, 951-962

27. Lee, V. W., and Cao, H. (1989). *Diffraction of SV Waves by Circular Cylindrical Canyons of Various Depths*, Journal of Engineering Mechanics, ASCE, 115(9), 2035-2056

28. Lee, V. W., and Karl, J. (1992). *Diffraction of SV Waves by underground, Circular, Cylindrical Cavities*, International Journal of Soil Dynamics and Earthquake Engineering, 11(8), 445-456.

29. Lee, V. W., and Karl, J. (1993). *Diffraction of Elastic Plane P Waves by Circular, Underground Unlined Tunnels*, European Journal of Earthquake Engineering, VI(1), 29-36.

30. Lee, V. W., Luo, H., and Liang, J. W. (2004). *Diffraction of Anti-Plane SH Waves by a Semi-Circular Cylindrical Hill with an Inside Semi-Circular Concentric Tunnel*, Earthquake Engineering and Engineering Vibration, 3(2), 249-262.

31. Lee, V. W., Luo, H., and Liang, J. W. (2006). *Anti-Plane (SH) Waves Diffraction by a Semi-Circular Cylindrical Hill Revisited: An Improved Accurate Wave Series Analytic Solution*, Journal of Engineering Mechanics, ASCE, 132(10), 1106-1114.

32. Lee, V. W., and Sherif, R. I. (1996). *Diffraction around Circular Canyon in Elastic Wedge Space by Plane SH Waves*, Journal of Engineering Mechanics, ASCE, 122(6), 539-544.

33. Lee, V. W., and Trifuanc, M. D. (1979). *Response of Tunnels to Incident SH-Waves*. Journal of the Engineering Mechanics Division, ASCE, 105(4), 643-659.

34. Liang, J. W., Luo, H., and Lee, V. W. (2004). *Scattering of Plane SH Waves by a Circular-Arc Hill with a Circular Tunnel*, ACTA Seismologica Sinica, 17(5), 549-563.

35. Liang, J. W., Zhang, Y., and Lee, V. W. (2005). *Scattering of Plane P Waves by a Semi-Cylindrical Hill: Analytical Solution*, Earthquake Engineering and Engineering Vibration, 4(1), 27-36.

36. Luco, J. E. (1969). *Dynamic Interaction of a Shear beam with the Soil*, Journal of Engineering Mechanics Division, ASCE, 95(EM2), 333-346.

37. Luco, J. E. (1982). *Linear Soil-Structure Interaction: a Review*, Earthquake Ground Motion and its Effects on Structures, ASME, 53, New York, N.Y., 41-57.

38. MacDonald, H. M. (1902). *Electric Waves.* Cambridge University Press, London, England

39. Mendez, O. M., Cadilhac, M., and Petit, R. (1983). *Diffraction of a Two-Dimensional Electromagnetic Beam Wave by a Thick Slit Pierced in a Perfectly Conducting Screen*, Journal of Optical Society of America, 73(3), 328-331.

40. Mylonakis, G., and Gazetas, G. (2000). *Seismici Soil-Structure Interaction: Beneficial or Detrimental?*, Journal of Earthquake Engineering, 4(3), 277-301

41. Neumaier, Arnold. (1998). *Solving Ill-Conditioned and Singular Linear Systems: A Tutorial on Regularization*, SIAM Review, 40(3), 636-666.

42. Pao, Y.-H, and Mow, C. C. (1973). *Diffraction of Elastic Waves and Dynamics Stress Concentrations.* Crane, Russak & Company Inc., New York, N.Y.

43. Park, T. J., Eom, H. J., and Yoshitomi K. (1993). *An Analysis of Transverse Electric Scattering from a Rectangular Channel in a Conducting Plane*, Radio Science, 28(5), 663-673.

44. Parmelee, R. A. (1967). *Building-Foundation Interaction Effects*. Journal of the Engineering Mechanics Division, ASCE, 93(EM2), 131-152

45. Piessens, R., Doncker-Kapenga, E. d., Überhuber, C. W., and Kahaner, D. K. (1983). *QUADPACK: a Subroutine Package for Automatic Integration*, Springer-Verlag. Berlin Heidelberg, Germany

46. Press, W. H., Flannery, B. P., Teukolsky, S. A., and Vetterling, W. T. (1992). *Numerical Recipes in Fortran 77*: *The Art of Scientific Computing*, 2nd edition, Cambridge University Press.

47. Qiu, F.-Q, and Liu, D.-K. (1993). *Antiplane Response of Isosceles Triangular Hill to Incident SH Waves*, Earthquake Engineering and Engineering Vibration, 4(1), 37-46.

48. Reissner, E. (1936). *Stationäre, axialsymmetrische, durch eine schüttelnde Masseerregte Schwingungen eines homogenen elastichen Halbraumes*. Ingenieur-Archiv, 7(6), 381-396.

49. Reissner, E. (1945). *The Effect of Transverse Shear Deformation on the Bending of Elastic Plates*. Journal of Applied Mechanics, ASME, 12(2), 69-77.

50. Sánchez-Sesma, F. J., Herrera, I., and Avilés, J. (1982). *A Boundary Method for Elastic Wave Diffraction: Application to Scattering of SH-Waves by Surface Irregularities*, Bulletin of the Seismological Society of America, 72(2), 473-490.

51. Sánchez-Sesma, F. J., Palencia, V. J., and Luzón, F. (2002). *Estimation of Local Site Effects during Earthquakes: An Overview*, ISET Journal of Earthquake Engineering, 39(3), 167-193.

52. Tikhonov, A. N., and Arsenin, V. Y. (1977). *Solution of Ill-Posed Problems*, V.H. Winston & Sons, Washington, D.C.

53. Tikhonov, A. N., Goncharsky, A. V., Stepanov, V. V., and Yagola, A. G. (1995). *Numerical Methods for the Solution of Ill-Posed Problems*, Kluwer Academic Publishers.

54. Todorovska, M. I. (1993**a**). *In-Plane Foundation-Soil Interaction for Embedded Circular Foundations*, Soil Dynamics and Earthquake Engineering, 12(5), 283-297.

55. Todorovska, M. I., (1993**b**). *Effects of the Wave Passage and the Embedment Depth for In-plane Building-Soil Interaction*, Soil Dynamics and Earthquake Engineering, 12(6), 343-355.

56. Todorovska, M. I., and Lee, V. W. (1990). *A Note on Response of Shallow Circular Valleys to Rayleigh Waves: Analytical Approach*, Earthquake Engineering and Engineering Vibration, 10(1), 21-34.

57. Todorovska, M. I., and Lee, V. W. (1991). *Surface Motion of Shallow Circular Alluvial Valleys for Incident Plane SH Waves - Analytical Solution*, International Journal of Soil Dynamics and Earthquake Engineering, 10(4), 192-200.

58. Todorovska, M. I., Hayir, A., and Trifunac, M. D. (2001). *Antiplane Response of A Dike on Flexible Embedded Foundation to Incident SH-waves*, Soil Dynamics and Earthquake Engineering, 21(7), 593-601.

59. Trifunac, M. D. (1971). *Surface Motion of a Semi-Cylindrical Alluvial Valley for Incident Plane SH Wave*. Bulletin of Seismological and Society of America, 61(6), 1755-1770.

60. Trifunac, M. D. (1972). *Interaction of a Shear beam with the Soil for Incident Plane SH Waves*, Bulletin of the Seismological Society of America, 62(1), 63-83.

61. Trifunac, M. D. (1973). *Scattering of Plane SH Wave by a Semi-Cylindrical Canyon*. Earthquake Engineering and Structural Dynamics, 1(3), 267-281.

62. Trifunac, M. D., Todorovska, M. I., and Hao, T-Y. (2001). *Full-Scale Experimental Studies of Soil-Structure Interaction - A Review*. Proceeding of second U.S.-Japan Workshop on Soil-Structure Interaction, Tsukuba City, Japan, 1-52.

63. Wong, H. L., and Trifunac, M. D. (1974**a**). *Surface Motion of a Semi-Elliptical Alluvial Valley for Incident Plane SH Waves*, Bulletin of the Seismological Society of America, 64(5), 1389-1408.

64. Wong, H. L., and Trifunac, M. D. (1974**b**). *Interaction of a Shear beam with the Soil for Incident Plane SH Waves: Elliptical Rigid Foundation*, Bulletin of the Seismological Society of America, 64(6), 1825-1842.

65. Wong, H. L., and Trifunac, M. D. (1974**c**). *Scattering of Plane SH Waves by a Semi-Elliptical Canyon*, Earthquake Engineering and Structural Dynamics, 3(2), 157-169.

66. Wong, H. L., and Trifunac, M. D. (1975). *Two-dimensional, Antiplane, Building-Soil-Building Interaction for Two or More Buildings and for Incident Plane SH Waves*, Bulletin of the Seismological Society of America, 65(6), 1863-1885.

67. Wong, H. L. (1975). *Dynamic Soil-structure Interaction*, EERL 75-01, California Institute of Technology, Pasadena, California.

68. Yuan, X. (1996). *Effects of a Circular Underground Inclusion on Surface Motion under Incident Plane SH Waves*, Acta Geophysica Sinica, 39(3), 373-381 (in Chinese).

69. Yuan, X., and Men, F.-L. (1992). *Scattering of Plane SH Waves by a Semi-Cylindrical Hill*, Earthquake Engineering and Structural Dynamics, 21(12), 1091-1098.

70. Yuan, X., and Liao, Z.-P. (1994). *Scattering of Plane SH Waves by a Cylindrical Canyon of Circular-Arc Cross-Section*, Soil Dynamics and Earthquake Engineering, 13(6), 407-412.

71. Yuan, X., and Liao, Z.-P. (1995). *Scattering of Plane SH Waves by a Cylindrical Alluvial Valley of Circular-Arc Cross-Section*, Earthquake Engineering and Structural Dynamics, 24(10), 1303-1313.

72. Yuan, X., and Liao, Z.-P. (1996). *Surface Motion of a Cylindrical Hill of Circular-Arc Cross-Section for Incident Plane SH Waves*, Soil Dynamics and Earthquake Engineering, 15(3), 189-199.

APPENDICES

APPENDIX A: EVALUATION OF INTEGRAL $\int_{-a}^{a} \cos\left[a_m\left(x+a\right)\right] e^{\mathrm{i}kx} \mathrm{d}x$

Assume $b = a_m = m\pi/2a$.

$$\int_{-a}^{a} \cos\left[a_m\left(x+a\right)\right] e^{\mathrm{i}kx} \mathrm{d}x$$

$$= \frac{-k\mathrm{i} + 2\mathrm{i}e^{2\mathrm{i}ka} k \cos^2\left(ab\right) - e^{2\mathrm{i}ka} k\mathrm{i} + 2e^{2\mathrm{i}ka} b \sin\left(ab\right)\cos\left(ab\right)}{b^2 - k^2} e^{-\mathrm{i}ka}$$

$$= \frac{-k\mathrm{i}e^{-\mathrm{i}ka} + \mathrm{i}e^{\mathrm{i}ka} k\left[2\cos^2\left(ab\right) - 1\right] + e^{\mathrm{i}ka} b \sin\left(2ab\right)}{b^2 - k^2}$$

$$= \frac{-k\mathrm{i}e^{-\mathrm{i}ka} + \mathrm{i}ke^{\mathrm{i}ka}\cos\left(m\pi\right) + \left(m\pi/2a\right) e^{\mathrm{i}ka}\sin\left(m\pi\right)}{\left(m\pi/2a\right)^2 - k^2}$$

$$= \frac{e^{\mathrm{i}ka}\left(-1\right)^m - e^{-\mathrm{i}ka}}{k^2 - \left(m\pi/2a\right)^2}\left(-k\mathrm{i}\right)$$

So,

$$\int_{-a}^{a} \cos\left[a_m\left(x+a\right)\right] e^{\mathrm{i}kx} \mathrm{d}x = \frac{\left(-1\right)^m e^{\mathrm{i}ka} - e^{-\mathrm{i}ka}}{k^2 - \left(m\pi/2a\right)^2}\left(-k\mathrm{i}\right), \text{ for } m = 1, 2, 3, \ldots$$

Similarly, the following integration could be derived,

$$\int_{-a}^{a} \cos\left[a_m\left(x+a\right)\right] e^{-\mathrm{i}kx} \mathrm{d}x = \frac{\left(-1\right)^m e^{-\mathrm{i}ka} - e^{\mathrm{i}ka}}{k^2 - \left(m\pi/2a\right)^2}\left(k\mathrm{i}\right)$$

APPENDIX B: EVALUATION OF INTEGRAL I_{mn}

This appendix is to derive the expression of integral I_{mn} of equation (13.15). Different from Park et al (1993), which shows an analytic but intricate expression involving many complex number and special function computations, this report adopted directly numerically quadrature which was well treated in Mendez et al (1983).

As Eq. (13.15) says,

$$I_{mn} = \int_{-\infty}^{\infty} (ka)^2 F_m(ka) F_n(-ka) \zeta^{-1} \mathrm{d}k \text{, with } \zeta = \sqrt{k_\beta^2 - k^2} .$$

where,

$$F_m(ka) = \frac{(-1)^m e^{\mathrm{i}ka} - e^{-\mathrm{i}ka}}{(ka)^2 - (m\pi/2)^2} = \begin{cases} \dfrac{2\mathrm{i}\sin(ka)}{(ka)^2 - (m\pi/2)^2} & m \quad \text{even} \\ \dfrac{-2\cos(ka)}{(ka)^2 - (m\pi/2)^2} & m \quad \text{odd} \end{cases}$$

$$F_n(-ka) = \frac{(-1)^n e^{-\mathrm{i}ka} - e^{\mathrm{i}ka}}{(ka)^2 - (n\pi/2)^2} = \begin{cases} \dfrac{-2\mathrm{i}\sin(ka)}{(ka)^2 - (n\pi/2)^2} & n \quad \text{even} \\ \dfrac{-2\cos(ka)}{(ka)^2 - (n\pi/2)^2} & n \quad \text{odd} \end{cases}$$

So, $F_m(ka) F_n(-ka)$ is an odd function only if *m*, *n* are in the opposite parity, when $I_{mn} \equiv 0$. Therefore, I_{mn} exists only when *m*, *n* are both even or both odd. Then,

When *m*, *n* are both even,

$$F_m(ka) \cdot F_n(-ka) = \frac{4\sin^2(ka)}{\left[(ka)^2 - (m\pi/2)^2\right]\left[(ka)^2 - (n\pi/2)^2\right]} = \frac{2\left[1 - \cos(2ka)\right]}{\left[(ka)^2 - (m\pi/2)^2\right]\left[(ka)^2 - (n\pi/2)^2\right]}$$

When m, n are both odd,

$$F_m(ka)\cdot F_n(-ka)=\frac{4\cos^2(ka)}{\left[(ka)^2-(m\pi/2)^2\right]\left[(ka)^2-(n\pi/2)^2\right]}=\frac{2\left[1+\cos(2ka)\right]}{\left[(ka)^2-(m\pi/2)^2\right]\left[(ka)^2-(n\pi/2)^2\right]}$$

Summarize the above two cases, we could get

$$F_m(ka)F_n(-ka)=\frac{2\left[1-(-1)^n\cos(2ka)\right]}{\left[(ka)^2-(m\pi/2)^2\right]\left[(ka)^2-(n\pi/2)^2\right]}$$, when m, n are in the same parity.

Plugging it into I_{mn}, then $I_{mn}=\int_{-\infty}^{\infty}\frac{(ka)^2}{\sqrt{k_\beta^2-k^2}}\frac{2\left[1-(-1)^n\cos(2ka)\right]}{\left[(ka)^2-(m\pi/2)^2\right]\left[(ka)^2-(n\pi/2)^2\right]}\mathrm{d}k$.

Substituting the integration variable to $v=ka$. Thus,

$$I_{mn}=\begin{cases}\displaystyle\int_{-\infty}^{\infty}\frac{v^2}{\sqrt{(k_\beta a)^2-v^2}}\frac{2\left[1-(-1)^n\cos(2v)\right]}{\left[v^2-(m\pi/2)^2\right]\left[v^2-(n\pi/2)^2\right]}\mathrm{d}v, & m \,\&\, n \text{ both odd or even}\\ 0, & \text{otherwise}\end{cases}$$

For the cases of m, n are in the same parity,

$$I_{mn}=\int_{-\infty}^{\infty}G_1(v)\left[1-(-1)^n\cos(2v)\right]\mathrm{d}v$$

where,

$$G_1(v)=\frac{\beta(v)}{\left[v^2-(m\pi/2)^2\right]\left[v^2-(n\pi/2)^2\right]}$$

$$\beta(v)=\frac{2v^2}{\sqrt{(k_\beta a)^2-v^2}}$$

By means of theory of contour integration (some derivation and diagrams are omitted here),

$$I_{mn} = \int_{\Gamma_1} G_1(v)\left[1-(-1)^n \exp(\mathrm{i}\cdot 2v)\right]\mathrm{d}v = \rho_n \delta_{mn} + 2\int_{\Delta} G_1(v)\left[1-(-1)^n \exp(2\mathrm{i}v)\right]\mathrm{d}v$$

in which, $\rho_n = \dfrac{2\pi\varepsilon_n}{a\sqrt{k_\beta^2 - a_m^2}}$ is the residue of the pole at $\alpha = n\pi / l$, which appears now for *m*=*n*. δ_{mn} is the Kronecker Delta.

After replacing $\int \cos(2v)$ by $\int \dfrac{e^{\mathrm{i}2v}}{2} + \int \dfrac{e^{-\mathrm{i}2v}}{2}$, on Δ, $e^{2\mathrm{i}v} = e^{2\mathrm{i}(k_\beta a + \mathrm{i}\delta)} = e^{2\mathrm{i}k_\beta a} e^{-2\delta}$

$$I_{mn} = \frac{2\pi\varepsilon_n}{a\sqrt{k_\beta^2 - a_m^2}}\delta_{mn} + 2\int_0^\infty G_1(k_\beta a + \mathrm{i}\delta)\left[1-(-1)^n \exp(2\mathrm{i}k_\beta a)\exp(-2\delta)\right]\cdot \mathrm{i}\mathrm{d}\delta$$

Note that $\delta = 0$ is the singularity of this integral because the denominator of $\beta(v)$ equals zero. QUADPACK routines DQAGS and DQAGI are employed to numerically evaluate this integral.

APPENDIX C: AUTOMATIC SATISFACTION OF TRACTION-FREE BOUNDARY CONDITION

For the traction-free condition along the boundaries of the structure, i.e., Eqns (13.9) and (13.10), just simply substitute Eqn (13.6) into those two Eqns.

For Eqn. (13.9),

$$\mu_{\mathrm{B}} \left.\frac{\partial w^{(\mathrm{B})}}{\partial x}\right|_{x=\pm a} = -\mu_{\mathrm{B}} \frac{m\pi}{2a} \sum_{m=0}^{\infty} B_m \sin\left[\frac{m\pi}{2a}(x+a)\right] \cos\left[\sqrt{k_{\mathrm{B}}^2 - \left(\frac{m\pi}{2a}\right)^2}\,(y+d)\right]\Bigg|_{x=\pm a}$$

$$= -\mu_{\mathrm{B}} \frac{m\pi}{2a} \sum_{m=0}^{\infty} B_m \cos\left[\sqrt{k_{\mathrm{B}}^2 - \left(\frac{m\pi}{2a}\right)^2}\,(y+d)\right] \begin{Bmatrix} \sin(m\pi) = 0 & , & x = a \\ 0 & , & x = -a \end{Bmatrix} \equiv 0$$

So, boundary condition Eq. (13.9) is automatically satisfied.

As for Eqn. (13.10),

$$\mu_{\mathrm{B}} \left.\frac{\partial w^{(\mathrm{B})}}{\partial y}\right|_{y=-d} = -\mu_{\mathrm{B}} \sqrt{k_{\mathrm{B}}^2 - (m\pi/2a)^2} \sum_{m=0}^{\infty} B_m \cos\left[a_m (x+a)\right] \sin\left[\sqrt{k_{\mathrm{B}}^2 - (m\pi/2a)^2}\,(y+d)\right]\Bigg|_{y=-d} \equiv 0$$

So, boundary condition Eqn. (13.10) is automatically satisfied also.

APPENDIX D: EVLUATION OF $P^*(m,x)$

The four integrals of $P^*\left(m,x\right)$ in Eqn. (13.59) could be summarized into the following form,

$$2\int_0^\infty \frac{k\sin ck}{k^2-a_m^2}\mathrm{d}k \text{ , with } c=a\pm x$$

Then, replace integration variable k by $u=ck$, so for the cases when $c\neq 0$, integration could be rewritten to

$$2\int_0^\infty \frac{u\sin u}{u^2-\left(a_m c\right)^2}\mathrm{d}u = 2\left[\frac{1}{2}\int_0^\infty \frac{\sin u}{u+a_m c}\mathrm{d}u+\frac{1}{2}\int_0^\infty \frac{\sin u}{u-a_m c}\mathrm{d}u\right]=\int_0^\infty \frac{\sin u}{u+a_m c}\mathrm{d}u+\int_0^\infty \frac{\sin u}{u-a_m c}\mathrm{d}u$$

The resultant half-infinite integrations looks quite simple, but they do not converge at the same time. Those two integrals can be expressed explicitly,

$$\int_0^\infty \frac{\sin u}{u+a_m c}\mathrm{d}u=\begin{cases}\text{undefined} & , a_m c<0\\ -\mathrm{Si}(a_m c)\cos(a_m c)+\mathrm{Ci}(a_m c)\sin(a_m c)+\frac{\pi}{2}\cos(a_m c) & , a_m c>0\end{cases}$$

$$\int_0^\infty \frac{\sin u}{u-a_m c}\mathrm{d}u=\begin{cases}\text{undefined} & , a_m c>0\\ \mathrm{Si}(a_m c)\cos(a_m c)-\mathrm{Ci}(-a_m c)\sin(a_m c)+\frac{\pi}{2}\cos(a_m c) & , a_m c<0\end{cases}$$

those two integrals could not converge simultaneously, namely $\sin(u)/\left(u+b\right)$ does not converge for b less than 0. In the expressions above, $\mathrm{Si}\left(\cdot\right)$ and $\mathrm{Ci}\left(\cdot\right)$ respectively refer to Sine and Cosine integrals.

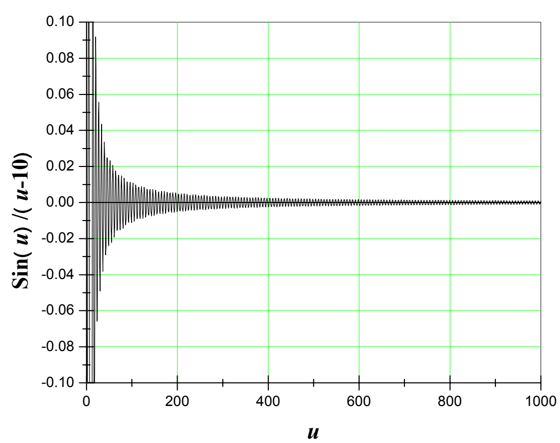

The above graph plots $\sin(u)/(u-10)$ with respect to u ranging from 0 to 1000. We can see that the integrand curve converges very slow. That may be the reason why the resultant stress curves in Fig. 7-7 oscillate.

About the parameter $a_m c = a_m\left(a \pm x\right) = \dfrac{m\pi}{2a}\left(a \pm x\right) = \dfrac{m\pi}{2}\left(1 \pm \dfrac{x}{a}\right)$,

$$a_m c > 0 \Rightarrow \begin{cases} 1+\dfrac{x}{a} > 0 \\ 1-\dfrac{x}{a} > 0 \end{cases} \Rightarrow \begin{cases} x > -a \\ x < a \end{cases}$$

$$a_m c < 0 \Rightarrow \begin{cases} 1+\dfrac{x}{a} < 0 \\ 1-\dfrac{x}{a} < 0 \end{cases} \Rightarrow \begin{cases} x < -a \\ x > a \end{cases}$$

So, both cases would happen for the same initial conditions. Integrals $\int_0^\infty \dfrac{\sin u}{u - a_m c}\mathrm{d}u$ and $\int_0^\infty \dfrac{\sin u}{u + a_m c}\mathrm{d}u$ could not converge at the same time.

APPENDIX E: EVALUATION OF SOME TRIGONOMETRIC INTEGRALS

Three identities used to derive the Lemma in Section 6.2.2.2. Here the following identities of trigonometric integrals are used:

(i) $\int_0^\pi \sin m\theta \sin n\theta \, \mathrm{d}\theta = \frac{\pi}{2}\delta_{mn} \qquad m, n = 1, 2, 3\ldots$

$$\int_0^\pi \sin m\theta \sin n\theta \, \mathrm{d}\theta = \frac{1}{2}\int_0^\pi \left(\cos(m-n)\theta - \cos(m+n)\theta\right)\mathrm{d}\theta$$
$$= \begin{cases} \frac{1}{2}\left(\frac{\sin(m-n)\theta}{m-n} - \frac{\sin(m+n)\theta}{m+n}\right)\Bigg|_0^\pi = 0 & m \neq n \\ \frac{\pi}{2} & m = n \end{cases}$$

(ii) $\int_0^\pi \cos m\theta \cos n\theta \, \mathrm{d}\theta = \frac{\pi}{\varepsilon_m}\delta_{mn} \qquad m, n = 0, 1, 2\ldots \qquad \varepsilon_0 = 1;\ \varepsilon_m = 2,\ m > 0$

$$\int_0^\pi \cos m\theta \cos n\theta \, \mathrm{d}\theta = \frac{1}{2}\int_0^\pi \left(\cos(m-n)\theta + \cos(m+n)\theta\right)\mathrm{d}\theta$$
$$= \begin{cases} \pi & m = n = 0 \\ \frac{1}{2}\left(\frac{\sin(m-n)\theta}{m-n} + \frac{\sin(m+n)\theta}{m+n}\right)\Bigg|_0^\pi = 0 & m \neq n \\ \frac{\pi}{2} & m = n \neq 0 \end{cases}$$

(iii) $\int_0^\pi \sin m\theta \cos n\theta \, \mathrm{d}\theta = \frac{1}{2}\int_0^\pi \left(\sin(m+n)\theta + \sin(m-n)\theta\right)\mathrm{d}\theta$

$$= \frac{1}{2}\left(\frac{-\cos(m+n)\theta}{m+n} + \frac{-\cos(m-n)\theta}{m-n}\right)\Bigg|_0^\pi$$
$$= \frac{1}{2}\left(\frac{1-(-1)^{m+n}}{m+n} + \frac{1-(-1)^{m-n}}{m-n}\right) = \begin{cases} \frac{2m}{m^2-n^2} & m+n \text{ odd} \\ 0 & m+n \text{ even} \end{cases}$$